Flocculation and transport of mud in rivers and deltas

Thesis by

Justin A. Nghiem

In Partial Fulfillment of the Requirements for
the degree of
Doctor of Philosophy

CALIFORNIA INSTITUTE OF TECHNOLOGY
Pasadena, California

2025
(Defended April 24, 2025)

Justin A. Nghiem
ORCID: 0000-0003-2772-9945

ACKNOWLEDGEMENTS

I dedicate my dissertation to those who have played such pivotal roles in my life not only during my time at Caltech, but also throughout my personal and academic journey. These people are truly responsible for my humble achievements.

I would first like to thank my thesis advisor, Mike Lamb, for mentoring me throughout my PhD career. You taught me so many tools of the scientific enterprise like making field observations, identifying important science questions, interpreting data, writing papers, and presenting my research. When I first came to Caltech, one of my goals was to gain more fieldwork experience. You not only gave me many field opportunities, but also showed me how to be a field scientist. I owe much of my development as a young geomorphologist to your generosity and care in sharing your knowledge. Beyond science, I am also thankful for unexpectedly useful practical life lessons from you in the field.

I am grateful for Woody Fischer, who has been another important mentor for me at Caltech. Your boundless enthusiasm for research and discovery is infectious and gave me greater confidence in my work. I am thankful to have worked with you on my first-year project. You were always generous with your time to have science discussions and gave me the incredible opportunity to work on the beamline. I have valued your feedback throughout the years as a collaborator and a member of my thesis committee. Thank you too for providing me the lab space to work on all my sediment samples.

I would like to acknowledge Gen Li for being a good friend and collaborator. I will always remember our adventures in the field and long hours spent together filtering suspended sediment samples and working in the lab. You took me under your wing and showed me how to analyze samples in the lab starting from square one. I am grateful for our many conversations on professional career advice and just life in general. Even after leaving Caltech, you have continued to be a friend and advocate to me.

I thank the wonderful members of the Lamb group, past and present, for their camaraderie and support: Austin Chadwick, Alistair Hayden, Madison Douglas, Oak Kanine, Hussain Alqattan, Samantha Baker, Emily Geyman, Maria Schmeer, Kenny Thai, Isaac Smith, Ayush Bhattacharya, Kaliyah Watson, Brayden Noh, Lisanne Braat, Tamara Pico, Gen Li, Tien-Hao Liao, Gerard Salter, Ben Cardenas, Kieran Dunne, Omar Wani, Abdallah Zaki, Yutian Ke, Dongchen Wang, Harrison Martin, Tingan Li, and Kim Miller. I have shared so many fun and scientifically productive times with you all in the field, office, lab, and camping trips.

I would not be here at Caltech earning my degree without the support of Kurt Cuffey and Laurel Larsen during my undergraduate days at UC Berkeley. Kurt introduced me to the world of geomorphology and made me excited to pursue geomorphology research and grad school. Laurel welcomed me into her lab and gave me my first research opportunity, which eventually set me on my way to Caltech.

I would not have been able to be so productive without the help of the following Caltech faculty and staff. I thank Andy Thompson for useful science feedback as part of my thesis committee. Julie Lee, Jen Shechet, and Julia Zuckerman for helping me with logistical tasks in the division. Mark Garcia for keeping field gear and vehicles stocked and maintained. Jay Dickson for help with GIS tasks. Janice Grancich, Mary Scott, Margaret Carlos, and Claire Fredrickson for handling the financial and budget sides of research. John Magyar, Kim Miller, and Nathan Dalleska for managing the labs that I frequented.

Thank you to all the friends I have made along the way at Caltech. The PhD journey, as rewarding as it was, was stressful and lonely at times. You all gave me much needed entertainment, levity, and friendship to make it through. I have gotten to know so many of you over the years, but I would like to acknowledge in particular Josh Anadu, Juan David Hernández Montenegro, Maria Schmeer, Yutian Ke, Dongchen Wang, Kim Miller, Eran Funaro, Abdallah Zaki, Harrison Martin, Ruolin Deng, Hussain Alqattan, Vincent Lee, and all the Caltech squirrels.

I owe much to friends outside of Caltech too: Cibi Pari, Chris Powers, and Shuchay Subramanian. Thank you for all the fun times at conventions, concerts, and fantasy sumo when I needed a break from research.

I am eternally grateful for my loved ones from the bottom of my heart. Maria, you brighten my days and have been an endless source of joy, love, and hope for me always, anywhere from low stressful points to our fun and exciting adventures. I thank my sister, Athena, for a literal lifetime of friendship and setting a high example for me to follow. I thank my brother-in-law, Neil, for his humor, friendship, and reliability. Finally, and most importantly, I am here now because of my parents, Anh Lieu and Son Nghiem, and my grandparents. They dedicated their whole lives to ensuring that I could succeed. They are truly responsible for anything and everything I have accomplished.

ABSTRACT

Mud (grains < 62.5 μm) dominates the sediment load of rivers from continents to the ocean and contributes to building coastal land and sequestering organic carbon. However, predicting mud transport is challenging because flocculation causes mud grains to aggregate into larger, faster settling particles called flocs, which dynamically respond to local flow, water, and sediment properties. In this thesis, I examined the factors controlling mud flocculation in rivers and deltas and the effects of enhanced floc settling velocity on mud accretion in a river delta using fieldwork and data compilations from the river sediment literature. Flocs have the potential to dictate mud deposition rates and transport patterns by effectively enhancing mud settling velocity. First, I developed a semi-empirical model to predict floc diameter and settling velocity in rivers using a global river data compilation (Chapter 2). Results show that turbulence, sediment concentration and mineralogy, organic matter concentration, and water chemistry are the key flocculation factors in rivers. I conducted fieldwork in the Wax Lake Delta, Louisiana, a river delta in the Mississippi River Delta complex. Based on floc measurements at the Wax Lake Delta, I validated the semi-empirical model and showed that a complementary physics-based floc settling velocity model relies on the permeability and fractal structure of flocs (Chapter 3). To better link floc settling velocity and mud transport, I used the Wax Lake Delta field data to demonstrate that flocculated mud might behave as bed-material load rather than washload (Chapter 4). This result implies that mud concentration and flux might be readily predictable from bed-material entrainment theory using local bed and flow measurements. Connecting mud transport to delta island sedimentation and delta resilience, I analyzed discharge and sediment flux in the Wax Lake Delta to understand how sediment is delivered to and transported in islands (Chapter 5). Field data and backwater modeling results show that tall levees can block flow, but intricate feedbacks between flow depth, velocity, and water surface slope set discharge and sediment flux into the island once primary channels overflow into islands. Suspended mud settles fast enough relative to island flow depth and velocity to settle out within the island rather than bypass. As such, mud can accrete and build up the island over time as evidenced by mud-rich island deposits in Wax Lake Delta. Finally, combining Wax Lake Delta data and a river data compilation on suspended sediment grain size and mineralogy, I showed that most suspended sediment in rivers is flocculated silt (Chapter 6). This silt likely flocculates due to physical trapping mechanisms rather than typically considered interactions between clay minerals and salinity because clay minerals compose a minority of the silt. Overall, this thesis informs how flocculation affects mud transport in rivers and deltas, encompassing the mechanisms of mud flocculation, predictions of floc settling velocity and mud concentration, and the significance of mud flocculation in shaping depositional landscapes.

PUBLISHED CONTENT AND CONTRIBUTIONS

Journal Publications

Nghiem, J. A., Fischer, W. W., Li, G. K., & Lamb, M. P. (2022). A Mechanistic Model for Mud Flocculation in Freshwater Rivers. *Journal of Geophysical Research: Earth Surface*, *127*(5), e2021JF006392. https://doi.org/10.1029/2021JF006392

J.A.N. participated in the project conception, compiled and analyzed data, and led the writing of the manuscript.

Nghiem, J. A., Li, G. K., Harringmeyer, J. P., Salter, G., Fichot, C. G., Cortese, L., & Lamb, M. P. (2024). Testing floc settling velocity models in rivers and freshwater wetlands. *Earth Surface Dynamics*, *12*(6), 1267–1294. https://doi.org/10.5194/esurf-12-1267-2024

J.A.N. participated in the project conception, collected and analyzed field data, and led the writing of the manuscript.

Datasets

Christensen, A. L., Mallard, J. M., Nghiem, J., Harringmeyer, J., Simard, M., Pavelsky, T. M., Lamb, M. P., & Fichot, C. G. (2022). *Delta-X: Sonar Bathymetry Survey of Channels, MRD, Louisiana, 2021* [Dataset]. ORNL DAAC. https://doi.org/10.3334/ORNLDAAC/2085

Christensen, A. L., Mallard, J. M., Nghiem, J., Simard, M., Pavelsky, T. M., & Lamb, M. P. (2022). *Delta-X: Acoustic Doppler Current Profiler Channel Surveys, MRD, Louisiana, 2021, V2* [Dataset]. ORNL DAAC. https://doi.org/10.3334/ORNLDAAC/2081

Nghiem, J. (2022). *Sediment Accretion Rates and Spatial Patterns in the Wax Lake Delta, LA 2020* [Dataset]. OpenTopography. https://doi.org/10.5069/G99W0CP6

Nghiem, J., Salter, G., & Lamb, M. P. (2024). *Delta-X: Bed and Suspended Sediment Grain Size, MRD, LA, USA, 2019-2021, V3* [Dataset]. ORNL DAAC. https://doi.org/10.3334/ORNLDAAC/2379

Nghiem, J., Salter, G., & Lamb, M. P. (2025). *Delta-X: Sediment Core Grain Size Distribution, Wax Lake Delta, MRD, LA* [Dataset]. ORNL DAAC. https://doi.org/10.3334/ORNLDAAC/2382

Nghiem, J., Salter, G., Wright, K. A., Passalacqua, P., & Lamb, M. P. (2022). *Delta-X: Turbidity, Water and Air Pressure, Temperature, MRD, Louisiana, 2021, V4* [Dataset]. ORNL DAAC. https://doi.org/10.3334/ORNLDAAC/2241

TABLE OF CONTENTS

LIST OF FIGURES AND TABLES

Figures *Page*

Tables *Page*

Chapter 1

INTRODUCTION

Rivers move enormous volumes of water, sediment, and solutes globally through continents and into the ocean. Rivers typically deposit sediment and build land as they approach the coast. These fluvial landscapes host large populations, diverse ecosystems, and infrastructure, but are subject to dynamic river flooding and sedimentation processes that often constitute natural hazards to humans. In particular, mud (grains < 62.5 μm) plays a key role in these processes because it is ubiquitous in rivers (Fig. 1.1).

Figure 1.1. A mud-rich island in the Wax Lake Delta, Louisiana, USA, a river delta in the Mississippi River Delta complex.

Why is it important to understand mud transport in rivers?

One reason is that river mud is a vehicle for carrying materials like organic carbon (Galy et al., 2008; Blair and Aller, 2012) and pollutants (Nelson and Lamothe, 1993; Pizzuto, 2014) on the surface of grains. Mud has great capacity to host these materials because its fine grain size gives it greater surface area per mass compared to coarser sediment like sand. If one wants to know where sediment-bound materials are going, then one needs to know where the mud is going. This idea is critical in the terrestrial carbon cycle because the vulnerability of sediment-bound river organic carbon to oxidation (i.e., carbon release to the atmosphere) relies on the degree to which mud deposition protects organic carbon.

Another reason to study mud transport in rivers is that mud is the key natural resource to build land in coasts and offset sea level rise. In particular, river deltas have become increasingly at risk of losing large areas of land to sea level rise (Syvitski et al., 2009; Couvillion et al., 2017). One solution is to build up land in deltas by accreting sediment, most of which is mud in these distal low-gradient coastal zones. If mud sedimentation rate is sufficiently high to keep pace with sea level rise (Giosan et al., 2014), then land loss could be mitigated in deltas. Faster sedimentation rates also aid efficient organic carbon burial and limit atmospheric carbon release (Blair and Aller, 2012). However, coastal restoration engineering faces high uncertainty because of knowledge gaps in sediment transport mechanisms (e.g., Allison and Meselhe, 2010).

Although mud sedimentation and land building can help combat sea level rise, the alluvial sedimentary record suggests that mud did not always build land. McMahon and Davies (2018) showed that pre-Silurian alluvial rocks contain very little mud, but mud dominates alluvial rocks from the Silurian onward. So although mud is an important part of modern rivers and floodplains, ancient rivers might not have been able to preserve mud for reasons that remain unclear (Zeichner, Nghiem et al., 2021). This dichotomy has the potential to reveal the core features of mud transport that allow mud to construct modern alluvial landscapes.

How is mud transported in rivers?

Understanding mud transport in rivers is critical for evaluating these motivating factors. The classic paradigm is that mud behaves as washload. That is, mud simply washes through rivers without exchange between the river bed and flow because its grain size and hence settling velocity are so small (Einstein et al., 1940; Church, 2006; Fig. 1.2). It implies that external sediment supply, like soil erosion, controls mud concentration in rivers. In other words, local flow conditions and bed grain size composition in the river are thought to be unrelated to mud concentration because local mud entrainment and deposition are assumed to not occur. If mud behaves as washload, then predicting mud transport is difficult because one must be able to predict the sources of mud distributed all along the river.

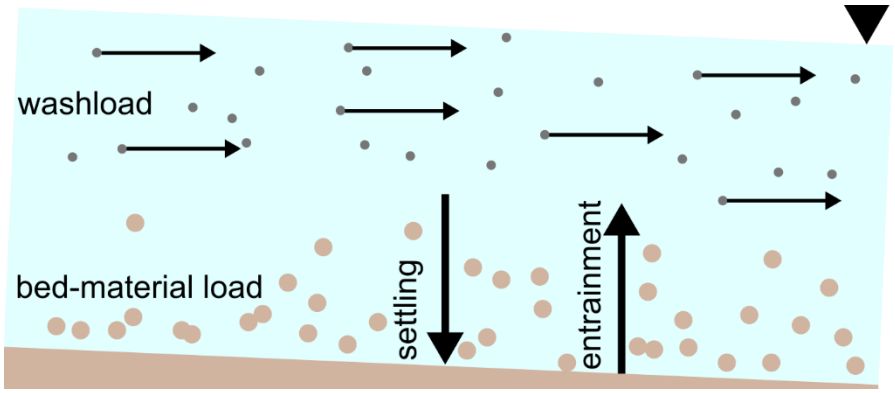

Figure 1.2. Schematic of a river cross-section showing washload versus bed-material load.

However, it is clear that the washload paradigm is flawed because mud is clearly abundant in river and coastal deposits (Fig. 1.1). An alternative hypothesis of mud transport is that flocculation increases mud settling velocity such that mud behaves as bed-material load. Bed-material load is the sediment that is actively exchanged between the river bed and flow, making it possible to predict the entrainment rate and concentration of bed-material load using local flow conditions and bed grain size distribution (Einstein, 1950; García and Parker, 1991; De Leeuw et al., 2020). The bed-material load treatment is standard for sand because sand is relatively coarse and settles quickly, but thought to be not applicable to mud because mud settles too slowly.

Flocculation of mud has the potential to increase mud settling velocity and cause mud to behave more like bed-material load. Small grain size and the presence of clay minerals often cause mud to be cohesive (e.g., Ternat et al., 2008) and flocculate (e.g., Van Leussen, 1988). Flocculation is the process by which sediment grains aggregate in situ into larger particles called flocs. Flocculation increases the settling velocity of mud because flocs settle faster than individual mud grains. Faster mud settling velocity might cause mud to behave more as bed-material load by promoting active mud exchange between the bed and flow (Fig. 1.2). In this case, it would be possible to predict mud concentrations based on local bed and flow properties as Lamb et al. (2020) showed. They developed a model to predict mud concentration in rivers as bed-material rather than washload, but relied on inferred river floc settling velocity data. Additionally, it is unknown whether the bed-material load treatment applies in river deltas, where the bed tends to be muddier and more cohesive than that in rivers and might instead follow a cohesive entrainment equation (Partheniades, 1965).

Research Questions

To evaluate these hypotheses on mud transport in rivers, my thesis focuses on three broad goals that span increasing spatial scales: (1) predicting floc settling velocity (individual floc scale), (2) understanding the impact of flocculation on mud transport mechanics and the construction of rivers and deltas (reach scale), and (3) assessing the overall grain size, mineralogy, and flocculation state in rivers globally (continental scale).

First, floc settling velocity in rivers is important because it dictates the sediment transport behavior of flocculated sediment (e.g., Lamb et al., 2020). But predicting floc settling velocity is difficult because flocs dynamically grow and break up in response to flow conditions and sediment properties (Kranck and Milligan, 1980; Winterwerp, 1998). Classically, Stokes law is used to predict the settling velocity as a function of grain size (Stokes, 1851; Ferguson and Church, 2004; Fig. 1.3). But Stokes law only applies to individual grains and not flocs. To overcome this problem, Strom and Keyvani (2011) modified Stokes law to derive a floc settling velocity equation as a function of floc diameter. In conjunction, Winterwerp (1998) developed a model to predict floc diameter based on turbulence driving particle collisions and floc breakage and calibrated the model using estuarine floc data. However, the Winterwerp model is limited because (1) the effects of other key flocculation factors like organic matter binding and sediment mineralogy are not explicitly included and (2) the model has not been calibrated on river floc data.

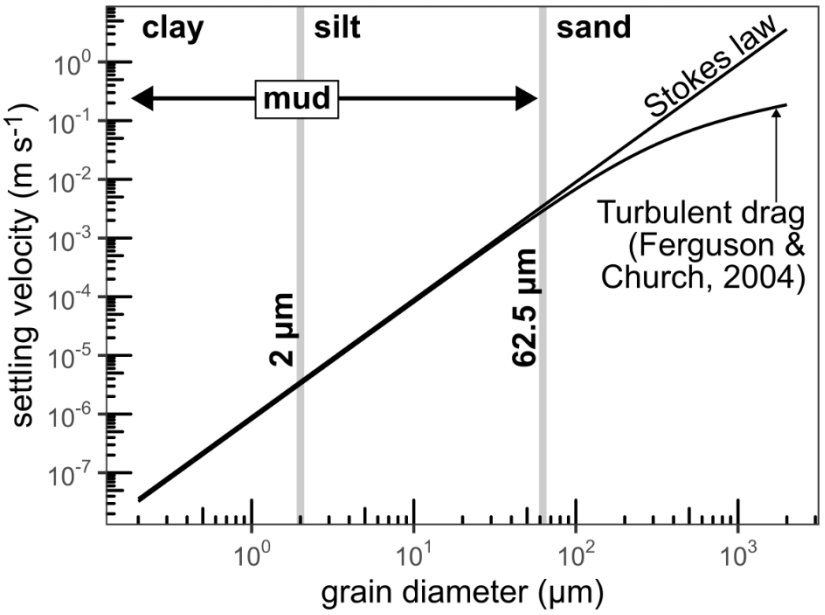

Figure 1.3. Settling velocity versus grain diameter predicted by Stokes law. The Ferguson and Church (2004) curve is a modification of Stokes law that accounts for the turbulent drag of coarser grains.

In this thesis, I develop a semi-empirical model to predict river floc diameter and settling velocity as an explicit function of turbulence, sediment concentration and mineralogy, organic matter concentration, and water chemistry (Chapter 2). I calibrate the model using river floc settling velocities inferred from fitting sediment transport theory to a data compilation of vertical profiles of suspended sediment concentration in rivers. To better validate this semi-empirical settling velocity model, I conducted fieldwork at the Wax Lake Delta, Louisiana, USA, a river delta in the Mississippi River Delta complex, to measure floc properties. I use these direct measurements of flocs to validate the semi-empirical model and, additionally, the Strom and Keyvani (2011) floc settling velocity model (Chapter 3).

The second goal is to understand the role of flocculation in mud transport mechanisms and alluvial landscapes. I use the Wax Lake Delta field data to investigate whether mud in river deltas can be treated as flocculated bed-material load (Chapter 4). Flocculation might not only facilitate mud concentration prediction, but also aid land building by promoting faster mud sedimentation rates in more proximal parts of river deltas. Sediment in suspension in a river moves both vertically because of its settling velocity and horizontally because of the river flow velocity. Faster settling sediment travels a shorter distance (i.e., advection length) before reaching the bed and potentially building sediment deposits (Lamb et al., 2010; Fig. 1.4). If flocculation can sufficiently increase the settling velocity of mud, then mud can be more easily captured in nearshore environments like deltas and build land rather than being washed away to the ocean.

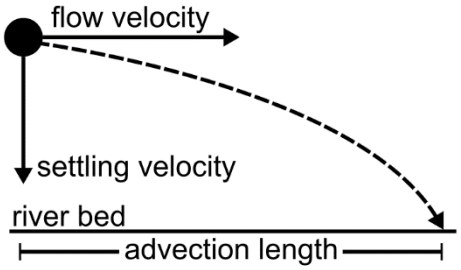

Figure 1.4. Schematic of sediment advection length, $l_a = \bar{u}h/w_s$ where $\bar{u}$ is the depth-averaged flow velocity (m s^{-1}), h is the flow depth (m), and w_s is the settling velocity (m s^{-1}).

Ultimately, understanding how sediment is delivered to delta islands is critical for forecasting whether river deltas will survive sea level rise. Delta islands are the shallow loci of sedimentation in river deltas, so they must keep pace with sea level rise for the delta to avoid being irreversibly drowned (Salter and Lamb, 2022). Numerical models have shed light on the factors controlling sediment retention and accretion rate in deltas (Nardin and Edmonds, 2014; Olliver et al., 2020), but field measurements of flow hydraulics and sediment fluxes have been limited. In this thesis, I report field data of hydraulics, suspended sediment, and sediment deposits from the Wax Lake Delta to provide insight into the tidal and river processes that contribute sediment to delta islands (Chapter 5).

The third goal, at the broadest spatial scale, is to understand the typical grain size, mineralogy, and flocculation state of suspended sediment in alluvial rivers globally. Wentworth (1922) presented a now-standard clastic sediment grain size system in which clay size is the finest sediment class and is assumed to consist of clay minerals, while coarser grains are expected to consist of non-clay minerals. Clay minerals are often thought to be the most susceptible to flocculation because of their mineralogy and small grain size (Velde, 1995). But sediment grains coarser than clay sizes have been shown to readily flocculate in rivers too (Lamb et al., 2020) despite their expected non-clay mineralogy. I resolve this paradox and reveal the typical state of river suspended sediment by synthesizing sediment grain size, clay mineralogy, and flocculation measurements from the Wax Lake Delta and rivers compiled from the literature (Chapter 6).

References

Allison, M. A., & Meselhe, E. A. (2010). The use of large water and sediment diversions in the lower Mississippi River (Louisiana) for coastal restoration. *Journal of Hydrology, 387*(3–4), 346–360. https://doi.org/10.1016/j.jhydrol.2010.04.001

Blair, N. E., & Aller, R. C. (2012). The Fate of Terrestrial Organic Carbon in the Marine Environment. *Annual Review of Marine Science, 4*(1), 401–423. https://doi.org/10.1146/annurev-marine-120709-142717

Church, M. (2006). Bed material transport and the morphology of alluvial river channels. *Annual Reviews of Earth and Planetary Science*, *34*, 325–354. https://doi.org/10.1146/annurev.earth.33.092203.122721

Couvillion, B. R., Beck, H., Schoolmaster, D., & Fischer, M. (2017). Land area change in coastal Louisiana (1932 to 2016). *USGS Scientific Investigations Maps*. https://doi.org/10.3133/sim3381

De Leeuw, J., Lamb, M. P., Parker, G., Moodie, A. J., Haught, D., Venditti, J. G., & Nittrouer, J. A. (2020). Entrainment and suspension of sand and gravel. *Earth Surface Dynamics*, *8*(2), 485–504. https://doi.org/10.5194/esurf-8-485-2020

Einstein, H. A. (1950). *The bed-load function for sediment transportation in open channel flows* (Issue 1026). US Department of Agriculture.

Einstein, H. A., Anderson, A. G., & Johnson, J. W. (1940). A distinction between bed-load and suspended load in natural streams. *Eos, Transactions American Geophysical Union*, *21*(2), 628–633. https://doi.org/10.1029/TR021i002p00628

Ferguson, R. I., & Church, M. (2004). A Simple Universal Equation for Grain Settling Velocity. *Journal of Sedimentary Research*, *74*(6), 933–937. https://doi.org/10.1306/051204740933

Galy, V., France-Lanord, C., & Lartiges, B. (2008). Loading and fate of particulate organic carbon from the Himalaya to the Ganga–Brahmaputra delta. *Geochimica et Cosmochimica Acta*, *72*(7), 1767–1787. https://doi.org/10.1016/j.gca.2008.01.027

García, M., & Parker, G. (1991). Entrainment of Bed Sediment into Suspension. *Journal of Hydraulic Engineering*, *117*(4), 414–435. https://doi.org/10.1061/(ASCE)0733-9429(1991)117:4(414)

Giosan, L., Syvitski, J., Constantinescu, S., & Day, J. (2014). Climate change: Protect the world's deltas. *Nature News*, *516*(7529), 31. https://doi.org/10.1038/516031a

Kranck, K., & Milligan, T. (1980). Macroflocs: Production of marine snow in the laboratory. *Marine Ecology - Progress Series*, *3*, 19–24.

Lamb, M. P., De Leeuw, J., Fischer, W. W., Moodie, A. J., Venditti, J. G., Nittrouer, J. A., Haught, D., & Parker, G. (2020). Mud in rivers transported as flocculated and suspended bed material. *Nature Geoscience*, *13*(8), 566–570. https://doi.org/10.1038/s41561-020-0602-5

Lamb, M. P., McElroy, B., Kopriva, B., Shaw, J., & Mohrig, D. (2010). Linking river-flood dynamics to hyperpycnal-plume deposits: Experiments, theory, and geological implications. *GSA Bulletin*, *122*(9–10), 1389–1400. https://doi.org/10.1130/B30125.1

McMahon, W. J., & Davies, N. S. (2018). Evolution of alluvial mudrock forced by early land plants. *Science*, *359*(6379), 1022–1024. https://doi.org/10.1126/science.aan4660

Nardin, W., & Edmonds, D. A. (2014). Optimum vegetation height and density for inorganic sedimentation in deltaic marshes. *Nature Geoscience*, *7*(10), 722–726. https://doi.org/10.1038/ngeo2233

Nelson, C. H., & Lamothe, P. J. (1993). Heavy metal anomalies in the Tinto and Odiel river and estuary system, Spain. *Estuaries*, *16*(3), 496–511. https://doi.org/10.2307/1352597

Olliver, E. A., Edmonds, D. A., & Shaw, J. B. (2020). Influence of Floods, Tides, and Vegetation on Sediment Retention in Wax Lake Delta, Louisiana, USA. *Journal of Geophysical Research: Earth Surface*, *125*(1), e2019JF005316. https://doi.org/10.1029/2019JF005316

Partheniades, E. (1965). Erosion and deposition of cohesive soils. *Journal of the Hydraulics Division*, *91*(1), 105–139. https://doi.org/10.1061/JYCEAJ.0001165

Pizzuto, J. E. (2014). Long-term storage and transport length scale of fine sediment: Analysis of a mercury release into a river. *Geophysical Research Letters*, *41*(16), 5875–5882. https://doi.org/10.1002/2014GL060722

Salter, G., & Lamb, M. P. (2022). Autocyclic secondary channels stabilize deltaic islands undergoing relative sea level rise. *Geophysical Research Letters*, e2022GL098885. https://doi.org/10.1029/2022GL098885

Stokes, G. G. (1851). On the effect of the internal friction of fluids on the motion of pendulums. *Transactions of the Cambridge Philosophical Society*, *9*, 8–106.

Strom, K., & Keyvani, A. (2011). An explicit full-range settling velocity equation for mud flocs. *Journal of Sedimentary Research*, *81*(12), 921–934. https://doi.org/10.2110/jsr.2011.62

Syvitski, J. P., Kettner, A. J., Overeem, I., Hutton, E. W., Hannon, M. T., Brakenridge, G. R., Day, J., Vörösmarty, C., Saito, Y., & Giosan, L. (2009). Sinking deltas due to human activities. *Nature Geoscience*, *2*(10), 681–686. https://doi.org/10.1038/ngeo629

Ternat, F., Boyer, P., Anselmet, F., & Amielh, M. (2008). Erosion threshold of saturated natural cohesive sediments: Modeling and experiments. *Water Resources Research*, *44*(11). https://doi.org/10.1029/2007WR006537

Van Leussen, W. (1988). Aggregation of Particles, Settling Velocity of Mud Flocs A Review. In J. Dronkers & W. van Leussen (Eds.), *Physical Processes in Estuaries* (pp. 347–403). Springer. https://doi.org/10.1007/978-3-642-73691-9_19

Velde, B. (1995). Composition and Mineralogy of Clay Minerals. *Origin and Mineralogy of Clays*, 8–42. https://doi.org/10.1007/978-3-662-12648-6_2

Wentworth, C. K. (1922). A scale of grade and class terms for clastic sediments. *The Journal of Geology*, *30*(5), 377–392. https://doi.org/10.1086/622910

Winterwerp, J. C. (1998). A simple model for turbulence induced flocculation of cohesive sediment. *Journal of Hydraulic Research*, *36*(3), 309–326. https://doi.org/10.1080/00221689809498621

Zeichner, S. S., Nghiem, J., Lamb, M. P., Takashima, N., De Leeuw, J., Ganti, V., & Fischer, W. W. (2021). Early plant organics increased global terrestrial mud deposition through enhanced flocculation. *Science*, *371*(6528), 526–529. https://doi.org/10.1126/science.abd0379

Chapter 2

A MECHANISTIC MODEL FOR MUD FLOCCULATION IN FRESHWATER RIVERS

Justin A. Nghiem, Woodward W. Fischer, Gen K. Li, and Michael P. Lamb

Chapter 2 is modified from a previously published manuscript: Nghiem, J. A., Fischer, W. W., Li, G. K., & Lamb, M. P. (2022). A Mechanistic Model for Mud Flocculation in Freshwater Rivers. *Journal of Geophysical Research: Earth Surface*, *127*(5), e2021JF006392. https://doi.org/10.1029/2021JF006392

Abstract

The transport and deposition of mud in rivers are key processes in fluvial geomorphology and biogeochemical cycles. Recent work indicates that flocculation might regulate fluvial mud transport by increasing mud settling velocities, but we lack a calibrated mechanistic model for flocculation in freshwater rivers. Here, we developed and calibrated a semi-empirical model for floc diameter and settling velocity in rivers. We compiled a global dataset of river suspended sediment concentration-depth profiles and inverted them for *in situ* settling velocity using the Rouse-Vanoni equation. On average, clay and silt (diameters < 39 μm) are flocculated with settling velocity of 1.8 mm s^{-1} and floc diameter of 130 μm. Among model variables, Kolmogorov microscale has the strongest positive correlation with floc diameter, supporting the idea that turbulent shear limits floc size. Sediment Al/Si (a mineralogy proxy) has the strongest negative correlation with floc diameter and settling velocity, indicating the importance of clay abundance and composition for flocculation. Floc settling velocity increases with greater mud and organic matter concentrations, consistent with flocculation driven by particle collisions and binding by organic matter which is often concentrated in mud. Relative charge density (a salinity proxy) correlates with smaller floc settling velocities, a finding that might reflect the primary particle size distribution and physical hosting of organic matter. The calibrated model explains river floc settling velocity data within a factor of about two. Results highlight that flocculation can impact the fate of mud and particulate organic carbon, holding implications for global biogeochemical cycles.

Plain Language Summary

The fate of fine sediment in rivers is important for understanding contaminant dispersal, organic carbon burial, and the construction of river floodplains and deltas. Individual grains of silt and clay dispersed in water settle under the pull of gravity at extremely slow rates. However, in natural rivers, these mud particles can aggregate together into larger structures called flocs, resulting in far faster settling rates. Here, we built on prior work from estuaries to develop a settling velocity model for flocculated mud in freshwater rivers. Our results

demonstrate that mud settling velocity increases in rivers with less vigorous turbulence because turbulence can break flocs apart. Mud settling velocity also increases with greater concentrations of mud and particulate organic matter, which promote particle collisions and binding. Counterintuitively, settling velocity decreases with greater clay abundance and greater river water salinity, possibly due to how they affect organic matter in binding mud particles into flocs. Our results improve understanding of floc behavior in rivers and indicate potential links between the routing of mud and organic matter, river geomorphology, and global climate.

2.1 Introduction

Mud (grain diameter, $D < 62.5$ μm) dominates the sediment load carried by rivers globally (e.g., Baronas et al., 2020; Lupker et al., 2011) and its fate is important for our understanding of fluvial geomorphology and biogeochemical cycling. For example, mud-rich fluvial deposits are a major component of the rock record (Aller, 1998; McMahon and Davies, 2018; Zeichner et al., 2021). Mud cohesion increases bank strength in alluvial rivers, affecting river morphodynamics (e.g, Dunne and Jerolmack, 2020; Kleinhans et al., 2018; Lapôtre et al., 2019; Millar and Quick, 1998). Mud is also a primary carrier of organic carbon and pollutants because of its high specific surface area (e.g., France-Lanord and Derry, 1997; Galy et al., 2015; Pizzuto et al., 2014). Despite its importance, we lack well-tested mechanistic models for mud transport in rivers.

Mud in rivers has traditionally been treated as washload, or sediment that is too fine to regularly settle to and interact with the riverbed (Church, 2006; Garcia, 2008). In contrast, recent work suggests that flocculation—the aggregation of particles into composite structures called flocs—can enhance mud settling velocities and drastically affect mud transport dynamics in rivers (Bouchez et al., 2011b; Lamb et al., 2020; Zeichner et al., 2021). Similar to sand, flocculated mud might be in a dynamic interchange between the flow and bed material (Lamb et al., 2020). Mud flocculation has been well-studied in estuarine and marine systems where flocs form in part because salinity promotes van der Waals attraction between particles (e.g., Hill et al., 2000; Mehta and Partheniades, 1975;Winterwerp, 2002; Fig. 1). In addition, flow turbulence, sediment concentration, organic matter concentration, and clay mineralogy are important for estuarine and marine flocculation (e.g., Kranck and Milligan, 1980; Meade, 1972; Verney et al., 2009). In contrast to the wealth of studies on flocculation in saline environments, knowledge on flocculation in freshwater rivers is relatively limited (e.g., Bungartz and Wanner, 2004; Droppo and Ongley, 1994; Droppo et al., 1997).

Studies in rivers identified flow characteristics, organic matter concentration, and suspended sediment concentration as potential controls on floc size, settling velocity, and strength (Fig. 1). Through microscopy of samples from Canadian rivers, Droppo and Ongley (1994) observed organic matrices binding together mineral sediment into flocs. They observed correlations between floc size and suspended sediment concentration, attached bacteria count, and particulate organic carbon concentration. Bungartz et al. (2006) characterized floc setting velocities at three transects along a lake outlet and found faster-settling flocs at higher

discharge, a result they attributed to faster floc growth at higher flow turbulence. They also showed that settling patterns of suspended sediment and particulate organic carbon were similar, supporting the idea that flocculation controlled transport of both mineral sediment and organic carbon. Gerbersdorf et al. (2008) examined bed material composition in the Neckar River, Germany, and identified rich networks of microbe-derived extracellular polymeric substances (EPS). They found positive correlations between concentrations of EPS moieties and the critical shear stress for erosion, indicating that EPS can help stabilize bed sediment. Lamb et al. (2020) used a field data compilation to infer the presence of widespread mud flocculation in rivers. They showed that *in situ* particle settling velocity can be inferred by fitting the Rouse-Vanoni equation to grain size-specific suspended sediment concentration-depth profiles. However, they did not explain the order-of-magnitude variation in the inferred floc settling velocities.

Experiments have also supported organic matter, dissolved species, and sediment concentration as important controls on freshwater flocculation (Fig. 1). Chase (1979) showed that the presence of organics increased floc settling velocity, a result attributed to the interaction of sediment surface coatings, organic chemistry, and dissolved solutes. Subsequent experiments showed that sediment concentration positively correlated with floc size while fluid shear rate affected floc size and settling velocity differently (e.g., Burban et al., 1990; Tsai et al., 1987). More recent experiments examining the role of organics on flocculation in freshwater highlighted the importance of nutrients, biomass, and organic matter composition on floc size and settling velocity (Furukawa et al., 2014; Lee et al., 2017; Lee et al., 2019; Tang and Maggi, 2016; Zeichner et al., 2021). For instance, Zeichner et al. (2021) showed in experiments modeled after rivers that organic matter increased clay floc settling velocities by up to three orders of magnitude, depending on organic matter type and clay mineralogy.

Process-based flocculation theory is required to link field studies and experiments into a coherent framework. Floc population balance models use particle aggregation and breakage kernels, and have been successful at reproducing floc size distributions (e.g., Lick and Lick, 1988; Spicer and Pratsinis, 1996; Xu et al., 2008). These studies showed that sediment concentration and fluid shear enhance floc aggregation by increasing particle collision frequency, but greater shear causes floc breakage (Fig. 1). Winterwerp (1998) introduced a simplified model (hereafter, the Winterwerp model) tracking a characteristic floc diameter (e.g., the median), making it more easily coupled to hydrodynamic models (e.g., Maggi, 2008; Son and Hsu, 2011; Winterwerp, 2002). The Winterwerp model includes the effects of fluid shear and sediment concentration, but subsumes other factors into coefficients of the aggregation and breakage rates. The model describes well the equilibrium size of flocculated estuarine mud (Winterwerp, 1998) and flocs in saline laboratory experiments (e.g., Kuprenas et al., 2018; Maggi, 2009; Son and Hsu, 2008). However, these models have yet to be compared or adapted to freshwater rivers.

Here, we built on the Winterwerp approach to develop a semi-empirical process-based model for mud flocculation in freshwater rivers. First, we proposed new forms for flocculation

efficiency coefficients to explicitly cast floc diameter and settling velocity as functions of physicochemical variables that prior work has shown are important for flocculation in freshwater: turbulence, sediment concentration, sediment mineralogy, organic matter concentration, and dissolved ion concentration (Fig. 1). Next, we calibrated the new model against field data. We compiled a global dataset of river grain size-specific suspended sediment concentration-depth profiles and inverted them for *in situ* settling velocity using the Rouse-Vanoni equation (Lamb et al., 2020). Together with a river geochemistry data compilation, we fitted the model to help explain the variance in floc settling velocities. Finally, the results are discussed in the context of fluvial geomorphology, organic carbon, tectonics, and climate.

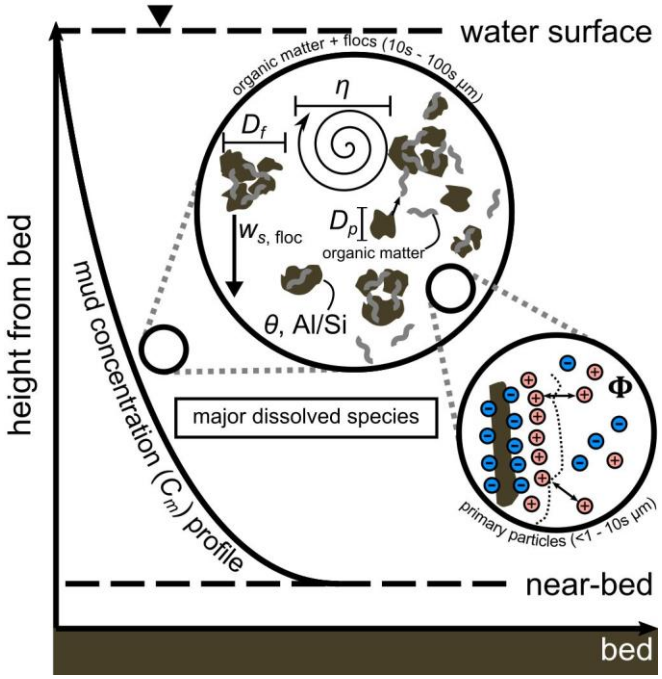

Figure 1. Schematic of a cross-section through a river water column illustrating physicochemical processes operating at different scales that could be important for mud flocculation in rivers. Key variables are turbulence (Kolmogorov microscale, η), volumetric mud concentration (C_m), sediment mineralogy (molar Al/Si of river suspended sediment), organic matter concentration (fraction of sediment surface covered by organic matter, θ), and dissolved species concentrations (relative charge density of river water, Φ). These variables affect the diameter, D_f, and settling velocity, $w_{s,floc}$, of flocs composed of primary particles with diameter D_p.

2.2 Model Development

2.2.1 Winterwerp Model

Winterwerp (1998) proposed a flocculation model in which fluid shear drives particle collisions and floc aggregation and breakage. The model casts the time rate of change of floc

diameter, D_f, (or median D_f for a floc size distribution) as the difference of floc aggregation and breakage rates:

$$\frac{\mathrm{d}D_f}{\mathrm{d}t} = \frac{k_A}{n_f \eta^2} \nu C D_f \left(\frac{D_f}{D_p}\right)^{3-n_f} - \frac{k_B}{n_f \eta^2} \nu D_f \left(\frac{D_f - D_p}{D_p}\right)^{3-n_f} \left(\frac{\tau_t}{\tau_y}\right)^j \quad (1)$$

On the right-hand side of Equation (1), the first term is the floc aggregation rate, scaled by the aggregation efficiency, k_A (dimensionless), and the second term is the floc breakage rate, scaled by the breakage efficiency, k_B (dimensionless). The shear rate, G (s^{-1}), quantifies fluid mixing and relates to the smallest turbulence length scale— the Kolmogorov microscale, $\eta = \sqrt{\nu/G}$ (m), where ν is the fluid kinematic viscosity ($m^2\ s^{-1}$) (Tennekes and Lumley, 1972). Greater fluid mixing and volumetric sediment concentration, C (volume sediment/total volume; dimensionless), drive more frequent collisions of primary particles with diameter D_p (m) and thereby increase aggregation rate (Fig. 1).

Flocs break up if fluid shear is too high relative to floc strength, an effect that Winterwerp (1998) expressed in Equation (1) using the ratio of fluid stress on the floc, $\tau_t = \rho(\nu/\eta)^2$ (Pa), and floc strength, $\tau_y = F_y/D_f^2$ (Pa), where ρ is fluid density ($kg\ m^{-3}$). F_y is floc yield strength (in terms of force) and has been estimated to be of order 10^{-10} N (Matsuo and Unno, 1981). Floc fractal dimension, $n_f \in [1, 3]$ (dimensionless), describes floc structure assuming it is approximately self-similar (Kranenburg, 1994). Floc structure can vary from a linear string of particles ($n_f = 1$) to a solid, compact particle ($n_f = 3$). An average $n_f = 2$ is typical for natural flocs (e.g., Tambo and Watanabe, 1979; Winterwerp, 1998). In practice, n_f describes the relationship between floc diameter and floc density by $R_f/R_s = \left(D_f/D_p\right)^{n_f-3}$ where R_f is the floc submerged specific gravity (dimensionless) and R_s is the submerged specific gravity of the primary particle sediment (dimensionless) (Kranenburg, 1994). Although the parameter j in Equation (1) is an empirical constant, Winterwerp (1998) used $j = 1/2$ to ensure that floc settling velocity, floc diameter, and sediment concentration are linearly related to each other based on estuarine floc data. We retained j as a fit parameter to maintain generality.

2.2.2 Modifications to the Winterwerp Model for river flocs

We proposed changes to floc strength, and floc aggregation and breakage efficiencies to adapt the Winterwerp model to rivers.

2.2.2.1 Floc strength

Experiments in freshwater have shown that, for constant D_f, floc settling velocity, $w_{s,floc}$, increases with larger mixing rate due to an increase in floc density (Burban et al., 1990). This behavior suggests that flow conditions during floc formation can affect floc strength, where more porous and lighter flocs are weaker because they have fewer interparticle contacts and

vice versa. Bache (2004) proposed that floc strength, τ_y, is a balance of local turbulent kinetic energy per unit volume acting on the floc and the energy per unit volume required to rupture the floc:

$$\tau_y = \frac{\rho}{30}\left(\frac{\nu}{\eta}\right)^2\left(\frac{D_f}{\eta}\right)^2 \quad (2)$$

The power-law form of Equation (2) holds in general but the numerical constants apply for small D_f/η (Bache, 2004).

2.2.2.2 Floc aggregation and breakage efficiencies

In the Winterwerp model, all contributions to flocculation outside of fluid shear and sediment concentration are captured in the constant floc aggregation and breakage efficiency terms, k_A and k_B, respectively. We investigated whether k_A and k_B in rivers depend on organic matter concentration, sediment mineralogy, and dissolved ion concentration, as functions rather than fit constants.

Organic matter can adsorb onto sediment surfaces and form connective "bridges" between grains (Ruehrwein and Ward, 1952; Smellie and La Mer, 1958; Molski, 1989; Fig. 1). In rivers, biogenic molecules like EPS can act as sticky media for bridging flocculation (Droppo and Ongley, 1994; Gerbersdorf et al., 2008; Larsen et al., 2009; Lee et al., 2019). Smellie and La Mer (1958) proposed a functional form of bridging flocculation efficiency,

$$k_A, k_B^{-1} \propto \theta(1-\theta) \quad (3)$$

in which θ is the fraction of the sediment surface covered by a polymeric substance. We used Equation (3) and calculated θ for organic matter (Section 3.3).

We accounted for sediment mineralogy using the molar elemental ratio Al/Si as a proxy variable (Fig. 1). More intensely weathered rocks typically generate sediment with larger Al/Si because chemical weathering produces Al-rich clay minerals (e.g., Ito and Wagai, 2017; Jackson et al., 1948; Lupker et al., 2012). Mineralogy can affect flocculation because it determines the range of potential chemical interactions between particles through cation exchange capacity (CEC) and therefore the ability to attract cations in solution (Mehta and McAnally, 2008). Furthermore, cations can affect the ability of organic matter to adsorb to particle surfaces and the physical orientation of adsorbed organic matter (Galy et al., 2008; Mehta and McAnally, 2008). We used a simple power law model as a starting point,

$$k_A \propto (\mathrm{Al/Si})^{A_1} \quad (4)$$

$$k_B \propto (\mathrm{Al/Si})^{B_1} \quad (5)$$

where A_1 and B_1 are dimensionless fit constants.

Dissolved ions in river water might promote flocculation through the same mechanism as salinity by boosting the effectiveness of van der Waals attraction between particles (e.g., Seiphoori et al., 2021; Fig. 1). To express ionic effects, we used a dimensionless parameter, Φ, to quantify the relative densities of charges in solution and on the sediment (Rommelfanger et al., 2020):

$$\Phi = \frac{\lambda I}{\mathrm{CEC}\ \rho_s\ L/2} \quad (6)$$

in which the Debye length, λ (m), is the average length from the particle in which an electrostatic effect from the charged surface is sustained, I is the solution ionic strength ([number ions] m^{-3}), CEC is the sediment cation exchange capacity ([number ions] kg^{-1}), ρ_s is sediment density (kg m^{-3}), and L (m) is a grain length scale that is nominally the face length of a plate-shaped clay particle, which we set to D_p. Physically, Φ quantifies the ionic strength of river water relative to the ionic strength in a volume surrounding primary particles. As Φ increases, the positive charge in the water within the Debye length overcomes the negative charge on the sediment surface and causes attraction between nearby sediment grains (Rommelfanger et al., 2020). We proposed power-law relations as starting points to relate Φ and the flocculation efficiencies:

$$k_A \propto \Phi^{A_2} \quad (7)$$

$$k_B \propto \Phi^{B_2} \quad (8)$$

where A_2 and B_2 are dimensionless fit constants.

2.2.3 River floc model

We substituted Equations (2) – (8) into Equation (1) to derive a modified semi-empirical model for floc diameter, D_f:

$$\frac{\mathrm{d}D_f}{\mathrm{d}t} = \frac{k_A'\theta(1-\theta)(\mathrm{Al/Si})^{A_1}\Phi^{A_2}}{n_f\eta^2}\nu C D_f\left(\frac{D_f}{D_p}\right)^{3-n_f} - \frac{k_B'(\mathrm{Al/Si})^{B_1}\Phi^{B_2}}{\theta(1-\theta)n_f\eta^2}\nu D_f\left(\frac{D_f-D_p}{D_p}\right)^{3-n_f}\left(\frac{\eta}{D_f}\right)^{2j} \quad (9)$$

in which k_A' and k_B' are new dimensionless constants that absorb all constant dimensionless parameters related to floc aggregation and breakage, respectively. At dynamic equilibrium, the time derivative of D_f vanishes, resulting in

$$D_f = k\eta(C\theta^2(1-\theta)^2)^q(\mathrm{Al/Si})^r\Phi^s\left(1-\frac{D_p}{D_f}\right)^{-q(3-n_f)} \quad (10)$$

in which $k = (k'_B/k'_A)^{1/(2j)}$, $q = -1/(2j)$, $r = (B_1 - A_1)/(2j)$, and $s = (B_2 - A_2)/(2j)$. We consolidated the unknown dimensionless coefficients and variables into the coefficient k and exponents q, r, and s. D_f appears on both sides of Equation (10), so we simplified the equation by assuming that $D_f \gg D_p$:

$$D_f = k\eta(C\theta^2(1-\theta)^2)^q(\text{Al/Si})^r\Phi^s \quad (11)$$

The assumption $D_f \gg D_p$ makes D_f independent of D_p in Equation (11) and implies a model domain of validity of intermediate fluid shear such that D_f does not converge to D_p. We validated the assumption through analysis of our field data compilation (Section 4.1). The equilibrium D_f model is plausible in rivers because experiments and field studies have shown the time scale for unsteady floc behavior to reach equilibrium in river conditions is typically on the order of tens of minutes to hours, and most dynamic river processes (e.g., floods) have longer time scales (e.g., Bungartz et al., 2006; Garcia-Aragon et al., 2011).

Floc settling velocity, $w_{s,\text{floc}}$, relates to D_f using an adaptation of the Stokes settling law for flocs (Strom and Keyvani, 2011; Winterwerp, 1998) as

$$w_{s,\text{ floc}} = \frac{R_s g D_p^2}{c_1 \nu}\left(\frac{D_f}{D_p}\right)^{n_f - 1} \quad (12)$$

Substituting Equation (11) into Equation (12) yields a model for $w_{s,\text{floc}}$

$$w_{s,\text{ floc}} = \frac{R_s g D_p}{c_1 \nu}\left[k\frac{\eta}{D_p}(C\theta^2(1-\theta)^2)^q(\text{Al/Si})^r\Phi^s\right]^{n_f - 1} \quad (13)$$

Flocs have irregular shapes and variable porosity which complicate the relationship between floc diameter and settling velocity (van Leussen, 1988). In Equation (13), the effects of floc shape and porosity on $w_{s,\text{floc}}$ are captured in the dimensionless parameters c_1 and n_f. We held them constant at $c_1 = 20$ (Strom and Keyvani, 2011; Winterwerp, 1998) and $n_f = 2$ (Kranenburg, 1994; Tambo and Watanabe, 1979). Combining these assumptions with Equation (13) yields

$$w_{s,\text{ floc}} = \frac{R_s g D_p}{20\nu} k\eta(C\theta^2(1-\theta)^2)^q(\text{Al/Si})^r\Phi^s \quad (14)$$

Equation (14) demonstrates that different c_1 values do not affect model calibration because model fitting absorbs multiplicative constants into the prefactor k. However, different n_f values affect model calibration because Equation (13) depends nonlinearly on n_f, an effect we explored in sensitivity tests (Section 4.2).

2.3 Field Data Methods

2.3.1 River suspended sediment concentration-depth profiles

We compiled a dataset of grain size-specific suspended sediment concentration-depth profiles containing 122 profiles from 12 rivers distributed globally (Table S1). We targeted datasets with suspended sediment concentration for multiple heights in the water column, laser-diffraction grain size analysis, water depth, and boundary shear velocity data. We used datasets analyzed by de Leeuw et al. (2020) and Lamb et al. (2020), and included additional datasets (Abraham et al., 2017; Baronas et al., 2020; Bouchez et al., 2011a; Bouchez et al., 2012; Bouchez, 2022; Dingle, 2021; Dingle et al., 2020) (Table S1).

Having a detailed grain size distribution for each suspended sediment sample is vital because it permits the construction of concentration-depth profiles for every grain size class (denoted *i*). We refer to these profiles as grain size-specific concentration-depth profiles. In other words, a single profile of suspended sediment samples yields as many grain size-specific concentration-depth profiles as there are measured grain size classes. We took advantage of grain size data to fit the Rouse-Vanoni equation and invert for *in situ* settling velocity as a function of the measured grain size (Fig. 1). The measured grain sizes are those of unflocculated sediment (i.e., the primary particles) because size distribution measurements were made after dispersing the sediment (e.g., Baronas et al., 2020).

The Rouse-Vanoni equation is

$$C_i(z) = C_{bi}\left(\frac{\frac{h-z}{z}}{\frac{h-h_b}{h_b}}\right)^{p_i} \quad (15)$$

in which the volumetric sediment concentration for the i^{th} grain size class, C_i, is a function of height from the bed, z, water depth, h, and a near-bed concentration, C_{bi}, specified at a near-bed height, $z = h_b$ (Rouse, 1937). The Rouse number (dimensionless) is $p_i = w_{si}/(\beta_i \kappa u_*)$ in which $\kappa = 0.41$ is the von Kármán constant (dimensionless), u_* (m s^{-1}) is the boundary shear velocity, w_s (m s^{-1}) is the sediment settling velocity, and β is the ratio of sediment and fluid diffusivities (Rouse, 1937) where *i* indexes the grain size class. Following de Leeuw et al. (2020) and Lamb et al., (2020), we fitted Equation (15) to the compiled grain size-specific concentration-depth profiles to estimate C_b and p for each grain size class. We estimated p_i and C_{bi} (at $z = h_b = 0.1h$) from fitting the log-transformed Equation (15) using ordinary least squares regression. We computed the 68% confidence intervals on the fitted p_i from the regression and discarded profiles in which the lower confidence bound on p_i is negative because these profiles do not follow Rouse-Vanoni theory for unknown reasons (e.g., non-equilibrium sediment transport, sampling and/or measurement errors).

We needed to specify u_* and β_i to estimate the grain size-specific *in situ* settling velocity, w_{si}, from the fitted value of p_i. We used u_* reported in the original data sources, which were measured concurrently with suspended sediment samples and typically calculated by fitting

flow velocity profiles measured using an acoustic Doppler current profiler to the law of the wall (e.g., Wilcock, 1996). β is a major unknown in calculating settling velocities from fitted Rouse numbers (e.g., de Leeuw et al., 2020). Empirically, β is commonly found to increase with w_s/u_* (de Leeuw et al., 2020; Graf and Cellino, 2002; Santini et al., 2019; van Rijn, 1984). $\beta < 1$ corresponds to greater sediment concentration stratification compared to $\beta = 1$, which could result from turbulence damping due to suspended sediment-induced density stratification (Graf and Cellino, 2002; Wright and Parker, 2004; discussion in de Leeuw et al. 2020). The reasons for $\beta > 1$ are less clear, but might be linked to enhanced mixing from bedform-generated turbulence (Graf and Cellino, 2002) or the high vertical concentration gradient of fast-settling particles promoting sediment diffusion relative to eddy diffusion (Smith and McLean, 1977).

We followed de Leeuw et al. (2020) and empirically fitted functions for β_i using only suspended sand because we assumed sand was unflocculated and settled *in situ* at theoretical settling velocities. To calculate theoretical sand settling velocities, we used the Ferguson and Church (2004) model [i.e., $w_s = (R_s g D^2)/\left(c_{1,\text{sand}}\nu + \sqrt{0.75 c_{2,\text{sand}} R_s g D^3}\right)$ with $c_{1,\text{sand}} = 20$ and $c_{2,\text{sand}} = 1.1$], which follows Stokes law for small particles and accounts for inertial affects for large particles. We calculated β_i using these theoretical sand settling velocities, u_*, and the fitted p_i. We found values of β_i and w_{si}/u_* that agree with previously proposed relations for $\beta(w_s/u_*)$ (Fig. 2). Next, we calibrated the power-law equation $\beta \propto (w_s/u_*)^l$ on the sand data within each concentration-depth profile, resulting in a fitted equation for each concentration-depth profile. The median coefficient of determination of the fits is 0.88, indicating a good fit. We assumed that the profile-specific functions $\beta_i = \beta(w_{si}/u_*)$, calibrated on the sand data, were valid for the mud data and extrapolated the fitted β_i functions to calculate w_{si} for the mud size classes (Lamb et al., 2020). We did not explicitly account for the potential effect of hindered settling because 93% of concentration-depth profiles analyzed had mud concentration < 5% solids by volume for which hindered settling and density-induced stratification are not expected to be important (Gratiot et al., 2005). However, if hindered settling affected the data, it is implicitly included in our fit values of β_i.

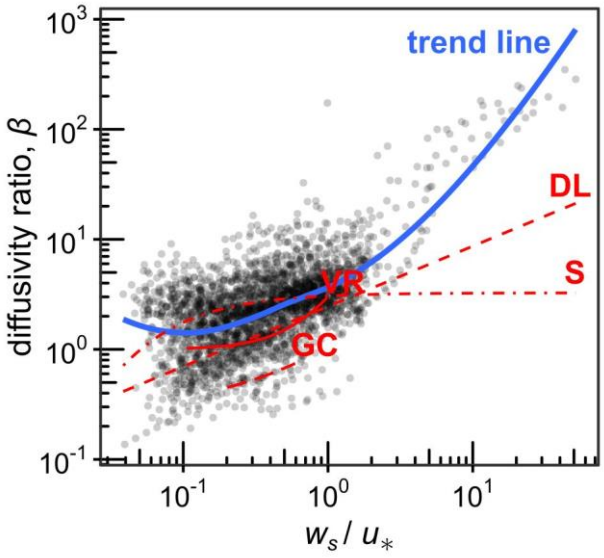

Figure 2. Sediment-fluid diffusivity ratio, β, as a function of settling velocity-shear velocity ratio, w_s/u_*, for sand (diameter, $D > 62.5$ μm) in our concentration-depth profile compilation. Trend line was computed using local polynomial regression. Function abbreviations are VR: van Rijn (1984); GC: Graf and Cellino (2002), their model without bedforms and using a constant median ratio of water depth and bed grain size; S: Santini et al. (2019); DL: de Leeuw et al. (2020), their best-fit one-parameter model for Rouse number.

2.3.2 Extracting river floc data

We inferred floc settling velocity, $w_{s,floc}$, by examining the relationship of particle diameter, D, and the *in situ* settling velocity, w_s, calculated from fitting the Rouse-Vanoni equation to the concentration-depth profile data. We found good agreement between the Rouse-estimated and predicted settling velocities for sand, but a continuous transition to a settling velocity plateau larger than the theoretical predictions for coarse silt and clay (Fig. 3). We attributed the elevated settling velocity of coarse silt and clay to flocculation (Lamb et al., 2020). We found a best-fit two-part piecewise function to quantitatively describe these two settling regimes for each concentration-depth profile (Fig. 3; see Text S1 for details on the fitting method). We termed the diameter at the regime transition the *floc cutoff diameter*, D_t, and interpreted all sediment finer than D_t to be flocculated with a constant $w_{s,floc}$ for each concentration-depth profile (Lamb et al., 2020; Fig. 3).

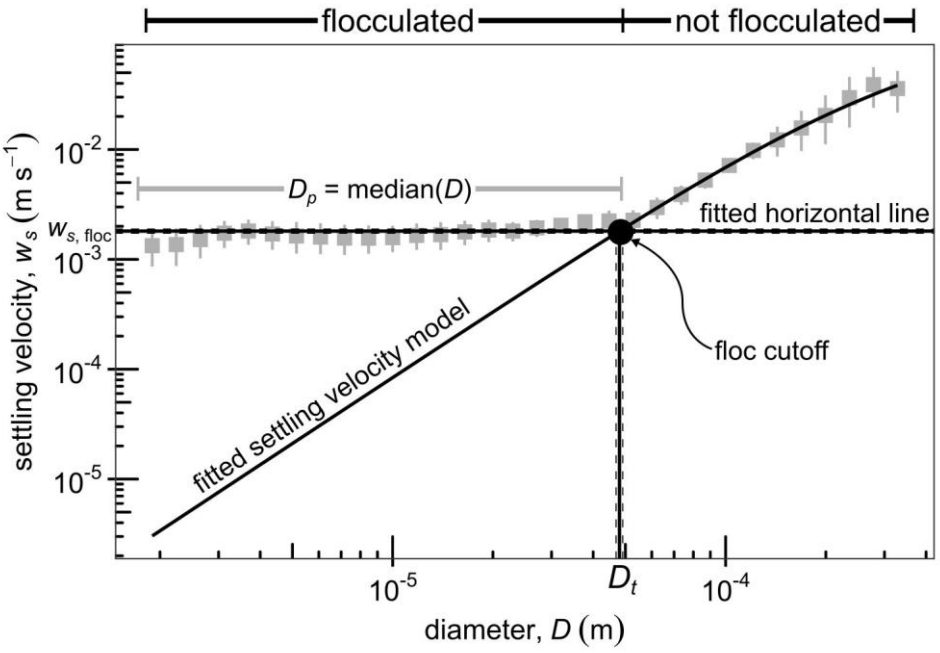

Figure 3. Example of the fitting procedure to estimate floc cutoff diameter, D_t, floc settling velocity, $w_{s,floc}$, and primary particle diameter, D_p, for a single concentration-depth profile. Each data point represents a single grain size-specific concentration-depth profile. Error bars represent 68% confidence intervals of the linear regression fit to Equation (15). The dashed lines indicate the 68% confidence intervals for $w_{s,floc}$ and D_t.

Next, we computed the floc settling velocity, $w_{s,floc}$, and primary particle diameter, D_p, from the flocculated data ($D < D_t$). We computed $w_{s,floc}$ as the mean *in situ* settling velocities for $D < D_t$ (Fig. 3). This method is oversimplified because it implies that all sediment in a given size class for $D < D_t$ was flocculated and settling at the same rate. In reality, some sediment might not have been flocculated and there was likely a distribution of floc sizes and settling velocities *in situ* (Osborn et al., 2020; Osborn et al., 2021), but these distributions cannot be constrained by our data. We also cannot constrain floc structure and the size distribution of the primary particles in individual flocs (e.g., a floc composed of mostly clay might have the same settling velocity as a smaller floc composed of coarse silt with finer sediment bound to its surface). D_p might vary with depth, so we calculated D_p as the median grain size for $D < D_t$ using the depth-averaged concentration of each grain size class as relative weights (Fig. 3). We propagated uncertainty to find the 68% confidence intervals for $w_{s,floc}$ and D_t (Fig. 3; Text S1). Some profiles had data gaps because of the data quality filtering (Section 3.1). We discarded concentration-depth profiles in which D_t was in a data gap greater than one order of magnitude in D. 96 concentration-depth profiles, or about 79% of the initial profiles, remained after this filtering.

We estimated floc diameter, D_f, from the floc cutoff diameter, D_t. D_t, can be interpreted as the diameter of unflocculated grains that settle at the same rate as flocs (Fig. 3). Therefore, Stokes law for unflocculated particles applied to D_t results in

$$w_{\text{s, floc}} = \frac{R_s g D_t^2}{c_1 \nu} \quad (16)$$

Combining Equations (12) and (16), we found

$$D_f = D_p \left(\frac{D_t}{D_p}\right)^{\frac{2}{n_f - 1}} \quad (17)$$

We used Equation (17) with $n_f = 2$ to calculate D_f. We then combined Equations (11) and (17) to derive a model for D_t:

$$D_t = k\left(\eta D_p\right)^{1/2} (C\theta^2(1-\theta)^2)^q (\text{Al/Si})^r \Phi^s \quad (18)$$

2.3.3 Estimating other variables

We used the depth-averaged volumetric mud concentration, C_m, as the representative sediment concentration in the model (Equations 11, 14, and 18) because we expect flocculation to mainly occur within mud. We found the model goodness-of-fit to be insensitive to the choice of total or mud concentration because they are correlated. We chose typical values for river water density, ρ = 1000 kg m^{-3}, sediment density, ρ_s = 2650 kg m^{-3}, and kinematic viscosity of water, $\nu = 10^{-6}$ m^2 s^{-1}. We calculated the Kolmogorov microscale using $\eta = \left[(\kappa h z \nu^3)/\left(u_*^3 (h - z)\right)\right]^{1/4}$ for open-channel flow (Nezu and Nakagawa, 1993). The near-bed (at $z = h_b = 0.1h$) and depth-averaged η did not vary significantly from each other (within a factor of about 2), so we used the near-bed η in our calculations.

Most data sources for the concentration-depth profiles do not have the requisite geochemical measurements to evaluate the floc model. To supplement, we compiled river geochemistry data from other sources for the same rivers (Table S2). We matched geochemical measurements to each profile by finding the closest measurements in terms of geographic distance and time of year, weighted equally. The median deviations of the concentration-depth profiles and matched geochemical measurements in time and space are about 4 days and 22 km (or about 54 channel widths). Although these sources of error are difficult to quantify, they should be considered together with the results.

Al/Si is commonly measured for suspended sediment samples, but almost all Al/Si values are measured in bulk without grain size distinction. We compiled and used bulk suspended sediment Al/Si measurements for fitting the model.

We compiled measurements of percent weight organic carbon of suspended sediment samples to estimate θ, the average fraction of sediment covered by organic matter. We assumed cellulose organic matter composition (molar ratio C:H:O of 6:10:5) because it is the most abundant organic compound in the terrestrial biosphere (e.g., Brigham, 2018). We

converted measured percent weight organic carbon into percent weight organic matter as cellulose, %OM, using molar mass ratios. Although organic matter usually adsorbs onto sediment in irregular patches (e.g., Ransom et al., 1997), we assumed for simplicity that the volume of organic matter, V_{OM}, is hosted uniformly on the surface of spherical grains with diameter D_p in a shell with volume V_{shell} and thickness δ. With these assumptions, we obtained

$$\theta = \frac{V_{\mathrm{OM}}}{V_{\mathrm{shell}}} = \frac{(\%\mathrm{OM}/100)\frac{\rho_s}{\rho_{\mathrm{OM}}}D_p^3}{\left(D_p + 2\delta\right)^3 - D_p^3} \quad (19)$$

We assumed neutrally-buoyant organic matter, $\rho_{\mathrm{OM}} = 1000$ kg m^{-3}, and $\delta = 10^{-6}$ m (Barber et al., 2017; Hackley et al., 2017). Measurements of θ for river suspended sediment are unavailable, so we chose δ to obtain θ consistent with $\theta \sim 0.15$ for marine sediment (Bock and Mayer, 2000; Mayer, 1999).

To estimate relative charge density, Φ, we compiled major ion concentrations in rivers (cations: Na^+, K^+, Ca^{2+}, Mg^{2+}; anions: HCO_3^-, SO_4^{2-}, Cl^-). We calculated the ionic strength, I, using dissolved ion concentration measurements as $I = 0.5\sum_i c_i z_i^2$ in which c_i is the concentration of the ith ion ((number ions) m^{-3}) and z_i is its charge number. We calculated the ion concentration using charge balance for cases in which one ion was missing. The Debye length, λ, is expressed as:

$$\lambda = \left(\frac{\epsilon_0 \epsilon_r k_{\mathrm{BM}} T}{2e^2 z_{\mathrm{cation}}^2 s_{\mathrm{cation}}}\right)^{1/2} \quad (20)$$

λ is a function of vacuum permittivity, ϵ_0 (=8.854×10^{-12} F m^{-1}), dielectric constant of water, ϵ_r (dimensionless), Boltzmann constant, k_{BM} (=1.381×10^{-23} J K^{-1}), water temperature, T (K), elementary charge magnitude, e (=1.602×10^{-19} C), cation charge number, z_{cation}, and cation concentration, s_{cation} (Rommelfanger et al., 2020). We assumed T = 15°C if it was not reported. We used a temperature-dependent formula to compute ϵ_r (Owen et al., 1961). Since concentration and charge vary by cation, we calculated $1/\left(z_{cation}\sqrt{s_{cation}}\right)$ as the mean over the cations weighted by relative concentration. Due to data gaps, we estimated sediment CEC (mol kg^{-1}) from the percent clay of the depth-averaged concentration for each profile using (Ersahin et al., 2006)

$$\mathrm{CEC} = (4.97 + 0.53\ \%\mathrm{clay})/100 \quad (21)$$

in which %clay is the percentage by weight of the total suspended sediment concentration with particle diameters smaller than 2 μm. Equation (21) assumes grain size is a suitable mineralogy proxy to compute CEC.

2.4 Results

2.4.1 Floc and physicochemical parameters

Results for mud demonstrate an orders-of-magnitude departure of *in situ* settling velocities, inferred from concentration-depth profile fitting, from predicted settling velocities of unflocculated mud (Fig. 4a). Physically, faster mud settling velocity causes a more stratified suspended mud concentration-depth profile (Fig. 4b). For example, the Rouse-Vanoni equation predicts particles with D_p = 2 □m should be nearly uniformly mixed in the water column. However, the data show similar stratification between mud and sand profiles (Fig. 4b). We interpreted elevated mud settling velocities as a signature of mud flocculation (Lamb et al., 2020).

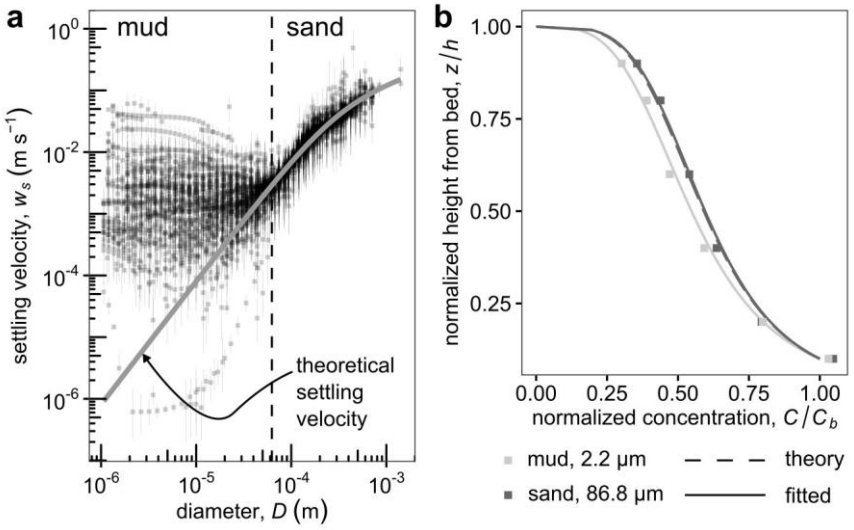

Figure 4. (a) Settling velocity as a function of particle diameter using the Rouse-Vanoni equation method for all compiled suspended sediment concentration-depth profiles. Each data point represents a single grain size-specific concentration-depth profile. Ferguson and Church (2004) shows theoretical settling velocity for unflocculated particles, and follows Stokes law for small particles (D < ~10^{-4} m). Error bars represent 68% confidence intervals of the linear regression fit to Equation (15). (b) Example suspended sediment concentration-depth profiles (Moodie et al., 2020) with fitted Rouse-Vanoni equation curves. The dashed lines about each curve mark the 68% confidence interval range.

We estimated the floc cutoff diameter, D_t, primary particle diameter, D_p, floc diameter, D_f, and floc settling velocity, $w_{s,floc}$, for each concentration-depth profile using our piecewise function fits in D-w_s space (summarized in Table 1). The medians indicate that suspended sediment in rivers with diameter smaller than D_t = 39 μm (half the interquartile range, IQR/2 = 22 μm) is flocculated into aggregates with diameter D_f = 130 μm (IQR/2 = 100 μm), settling rates of $w_{s,floc}$ = 1.8 mm s^{-1} (IQR/2 = 1.7 mm s^{-1}), and primary particle diameter of D_p = 12 μm (IQR/2 = 4.5 μm). The estimated $w_{s,floc}$ and D_f indicate a median floc density of ρ_{floc} = 1100 kg m^{-3} (IQR/2 = 160 kg m^{-3}) using Equation (12). As expected, the ρ_{floc} estimates are much smaller than the mineral sediment density (ρ_s = 2650 kg m^{-3}) because flocs contain

lighter organic matter and pores. We found D_p/D_f = 0.097 (IQR/2 = 0.057), resulting in a negligible difference between Equations (10) and (11) and justifying the assumption of $D_f \gg D_p$ in the model derivation (Fig. 5).

Our finding of D_t = 39 μm is similar to the finding of D_t = 40 μm by Lamb et al. (2020) even though they used a different method to calculate β_i. Tests with different β_i formulations also demonstrate limited effect on w_{si} and yield the same general pattern of *in situ* settling velocity versus particle diameter (Text S2; Fig. S1). Although *in situ* river floc data are rare, Osborn et al. (2020) deployed an *in situ* camera in the Mississippi river and observed flocs with D_f of 70 to 130 μm, a range also consistent with our D_f estimates.

The Kolmogorov microscale, η, has been proposed as an upper bound on floc diameter, D_f, because flocs can be efficiently broken by turbulence once they grow to the size of the smallest eddies (e.g., Kuprenas et al., 2018; Tambo and Hozumi, 1979; van Leussen, 1988). We found a narrow range of η in our compilation with a typical value of 200 μm (Fig. 6a). D_f estimates are typically of the same scale or smaller than η, indicating that η might limit D_f (Fig. 5). However, the data suggest that floc size is not strictly turbulence-limited and can increase beyond η (36% of the data), perhaps due to other physicochemical factors that can be explained by the model (see discussion in Section 4.3) and/or uncertainties in calculating D_f (Equation 17; Section 4.2). Conversely, the cases in which D_f is smaller than η motivate examining effects of sediment concentration and mineralogy, organic matter, and water chemistry on flocculation (Section 4.2).

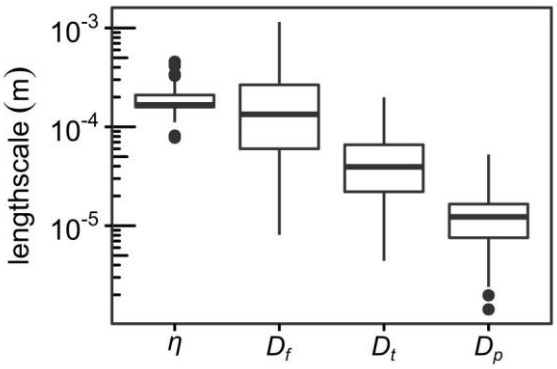

Figure 5. Boxplots of length scales: Kolmogorov microscale, η, floc diameter, D_f, floc cutoff diameter, D_t, and primary particle diameter, D_p, from the data compilation. The lower and upper sides of the boxes indicate the 25th and 75th percentiles, respectively. The whiskers extend 1.5 times the interquartile range below and above the lower and upper sides, respectively. Data beyond the whiskers plot as outlying points.

Table 1. Median values of parameters estimated from our data compilation. We used half the interquartile range (IQR/2) as a robust measure of spread.

Variable	**Median**	**IQR/2**
Floc cutoff diameter, D_t (μm)	39	22
Floc settling velocity, $w_{s,\mathrm{floc}}$ (mm s^{-1})	1.8	1.7
Floc diameter, D_f (μm)	130	100
Primary particle diameter, D_p (μm)	12	4.5
Floc density, ρ_{floc} (kg m^{-3})	1100	160
Kolmogorov microscale, η (μm)	170	26
Depth-averaged mud volumetric concentration, C_m	4.8×10^{-4}	5.1×10^{-4}
Fraction of sediment surface covered by organic matter, θ	0.070	0.039
Suspended sediment Al/Si [molar ratio]	0.23	0.081
Relative charge density, Φ	3.1×10^{-5}	3.5×10^{-5}

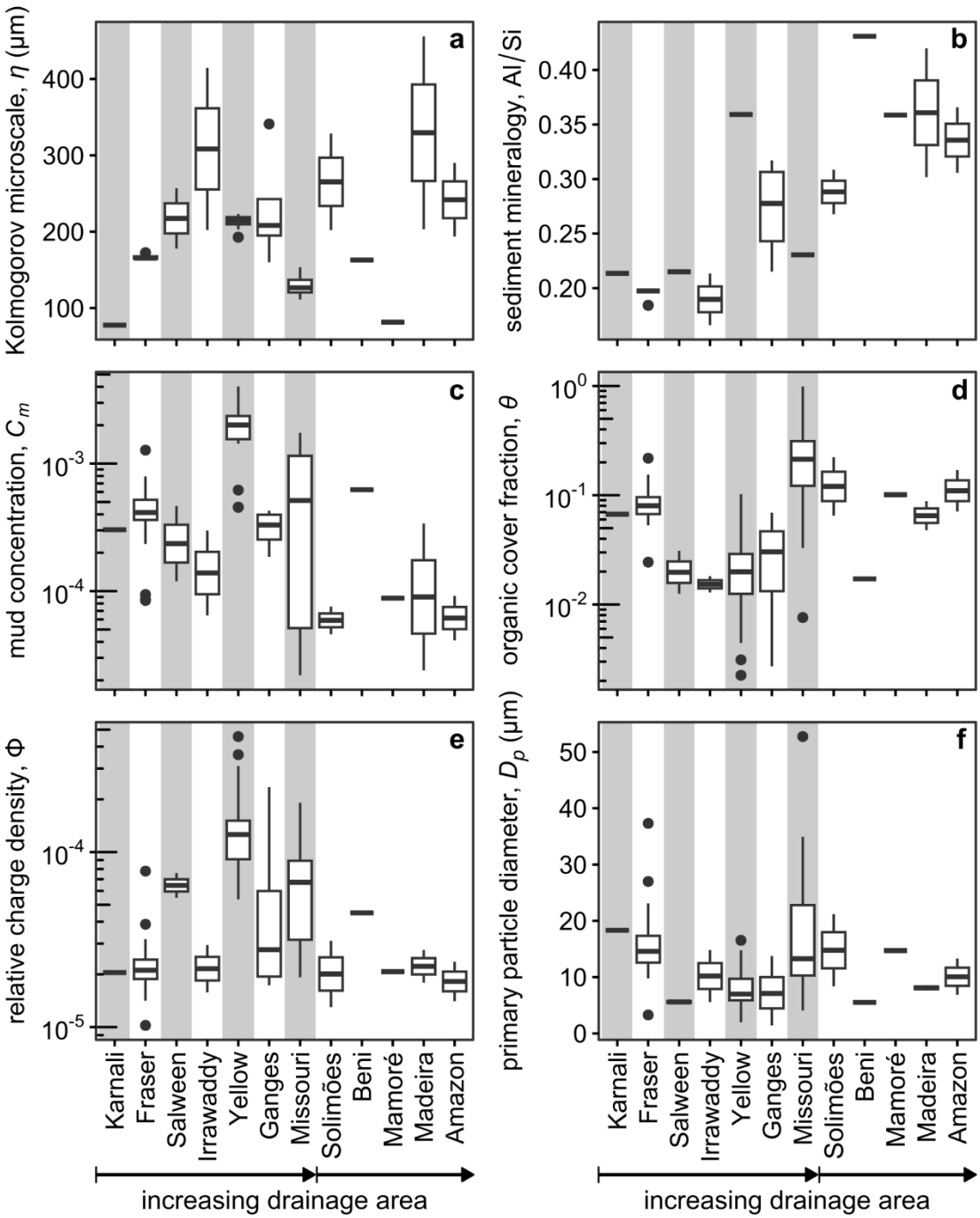

Figure 6. Boxplots of model input variables classified by river. Boxplots that appear as a horizontal line segment contain only a single data point. River names are ordered by increasing drainage area at the sample collection point, measured using HydroSHEDS digital elevation data (Lehner et al., 2008). Amazon basin rivers are plotted separately in order of increasing drainage area.

2.4.2 Floc Model Calibration

We used sediment Al/Si, depth-averaged volumetric mud concentration, C_m, fraction of sediment surface covered by organic matter, θ, relative charge density, Φ, and primary particle diameter, D_p as independent variables to calibrate the model (Fig. 6). Sediment Al/Si ranges from 0.2 to 0.5 (molar ratio) and generally increases with river drainage area (Fig. 6b)—a pattern that could reflect production of more Al-rich clay minerals with progressive silicate weathering downstream (e.g., Lupker et al., 2012; West et al., 2005). Depth-averaged volumetric mud concentration, C_m, varies widely across rivers on the order of 10^{-5} to 10^{-3}, a range that likely reflects regional variation in catchment lithology, sediment supply, and transport capacity (Figure 6c). The fraction of sediment surface covered by organic matter, θ, is typically close to 0.1 (Figure 6d). The relative charge density, Φ, largely varies between 10^{-5} and 10^{-4} for our data compilation (Figure 6e) and is a function of weathering contributions to river water ion concentration and electrostatic properties of sediment. Primary particle diameter, D_p, generally decreases with drainage area (Fig. 6f), consistent with downstream grain size fining due to sorting and abrasion (Paola et al., 1992).

We fitted the floc diameter, settling velocity, and cutoff diameter models (Equations 11, 14, and 18) to our D_f, $w_{s,\mathrm{floc}}$, and D_t estimates, respectively (Fig. 7; Table 2). The calibrated models with best-fit parameters are:

$$D_t = 0.134\left(\eta D_p\right)^{1/2}\left(C_m\theta^2(1-\theta)^2\right)^{0.0734}(\mathrm{Al/Si})^{-0.774}\Phi^{-0.180} \quad (22)$$

$$w_{s,\,\mathrm{floc}} = \frac{R_s g D_p}{20\nu}0.306\eta\left(C_m\theta^2(1-\theta)^2\right)^{0.167}(\mathrm{Al/Si})^{-2.15}\Phi^{-0.0358} \quad (23)$$

$$D_f = 0.0180\eta\left(C_m\theta^2(1-\theta)^2\right)^{0.147}(\mathrm{Al/Si})^{-1.55}\Phi^{-0.360} \quad (24)$$

The majority of the profiles in our compilation was sampled in lowland alluvial rivers, so application of the calibrated model is most appropriate for those settings. The high model goodness-of-fit supports the equilibrium floc assumption in the model (Fig. 7; Table 2).

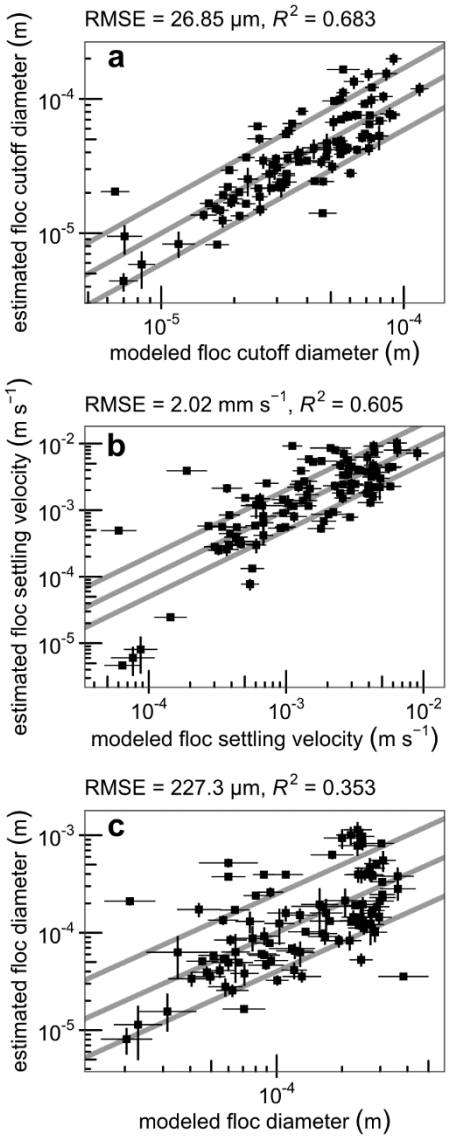

Figure 7. Comparison of the calibrated model for floc cutoff diameter, D_t (panel a), floc settling velocity, $w_{s,\mathrm{floc}}$ (panel b), and floc diameter, D_f (panel c). The central line is 1:1, and the bounding lines indicate the average factor of 1.7, 2, and 2.5 deviation of model values from the data for D_t, $w_{s,\mathrm{floc}}$, and D_f, respectively. Vertical error bars represent the propagated 68% confidence interval. Horizontal error bars represent the standard error range of modeled values.

Table 2. Fitted parameters in the floc model. The uncertainties indicate the 95% confidence intervals from an ordinary least squares regression fit. The values in parentheses indicate the lower and upper confidence intervals for *k* because the interval is asymmetrical.

	Floc cutoff diameter model (Equation 18) $D_t = k(\eta D_p)^{1/2}(C_m\theta^2(1-\theta)^2)^q(\mathrm{Al/Si})^r\Phi^s$	**Floc settling velocity model (Equation 14)** $w_{s,\,\mathrm{floc}} = \frac{R_s g D_p}{20\nu} k\eta(C_m\theta^2(1-\theta)^2)^q(\mathrm{Al/Si})^r\Phi^s$	**Floc diameter model (Equation 11)** $D_f = k\eta(C_m\theta^2(1-\theta)^2)^q(\mathrm{Al/Si})^r\Phi^s$
k	0.134 (0.0320, 0.561)	0.306 (0.0131, 7.17)	0.0180 (1.02×10^{-3}, 0.315)
q	0.0734 ± 0.0449	0.167 ± 0.0989	0.147 ± 0.0898
r	-0.774 ± 0.409	-2.15 ± 0.900	-1.55 ± 0.818
s	-0.180 ± 0.126	-0.0358 ± 0.278	-0.360 ± 0.253

Although the three models are dependent, we fitted the regressions independently of each other because the D_t, $w_{s,\mathrm{floc}}$, and D_f models each include different assumptions. The D_t model is the most direct evaluation of the proposed model parameters because we directly estimated D_t from the concentration-depth profiles (Figure 3) and it is independent of c_1 (Equations 17 and 18), yielding the highest goodness-of-fit among the models (coefficient of determination, R^2 = 0.683; root mean square error, RMSE = 26.85 μm). We assumed $n_f = 2$ to derive the D_t model (Equation 17), but model calibrations with different choices of constant n_f show that n_f has a negligible effect on overall goodness-of-fit and minimal effect on calibrated model exponents (Text S3; Fig. S2). Similar to D_t, we estimated $w_{s,\mathrm{floc}}$ directly (Figure 3) and assumed n_f = 2 to derive the model (Equation 14). But, in addition, we assumed a constant c_1 = 20 (Ferguson & Church, 2004; Strom & Keyvani, 2011) to derive the $w_{s,\mathrm{floc}}$ model (Equation 14), leading to a reduction in the goodness-of-fit (R^2 = 0.605; RMSE = 2.02 mm s^{-1}) compared to the D_t model. In contrast to the direct D_t and $w_{s,\mathrm{floc}}$ estimates, D_f was calculated from $w_{s,\mathrm{floc}}$ or D_t. We assumed n_f = 2 to calculate D_f from D_t (Equation 17), causing a relatively large drop in goodness-of-fit (R^2 = 0.353; RMSE = 227.3 μm) relative to both the D_t and $w_{s,\mathrm{floc}}$ models despite the fact that the D_f model is independent of c_1 and n_f (Equation 11). The differences in goodness-of-fit between the three models indicate the importance of constraining c_1 and n_f, which depend on floc shape and structure (Maggi et al., 2007; Strom and Keyvani, 2011). We calculated the ratio of model predictions and data and took quantiles at 16%, 50% (median), and 84% to characterize the deviation of predictions from the data. We computed quantiles of this ratio at {0.61 (16%), 1.1 (50%), and 1.4 (84%)} for D_t, {0.47, 1.0, and 2.2} for $w_{s,\mathrm{floc}}$, and {0.37, 1.2, and 2.0} for D_f. These results show that the model explains the data within factors of about 1.7 for D_t, 2 for $w_{s,\mathrm{floc}}$, and 2.5 for D_f (Fig. 7).

All model exponents (q, r, and s) are significantly different than 0 according to the 95% confidence interval (0.05 significance level) except for the exponent of Φ in the $w_{s,\mathrm{floc}}$ model (Table 2). The reason for the statistical insignificance of Φ in the $w_{s,\mathrm{floc}}$ model is unclear, but might be related to errors in assuming constant c_1 or in matching geochemical measurements to the concentration-depth profiles. The statistical significance of the remaining parameters supports the hypothesis that organic matter, sediment concentration and mineralogy, water chemistry, and turbulence are important predictors of floc properties in rivers.

2.4.3 Floc model dependencies and interpretation

To isolate the effect of individual parameters on floc settling velocity, we plotted each parameter against the $w_{s,floc}$ data normalized by all other model terms (Fig. 8). We also divided by the median for each normalized quantity to provide comparable scales. The gross trends between individual parameters and $w_{s,floc}$ are similar to those for D_t and D_f (Fig. S3 and S4).

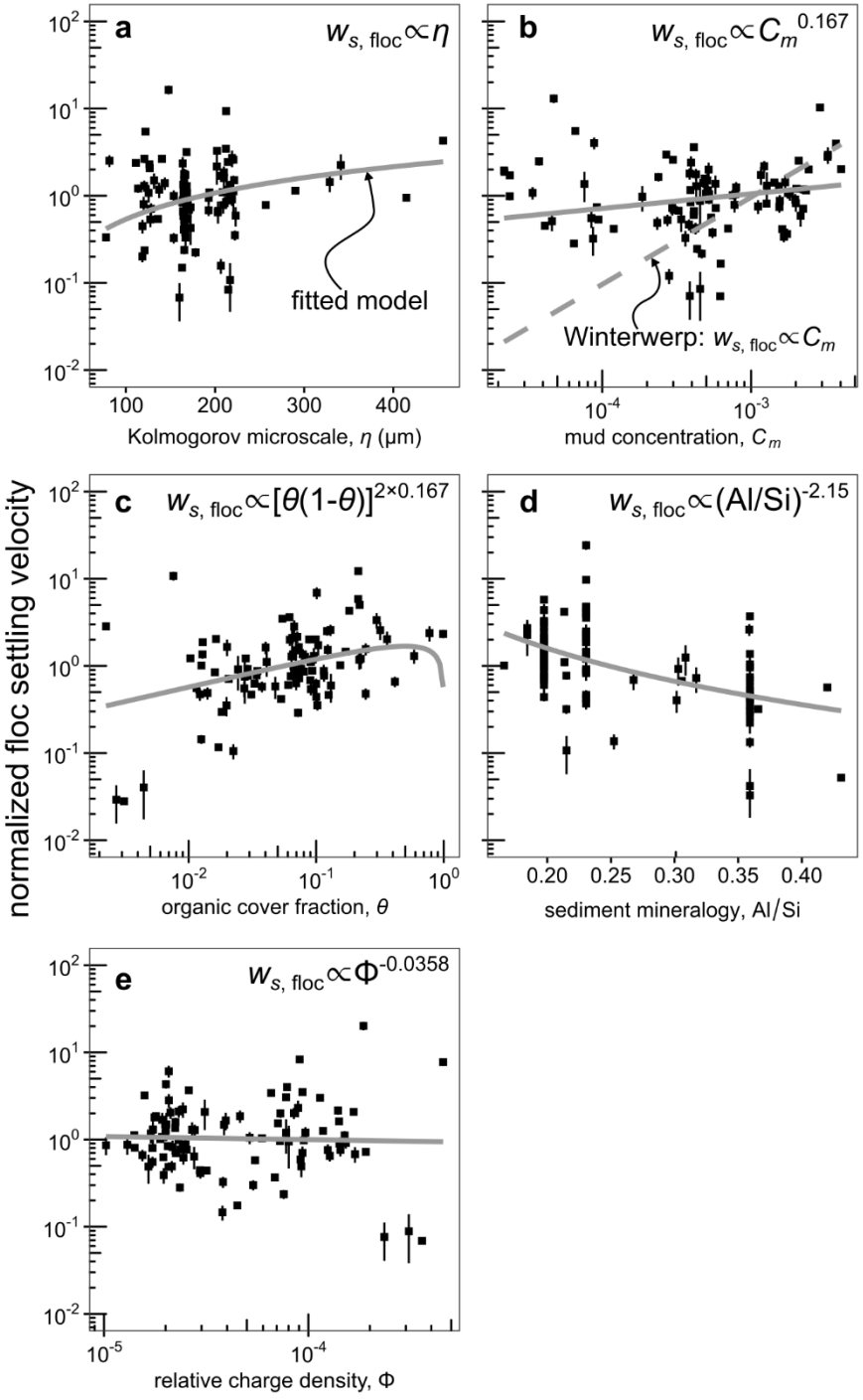

Figure 8. Individual parameters plotted against floc settling velocity, $w_{s,floc}$, data normalized by the effects of all other predictors in the fitted $w_{s,floc}$ model (Equation 23). In all panels, the solid line, labeled in panel a, indicates the fitted relationship (Table 2). In

panel b, the dashed line is the prediction from the equilibrium Winterwerp model. Error bars represent the propagated 68% confidence interval.

The Kolmogorov microscale, η, expresses the effect of turbulence on flocs and is predicted to have a positive linear relationship with $w_{s,floc}$ and D_f (Fig. 8a; Fig. S4a; Winterwerp, 1998). We tested the plausibility of the relationship between (normalized) $w_{s,floc}$ and η (e.g., the trend in Fig. 8a) using regression *F*-tests of the linear relation and an alternative power-law relation. We found a statistically significant linear relationship between normalized $w_{s,floc}$ and η (p-value = 6.0×10^{-10}) and a statistically insignificant power-law relationship (p-value = 0.37). The linearity between D_f and η agrees with the steady-state equilibrium form of the Winterwerp model (Kuprenas et al., 2018; Winterwerp, 1998).

Mud concentration, C_m, displays a positive sublinear trend with $w_{s,floc}$ (exponent = 0.167 ± 0.0989; Figure 8b) in contrast to the linear trend predicted by the equilibrium model of Winterwerp (1998). The equilibrium Winterwerp model predicts a linear trend between sediment concentration and floc settling velocity because greater sediment concentration results in proportionally greater interparticle collisions. However, there is a different scaling relation in our model because we allowed the exponent j, which controls the importance of floc strength on the floc breakup rate, to vary (Equations 10 and 11). Inspecting Equation (11), linearity between C_m and $w_{s,floc}$ occurs only when j = -0.5, or $D_f \propto (\tau_y/\tau_t)^{0.5}$, while our calibration indicates that j = -2.99, or $D_f \propto (\tau_y/\tau_t)^{2.99}$, which in turn reveals $(\tau_y/\tau_t)^{2.99} \propto (D_f/\eta)^{-2j = 2\times2.99 = 5.99}$. Thus, our calibrated model indicates that the floc breakage rate becomes very large when $D_f > \eta$—much more so than in the Winterwerp model. This finding is consistent with the limiting effect of η on floc size proposed by Kuprenas et al. (2018). But in contrast to their work, our model does not feature a built-in turbulence limit. Rather, D_f can exceed η, but the rapid breakage rates for large flocs make $D_f >> \eta$ less likely. In our equilibrium model, the strong dependence of D_f on η effectively reduces the strengths of dependency on the other input variables. In the case of C_m, fluid shear stresses inhibit the efficiency of sediment concentration to drive floc growth. Thus, although the aggregation rate still depends linearly on C_m in our model, we found a sublinear dependence on C_m for floc diameter and settling velocity.

Organic matter affects flocculation through the fractional cover of organic matter on the surface of sediment grains, θ, according to the function $(\theta^2(1-\theta)^2)^q$ with an exponent, q = 0.167 ± 0.0989, identical to that of C_m (Figure 8c). The shared exponent, q, indicates an analogous interpretation: turbulence can promote floc breakage and disrupt the ability of organic matter to facilitate bonding between particle surfaces. Most data display $\theta < 0.5$, a regime in which the function $\theta(1-\theta)$ increases with θ. In this domain, the model predicts that increased loading of organic matter promotes larger $w_{s,floc}$ because the areas of bare sediment and organic matter become more comparable for binding. The positive sublinear exponent implies that increasing organic matter coverage on sediment causes a much larger enhancement of floc size at low θ compared to high θ (but still less than 0.5). Thus, the addition of even small amounts of organic matter to an organics-poor system can trigger an appreciable flocculation response, consistent with experiment results (Zeichner et al. 2021).

The model predicts a reverse effect for organics-rich systems, but the sparsity of data for $\theta > 0.5$ precludes confirmation of this behavior.

Sediment Al/Si shows a decreasing trend with $w_{s,\mathrm{floc}}$ (exponent $r = -2.15 \pm 0.900$; Figure 8d). The negative relationship with Al/Si is surprising because Al/Si is typically treated as a clay abundance proxy and clay is expected to be the grain size fraction most susceptible to flocculation (e.g., Mehta and Partheniades, 1975; van Leussen, 1988). Equation (10) shows that $r = (B_1 - A_1)/(2j)$ where A_1 and B_1 are the respective power-law aggregation and breakage exponents (Equations 4 and 5). We found $j = -2.99$, $r = -2.15$, and hence $B_1 - A_1 \cong 12.9$, which indicates that the negative trend between Al/Si and $w_{s,\mathrm{floc}}$ occurs because the breakage rate exponent exceeds the aggregation rate exponent ($B_1 > A_1$). We expect that A_1 is positive because Al/Si is correlated with higher clay mineral abundance, and clays with stronger surface charges promote flocculation (Mehta and McAnally, 2008; van Olphen and Hsu, 1977). If $A_1 > 0$, then our analysis implies that $B_1 > 12.9$. In other words, the floc breakage rate is increasingly sensitive to Al/Si at greater values of Al/Si. We speculated two explanations. First, Equation (16) shows that $w_{s,\mathrm{floc}} \propto D_t^2$, suggesting that the inclusion of progressively coarser sediment into flocs has a strong control on increasing floc settling velocity and vice versa. Clay might flocculate more readily than coarser sediment because it is more cohesive, so greater clay abundance (correlated with greater Al/Si) might cause clay-rich flocs and exclude coarser grain sizes (smaller D_t) thus reducing floc settling velocity. For a given floc size, flocs composed of smaller, high Al/Si primary particles must necessarily have more interparticle contacts and thus may be more fragile and prone to breakage in a turbulent fluid. We found evidence for this idea in the fact that (normalized) floc cutoff diameter varies inversely with Al/Si, indicating coarser grain sizes were increasingly excluded from flocs at higher Al/Si (Fig. 9a).

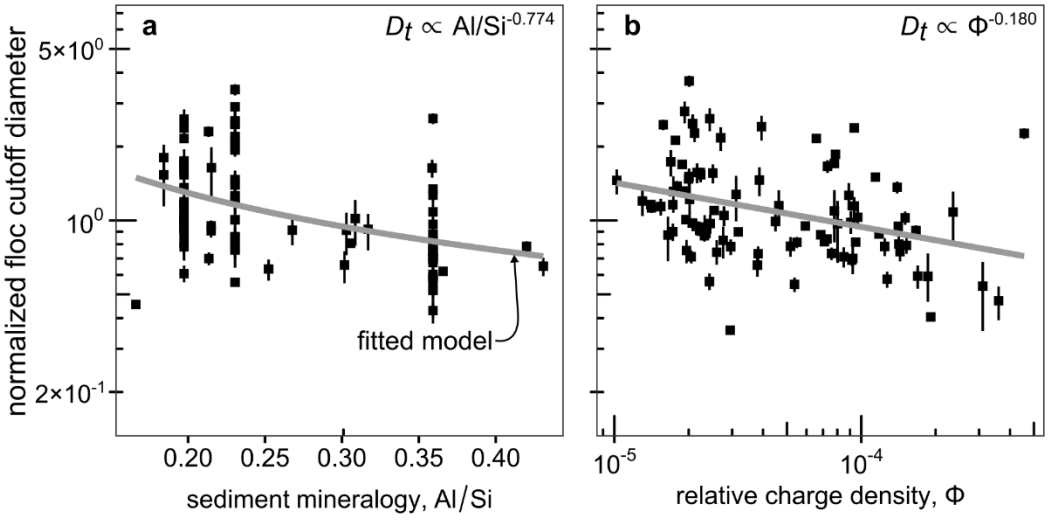

Figure 9. Sediment Al/Si (panel a) and relative charge density Φ (panel b) plotted against floc cutoff diameter, D_t, normalized by the effects of all other predictors in the fitted D_t model (Equation 18). The normalized values were further scaled by dividing the median to better compare each variable. In all panels, the solid line, labeled in panel a, indicates the fitted relationship (Table 2).

A second possible reason for the greater sensitivity of floc breakage to larger Al/Si could be tied to the prevalence of a flat orientation of adsorbed organic matter on sediment. This orientation might be common in sediment with high specific surface area, like high Al/Si clay, because they have more adsorption sites to increase the chance of organic matter adsorbing to multiple sites on the same grain. However, a flat orientation is less effective for flocculation due to the lower probability of organic matter interacting with nearby particles (Gregory, 1978; Healy and La Mer, 1962). Thus, clay might have diminished sensitivity of floc aggregation to Al/Si (smaller A_1) and weaker floc structure (larger B_1). A flat orientation might also be less effective at capturing and retaining larger grains in flocs. Polymer chemistry and structure could also play a role by setting the binding strength to surface sites through mineralogy-specific interactions (Furukawa et al., 2014; Hemingway et al., 2019; Zeichner et al., 2021).

The relative charge density, Φ, displays a negative correlation with $w_{s,floc}$ (exponent $s = -0.0358 \pm 0.278$; Figure 8e). This relationship opposes the conventional idea that greater salinity enhances flocculation (e.g., Mehta and McAnally, 2008; van Leussen, 1988). The exponent on Φ is defined as $s = (B_2 - A_2)/(2j)$ (Equation 10) where A_2 and B_2 are the respective power-law aggregation and breakage exponents (Equations 7 and 8). Similar to the rationale for interpreting Al/Si, we estimated $j = -2.99$ so we must have $B_2 > A_2$. We again expected $A_2 > 0$ because greater ionic strength and Φ typically increase the ability of van der Waals attraction to aggregate sediment grains in the perspective of salinity-driven flocculation (Mehta and McAnally, 2008; Seiphoori et al., 2021). Assuming $A_2 > 0$, we have $B_2 > 0.21$. Although flocs are more sensitive to breakage with increasing salinity only if $B_2 > 1$, we expected that B_2 indeed exceeds 1 because $B_2 > 1$ is consistent with the D_t and D_f models where the estimated *s* is statistically-significant. We propose that salinity could have similar interactions as Al/Si on floc size and settling velocity. First, greater ionic strength should primarily affect the flocculation of clay, on which negative surface charges are concentrated compared to coarser grain sizes. However, the bulk of mud in rivers is silt, for which ionic effects should be weaker (Table 2). Thus, larger Φ might preferentially flocculate clay, rather than silt, leading to more fragile flocs with a greater number of contact points. The inverse relationship between D_t and Φ is consistent with clay enrichment by excluding coarser silt from flocs at larger Φ (Fig. 9b). Second, higher Φ could affect the physical organic matter orientation and organic matter binding capacity on sediment (e.g., through competition of ions and organic matter for binding sites on sediment surfaces).

In summary, the model calibration reveals that, out of the fitted parameters, D_t, $w_{s,floc}$, and D_f in rivers are most sensitive to sediment Al/Si and relative charge density, Φ, because their exponent magnitudes are largest (Table 2). This fact should not be interpreted to mean that

C_m and θ are less important mechanistically for flocculation because these variables might be correlated, a possibility that is masked in our calibration. The model also depends on η to a relatively large positive power (0.5 for D_t; 1 for $w_{s,\mathrm{floc}}$, and D_f) based on theory.

2.5 Discussion

Our results show that mud flocculation is widespread in rivers from geographically diverse regions spanning heterogeneous catchment lithologies and climates. Here we considered how flocculation might interplay with mud transport kinematics, channel morphology, organic carbon, tectonics, and climate.

2.5.1 Mud transport kinematics

Flocculation in rivers greatly increases mud settling velocity up to orders-of-magnitude larger than rates for individual particles (Fig. 4a). The total range of observed floc settling velocities is likely set by the primary particle diameter and Kolmogorov microscale. The minimum floc settling velocity simply occurs in the limit of increasingly fewer primary particles until the floc converges to a single particle settling according to Stokes theory. For an upper bound, prior work suggests that the Kolmogorov microscale sets the maximum floc diameter (e.g., Coufort et al., 2005; Kumar et al., 2010; Kuprenas et al., 2018). Our data compilation indicates a typical Kolmogorov microscale of 200 μm with a relatively narrow distribution across different rivers (Fig. 5 and 6; Table 1), from which we calculated a maximal floc settling velocity assuming a solid particle (n_f = 3; Fig 10). Our data support the plausibility of these bounds because they bracket all of our floc settling velocity observations (Fig. 10).

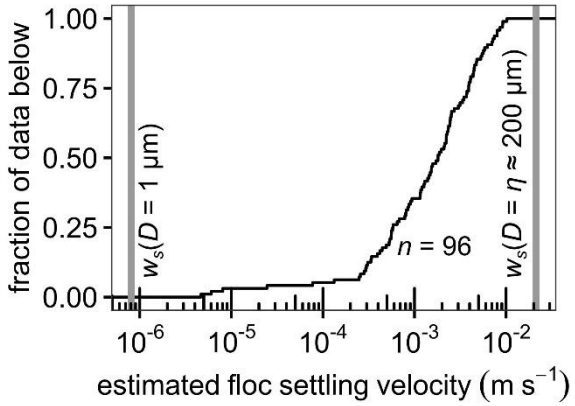

Figure 10. Empirical cumulative distribution function of river floc settling velocity estimates from the suspended sediment concentration-depth profile data compilation. The vertical lines indicate possible bounds on floc settling velocity in rivers: at 1-μm clay and at Kolmogorov microscale, η, of 200 μm typical of rivers and assuming solid particles (n_f

= 3). We computed the settling velocity bounds using the model of Ferguson and Church (2004) (Section 3.1).

Enhanced mud settling velocity due to flocculation reduces mud advective transport lengths, with implications for setting the spatial distribution and rates of mud accretion and retention in depositional zones (e.g., floodplains, deltas, wetlands). The enhanced settling velocity of mud flocs might also cause mud to be exchanged between the flow and bed as suspended bed-material load rather than washload in alluvial rivers (Lamb et al., 2020). As a result, a dynamic equilibrium of suspended mud in rivers could lead to predictive mud flux models based on bed grain size distribution as are common for cohesionless sediment (Lamb et al., 2020; Ma et al., 2020).

2.5.2 River channel-scale geomorphology

We found Kolmogorov microscale to be an important predictor of floc parameters relative to other factors, scaling linearly with floc settling velocity and diameter (Table 2). Channel hydraulic geometry (e.g., water depth and channel slope) controls the observed variation in shear velocity and Kolmogorov microscale between sites. Extremes in shear velocity inhibit mud flocculation because more intense turbulence reduces Kolmogorov microscale and less turbulent flows are less effective at suspending sediment and driving particle collisions. All else being equal, floc diameter and settling velocity might peak at moderate flows and shear velocities leading to higher relative contribution to mud accretion at those conditions. For example, repeat concentration-depth profiles sampled from 2012 to 2014 in the Fraser river show, at an intermediate flow, maximum floc settling velocity about 2.5 times greater than that at the lowest and highest flows (Environment Canada, 2021; Haught et al., 2017; Fig. 11). Discharge also covaries with other biogeochemical factors in rivers, complicating the relationship between discharge and floc properties. For instance, floods tend to dilute dissolved load concentrations (e.g., Torres et al., 2015), which could promote larger flocs and offset floc breakage.

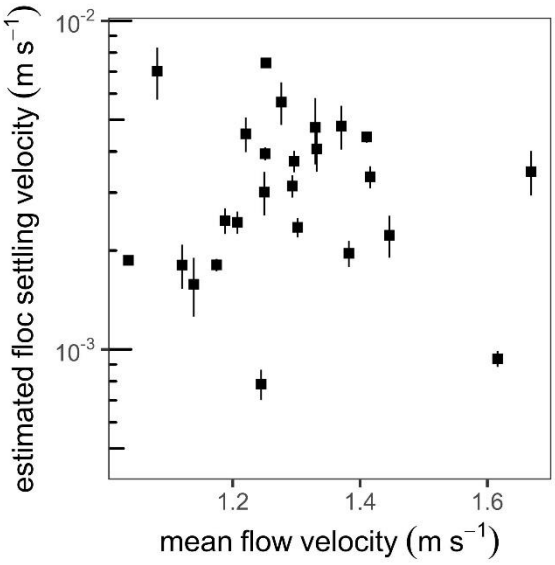

Figure 11. Comparison of mean flow velocity and floc settling velocity, estimated from our data compilation, for the Fraser river (Haught et al., 2017). We calculated mean flow velocity from continuity using channel width and depth (Haught et al., 2017) and water discharge at the Mission gaging station (station number 08MH024; Environment Canada, 2021).

Faster mud settling due to flocculation could contribute to finer channel-proximal deposits during overbank flow (Zeichner et al., 2021), and might help explain the existence of muddy levees (e.g., Adams et al., 2004; Nicholas and Walling, 1996). More cohesive channel-proximal deposits strengthen banks and limit channel lateral migration rates (Ielpi and Lapôtre, 2019; Peakall et al., 2007; van Dijk et al., 2013), thereby establishing a morphodynamic feedback between mud deposition and the long-term evolution of channel and floodplain morphology (Dunne and Jerolmack, 2020; Lapôtre et al., 2019). Mud flocculation could thus be an important control on equilibrium channel width in lowland alluvial rivers and river planform geometry. Over geologic time, mud flocculation could influence the development of alluvial stratigraphic architecture (Mackey and Bridge, 1995; Nicholas and Walling, 1996). More cohesive banks might favor aggradation and avulsion rather than lateral migration, leading to a mudrock-dominated alluvial architecture with sparse sandy channel bodies rather than laterally-extensive amalgamated channel belts (Jerolmack and Mohrig, 2007; Zeichner et al., 2021).

More accurate modeling of flocculation across floodplains with relatively slow flow likely requires the time-dependent flocculation model (Equation 9), rather than the equilibrium model on which we focused here for channels. The importance of using the unsteady model relies on the relative timescales of variation in Kolmogorov microscale and floc equilibration to local conditions, which we expect are comparable to each other in floodplains. Key parameters (n_f, j, k'_A, k'_B, A_1, A_2, B_1, B_2) remain to be evaluated in the time-dependent model in rivers.

2.5.3 Organic carbon

Organic carbon flux in rivers is closely tied to mud because its high specific surface area provides ample sites to host particulate organic carbon (France-Lanord and Derry, 1997; Galy et al., 2008; Schlünz and Schneider, 2000). We found that binding of organic matter to mud is an important predictor for floc diameter and settling velocity through θ. The functional form of θ in the model indicates an optimum for the largest and fastest-settling flocs at $\theta = 0.5$. The bulk of our θ estimates lies in the regime of $\theta < 0.5$ in which increasing organic cover leads to larger floc size and settling velocity (Fig. 6d). In this regime, the model predicts that river suspended sediment with greater organic carbon concentration form larger, faster-settling flocs. Thus, there is potential for a feedback in net depositional zones whereby higher organic carbon concentration causes faster floc and organic carbon settling rates, which increase carbon preservation potential (Galy et al., 2007; Hartnett et al., 1998; Torres et al., 2020).

Field and laboratory flocculation studies have indicated that organic matter composition can be important for determining the degree to which organic matter affects flocculation (e.g., Furukawa et al., 2014; Lee et al., 2017; Zeichner et al., 2021), an effect not accounted for in our model. Previous work suggested that bacteria-derived EPS tends to encourage flocculation because its molecular composition and structure can generate a chain-like physical orientation when adsorbed on sediment, while aromatic-rich materials tend to discourage flocculation because they coat sediment evenly and limit interparticle contact between organic matter and bare sediment surfaces (Furukawa et al., 2014; Healy and La Mer, 1962; Lee et al., 2019). Shifts in organic matter composition and/or abundance (i.e., due to changes in terrestrial vegetation, algal productivity, hillslope input of organic detritus) and the covariation of such factors due to climate change and human activity (e.g., Li et al., 2021) could trigger changes in flocculation. Floods are an additional catchment-specific factor for organic matter because floods of different magnitude can source different parts of the catchment (e.g., Dunne and Black, 1970) with different types of organic matter (Golombek et al., 2021).

Our results indicate that greater river water ionic strength, through Φ, reduces floc size in rivers. However, as rivers approach the ocean in estuaries, it is well known that the increasing salinity typically enhances flocculation. The salinity to induce flocculation usually occurs at a few parts per thousand (e.g., Drake, 1976; Einstein and Krone, 1962; Whitehouse et al., 2013), which is an order of magnitude larger than the values measured in rivers in our compilation (median salinity of 0.2 parts per thousand). Given that flocculation appears common in rivers, there could be a process transition from organics-mediated flocculation in freshwater to salinity-mediated flocculation in estuaries. In line with this view, Eisma et al. (1991) analyzed C isotope ratios of suspended sediment organic matter and found a transition in organic matter from freshwater- to marine-origin entering the Gironde estuary. In contrast, data from the Rhine and Elbe estuaries show that organic matter binding river flocs persisted in estuaries and led to minimal change in floc size in estuaries (Eisma et al., 1982; Puls and Kühl, 1986).

2.5.4 Climate, tectonics, and lithology

Climate, tectonics, and lithology affect chemical weathering and the delivery of weathering products (solids and solutes) to rivers, setting the chemical composition of sediment and river water (Hilton and West, 2020; West et al., 2005). In our model, these basinwide geochemical effects are expressed in Al/Si, Φ, and θ. Weathering-limited catchments (e.g., in rapidly uplifting mountains) yield fresher, less weathered sediment with smaller Al/Si and supply fewer dissolved ions (smaller Φ) to a river system (West et al., 2005). The rock and soil composition of source areas can also affect the composition and concentration of dissolved species in river water, which both contribute to Φ. Organic matter concentration in rivers might be higher in areas with more humid climates and/or relatively younger organics-rich soils and promote flocculation because of greater biological productivity and θ (Galy et al., 2015). Tectonic uplift, in concert with climate, could enhance mountain export of sediment load, weathering products, and nutrients, which could also promote biological productivity (Geider et al., 2001; Godard et al., 2014; Raymo and Ruddiman, 1992).

With climate warming, rivers might source more weathering products and dissolved ions (Li et al., 2016; Perron, 2017), reducing the settling velocity of mud flocs in rivers. Warming could also change the magnitudes of sediment and organic carbon supply to rivers because of changes in catchment erosion rates (e.g., Perron, 2017) and biological productivity (e.g., Godard et al., 2014). These scenarios could alter the rates of mud and organic carbon delivery to floodplains via flocs and could be explored using our calibrated model.

2.6 Conclusion

Evidence from a global river suspended sediment data compilation shows that mud flocculation in rivers is common. Results from fitting the Rouse-Vanoni equation to grain size-specific concentration-depth profiles show, on average, that mud flocs in rivers have diameter of 130 μm, settle at a rate of 1.8 mm s^{-1}, and are composed of primary particles smaller than 39 μm (clay and silt). We proposed and verified a semi-empirical model for floc diameter and settling velocity in rivers. The calibrated model explains the estimated river floc settling velocities within a factor of about two. Out of the variables considered, sediment Al/Si has the strongest negative correlation with a fitted model exponent -2.15 ± 0.900. Kolmogorov microscale has the strongest positive correlation because it scales linearly with floc settling velocity. Higher floc settling velocity also scales with smaller relative charge density of river water compared to sediment (exponent -0.0358 ± 0.278) and larger mud concentration and organic matter coverage on sediment grains (shared exponent 0.167 ± 0.0989). These relationships highlight the key role of geochemical interactions between primary particles and organic matter. Our model predicts a turbulence control for which floc diameter is generally smaller than the Kolmogorov microscale because floc breakage rate rapidly increases at large floc diameter, but floc diameter can exceed the microscale depending on the effects of the other predictor variables. The model dependencies imply that allogenic controls can affect floc properties, mud and organic carbon accretion in floodplains,

and fluvial morphodynamics, resulting in possible new links between mud transport, tectonics, climate, and the global carbon cycle.

2.7 Notation

Al/Si	aluminum-silicon molar ratio of suspended sediment, dimensionless
C	Volumetric sediment concentration, dimensionless
C_{bi}	Volumetric near-bed sediment concentration for *i*th grain size class, dimensionless
C_m	Volumetric depth-averaged mud concentration, dimensionless
D	Particle diameter (unflocculated sediment), m
D_f	Floc diameter, m
D_p	Primary particle diameter, m
D_t	Floc cutoff diameter, m
e	Elementary charge magnitude (= 1.602×10^{-19}), C
g	Gravitational acceleration (= 9.81 m s^{-2}), m s^{-2}
h	River water depth, m
h_b	Near-bed reference height, m
k	Calibrated model prefactor constant, dimensionless
k_A	Floc aggregation efficiency, dimensionless
k_B	Floc breakage efficiency, dimensionless
k_{BM}	Boltzmann constant (= 1.381), J K^{-1}
n_f	Floc fractal dimension (= 2), dimensionless
p_i	Rouse number for *i*th grain size class, dimensionless
q	Calibrated model exponent of $C_m\theta^2(1-\theta)^2$ term, dimensionless
r	Calibrated model exponent of Al/Si term, dimensionless

s	Calibrated model exponent of Φ term, dimensionless
u_*	Shear velocity, m s^{-1}
$w_{s,\mathrm{floc}}$	Floc settling velocity, m s^{-1}
w_{si}	*In situ* particle settling velocity for *i*th grain size class, m s^{-1}
β_i	Ratio of sediment and fluid diffusivities for *i*th grain size class, dimensionless
ϵ_0	Vacuum permittivity (= 8.854×10^{-12}), F m^{-1}
ϵ_r	Dielectric constant of water, dimensionless
η	Kolmogorov microscale, m
θ	Fraction of sediment surface covered by organic matter, dimensionless
Φ	Ratio of charge densities in river water and on the sediment
κ	Von Kármán constant (= 0.41), dimensionless
λ	Debye length, m
ν	Kinematic viscosity of water (= 10^{-6}), m^2 s^{-1}
ρ	Water density (= 1000), kg m^{-3}
ρ_s	Sediment density (= 2650), kg m^{-3}

2.8 Acknowledgments and Data

JN acknowledges NASA FINESST grant 80NSSC20K1645. WWF and MPL acknowledge funding by the Discovery Fund and the Resnick Sustainability Institute at Caltech. GKL acknowledges the Caltech Geology Option Postdoc Fellowship. MPL acknowledges funding from the NASA Delta-X project by the Science Mission Directorate's Earth Science Division through the Earth Venture Suborbital-3 Program NNH17ZDA001N-EVS3 and the National Science Foundation Geomorphology and Land-use Dynamics grant number 2136991. The authors thank reviewer Scott Wright and four anonymous reviewers for their feedback, which improved the paper. The authors also thank Editor Ton Hoitink and Associate Editor Florent Grasso.

The suspended sediment concentration-depth profile, grain size distribution, and geochemical data used in this paper are freely available in the respective original

publications. The authors are grateful to J. Bouchez, E. Dingle, and J. Shelley for sharing data used in this paper. Derived data are available online at https://doi.org/10.22002/5f3zb-9xm59.

2.9 References

Abraham, D., Ramos-Villanueva, M., Pratt, T., Ganesh, N., May, D., Butler, W., McAlpin, T., Jones, K., Shelley, J., & Pridal, D. (2017). *Sediment and Hydraulic Measurements with Computed Bed Load on the Missouri River, Sioux City to Hermann, 2014*. U. S. Army Corps of Engineers ERDC Coastal and Hydraulics Laboratory.

Adams, P. N., Slingerland, R. L., & Smith, N. D. (2004). Variations in natural levee morphology in anastomosed channel flood plain complexes. *Geomorphology*, *61*(1), 127–142. https://doi.org/10.1016/j.geomorph.2003.10.005

Alexander, R. B., Ludtke, A. S., Fitzgerald, K. K., & Schertz, T. L. (1997). Data from selected U.S. Geological Survey national stream water-quality monitoring networks (WQN) on CD-ROM. In *Data from selected U.S. Geological Survey national stream water-quality monitoring networks (WQN) on CD-ROM* (USGS Numbered Series No. 96–337; Open-File Report, Vols. 96–337). https://doi.org/10.3133/ofr96337

Aller, R. C. (1998). Mobile deltaic and continental shelf muds as suboxic, fluidized bed reactors. *Marine Chemistry*, *61*(3–4), 143–155. https://doi.org/10.1016/S0304-4203(98)00024-3

Azam, M. M., Kumari, M., Maharana, C., Singh, A. K., & Tripathi, J. K. (2018). Recent insights into the dissolved and particulate fluxes from the Himalayan tributaries to the Ganga River. *Environmental Earth Sciences*, *77*(8), 313. https://doi.org/10.1007/s12665-018-7490-7

Bache, D. H. (2004). Floc rupture and turbulence: A framework for analysis. *Chemical Engineering Science*, *59*(12), 2521–2534. https://doi.org/10.1016/j.ces.2004.01.055

Barber, A., Brandes, J., Leri, A., Lalonde, K., Balind, K., Wirick, S., Wang, J., & Gélinas, Y. (2017). Preservation of organic matter in marine sediments by inner-sphere interactions with reactive iron. *Scientific Reports*, *7*(1), 1–10. https://doi.org/10.1038/s41598-017-00494-0

Baronas, J. J., Stevenson, E. I., Hackney, C. R., Darby, S. E., Bickle, M. J., Hilton, R. G., Larkin, C. S., Parsons, D. R., Myo Khaing, A., & Tipper, E. T. (2020). Integrating suspended sediment flux in large alluvial river channels: Application of a synoptic Rouse-based model to the Irrawaddy and Salween rivers. *Journal of Geophysical Research: Earth Surface*, *125*(9), e2020JF005554. https://doi.org/10.1029/2020JF005554

Bird, M. I., Robinson, R. A. J., Oo, N. W., Aye, M. M., Lu, X. X., Higgitt, D. L., Swe, A., Tun, T., Win, S. L., & Aye, K. S. (2008). A preliminary estimate of organic carbon transport by the Ayeyarwady (Irrawaddy) and Thanlwin (Salween) Rivers of Myanmar. *Quaternary International*, *186*(1), 113–122. https://doi.org/10.1016/j.quaint.2007.08.003

Bock, M. J., & Mayer, L. M. (2000). Mesodensity organo–clay associations in a near-shore sediment. *Marine Geology*, *163*(1–4), 65–75. https://doi.org/10.1016/S0025-3227(99)00105-X

Bonotto, D. M., & da Silveira, E. G. (2003). Preference ratios for mercury and other chemical elements in the Madeira River, Brazil. *Journal of South American Earth Sciences*, *15*(8), 911–923. https://doi.org/10.1016/S0895-9811(02)00144-X

Bouchez, J., Gaillardet, J., Lupker, M., Louvat, P., France-Lanord, C., Maurice, L., Armijos, E., & Moquet, J.-S. (2012). Floodplains of large rivers: Weathering reactors or simple silos? *Chemical Geology*, *332*, 166–184. https://doi.org/10.1016/j.chemgeo.2012.09.032

Bouchez, J., Galy, V., Hilton, R. G., Gaillardet, J., Moreira-Turcq, P., Pérez, M. A., France-Lanord, C., & Maurice, L. (2014). Source, transport and fluxes of Amazon River particulate organic carbon: Insights from river sediment depth-profiles. *Geochimica et Cosmochimica Acta*, *133*, 280–298. https://doi.org/10.1016/j.gca.2014.02.032

Bouchez, J., Lupker, M., Gaillardet, J., France-Lanord, C., & Maurice, L. (2011a). How important is it to integrate riverine suspended sediment chemical composition with depth? Clues from Amazon River depth-profiles. *Geochimica et Cosmochimica Acta*, *75*(22), 6955–6970. https://doi.org/10.1016/j.gca.2011.08.038

Bouchez, J., Métivier, F., Lupker, M., Maurice, L., Perez, M., Gaillardet, J., & France-Lanord, C. (2011b). Prediction of depth-integrated fluxes of suspended sediment in the Amazon River: Particle aggregation as a complicating factor. *Hydrological Processes*, *25*(5), 778–794. https://doi.org/10.1002/hyp.7868

Bouchez, J. (2022). *Grain size distribution of Amazon river sediment samples collected over the period 2005-2008; and ADCP water velocity profiles collected on the major tributaries of the Amazon in Bolivia and Peru, 2007-2008*. https://doi.org/10.5281/zenodo.6458298

Brigham, C. (2018). Biopolymers: Biodegradable Alternatives to Traditional Plastics. *Green Chemistry: An Inclusive Approach*, 753–770. https://doi.org/10.1016/B978-0-12-809270-5.00027-3

Bungartz, H., Krüger, A., & Engelhardt, C. (2006). Fluvial suspended sediment dynamics: Implications for particulate organic carbon transport modeling. *Water Resources Research*, *42*(10). https://doi.org/10.1029/2005WR004486

Bungartz, H., & Wanner, S. C. (2004). Significance of particle interaction to the modelling of cohesive sediment transport in rivers. *Hydrological Processes*, *18*(9), 1685–1702. https://doi.org/10.1002/hyp.1412

Burban, P.-Y., Xu, Y.-J., McNeil, J., & Lick, W. (1990). Settling speeds of flocs in fresh water and seawater. *Journal of Geophysical Research: Oceans*, *95*(C10), 18213–18220. https://doi.org/10.1029/JC095iC10p18213

Cameron, E. M., Hall, G. E., Veizer, J., & Krouse, H. R. (1995). Isotopic and elemental hydrogeochemistry of a major river system: Fraser River, British Columbia, Canada. *Chemical Geology*, *122*(1–4), 149–169. https://doi.org/10.1016/0009-2541(95)00007-9

Canfield, D. E. (1997). The geochemistry of river particulates from the continental USA: major elements. *Geochimica et Cosmochimica Acta*, *61*(16), 3349–3365. https://doi.org/10.1016/S0016-7037(97)00172-5

Chapman, H., Bickle, M., Thaw, S. H., & Thiam, H. N. (2015). Chemical fluxes from time series sampling of the Irrawaddy and Salween Rivers, Myanmar. *Chemical Geology*, *401*, 15–27. https://doi.org/10.1016/j.chemgeo.2015.02.012

Chase, R. R. (1979). Settling behavior of natural aquatic particulates. *Limnology and Oceanography*, *24*(3), 417–426. https://doi.org/10.4319/lo.1979.24.3.0417

Christiansen, D. E. (2004). *Riverbed elevations and water quality of the Missouri River at Sioux City, Iowa, 2002-03* (Report No. 2004–5079; Scientific Investigations Report). USGS Publications Warehouse. https://doi.org/10.3133/sir20045079

Church, M. (2006). Bed material transport and the morphology of alluvial river channels. *Annual Reviews of Earth and Planetary Science*, *34*, 325–354. https://doi.org/10.1146/annurev.earth.33.092203.122721

Coufort, C., Bouyer, D., & Liné, A. (2005). Flocculation related to local hydrodynamics in a Taylor–Couette reactor and in a jar. *Chemical Engineering Science*, *60*(8–9), 2179–2192. https://doi.org/10.1016/j.ces.2004.10.038

De Leeuw, J., Lamb, M. P., Parker, G., Moodie, A. J., Haught, D., Venditti, J. G., & Nittrouer, J. A. (2020). Entrainment and suspension of sand and gravel. *Earth Surface Dynamics*, *8*(2), 485–504. https://doi.org/10.5194/esurf-8-485-2020

Ding, T., Gao, J., Tian, S., Wang, H., Li, L. I., Wang, C., Luo, X., & Hang, D. (2016). Chemical and isotopic characters of the water and suspended particulate materials in the Yellow River and their geological and environmental implications. *Acta Geologica Sinica-English Edition*, *90*(1), 285–351. https://doi.org/10.1111/1755-6724.12658

Dingle, E. H. (2021). *Karnali River Suspended Sediment Sampling*. https://doi.org/10.5281/zenodo.4923989

Dingle, E. H., Sinclair, H. D., Venditti, J. G., Attal, M., Kinnaird, T. C., Creed, M., Quick, L., Nittrouer, J. A., & Gautam, D. (2020). Sediment dynamics across gravel-sand transitions: Implications for river stability and floodplain recycling. *Geology*. https://doi.org/10.1130/G46909.1

Dosseto, A., Bourdon, B., Gaillardet, J., Allègre, C. J., & Filizola, N. (2006a). Time scale and conditions of weathering under tropical climate: Study of the Amazon basin with U-series. *Geochimica et Cosmochimica Acta*, *70*(1), 71–89. https://doi.org/10.1016/j.gca.2005.06.033

Dosseto, A., Bourdon, B., Gaillardet, J., Maurice-Bourgoin, L., & Allègre, C. J. (2006b). Weathering and transport of sediments in the Bolivian Andes: Time constraints from uranium-series isotopes. *Earth and Planetary Science Letters*, *248*(3–4), 759–771. https://doi.org/10.1016/j.epsl.2006.06.027

Drake, D. E. (1976). Suspended sediment transport and mud deposition on continental shelves. *Marine Sediment Transport and Environmental Management*, *40*, 127–158.

Droppo, I. G., Leppard, G. G., Flannigan, D. T., & Liss, S. N. (1997). The Freshwater Floc: A Functional Relationship of Water and Organic and Inorganic Floc Constituents Affecting Suspended Sediment Properties. *The Interactions Between Sediments and Water: Proceedings of the 7th International Symposium, Baveno, Italy 22–25 September 1996*, 43–53. https://doi.org/10.1007/978-94-011-5552-6_5

Droppo, I. G., & Ongley, E. D. (1994). Flocculation of suspended sediment in rivers of southeastern Canada. *Water Research*, *28*(8), 1799–1809. https://doi.org/10.1016/0043-1354(94)90253-4

Dunne, K. B., & Jerolmack, D. J. (2020). What sets river width? *Science Advances*, *6*(41), eabc1505. https://doi.org/10.1126/sciadv.abc1505

Dunne, T., & Black, R. D. (1970). Partial area contributions to storm runoff in a small New England watershed. *Water Resources Research*, *6*(5), 1296–1311. https://doi.org/10.1029/WR006i005p01296

Einstein, H. A., & Krone, R. B. (1962). Experiments to determine modes of cohesive sediment transport in salt water. *Journal of Geophysical Research*, *67*(4), 1451–1461. https://doi.org/10.1029/JZ067i004p01451

Eisma, D., Bernard, P., Cadée, G. C., Ittekkot, V., Kalf, J., Laane, R., Martin, J. M., Mook, W. G., Van Put, A., & Schuhmacher, T. (1991). Suspended-matter particle size in some

West-European estuaries; Part I: Particle-size distribution. *Netherlands Journal of Sea Research*, *28*(3), 193–214. https://doi.org/10.1016/0077-7579(91)90017-U

Eisma, D., Cadée, G. C., Laane, R., & Kalf, J. (1982). Preliminary results of AURELIA-and NAVICULA Cruises in the Rhine-and Ems-estuaries, January-February, 1982. *Mitteilungen Aus Dem Geologisch-Paläontologischen Institut Der Universität Hamburg*, *52*, 633–654.

Elbaz-Poulichet, F., Seyler, P., Maurice-Bourgoin, L., Guyot, J.-L., & Dupuy, C. (1999). Trace element geochemistry in the upper Amazon drainage basin (Bolivia). *Chemical Geology*, *157*(3–4), 319–334. https://doi.org/10.1016/S0009-2541(99)00015-7

English, N. B., Quade, J., DeCelles, P. G., & Garzione, C. N. (2000). Geologic control of Sr and major element chemistry in Himalayan Rivers, Nepal. *Geochimica et Cosmochimica Acta*, *64*(15), 2549–2566. https://doi.org/10.1016/S0016-7037(00)00379-3

Environment Canada. (2021). *Environment and Climate Change Canada Historical Hydrometric Data*. https://wateroffice.ec.gc.ca/mainmenu/historical_data_index_e.html

Ersahin, S., Gunal, H., Kutlu, T., Yetgin, B., & Coban, S. (2006). Estimating specific surface area and cation exchange capacity in soils using fractal dimension of particle-size distribution. *Geoderma*, *136*(3–4), 588–597. https://doi.org/10.1016/j.geoderma.2006.04.014

Ferguson, R. I., & Church, M. (2004). A Simple Universal Equation for Grain Settling Velocity. *Journal of Sedimentary Research*, *74*(6), 933–937. https://doi.org/10.1306/051204740933

France-Lanord, C., & Derry, L. A. (1997). Organic carbon burial forcing of the carbon cycle from Himalayan erosion. *Nature*, *390*(6655), 65–67. https://doi.org/10.1038/36324

Friedman, J., Hastie, T., & Tibshirani, R. (2010). Regularization paths for generalized linear models via coordinate descent. *Journal of Statistical Software*, *33*(1), 1. https://doi.org/10.18637/jss.v033.i01

Furukawa, Y., Reed, A. H., & Zhang, G. (2014). Effect of organic matter on estuarine flocculation: A laboratory study using montmorillonite, humic acid, xanthan gum, guar gum and natural estuarine flocs. *Geochemical Transactions*, *15*(1), 1. https://doi.org/10.1186/1467-4866-15-1

Galy, A., & France-Lanord, C. (1999). Weathering processes in the Ganges–Brahmaputra basin and the riverine alkalinity budget. *Chemical Geology*, *159*(1–4), 31–60. https://doi.org/10.1016/S0009-2541(99)00033-9

Galy, V., France-Lanord, C., Beyssac, O., Faure, P., Kudrass, H., & Palhol, F. (2007). Efficient organic carbon burial in the Bengal fan sustained by the Himalayan erosional system. *Nature*, *450*(7168), 407–410. https://doi.org/10.1038/nature06273

Galy, V., France-Lanord, C., & Lartiges, B. (2008). Loading and fate of particulate organic carbon from the Himalaya to the Ganga–Brahmaputra delta. *Geochimica et Cosmochimica Acta*, *72*(7), 1767–1787. https://doi.org/10.1016/j.gca.2008.01.027

Galy, V., Peucker-Ehrenbrink, B., & Eglinton, T. (2015). Global carbon export from the terrestrial biosphere controlled by erosion. *Nature*, *521*(7551), 204–207. https://doi.org/10.1038/nature14400

Garcia, M. (2008). *Sedimentation engineering: Processes, measurements, modeling, and practice*. https://doi.org/10.1061/9780784408148

Garcia-Aragon, J., Droppo, I. G., Krishnappan, B., Trapp, B., & Jaskot, C. (2011). Experimental assessment of Athabasca River cohesive sediment deposition dynamics. *Water Quality Research Journal of Canada*, *46*(1), 87–96. https://doi.org/10.2166/wqrjc.2011.030

Garzanti, E., Wang, J.-G., Vezzoli, G., & Limonta, M. (2016). Tracing provenance and sediment fluxes in the Irrawaddy River basin (Myanmar). *Chemical Geology*, *440*, 73–90. https://doi.org/10.1016/j.chemgeo.2016.06.010

Geider, R. J., Delucia, E. H., Falkowski, P. G., Finzi, A. C., Grime, J. P., Grace, J., Kana, T. M., La Roche, J., Long, S. P., & Osborne, B. A. (2001). Primary productivity of planet earth: Biological determinants and physical constraints in terrestrial and aquatic habitats. *Global Change Biology*, *7*(8), 849–882. https://doi.org/10.1046/j.1365-2486.2001.00448.x

Gerbersdorf, S. U., Jancke, T., Westrich, B., & Paterson, D. M. (2008). Microbial stabilization of riverine sediments by extracellular polymeric substances. *Geobiology*, *6*(1), 57–69. https://doi.org/10.1111/j.1472-4669.2007.00120.x

Godard, V., Bourlès, D. L., Spinabella, F., Burbank, D. W., Bookhagen, B., Fisher, G. B., Moulin, A., & Léanni, L. (2014). Dominance of tectonics over climate in Himalayan denudation. *Geology*, *42*(3), 243–246. https://doi.org/10.1130/G35342.1

Golombek, N. Y., Scheingross, J. S., Repasch, M. N., Hovius, N., Menges, J., Sachse, D., Lupker, M., Eglinton, T. I., Haghipour, N., & Poulson, S. R. (2021). Fluvial organic carbon composition regulated by seasonal variability in lowland river migration and water discharge. *Geophysical Research Letters*, e2021GL093416. https://doi.org/10.1029/2021GL093416

Graf, W. H., & Cellino, M. (2002). Suspension flows in open channels; experimental study. *Journal of Hydraulic Research*, *40*(4), 435–447. https://doi.org/10.1080/00221680209499886

Gratiot, N., Michallet, H., & Mory, M. (2005). On the determination of the settling flux of cohesive sediments in a turbulent fluid. *Journal of Geophysical Research: Oceans*, *110*(C6). https://doi.org/10.1029/2004JC002732

Gregory, J. (1978). Effects of polymers on colloid stability. *The Scientific Basis of Flocculation*, 101–130. https://doi.org/10.1007/978-94-009-9938-1_6

Guyot, J.-L., Jouanneau, J.-M., Quintanilla, J., & Wasson, J.-G. (1993). Dissolved and suspended sediment loads exported from the Andes by the Beni river (Bolivian Amazonia), during a Flood. *Geodinamica Acta*, *6*(4), 233–241. https://doi.org/10.1080/09853111.1993.11105251

Hackley, P. C., Valentine, B. J., Voortman, L. M., Van Oosten Slingeland, D. S., & Hatcherian, J. (2017). Utilization of integrated correlative light and electron microscopy (iCLEM) for imaging sedimentary organic matter. *Journal of Microscopy*, *267*(3), 371–383. https://doi.org/10.1111/jmi.12576

Hartnett, H. E., Keil, R. G., Hedges, J. I., & Devol, A. H. (1998). Influence of oxygen exposure time on organic carbon preservation in continental margin sediments. *Nature*, *391*(6667), 572–575. https://doi.org/10.1038/35351

Haught, D., Venditti, J. G., & Wright, S. A. (2017). Calculation of in situ acoustic sediment attenuation using off-the-shelf horizontal ADCPs in low concentration settings. *Water Resources Research*, *53*(6), 5017–5037. https://doi.org/10.1002/2016WR019695

Healy, T. W., & La Mer, V. K. (1962). The adsorption-flocculation reactions of a polymer with an aqueous colloidal dispersion. *The Journal of Physical Chemistry*, *66*(10), 1835–1838. https://doi.org/10.1021/j100816a014

Hedges, J. I., Mayorga, E., Tsamakis, E., McClain, M. E., Aufdenkampe, A., Quay, P., Richey, J. E., Benner, R., Opsahl, S., & Black, B. (2000). Organic matter in Bolivian tributaries of the Amazon River: A comparison to the lower mainstream. *Limnology and Oceanography*, *45*(7), 1449–1466. https://doi.org/10.4319/lo.2000.45.7.1449

Hemingway, J. D., Rothman, D. H., Grant, K. E., Rosengard, S. Z., Eglinton, T. I., Derry, L. A., & Galy, V. V. (2019). Mineral protection regulates long-term global preservation of natural organic carbon. *Nature*, *570*(7760), 228–231. https://doi.org/10.1038/s41586-019-1280-6

Hill, P. S., Milligan, T. G., & Geyer, W. R. (2000). Controls on effective settling velocity of suspended sediment in the Eel River flood plume. *Continental Shelf Research*, *20*(16), 2095–2111. https://doi.org/10.1016/S0278-4343(00)00064-9

Hilton, R. G., & West, A. J. (2020). Mountains, erosion and the carbon cycle. *Nature Reviews Earth & Environment*, *1*(6), 284–299. https://doi.org/10.1038/s43017-020-0058-6

Hossain, H. Z., Kawahata, H., Roser, B. P., Sampei, Y., Manaka, T., & Otani, S. (2017). Geochemical characteristics of modern river sediments in Myanmar and Thailand: Implications for provenance and weathering. *Geochemistry*, *77*(3), 443–458. https://doi.org/10.1016/j.chemer.2017.07.005

Hu, B., Li, J., Bi, N., Wang, H., Wei, H., Zhao, J., Xie, L., Zou, L., Cui, R., & Li, S. (2015). Effect of human-controlled hydrological regime on the source, transport, and flux of particulate organic carbon from the lower Huanghe (Yellow River). *Earth Surface Processes and Landforms*, *40*(8), 1029–1042. https://doi.org/10.1002/esp.3702

Huang, W. W., Jing, Z., & Zhou, Z. H. (1992). Particulate element inventory of the Huanghe (Yellow River): A large, high-turbidity river. *Geochimica et Cosmochimica Acta*, *56*(10), 3669–3680. https://doi.org/10.1016/0016-7037(92)90160-K

Huang, X., Sillanpää, M., Gjessing, E. T., & Vogt, R. D. (2009). Water quality in the Tibetan Plateau: Major ions and trace elements in the headwaters of four major Asian rivers. *Science of the Total Environment*, *407*(24), 6242–6254. https://doi.org/10.1016/j.scitotenv.2009.09.001

Ielpi, A., & Lapôtre, M. G. (2019). Biotic forcing militates against river meandering in the modern Bonneville Basin of Utah. *Sedimentology*, *66*(5), 1896–1929. https://doi.org/10.1111/sed.12562

Ito, A., & Wagai, R. (2017). Global distribution of clay-size minerals on land surface for biogeochemical and climatological studies. *Scientific Data*, *4*, 170103. https://doi.org/10.1038/sdata.2017.103

Jackson, M. L., Tyler, S. A., Willis, A. L., Bourbeau, G. A., & Pennington, R. P. (1948). Weathering sequence of clay-size minerals in soils and sediments. I. Fundamental generalizations. *The Journal of Physical Chemistry*, *52*(7), 1237–1260. https://doi.org/10.1021/j150463a015

Jerolmack, D. J., & Mohrig, D. (2007). Conditions for branching in depositional rivers. *Geology*, *35*(5), 463–466. https://doi.org/10.1130/G23308A.1

Kelly, V., Hooper, R., Aulenbach, B., & Janet, M. (2001). *Concentrations and annual fluxes for selected water-quality constituents from the USGS National Stream Quality Accouting Network (NASQAN), 1996-2000* (Report No. 01–4255; Water-Resources Investigations Report). United States Geological Survey.

Kleeschulte, M. J. (1993). Water-quality data for the Missouri River and Missouri River alluvium near Weldon Spring, St. Charles County, Missouri; 1991-92. In *Open-File Report* (No. 93–109). https://doi.org/10.3133/ofr93109

Kleinhans, M. G., de Vries, B., Braat, L., & van Oorschot, M. (2018). Living landscapes: Muddy and vegetated floodplain effects on fluvial pattern in an incised river. *Earth Surface Processes and Landforms*, *43*(14), 2948–2963. https://doi.org/10.1002/esp.4437

Kranck, K., & Milligan, T. (1980). Macroflocs: Production of marine snow in the laboratory. *Marine Ecology - Progress Series*, *3*, 19–24.

Kranenburg, C. (1994). The fractal structure of cohesive sediment aggregates. *Estuarine, Coastal and Shelf Science*, *39*(6), 451–460. https://doi.org/10.1016/S0272-7714(06)80002-8

Kumar, R. G., Strom, K. B., & Keyvani, A. (2010). Floc properties and settling velocity of San Jacinto estuary mud under variable shear and salinity conditions. *Continental Shelf Research*, *30*(20), 2067–2081. https://doi.org/10.1016/j.csr.2010.10.006

Kuprenas, R., Tran, D., & Strom, K. (2018). A Shear-Limited Flocculation Model for Dynamically Predicting Average Floc Size. *Journal of Geophysical Research: Oceans*, *123*(9), 6736–6752. https://doi.org/10.1029/2018JC014154

Lamb, M. P., De Leeuw, J., Fischer, W. W., Moodie, A. J., Venditti, J. G., Nittrouer, J. A., Haught, D., & Parker, G. (2020). Mud in rivers transported as flocculated and suspended bed material. *Nature Geoscience*, *13*(8), 566–570. https://doi.org/10.1038/s41561-020-0602-5

Lapôtre, M. G., Ielpi, A., Lamb, M. P., Williams, R. M., & Knoll, A. H. (2019). Model for the formation of single-thread rivers in barren landscapes and implications for pre-Silurian and martian fluvial deposits. *Journal of Geophysical Research: Earth Surface*, *124*(12), 2757–2777. https://doi.org/10.1029/2019JF005156

Larsen, L. G., Harvey, J. W., & Crimaldi, J. P. (2009). Morphologic and transport properties of natural organic floc. *Water Resources Research*, *45*(1). https://doi.org/10.1029/2008WR006990

Lee, B. J., Hur, J., & Toorman, E. A. (2017). Seasonal variation in flocculation potential of river water: Roles of the organic matter pool. *Water*, *9*(5), 335. https://doi.org/10.3390/w9050335

Lee, B. J., Kim, J., Hur, J., Choi, I. H., Toorman, E. A., Fettweis, M., & Choi, J. W. (2019). Seasonal Dynamics of Organic Matter Composition and Its Effects on Suspended Sediment Flocculation in River Water. *Water Resources Research*, *55*(8), 6968–6985. https://doi.org/10.1029/2018WR024486

Lee, C. (2020). *Nutrient and pesticide data collected from the USGS National Water Quality Network and previous networks, 1963-2019* [Data set]. https://doi.org/10.5066/P9AEWTB9

Leenheer, J. A., Barber, L. B., Rostad, C. E., & Noyes, T. I. (1995). *Data on natural organic substances in dissolved, colloidal, suspended-silt and -clay, and bed-sediment phases in the Mississippi River and some of its tributaries, 1991-92* (Report No. 94–4191; Water-Resources Investigations Report). USGS Publications Warehouse. https://doi.org/10.3133/wri944191

Lehner, B., Verdin, K., & Jarvis, A. (2008). New global hydrography derived from spaceborne elevation data. *Eos, Transactions American Geophysical Union*, *89*(10), 93–94. https://doi.org/10.1029/2008EO100001

Li, G., Hartmann, J., Derry, L. A., West, A. J., You, C.-F., Long, X., Zhan, T., Li, L., Li, G., & Qiu, W. (2016). Temperature dependence of basalt weathering. *Earth and Planetary Science Letters*, *443*, 59–69. https://doi.org/10.1016/j.epsl.2016.03.015

Li, G. K., Fischer, W. W., Lamb, M. P., West, A. J., Zhang, T., Galy, V., Wang, X. T., Li, S., Qiu, H., & Li, G. (2021). Coal fly ash is a major carbon flux in the Chang Jiang (Yangtze River) basin. *Proceedings of the National Academy of Sciences*, *118*(21). https://doi.org/10.1073/pnas.1921544118

Li, J.-Y., & Zhang, J. (2003). Chemical Weathering Processes and Atmospheric CO2 Consumption in the Yellow River Drainage Basin. *Marine Geology and Quaternary Geology*, *23*(2), 43–49.

Lick, W., & Lick, J. (1988). Aggregation and disaggregation of fine-grained lake sediments. *Journal of Great Lakes Research*, *14*(4), 514–523. https://doi.org/10.1016/S0380-1330(88)71583-X

Lupker, M., France-Lanord, C., Galy, V., Lavé, J., Gaillardet, J., Gajurel, A. P., Guilmette, C., Rahman, M., Singh, S. K., & Sinha, R. (2012). Predominant floodplain over mountain weathering of Himalayan sediments (Ganga basin). *Geochimica et Cosmochimica Acta*, *84*, 410–432. https://doi.org/10.1016/j.gca.2012.02.001

Lupker, M., France-Lanord, C., Lavé, J., Bouchez, J., Galy, V., Métivier, F., Gaillardet, J., Lartiges, B., & Mugnier, J.-L. (2011). A Rouse-based method to integrate the chemical composition of river sediments: Application to the Ganga basin. *Journal of Geophysical Research: Earth Surface*, *116*(F4). https://doi.org/10.1029/2010JF001947

Ma, H., Nittrouer, J. A., Wu, B., Lamb, M. P., Zhang, Y., Mohrig, D., Fu, X., Naito, K., Wang, Y., & Moodie, A. J. (2020). Universal relation with regime transition for sediment

transport in fine-grained rivers. *Proceedings of the National Academy of Sciences*, *117*(1), 171–176. https://doi.org/10.1073/pnas.1911225116

Mackey, S. D., & Bridge, J. S. (1995). Three-dimensional model of alluvial stratigraphy; theory and applications. *Journal of Sedimentary Research*, *65*(1b), 7–31. https://doi.org/10.1306/D42681D5-2B26-11D7-8648000102C1865D

Maggi, F. (2008). Stochastic flocculation of cohesive sediment: Analysis of floc mobility within the floc size spectrum. *Water Resources Research*, *44*(1). https://doi.org/10.1029/2007WR006109

Maggi, F. (2009). Biological flocculation of suspended particles in nutrient-rich aqueous ecosystems. *Journal of Hydrology*, *376*(1–2), 116–125. https://doi.org/10.1016/j.jhydrol.2009.07.040

Maggi, F., Mietta, F., & Winterwerp, J. C. (2007). Effect of variable fractal dimension on the floc size distribution of suspended cohesive sediment. *Journal of Hydrology*, *343*(1–2), 43–55. https://doi.org/10.1016/j.jhydrol.2007.05.035

Malcolm, R. L., & Durum, W. H. (1976). *Organic carbon and nitrogen concentrations and annual organic carbon load of six selected rivers of the United States* (Report No. 1817F; Water Supply Paper). USGS Publications Warehouse. https://doi.org/10.3133/wsp1817F

Manaka, T., Otani, S., Inamura, A., Suzuki, A., Aung, T., Roachanakanan, R., Ishiwa, T., & Kawahata, H. (2015). Chemical weathering and long-term CO2 consumption in the Ayeyarwady and Mekong river basins in the Himalayas. *Journal of Geophysical Research: Biogeosciences*, *120*(6), 1165–1175. https://doi.org/10.1002/2015JG002932

Matsuo, T., & Unno, H. (1981). Forces acting on floc and strength of floc. *Journal of the Environmental Engineering Division*, *107*(3), 527–545. https://doi.org/10.1061/JEEGAV.0001174

Mayer, L. M. (1999). Extent of coverage of mineral surfaces by organic matter in marine sediments. *Geochimica et Cosmochimica Acta*, *63*(2), 207–215. https://doi.org/10.1016/S0016-7037(99)00028-9

McMahon, W. J., & Davies, N. S. (2018). Evolution of alluvial mudrock forced by early land plants. *Science*, *359*(6379), 1022–1024. https://doi.org/10.1126/science.aan4660

Meade, R. H. (1972). Transport and deposition of sediments in estuaries. *Geological Society of America*, *133*(1), 91–120.

Mehta, A. J., & McAnally, W. H. (2008). Fine grained sediment transport. *Sedimentation Engineering: Processes, Measurements, Modeling, and Practice*, 253–306. https://doi.org/10.1061/9780784408148

Mehta, A. J., & Partheniades, E. (1975). An investigation of the depositional properties of flocculated fine sediments. *Journal of Hydraulic Research*, *13*(4), 361–381. https://doi.org/10.1080/00221687509499694

Millar, R. G., & Quick, M. C. (1998). Stable width and depth of gravel-bed rivers with cohesive banks. *Journal of Hydraulic Engineering*, *124*(10), 1005–1013. https://doi.org/10.1061/(ASCE)0733-9429(1998)124:10(1005)

Molski, A. (1989). On the collision efficiency approach to flocculation. *Colloid and Polymer Science*, *267*(4), 371–375. https://doi.org/10.1007/BF01413632

Moodie, A. J., Nittrouer, J. A., Ma, H., Carlson, B. N., Wang, Y., Lamb, M. P., & Parker, G. (2020). Suspended-sediment induced stratification inferred from concentration and velocity profile measurements in the lower Yellow River, China. *Water Resources Research*, e2020WR027192. https://doi.org/10.1029/2020WR027192

Nezu, I., & Nakagawa, H. (1993). Turbulence in open-channel flows. *AA Balkema, Rotterdam*, 1–281.

Nicholas, A. P., & Walling, D. E. (1996). The significance of particle aggregation in the overbank deposition of suspended sediment on river floodplains. *Journal of Hydrology*, *186*(1–4), 275–293. https://doi.org/10.1016/S0022-1694(96)03023-5

Osborn, R., Dillon, B., Tran, D., Abolfazli, E., Dunne, K. B., Nittrouer, J. A., & Strom, K. (2021). FlocARAZI: an in-situ, image-based profiling instrument for sizing solid and flocculated suspended sediment. *Journal of Geophysical Research: Earth Surface*, e2021JF006210. https://doi.org/10.1029/2021JF006210

Osborn, R., Dunne, K. B. J., Abolfazli, E., Strom, K., & Nittrouer, J. A. (2020). Characterization of In-Situ Floc Sizes Over the Vertical Within the Mississippi River and its Distributaries. *AGU Fall Meeting Abstracts*, *2020*, EP001-0005.

Owen, B. B., Miller, R. C., Milner, C. E., & Cogan, H. L. (1961). The dielectric constant of water as a function of temperature and pressure. *The Journal of Physical Chemistry*, *65*(11), 2065–2070. https://doi.org/10.1021/j100828a035

Paola, C., Parker, G., Seal, R., Sinha, S. K., Southard, J. B., & Wilcock, P. R. (1992). Downstream fining by selective deposition in a laboratory flume. *Science*, *258*(5089), 1757–1760. https://doi.org/10.1126/science.258.5089.1757

Peakall, J., Ashworth, P. J., & Best, J. L. (2007). Meander-Bend Evolution, Alluvial Architecture, and the Role of Cohesion in Sinuous River Channels: A Flume Study. *Journal of Sedimentary Research*, *77*(3), 197–212. https://doi.org/10.2110/jsr.2007.017

Perron, J. T. (2017). Climate and the pace of erosional landscape evolution. *Annual Review of Earth and Planetary Sciences*, *45*, 561–591. https://doi.org/10.1146/annurev-earth-060614-105405

Piper, D. Z., Ludington, S., Duval, J. S., & Taylor, H. E. (2006). Geochemistry of bed and suspended sediment in the Mississippi river system: Provenance versus weathering and winnowing. *Science of the Total Environment*, *362*(1–3), 179–204. https://doi.org/10.1016/j.scitotenv.2005.05.041

Pizzuto, J., Schenk, E. R., Hupp, C. R., Gellis, A., Noe, G., Williamson, E., Karwan, D. L., O'Neal, M., Marquard, J., & Aalto, R. (2014). Characteristic length scales and time-averaged transport velocities of suspended sediment in the mid-Atlantic Region, USA. *Water Resources Research*, *50*(2), 790–805. https://doi.org/10.1002/2013WR014485

Puls, W., & Kühl, H. (1986). Field measurements of the settling velocities of estuarine flocs. *In: Proceedings of the 3rd International Symposium on River Sedimentation, The University of Mississippi*, 525–536.

Qu, Y., Jin, Z., Wang, J., Wang, Y., Xiao, J., Gou, L.-F., Zhang, F., Liu, C.-Y., Gao, Y., & Suarez, M. B. (2020). The sources and seasonal fluxes of particulate organic carbon in the Yellow River. *Earth Surface Processes and Landforms*. https://doi.org/10.1002/esp.4861

Ran, L., Lu, X. X., Sun, H., Han, J., Li, R., & Zhang, J. (2013). Spatial and seasonal variability of organic carbon transport in the Yellow River, China. *Journal of Hydrology*, *498*, 76–88. https://doi.org/10.1016/j.jhydrol.2013.06.018

Ransom, B., Bennett, R. H., Baerwald, R., & Shea, K. (1997). TEM study of in situ organic matter on continental margins: Occurrence and the "monolayer" hypothesis. *Marine Geology*, *138*(1–2), 1–9. https://doi.org/10.1016/S0025-3227(97)00012-1

Raymo, M. E., & Ruddiman, W. F. (1992). Tectonic forcing of late Cenozoic climate. *Nature*, *359*(6391), 117–122. https://doi.org/10.1038/359117a0

Richey, J. E., Victoria, R. L., Hedges, J. I., Dunne, T., Martinelli, L. A., Mertes, L., & Adams, J. (2008). Pre-LBA Carbon in the Amazon River Experiment (CAMREX) Data. *ORNL DAAC*. https://doi.org/10.3334/ORNLDAAC/904

Rommelfanger, N., Vowinckel, B., Wang, Z., Meiburg, E., & Luzzatto-Fegiz, P. (2020). A simple theory and experiments for onset of flocculation in kaolin clay suspensions. In *River Flow 2020* (pp. 820–822). CRC Press.

Rouse, H. (1937). Modern conceptions of the mechanics of fluid turbulence. *Transactions of the American Society of Civil Engineers*, *102*(1), 463–505. https://doi.org/10.1061/TACEAT.0004872

Ruehrwein, R. A., & Ward, D. W. (1952). Mechanism of clay aggregation by polyelectrolytes. *Soil Science*, *73*(6), 485–492.

Santini, W., Camenen, B., Coz, J. L., Vauchel, P., Guyot, J.-L., Lavado, W., Carranza, J., Paredes, M. A., Pérez Arévalo, J. J., Arévalo, N., Espinoza Villar, R., Julien, F., & Martinez, J.-M. (2019). An index concentration method for suspended load monitoring in large rivers of the Amazonian foreland. *Earth Surface Dynamics*, *7*(2), 515–536. https://doi.org/10.5194/esurf-7-515-2019

Sarin, M. M., Krishnaswami, S., Dilli, K., Somayajulu, B. L. K., & Moore, W. S. (1989). Major ion chemistry of the Ganga-Brahmaputra river system: Weathering processes and fluxes to the Bay of Bengal. *Geochimica et Cosmochimica Acta*, *53*(5), 997–1009. https://doi.org/10.1016/0016-7037(89)90205-6

Schlünz, B., & Schneider, R. R. (2000). Transport of terrestrial organic carbon to the oceans by rivers: Re-estimating flux- and burial rates. *International Journal of Earth Sciences*, *88*(4), 599–606. https://doi.org/10.1007/s005310050290

Seiphoori, A., Gunn, A., Kosgodagan Acharige, S., Arratia, P. E., & Jerolmack, D. J. (2021). Tuning sedimentation through surface charge and particle shape. *Geophysical Research Letters*, *48*(7), e2020GL091251. https://doi.org/10.1029/2020GL091251

Seyler, P. T., & Boaventura, G. R. (2003). Distribution and partition of trace metals in the Amazon basin. *Hydrological Processes*, *17*(7), 1345–1361. https://doi.org/10.1002/hyp.1288

Smellie, R. H., & La Mer, V. K. (1958). Flocculation, subsidence and filtration of phosphate slimes: VI. A quantitative theory of filtration of flocculated suspensions. *Journal of Colloid Science*, *13*(6), 589–599. https://doi.org/10.1016/0095-8522(58)90071-0

Smith, J. D., & McLean, S. R. (1977). Spatially averaged flow over a wavy surface. *Journal of Geophysical Research*, *82*(12), 1735–1746. https://doi.org/10.1029/JC082i012p01735

SO-HYBAM. (n.d.). *SO-HYBAM: Amazon basin water resources observation service*. https://hybam.obs-mip.fr/

Son, M., & Hsu, T.-J. (2008). Flocculation model of cohesive sediment using variable fractal dimension. *Environmental Fluid Mechanics*, *8*(1), 55–71. https://doi.org/10.1007/s10652-007-9050-7

Son, M., & Hsu, T.-J. (2011). The effects of flocculation and bed erodibility on modeling cohesive sediment resuspension. *Journal of Geophysical Research: Oceans*, *116*(C3). https://doi.org/10.1029/2010JC006352

Spence, J., & Telmer, K. (2005). The role of sulfur in chemical weathering and atmospheric CO_2 fluxes: Evidence from major ions, δ13CDIC, and δ34SSO4 in rivers of the Canadian Cordillera. *Geochimica et Cosmochimica Acta*, *69*(23), 5441–5458. https://doi.org/10.1016/j.gca.2005.07.011

Spicer, P. T., & Pratsinis, S. E. (1996). Coagulation and fragmentation: Universal steady-state particle-size distribution. *AIChE Journal*, *42*(6), 1612–1620. https://doi.org/10.1002/aic.690420612

Stallard, R. F. (1980). *Major element geochemistry of the Amazon River system [Doctoral thesis, Massachusetts Institute of Technology]*. http://hdl.handle.net/1721.1/58120

Strom, K., & Keyvani, A. (2011). An explicit full-range settling velocity equation for mud flocs. *Journal of Sedimentary Research*, *81*(12), 921–934. https://doi.org/10.2110/jsr.2011.62

Su, X., Wu, X., Lin, X., Liao, Z., & Wang, J. (2006). Main chemical components of the Yellow River water and downstream variations of δ13C. *Yellow River Water Resources*, 29–31.

Tambo, N., & Hozumi, H. (1979). Physical characteristics of flocs—II. Strength of floc. *Water Research*, *13*(5), 421–427. https://doi.org/10.1016/0043-1354(79)90034-4

Tambo, N., & Watanabe, Y. (1979). Physical aspect of flocculation process—I: Fundamental treatise. *Water Research*, *13*(5), 429–439. https://doi.org/10.1016/0043-1354(79)90035-6

Tang, F. H., & Maggi, F. (2016). A mesocosm experiment of suspended particulate matter dynamics in nutrient-and biomass-affected waters. *Water Research*, *89*, 76–86. https://doi.org/10.1016/j.watres.2015.11.033

Tennekes, H., & Lumley, J. L. (1972). *A first course in turbulence*. MIT Press.

Tipper, E. T., Stevenson, E. I., Alcock, V., Knight, A. C., Baronas, J. J., Hilton, R. G., Bickle, M. J., Larkin, C. S., Feng, L., & Relph, K. E. (2021). Global silicate weathering flux overestimated because of sediment–water cation exchange. *Proceedings of the National Academy of Sciences*, *118*(1). https://doi.org/10.1073/pnas.2016430118

Torres, M. A., Kemeny, P. C., Lamb, M. P., Cole, T. L., & Fischer, W. W. (2020). Long-Term Storage and Age-Biased Export of Fluvial Organic Carbon: Field Evidence From West

Iceland. *Geochemistry, Geophysics, Geosystems*, *21*(4), e2019GC008632. https://doi.org/10.1029/2019GC008632

Torres, M. A., West, A. J., & Clark, K. E. (2015). Geomorphic regime modulates hydrologic control of chemical weathering in the Andes–Amazon. *Geochimica et Cosmochimica Acta*, *166*, 105–128. https://doi.org/10.1016/j.gca.2015.06.007

Tsai, C.-H., Iacobellis, S., & Lick, W. (1987). Flocculation of fine-grained lake sediments due to a uniform shear stress. *Journal of Great Lakes Research*, *13*(2), 135–146. https://doi.org/10.1016/S0380-1330(87)71637-2

Van Dijk, W. M., Van de Lageweg, W. I., & Kleinhans, M. G. (2013). Formation of a cohesive floodplain in a dynamic experimental meandering river. *Earth Surface Processes and Landforms*, *38*(13), 1550–1565. https://doi.org/10.1002/esp.3400

Van Leussen, W. (1988). Aggregation of particles, settling velocity of mud flocs a review. *Physical Processes in Estuaries*, 347–403. https://doi.org/10.1007/978-3-642-73691-9_19

Van Olphen, H., & Hsu, P. H. (1977). *An Introduction to Clay Colloid Chemistry*. Wiley.

Van Rijn, L. C. (1984). Sediment Transport, Part II: Suspended Load Transport. *Journal of Hydraulic Engineering*, *110*(11), 1613–1641. https://doi.org/10.1061/(ASCE)0733-9429(1984)110:11(1613)

Verney, R., Lafite, R., & Brun-Cottan, J.-C. (2009). Flocculation potential of estuarine particles: The importance of environmental factors and of the spatial and seasonal variability of suspended particulate matter. *Estuaries and Coasts*, *32*(4), 678–693. https://doi.org/10.1007/s12237-009-9160-1

Voss, B. M. (2014). *Spatial and temporal dynamics of biogeochemical processes in the Fraser River, Canada: A coupled organic-inorganic perspective.* http://hdl.handle.net/1721.1/95521

Wang, B., Li, X., Yuan, H., Zhou, H., & Zhao, Y. (2009). Geochemistry of the main ions and Sr isotopic composition in the lower reach of the Yellow River, North China. *Environmental Chemistry*, *28*, 876–882.

Wang, X., Ma, H., Li, R., Song, Z., & Wu, J. (2012). Seasonal fluxes and source variation of organic carbon transported by two major Chinese Rivers: The Yellow River and Changjiang (Yangtze) River. *Global Biogeochemical Cycles*, *26*(2). https://doi.org/10.1029/2011GB004130

West, A. J., Galy, A., & Bickle, M. (2005). Tectonic and climatic controls on silicate weathering. *Earth and Planetary Science Letters*, *235*(1–2), 211–228. https://doi.org/10.1016/j.epsl.2005.03.020

Whitehouse, U. G., Jeffrey, L. M., & Debbrecht, J. D. (2013). Differential settling tendencies of clay minerals in saline waters. *Clays and Clay Minerals*, 1–79. https://doi.org/10.1016/B978-0-08-009235-5.50006-1

Wilcock, P. R. (1996). Estimating local bed shear stress from velocity observations. *Water Resources Research, 32*(11), 3361–3366. https://doi.org/10.1029/96WR02277

Winterwerp, J. C. (1998). A simple model for turbulence induced flocculation of cohesive sediment. *Journal of Hydraulic Research*, *36*(3), 309–326. https://doi.org/10.1080/00221689809498621

Winterwerp, J. C. (2002). On the flocculation and settling velocity of estuarine mud. *Continental Shelf Research*, *22*(9), 1339–1360. https://doi.org/10.1016/S0278-4343(02)00010-9

Wright, S., & Parker, G. (2004). Flow Resistance and Suspended Load in Sand-Bed Rivers: Simplified Stratification Model. *Journal of Hydraulic Engineering*, *130*(8), 796–805. https://doi.org/10.1061/(ASCE)0733-9429(2004)130:8(796)

Xu, F., Wang, D.-P., & Riemer, N. (2008). Modeling flocculation processes of fine-grained particles using a size-resolved method: Comparison with published laboratory experiments. *Continental Shelf Research*, *28*(19), 2668–2677. https://doi.org/10.1016/j.csr.2008.09.001

Yu, M., Eglinton, T. I., Haghipour, N., Montluçon, D. B., Wacker, L., Hou, P., Zhang, H., & Zhao, M. (2019). Impacts of natural and human-induced hydrological variability on particulate organic carbon dynamics in the Yellow River. *Environmental Science & Technology*, *53*(3), 1119–1129. https://doi.org/10.1021/acs.est.8b04705

Zeichner, S. S., Nghiem, J., Lamb, M. P., Takashima, N., De Leeuw, J., Ganti, V., & Fischer, W. W. (2021). Early plant organics increased global terrestrial mud deposition through enhanced flocculation. *Science*, *371*(6528), 526–529. https://doi.org/10.1126/science.abd0379

Zhang, J., Huang, W. W., Letolle, R., & Jusserand, C. (1995). Major element chemistry of the Huanghe (Yellow River), China-weathering processes and chemical fluxes. *Journal of Hydrology*, *168*(1–4), 173–203. https://doi.org/10.1016/0022-1694(94)02635-O

Zhang, L.-J., & Wen, Z.-C. (2009). Discussion on Silicate Weathering in the Huanghe Drainage Basin. *Periodical of Ocean University of China*, *39*(5), 988–994.

Zhang, Q., Jin, Z., Zhang, F., & Xiao, J. (2015). Seasonal variation in river water chemistry of the middle reaches of the Yellow River and its controlling factors. *Journal of Geochemical Exploration*, *156*, 101–113. https://doi.org/10.1016/j.gexplo.2015.05.008

2.10 Supporting Information

2.10.1 Introduction

Text S1 describes the method for partitioning data for each concentration-depth profile in diameter-settling velocity space into flocculated and not flocculated regimes and extracting floc cutoff diameter. Texts S2 and S3 describe the procedure for exploring the sensitivity of the floc model to different diffusivity ratio, β, formulations (Text S2) and floc fractal dimension, n_f (Text S3).

Figures S1 and S2 demonstrate tests of the floc model sensitivity to the diffusivity ratio, β, and fractal dimension, n_f, respectively. Figures S3 and S4 show the relationships between individual predictor variables from the floc model and each of floc cutoff diameter (Fig. S3) and floc diameter (Fig. S4).

The supporting tables describe the data sources for the data compilation used to fit the floc model for freshwater rivers. The data include suspended sediment concentration-depth profiles (Table S1), percent weight organic carbon and Al/Si of river suspended sediment, and major dissolved species in river water (Table S2).

2.10.2 Text S1

We used a sequential repeated fitting approach in D-w_s space to find D_t for each profile (Fig. 3). We first grouped together the four data points with the smallest D. We fitted a horizontal line using ordinary least squares regression to this initial group to model the relatively constant w_s in the flocculated regime, then sequentially added the next data point with immediately larger D to the fitting group and refitted the horizontal line. We determined the best model as the one with the largest R^2 and fitted the remainder of the data with a settling velocity model to describe the settling velocity of unflocculated particles. We fitted the settling velocity model using the reciprocal $1/w_s$ instead of w_s to transform the settling velocity model into an equation that is linear in the fit parameters so that we could use linear regression (Ferguson and Church, 2004). We employed regularized linear regression with constraints on the estimated settling velocity model parameters, following the recommended parameter ranges in Ferguson and Church (2004), to maintain physically meaningful fits (Friedman et al., 2010). We numerically solved for the floc cutoff diameter by requiring continuity between the two parts of the resulting piecewise function. This sequence of fitting starting from small D and successively including data at larger D provided one candidate D_t. The procedure was repeated, but this time fitting the settling velocity model (rather than the horizontal line) starting at the largest D and successively including data at smaller D. We computed the average magnitude of residuals for each of the two candidate piecewise

functions and selected the function (and its corresponding D_t) that had the smaller average residual magnitude.

2.10.3 Text S2

We confirmed the reliability of our w_{si} estimation method against existing β_i closures by comparing our w_{si} estimates and the w_{si} estimates computed using other β_i relations (Fig. S1a-e). We tested five alternative β_i formulations: constant [$\beta = 1$], de Leeuw et al. (2020) [best-fit one-parameter model for Rouse number], Graf and Cellino (2002) [without bedforms], Santini et al. (2019), and van Rijn (1984). Our w_{si} estimates correlate well (Pearson correlation, r = ~0.66-0.70) with those estimated from the other methods. Our result of elevated *in situ* settling velocities compared to Stokes law predictions for clay to silt grain sizes holds for all β_i methods (Fig. S1f). In Fig. S1f, we elected to plot trend lines rather than individual points to summarize the general relationship and avoid overplotting. These tests demonstrate that our analysis of suspended sediment concentration-depth profiles is robust to the choice of β_i closure.

2.10.4 Text S3

We tested the sensitivity of the floc model calibration to floc fractal dimension, n_f, by recalibrating the model for different values of constant n_f and evaluating variation in goodness-of-fit and calibrated model exponents. We imposed an array of different (but constant) n_f from its full physical range of 1 to 3. We recalibrated the full D_t model given n_f:

$$\left(\frac{D_t}{D_p}\right)^{\frac{2}{n_f-1}} = k\frac{\eta}{D_p}(C\theta^2(1-\theta)^2)^q(\mathrm{Al/Si})^r\Phi^s \quad \text{(S1)}$$

The model recalibration results demonstrate that n_f has negligible influence on the model goodness-of-fit and fit exponents for realistic values of n_f for natural flocs (Fig. S2). Considering the entire range of n_f from 1 to 3, the model RMSE does not vary widely—the maximum RMSE is within a factor of 1.4 of the minimum (Fig. S2a). As such, the model is robust to different choices of n_f in terms of goodness-of-fit. The model achieves a minimum RMSE at $n_f \cong 1.1$. This n_f corresponds to a possible change in sign for the exponent of $C_m\theta^2(1-\theta)^2$, and this would alter our subsequent interpretation and conclusions (Fig. S2b). However, $n_f \cong 1.1$ is unrealistic because n_f tends to be between 1.4 and 2.2 for natural flocs (Winterwerp, 1998). In addition, n_f close to 1 indicates a linear, chain-like floc shape which do not appear abundant in rivers (Osborn et al., 2020; Osborn et al., 2021). Considering only realistic values ($1.4 < n_f < 2.2$), then the calibrated exponents do not change sign and only vary within a factor of about 2 (Fig. S2b-d). These variations in calibrated exponents do not alter our subsequent interpretation and conclusions.

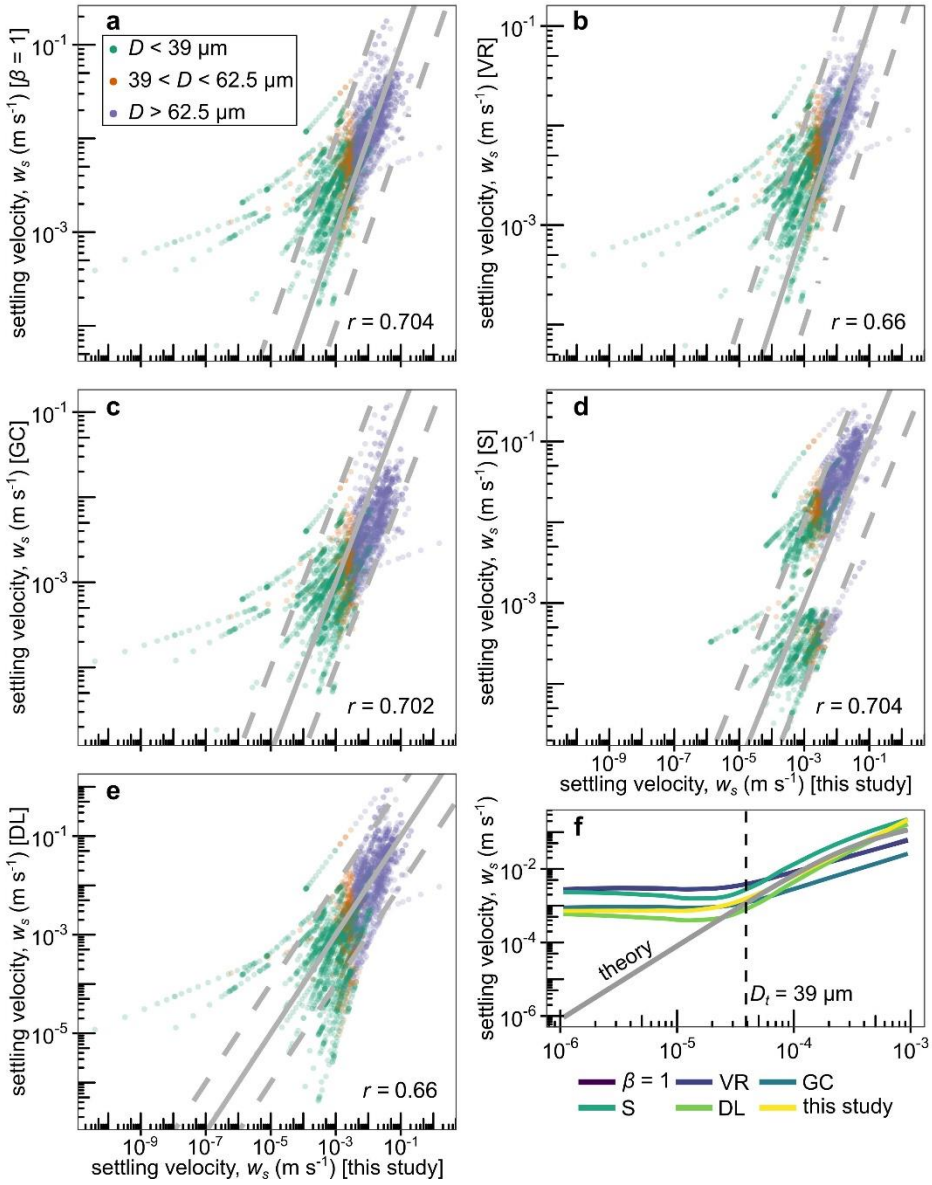

Figure S1. (a-e) Comparison of in situ settling velocity estimates, w_s, obtained with different formulations for diffusivity ratio, β, and fitting the Rouse-Vanoni equation to the river suspended sediment concentration profile data compilation. r denotes the Pearson correlation coefficient computed in log-log space. The solid line indicates the 1:1 line and the dashed lines indicate a factor of 10 above and below the 1:1 line. Legend in panel a applies to panels a-e. (f) Settling velocity as a function of particle diameter using the Rouse-Vanoni equation method for all concentration-depth profiles in the data compilation and different β relations. Data points have been summarized into trend lines using local polynomial regression fitting. Theoretical settling velocity curve (labeled "theory") is due to Ferguson and Church (2004). Vertical dashed line denotes our median estimated floc cutoff diameter, D_t = 39 μm. Abbreviations for β relations are as follows. VR: van Rijn

(1984). GC: Graf and Cellino (2002) without bedforms. S: Santini et al. (2019). DL: de Leeuw et al. (2020) best-fit one-parameter model for Rouse number.

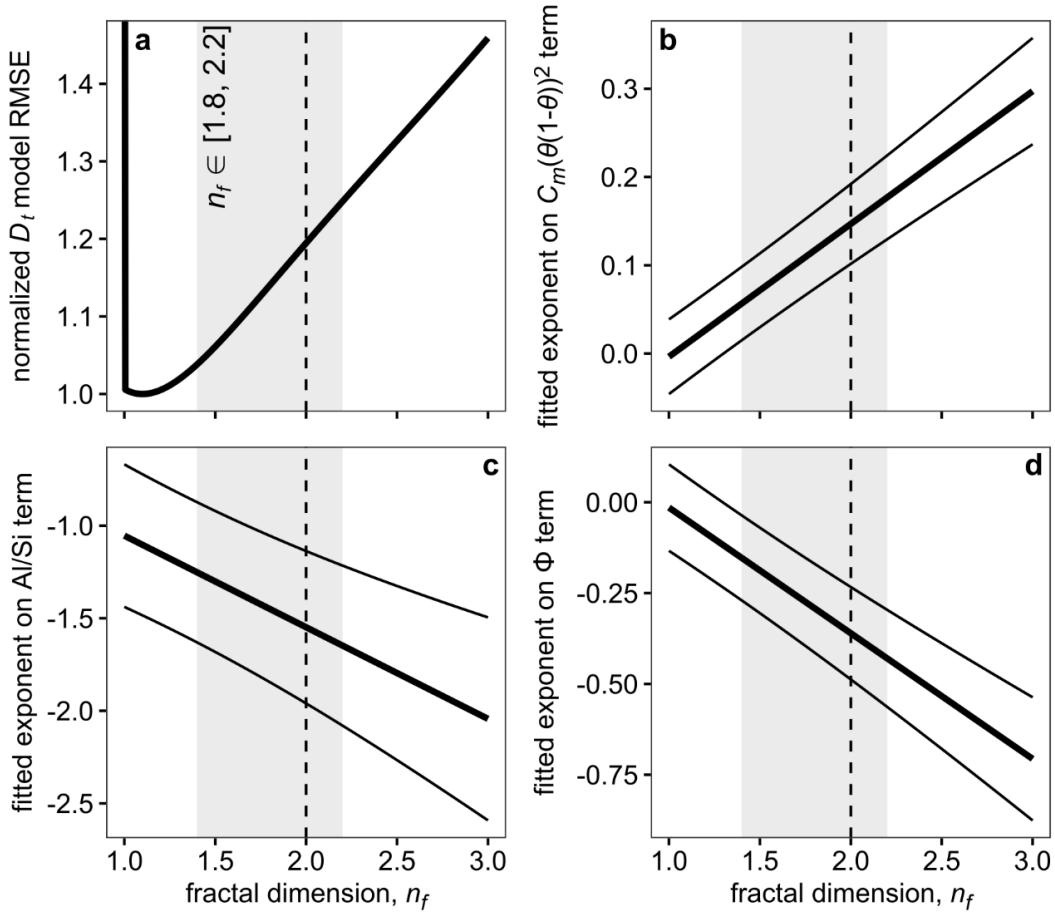

Figure S2. Sensitivity tests of the calibrated floc cutoff diameter, D_t, model (a) RMSE (normalized by minimum RMSE) and fitted exponents on the (b) $C_m\theta^2(1-\theta)^2$, (c) Al/Si, and (d) Φ terms as functions of fractal dimension, n_f. Vertical dashed line indicates the model assumption of $n_f = 2$. Shaded region indicates the range $1.4 < n_f < 2.2$, which is representative for natural flocs (Winterwerp, 1998). Thin lines about the thick line in panels b-d indicate the 68% confidence interval bound on the parameter estimates.

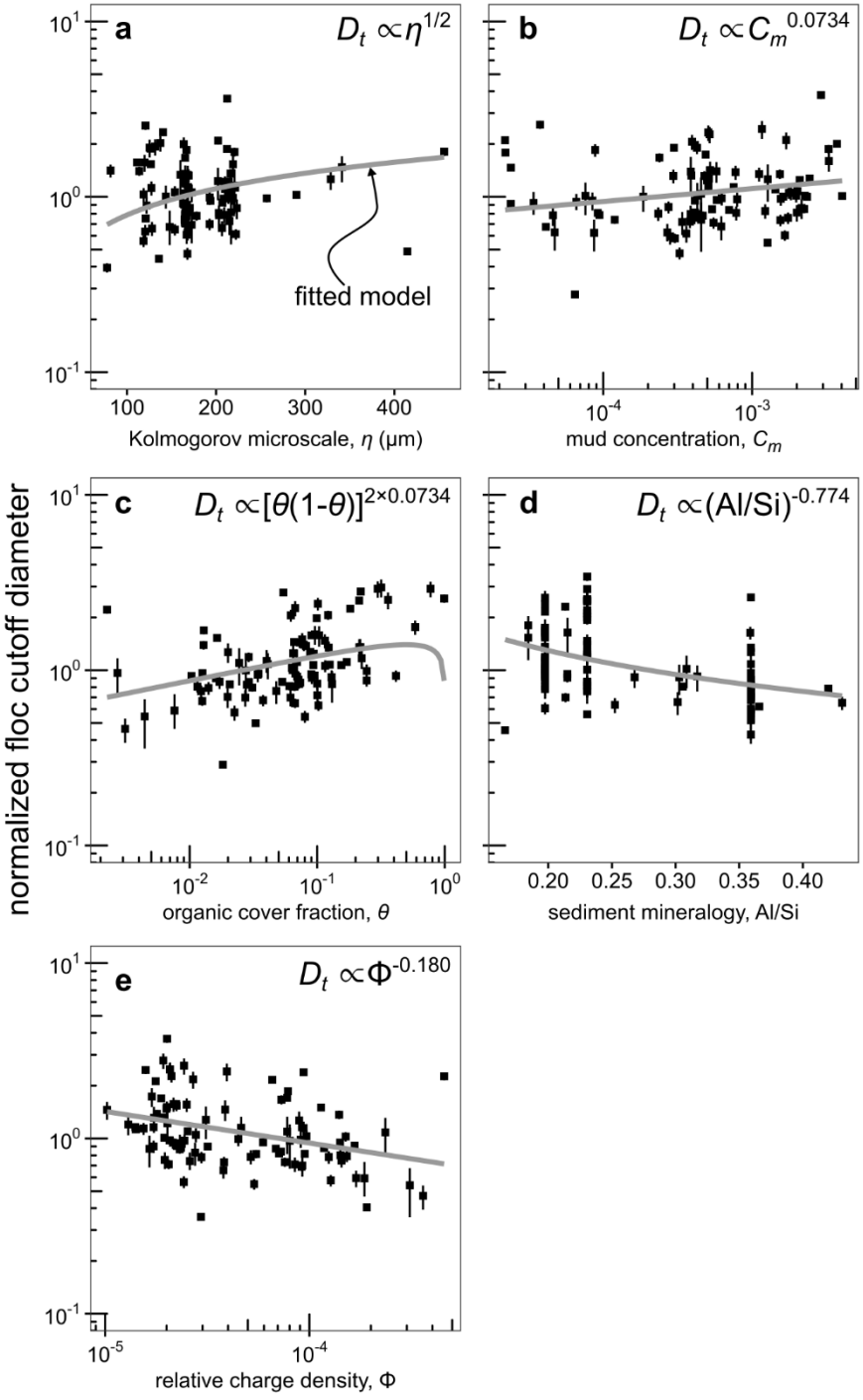

Figure S3. Individual parameters plotted against floc cutoff diameter, D_t, data normalized by the effects of all other predictors in the fitted D_t model (Equation 22). The normalized values were further scaled by dividing the median to better compare each variable. In all

panels, the solid line, labeled in panel a, indicates the fitted relationship (Table 2). Error bars represent the propagated 68% confidence interval.

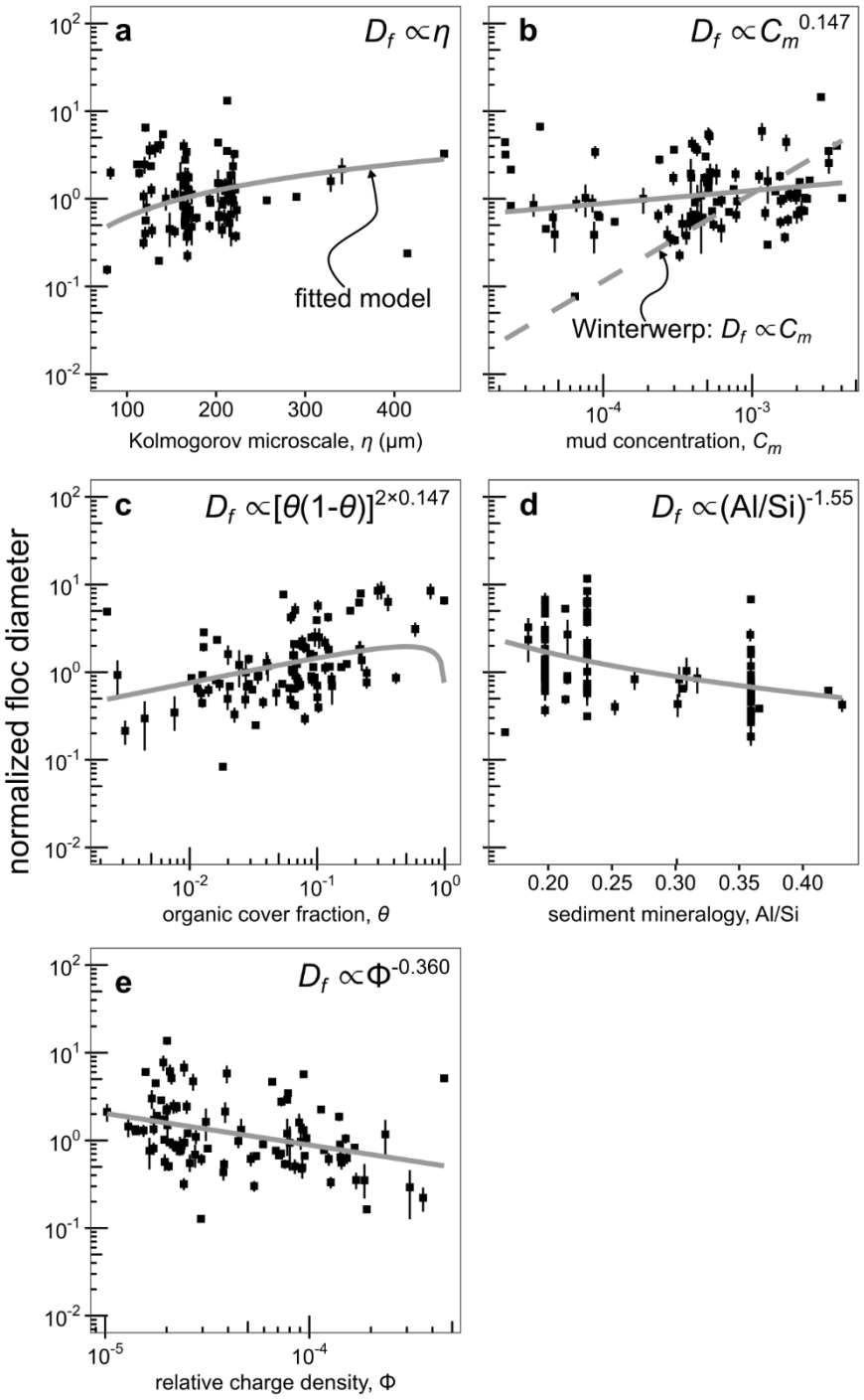

Figure S4. Individual parameters plotted against floc diameter, D_f, data normalized by the effects of all other predictors in the fitted D_f model (Equation 24). The normalized values were further scaled by dividing the median to better compare each variable. In all panels, the solid line, labeled in panel a, indicates the fitted relationship (Table 2). In panel b, the dashed line is the prediction from the equilibrium Winterwerp model. Error bars represent the propagated 68% confidence interval.

Table S1. Data sources for grain size-specific suspended sediment concentration profiles. The total number of profiles is 122.

River	Number of profiles	Reference
Amazon	5	Bouchez et al., 2011a; Bouchez, 2022
Beni	1	Bouchez et al., 2012; Bouchez, 2022
Fraser	40	Haught et al., 2017
Ganges	3	Lupker et al., 2011
Irrawaddy	1	Baronas et al., 2020
Karnali	3	Dingle, 2021; Dingle et al., 2020
Madeira	3	Bouchez et al., 2011a; Bouchez, 2022
Mamoré	1	Bouchez et al., 2012; Bouchez, 2022
Missouri	39	Abraham et al., 2017
Salween	1	Baronas et al., 2020
Solimões	3	Bouchez et al., 2011a; Bouchez, 2022
Yellow	23	Moodie et al., 2020

Table S2. River geochemistry data sources for suspended sediment Al/Si, percent weight organic carbon, and major dissolved species concentration.

River	Reference
Amazon	Bouchez et al., 2014; Dosseto et al., 2006a; Hedges et al., 2000; Richey et al., 2008; Seyler and Boaventura, 2003; SO-HYBAM; Stallard, 1980
Beni	Dosseto et al., 2006b; Elbaz-Poulichet et al., 1999; Guyot et al., 1993; Hedges et al., 2000; SO-HYBAM; Stallard, 1980
Fraser	Cameron et al., 1995; Spence and Telmer, 2005; Voss, 2014
Ganges	Galy and France-Lanord, 1999; Galy et al., 2008; Lupker et al., 2011; Sarin et al., 1989
Irrawaddy	Baronas et al., 2020; Bird et al., 2008; Chapman et al., 2015; Garzanti et al., 2016; Hossain et al., 2017; Manaka et al., 2015
Karnali	Azam et al., 2018; English et al., 2000; Galy and France-Lanord, 1999; Galy et al., 2008; Lupker et al., 2011; Sarin et al., 1989
Madeira	Bonotto and da Silveira, 2003; Bouchez et al., 2014; Dosseto et al., 2006a; Dosseto et al., 2006b; Hedges et al., 2000; Richey et al., 2008; Seyler and Boaventura, 2003; SO-HYBAM; Stallard, 1980

Mamoré	Dosseto et al., 2006b; Elbaz-Poulichet et al., 1999; Hedges et al., 2000; Stallard, 1980
Missouri	Alexander et al., 1997; Canfield, 1997; Christiansen, 2004; Kelly et al., 2001; Kleeschulte, 1993; Lee, 2020; Leenheer et al., 1995; Malcolm and Durum, 1976; Piper et al., 2006
Salween	Baronas et al., 2020; Bird et al., 2008; Chapman et al., 2015; Huang et al., 2009; Tipper et al., 2021
Solimões	Bouchez et al., 2014; Dosseto et al., 2006a; Richey et al., 2008; Seyler and Boaventura, 2003; SO-HYBAM; Stallard, 1980
Yellow	Ding et al., 2016; Hu et al., 2015; Huang et al., 1992; Li and Zhang, 2003; Qu et al., 2020; Ran et al., 2013; Su et al., 2006; Wang et al., 2009; Wang et al., 2012; Yu et al., 2019; Zhang and Wen, 2009; Zhang et al., 1995; Zhang et al., 2015

Chapter 3

TESTING FLOC SETTLING VELOCITY MODELS IN RIVERS AND FRESHWATER WETLANDS

Justin A. Nghiem, Gen K. Li, Joshua P. Harringmeyer, Gerard Salter, Cédric G. Fichot, Luca Cortese, and Michael P. Lamb

Chapter 3 is modified from a previously published manuscript: Nghiem, J. A., Li, G. K., Harringmeyer, J. P., Salter, G., Fichot, C. G., Cortese, L., & Lamb, M. P. (2024). Testing floc settling velocity models in rivers and freshwater wetlands. *Earth Surface Dynamics, 12*(6), 1267–1294. https://doi.org/10.5194/esurf-12-1267-2024

Abstract

Flocculation controls mud sedimentation and organic carbon burial rates by increasing mud settling velocity. However, calibration and validation of floc settling velocity models in freshwater are lacking. We used a camera, in situ laser diffraction particle sizing, and suspended sediment concentration-depth profiles to measure flocs in Wax Lake Delta, Louisiana. We developed a new workflow that combines our multiple floc data sources to distinguish between flocs and unflocculated sediment and measure floc attributes that were previously difficult to constrain. Sediment finer than ~10 to 55 μm was flocculated with median floc diameter of 30 to 90 μm, bulk solid fraction of 0.05 to 0.3, fractal dimension of ~2.1, and floc settling velocity of ~0.1 to 1 mm s^{-1}, with little variation along water depth. Results are consistent with a semi-empirical model indicating that sediment concentration and mineralogy, organics, water chemistry, and, above all, turbulence control floc settling velocity. Effective primary particle diameter is ~2 μm, about 2 to 6 times smaller than the median primary particle diameter, and is better described using a fractal theory. Flow through the floc increases settling velocity by an average factor of 2 and up to a factor of 7, and can be described by a modified permeability model that accounts for the effect of many primary particle sizes on flow paths. These findings help explain discrepancies between observations and an explicit Stokes law-type settling model that depends on floc diameter, permeability, and fractal properties.

3.1 Introduction

Mud, defined as grains with diameters finer than 62.5 μm, constitutes the bulk of sediment load in large alluvial rivers and deltas (Walling and Fang, 2003; Cohen et al., 2022). Mud deposition can counteract land loss in coastal areas experiencing sea level rise, subsidence, and reduced sediment supply (Blum and Roberts, 2009; Syvitski et al., 2009). Fluvial mud also hosts abundant mineral-bound organic carbon and pollutants and is thus important to

the global carbon cycle (Mayer, 1994; Galy et al., 2008; Blair and Aller, 2012) and water quality (Nelson and Lamothe, 1993; Pizzuto, 2014). Flocculation is key for understanding mud sedimentation because flocculation can drastically increase the in situ mud settling velocity (Lamb et al., 2020). Enhanced settling velocity affects mud exchange with the bed and bedform geometry (Partheniades, 1965; Schindler et al., 2015; Tran and Strom, 2019) and can ultimately alter landscape-scale mud transport (Nicholas and Walling, 1996; Craig et al., 2020, Zeichner et al., 2021).

Flocculation is the reversible process in which suspended sediment grains (i.e., primary particles) aggregate into larger and less dense particles called flocs, which can settle orders-of-magnitude faster than their primary particles (Chase, 1979; Winterwerp, 1998). Many physical, chemical, and biological factors affect flocculation like turbulence, sediment concentration and mineralogy, organics, and water chemistry (Kranck, 1984; Mietta et al., 2009; Nghiem et al., 2022). Researchers have long studied flocculation in estuaries and the ocean where salinity mainly affects flocculation (Kranck and Milligan, 1980; McCave, 1984; Hill et al., 2001). High salinity promotes flocculation because cations compress the electric double layer surrounding grains to the point that van der Waals attraction causes grains to aggregate (i.e., DLVO theory; Derjaguin and Landau, 1941; Verwey, 1947). However, recent studies found widespread flocculation in rivers (Lamb et al., 2020; Nghiem et al., 2022). Much less is known about flocculation in freshwater where organic matter might instead be the main flocculating agent (Eisma et al., 1982; Lee et al., 2019; Zeichner et al., 2021). Organic matter biopolymers can bind sediment depending on charge interactions and adsorption kinetics (Yu and Somasundaran, 1996; Gregory and Barany, 2011), which classic DLVO theory cannot describe (Deng et al., 2023). Limited direct observations have shown that freshwater flocs are ~10 to 100 μm in diameter and settle at ~0.1 to 1 mm s^{-1} (Droppo and Ongley, 1994; Krishnappan, 2000; Guo and He, 2011; Larsen et al., 2009; Osborn et al., 2021).

Although floc settling velocity is vital for understanding mud transport in rivers and freshwater wetlands, settling velocity models for freshwater flocs are still in their infancy. Many empirical models for estuarine flocs have been proposed (e.g., Gibbs, 1985; Manning and Dyer, 2007; Soulsby et al., 2013), but are not applicable to freshwater flocs because their parameters implicitly depend on sediment and water properties (e.g., Eisma, 1986). Strom and Keyvani (2011) derived a general floc settling velocity model by assuming that flocs are fractal aggregates and modifying Stokes settling velocity theory to include floc density and permeability. We refer to this model as the "explicit model" because it predicts floc settling velocity from physical principles. The explicit model was validated against a data compilation of floc diameter and settling velocity measurements (Strom and Keyvani, 2011), but is difficult to apply because it relies on floc permeability and primary particle diameter, which are poorly constrained.

Alternatively, floc diameter and settling velocity can be predicted using a flocculation model. In a seminal study, Winterwerp (1998) developed a turbulence-driven flocculation model in which the relative rates of floc aggregation (due to particle collisions) and

breakage (due to shear stress) set floc diameter and settling velocity. The Winterwerp model is a function of shear rate and sediment concentration, but the effects of other factors are not explicit. Nghiem et al. (2022) modified the Winterwerp model to include additional factors known to affect flocculation: organic matter, sediment mineralogy, and water chemistry. They fitted the model to a global river compilation. We refer to the Nghiem et al. (2022) model as the "semi-empirical model" because the fitted parameters empirically account for the effects of floc structure, density, and permeability on floc settling velocity. The semi-empirical model was calibrated on floc settling velocity inferred from sediment concentration-depth profiles using Rouse-Vanoni theory (Nghiem et al., 2022), but has yet to be verified against direct measurements.

Here we combined geochemical sampling, camera observations, in situ laser diffraction particle sizing, and Rouse-Vanoni analysis of sediment concentration-depth profiles in the freshwater Wax Lake Delta (WLD), Louisiana, USA to examine these knowledge gaps: floc permeability and primary particle diameter in the explicit model and validation of the semi-empirical model. First, we review the floc theories (Sect. 2). We introduce the study area in Sect. 3. Next, we describe the field methods and data analysis to calculate floc properties (Sect. 4). Importantly, our complementary data sources provide new constraints on floc properties, allowing us to isolate floc concentration and size distribution and estimate floc permeability and primary particle diameter for the explicit model. These properties, along with floc solid fraction, fractal dimension, and settling velocity distribution, are reported in Sect. 5. In Sect. 6, we discuss the advantages of our data combination, practical considerations for predicting freshwater floc settling velocity, the physical interpretation of primary particle and permeability effects on floc settling velocity, and the leading role of turbulence in setting floc settling velocity.

3.2 Floc Theory

3.2.1 Explicit Model

The explicit model for floc settling velocity, w_s (m s^{-1}), is Stokes law modified for flocs (Strom and Keyvani, 2011) and hence predicts w_s at the scale of the individual floc:

$$w_s = \frac{R_s g D_p^2}{b_1 \Omega \nu} \left(\frac{D_f}{D_p} \right)^{n_f - 1} \quad (1)$$

where R_s is the submerged specific gravity of sediment (1.65), g is gravitational acceleration (9.81 m s^{-2}), D_f (m) is floc diameter, and b_1 (dimensionless) is a shape factor assumed to be 20 (Ferguson and Church, 2004; see Sect. 6.3 for discussion). Equation (1) assumes that flocs are fractal aggregates (Kranenburg, 1994), for which a fractal solid fraction model applies:

$$\varphi = \left(\frac{D_f}{D_p} \right)^{n_f - 3} \quad (2)$$

where φ (dimensionless) is the solid fraction, the volume fraction of the floc composed of mineral sediment. Although fractal theory is an approximation because floc structure is heterogeneous (e.g., Spencer et al., 2021), it has been well-tested for natural flocs (Kranenburg, 1994; Winterwerp, 1998; Dyer and Manning, 1999). Natural flocs contain many primary particle sizes, so D_p (m) is an effective primary particle diameter that is representative of the primary particle size distribution. Given D_f and D_p, fractal dimension, $n_f \in [1, 3]$ (dimensionless), quantifies the packing efficiency of primary particles. A compact solid grain has $n_f = 3$, while a linear chain of primary particles has $n_f = 1$. A typical fractal dimension for natural flocs is ~2 (Kranenburg, 1994; Winterwerp, 1998). All else equal, Eq. (2) indicates that smaller flocs are denser than larger flocs and, in turn, the center of a given floc is denser than the edges.

Drag ratio, $\Omega \in (0, 1]$ (dimensionless), quantifies floc drag force reduction caused by flow passing through a permeable floc (Neale et al., 1973). Specifically, Ω is the ratio of the drag force of the floc and that of an impermeable particle with the same density and diameter at the same flow velocity (Neale et al., 1973). Equivalently, Ω is the ratio of the settling velocity of the impermeable particle and that of the floc. If $\Omega = 1$, then the floc is impermeable. $\Omega < 1$ indicates a permeability-induced drag force reduction and settling velocity enhancement. Based on creeping flow theory, Ω decreases with permeability according to

$$\Omega = \frac{2\xi^2 \left(1 - \frac{\tanh \xi}{\xi}\right)}{2\xi^2 + 3\left(1 - \frac{\tanh \xi}{\xi}\right)} \quad (3)$$

where the dimensionless permeability, $\xi^{-2} = 4kD_f^{-2}$, and k (m^2) is the floc permeability (Neale et al., 1973). Equation (3) shows that predicting Ω is tantamount to predicting ξ^{-2}.

The key inputs in the explicit model (Eq. 1) are floc diameter, D_f, fractal dimension, n_f, effective primary particle diameter, D_p, and drag ratio, Ω. Of these, D_p and Ω are the outstanding unknowns because prior studies have well constrained floc diameter and fractal dimension (e.g., Jarvis et al., 2005; Strom and Keyvani, 2011). Cameras are commonly used to measure floc diameter and settling velocity, but this data alone cannot separate the effects of D_p and Ω (Dyer and Manning, 1999; Strom and Keyvani, 2011). As such, D_p and Ω must be estimated from additional relations as follows, but these relations have yet to be tested against observations of natural flocs in freshwater rivers and deltas.

Determining an effective primary particle diameter, D_p, as required for the explicit model (Eq. 1), is uncertain because each floc carries many primary particle sizes. D_p is typically assumed to be the mean or median of the primary particle size distribution (e.g., Syvitski et al., 1995; Strom and Keyvani, 2011). Alternatively, Bushell and Amal (1998) proposed a fractal D_p model:

$$ND_p^{n_w} = \sum_{i=1}^{N} D_{pi}^{n_w} \quad (4a)$$

$$ND_p^{n_f} = \sum_{i=1}^{N} D_{pi}^{n_f} \quad (4b)$$

$$D_p = \left(\frac{\sum D_{pi}^{n_w}}{\sum D_{pi}^{n_f}} \right)^{\frac{1}{n_w - n_f}} \quad (4c)$$

where D_{pi} is the diameter of the *i*th primary particle in the floc and N is the number of primary particles in the floc. Equation (4a) shows that the effective primary particles of diameter D_p must have the same physical dimension, set by the weighting dimension, n_w (dimensionless), as the original primary particles. For example, $n_w = 3$ means that total primary particle volume is preserved. $n_w = 0$ means that the number of primary particles is preserved. By analogy, Eq. (4b) shows that the effective primary particles must also fill the same n_f-dimensional space as the original primary particles. Bushell and Amal (1998) combined Eq. (4a) and (4b) to obtain a fractal D_p model (Eq. 4c). The mean or median of the primary particle size distribution does not satisfy such conditions and thus might be very different from the fractal D_p. Equation (4c) has been validated using light scattering experiments on synthetic grains (Bushell and Amal, 2000). Since we could only resolve D_p over floc populations and not at the level of single flocs (Sect. 4.6.2), we followed Gmachowski (2003) and extended Eq. (4c) to average over the primary particle size distribution:

$$D_p = \left(\overline{D_p^{n_w}} / \overline{D_p^{n_f}} \right)^{1/(n_w - n_f)} \quad (5)$$

where the overbars denote calculating the moment using the number-based primary particle size distribution. We evaluate Eq. (5) herein for natural flocs.

Existing analytical permeability models can struggle to predict Ω (Eq. 3) because natural flocs do not fulfill model assumptions of uniformly sized primary particles and uniform porosity (Eq. 2). Several experimental studies observed particularly high floc permeability incompatible with typical permeability models altogether (e.g., Johnson et al., 1996; Li and Logan, 1997). Using a data compilation of field and lab flocs, Strom and Keyvani (2011) found that the classic Brinkman permeability model, which is based on drag theory for a cluster of uniformly sized grains (Brinkman, 1947), vastly overestimated the inferred Ω for flocs with $n_f < 2$. However, their conclusion is uncertain because they calculated Ω using reported primary particle diameters that might not reflect effective primary particle diameters. Kim and Stolzenbach (2002) found that the empirical Davies permeability model (Davies, 1953):

$$\xi^{-2} = \left(\frac{D_p}{D_f}\right)^2 [16\varphi^{1.5}(1 + 56\varphi^3)]^{-1} \quad (6)$$

predicted well the hydrodynamic force on simulated permeable fractal aggregates. Like the Brinkman model, the Davies model predicts ξ^{-2} (and hence Ω through Eq. 3) given φ and n_f because $\left(D_p/D_f\right)^2 = \varphi^{2/(3-n_f)}$ (Eq. 2). Modified permeability models have been proposed to capture the fact that clustering of primary particles might create macropores that disproportionately set permeability (Li and Logan, 2001; Woodfield and Bickert, 2001). In particular, Li and Logan (2001) replaced D_p with a larger cluster diameter, D_c (m), in any given permeability equation (e.g., Brinkman or Davies model). We tested the abilities of the Brinkman and Davies models and their Li and Logan variants, each coupled with Eq. (3), to describe drag ratio estimates.

3.2.2 Semi-Empirical Model

The semi-empirical model is the Winterwerp (1998) model as modified by Nghiem et al. (2022). Unlike the explicit model, the semi-empirical model predicts values representative of a floc population (Winterwerp, 1998) rather than those of individual flocs. At equilibrium between floc growth and breakage, the Winterwerp model predicts floc diameter, $D_f = (k_A/k_B)C\eta\sqrt{F_y/(\rho\nu^2)}$, in which k_A and k_B (dimensionless) are the floc aggregation and breakage efficiencies, ρ is water density (1000 kg m^{-3}), ν is water kinematic viscosity (10^{-6} m^2 s^{-1}), F_y is the floc yield force (N), and C (dimensionless) is the volumetric sediment concentration. The Kolmogorov microscale, η (m), is the length scale of the smallest turbulent eddies in the flow and scales inversely with turbulence intensity (Tennekes and Lumley, 1972).

The semi-empirical model (Nghiem et al., 2022) includes the effects of organic matter, sediment mineralogy, and water chemistry in k_A/k_B using standard geochemical variables measured from river sediment and water samples, which are often more readily available than the floc parameters in the explicit model. The semi-empirical model predicts w_s, D_f, and floc cutoff diameter, D_t (m), which is the threshold grain diameter between significantly flocculated (finer) and unflocculated (coarser) sediment. Using D_t, w_s, and D_f inferred from a global river data compilation of sediment concentration-depth profiles, Nghiem et al. (2022) calibrated the model:

$$D_t = 0.134\left(\eta\widetilde{D}_{p,50}\right)^{1/2}(C_m\theta^2(1-\theta)^2)^{0.0734}(\mathrm{Al/Si})^{-0.774}\Phi^{-0.180} \quad (7a)$$

$$w_s = \frac{R_s g\widetilde{D}_{p,50}}{20\nu}0.306\eta(C_m\theta^2(1-\theta)^2)^{0.167}(\mathrm{Al/Si})^{-2.15}\Phi^{-0.0358} \quad (7b)$$

$$D_f = 0.0180\eta(C_m\theta^2(1-\theta)^2)^{0.147}(\mathrm{Al/Si})^{-1.55}\Phi^{-0.360} \quad (7c)$$

The variables in the semi-empirical model (Eq. 7) describe the depth-averaged floc population because the floc calibration data are depth-averaged. Accordingly, depth-averaged mud volume concentration, C_m (dimensionless), is the representative sediment concentration for flocculation because, although sand can be incorporated in flocs (Whitehouse et al., 2000; Manning et al., 2010), mud is typically far more abundant (Lamb et al., 2020; Osborn et al., 2021). Depth-averaged median primary particle diameter, $\widetilde{D}_{p,50}$ (m), is taken as the primary particle size metric. Sediment Al/Si (molar ratio) represents mineralogy because clay minerals are enriched in Al/Si compared to feldspar and quartz (e.g., Galy et al., 2008; Bouchez et al., 2014). θ (dimensionless) is the organic cover fraction, the fraction of the sediment grain surface covered with organic matter (Smellie and LaMer, 1958). Relative charge density, Φ (dimensionless), quantifies the effect of salinity and sediment mineralogy on flocculation using diffuse double layer theory (Rommelfanger et al., 2022). Φ is the ratio of net cation charge in solution and that at the surface of sediment grains. Flocculation is expected at higher values of Φ where the cation concentration overcomes the negative charges on the surfaces of clay minerals.

In this study, we combined floc and geochemical measurements in the Wax Lake Delta to constrain explicit model parameters and verify the semi-empirical model. Our objective for the explicit model is to evaluate primary particle diameter and floc permeability theory because these parameters have not been fully tested before for natural flocs. Our objective for the semi-empirical model is to validate it using direct observations of floc diameter and settling velocity.

3.3 Study Site

We conducted fieldwork in the Wax Lake Delta, a river-dominated freshwater delta in the Mississippi River Delta complex (Fig. 1ab). The lower Mississippi River conveys water and sediment to WLD via the Atchafalaya River and Wax Lake Outlet, which was dredged in 1942 (Fig. 1b; Latimer and Schweizer, 1951). The topset of WLD became subaerial after the 1973 Mississippi River flood and has since been aggrading and prograding into the Gulf of Mexico with little human intervention (Roberts et al., 1980; Jensen et al., 2022). Interactions between the river, tides, wind, and vegetation cause wide variability in delta island inundation, which can expose and submerge much of the levees along island margins (Geleynse et al., 2015). Despite the proximity of WLD to the Gulf of Mexico, the water remains fresh even during low river discharge (Holm and Sasser, 2001).

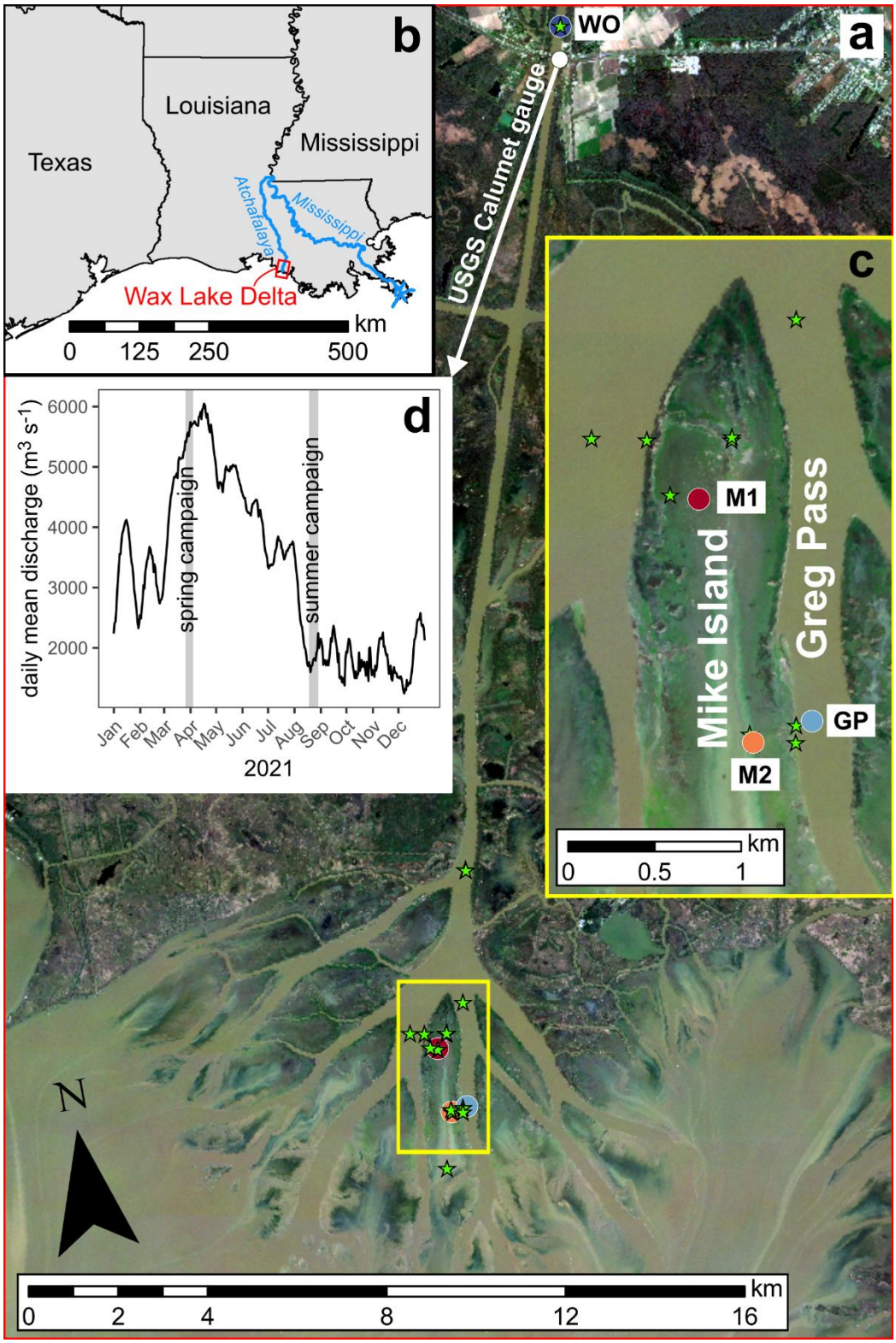

Figure 1: (a) Map of Wax Lake Delta, Louisiana with sample sites. Circles indicate main sample sites with sediment concentration-depth and LISST profiles. Stars indicate

additional sediment concentration-depth profile sites without LISST and floc cam measurements. Satellite image is from January 2021, Image © 2021 Planet Labs PBC, at relatively low discharge and tide to highlight the full island extents. (b) Map of Louisiana coast region. (c) Inset map of Mike Island and Greg Pass. Satellite image is the same as that in panel (a), Image © 2021 Planet Labs PBC. (d) 2021 hydrograph of Wax Lake Outlet at Calumet, LA (USGS stream gauge 07381590). Gray bands indicate fieldwork periods.

We completed fieldwork in WLD during March and April 2021 (spring campaign) and August 2021 (summer campaign) as part of the NASA Delta-X project. During the spring campaign, the discharge into WLD was ~5500 $m^3 s^{-1}$, which is near the peak for 2021 (Fig. 1d). During the summer campaign, the discharge was ~1800 $m^3 s^{-1}$ and is close to the low discharge for the year. We studied four sites: Wax Lake Outlet (WO), Greg Pass (GP), northern Mike Island (M1), and southern Mike Island (M2) (Fig. 1ac). Site WO is about 20 km upstream of the delta apex. Site GP is near the center of Greg Pass, the distributary channel east of Mike Island. Sites M1 and M2 on Mike Island are in a tidally forced shallow wetland. We sampled all sites during the spring campaign, but only sampled site GP during the summer campaign. At each site, we collected vertical profiles of suspended sediment samples (i.e., concentration-depth profiles) and in situ particle size distributions and concentrations with a Sequoia Scientific LISST-200X (LISST) instrument. We collected 8 profiles with paired LISST and sample measurements. We took floc images with a camera system (floc cam) for 4 profiles. We sampled 16 additional concentration-depth profiles distributed throughout WLD without matching LISST or floc cam data, including one profile in October 2019 during a separate field campaign. We also collected water samples to measure major cation and anion concentrations at 20 profile sites and dissolved inorganic carbon (DIC) concentration at 15 profile sites.

3.4 Methods

Herein we use the terms “grain” or “sediment” to mean the solid disaggregated mineral sediment, which might or might not have been flocculated in situ. As standard in the flocculation literature, we use “primary particle” to refer to the constituent sediment grains inside flocs. We use “particle” alone (i.e., without “primary”) to refer generically to the in situ suspended material, which includes flocs and unflocculated sediment. This nomenclature is standard throughout the paper and is critical for distinguishing between flocs, unflocculated sediment, and fully dispersed sediment.

We designed our field methods to measure all variables in the explicit and semi-empirical models and test their floc settling velocity predictions. We collected sediment concentration-depth profiles and acoustic Doppler current profiler (ADCP) flow velocity measurements (Sect. 4.1). We measured the major ion concentrations of the water, sediment organic matter concentration, and sediment elemental composition (Sect. 4.2). The primary floc data sources are in situ particle sizing with LISST (Sect. 4.3), a camera (Sect. 4.4), and analysis of suspended sediment concentration-depth profiles (Sect. 4.5),

each with different advantages and limitations. In situ particle sizing measures in situ particle size distribution and concentration using laser diffraction (e.g., Agrawal and Pottsmith, 2000; Guo and He, 2011), but cannot distinguish between flocs and unflocculated sediment. Although laser diffraction might be sensitive to primary particles within flocs (Graham et al., 2012), studies have found good agreement between floc size distributions measured by camera and laser diffraction (Mikkelsen and Pejrup, 2001; Mikkelsen et al., 2005). Cameras directly measure floc size and settling velocity (e.g., Mikkelsen et al., 2004; Benson and French, 2007; Osborn et al., 2021). However, camera methods require reliable image processing algorithms, can be limited by the small number of identifiable flocs, and cannot detect flocs finer than the pixel resolution. Depth-averaged floc settling velocity can be inferred from stratification in grain size-specific sediment concentration-depth profiles (Lamb et al., 2020; Nghiem et al., 2022), but this technique is indirect and does not reveal floc diameter. We combined these data sources in novel ways (Sect. 4.6) to derive floc variables (floc diameter, floc settling velocity, fractal dimension, effective primary particle diameter, and drag ratio) required to test theory and the floc settling velocity models.

Table 1: Estimated floc variables and their data sources. The variables are listed by order in the data processing workflow. In Data Source, "sediment" refers to sediment grain size distribution, concentration, and/or Rouse-Vanoni equation fitting results. The primary data source (if any) is listed first. In Description, the data sources are indicated in parentheses next to input variables if there are multiple sources.

Variable	Data Source	Description	Section or (Equation)
Paired diameter (m) and settling velocity (m s^{-1}) of individual flocs	floc cam	Diameter: Extracted using image analysis Settling velocity: Calculated by manually tracking particles	4.4
Floc cutoff diameter, D_t (m)	sediment	Selected by eye from grain diameter-settling velocity results from Rouse-Vanoni fitting of grain size-specific concentration-depth profiles	4.5
Floc size distribution (m) and concentration	LISST, sediment	Particle size distribution and concentration (LISST) removing the unflocculated sediment fraction in the classes coarser than D_t and finer than the maximum grain diameter (sediment)	4.6.1
Primary particle size distribution (m) and concentration	sediment	Grain size distribution and sediment concentration removing the fraction coarser than D_t	4.6.1

Bulk solid fraction, $\bar{\varphi}$	sediment, LISST	Ratio of primary particle (sediment) and floc concentrations (LISST, sediment)	4.6.1
Fractal dimension, n_f	LISST, sediment	Calculated to ensure consistency between $\bar{\varphi}$ (sediment, LISST) and mean settling velocity over the floc size distribution (LISST, sediment)	4.6.2 (11)
Effective primary particle diameter, D_p (m)	LISST, sediment	Calculated using n_f (LISST, sediment) and $\bar{\varphi}$ (sediment, LISST)	4.6.2 (9)
Drag ratio, Ω	floc cam, LISST, sediment	Calculated using floc cam-measured floc diameter and settling velocity (floc cam) by solving the explicit model (Eq. 1) for Ω with the calculated n_f (LISST, sediment) and D_p (LISST, sediment)	4.6.3 (1)
Floc settling velocity distribution (m s^{-1})	LISST, floc cam, sediment	Converted floc size distribution (LISST, sediment) using the floc settling velocity equation (Eq. 1) with calculated Ω (floc cam, LISST, sediment), n_f, and D_p (both LISST, sediment)	4.6.4 (1)

3.4.1 Sediment Sampling and Hydrodynamic Measurements

Nghiem et al. (2021) describe our sediment sampling and lab analysis in full, which are summarized here. For each profile, we collected suspended sediment samples at different heights above the bed from a boat with a Van Dorn sampler. At the channel sites (WO and GP), we collected samples isokinetically by drifting over the target location at the local current speed (Edwards and Glysson, 1999). We sampled while stationary at the wetland sites (M1 and M2) because of the relatively slow flow velocities inside the wetland (~0.1 m s^{-1}). We also sampled bed sediment with a Ponar grab sampler and shallow sediment cores using a piston core to supplement the samples for XRF analysis (Sect. 4.2). We filtered each sample through 0.2 μm pore size polyethersulfone filter paper (Sterlitech) and froze the filtered sediment. In the lab, we dried and weighed samples to measure sediment concentration. We decarbonated, oxidized, and deflocculated an aliquot of each sample for grain size analysis following Douglas et al. (2022) to fully disperse the sediment.

We measured the volume-based grain size distribution using a Malvern Mastersizer 3000E laser diffraction analyzer with the non-spherical scattering model from 0.2 to 2100 μm in 100 logarithmically spaced bins. This method calculates the grain size distribution using

Mie theory to model light scattering from particles. Mie theory is sensitive to the refractive index, RI, and absorption index, AI, of the particles. We determined appropriate values of these optical properties for each measurement using the Mastersizer's optical property optimizer, which finds the best values to minimize the difference between measured and modeled light scattering intensity (Rawle, 2015; Malvern Panalytical, 2024). We limited RI between 1.5 and 1.7, which covers the range of common sedimentary minerals (Özer et al., 2010), and AI between 0.001 and 0.01, which we empirically found to best suit our samples. The median optimized RI and AI across all measurements are 1.57 and 0.01, respectively. For each concentration-depth profile, we calculated the depth-averaged grain size distribution by depth-averaging the concentration in each grain size class with the trapezoidal rule and renormalizing the depth-averaged concentrations. We extrapolated a constant concentration in the unmeasured regions below the deepest measurement and above the shallowest measurement for the integration. We summed the class-specific depth-averaged concentrations to obtain the total depth-averaged sediment concentration. To obtain depth-averaged mud concentration, C_m, for the semi-empirical model, we summed the concentrations in the mud classes only.

We measured flow velocity profiles using a Teledyne RiverPro ADCP instrument concurrent with suspended sediment sampling. We deployed the ADCP near the water surface looking downward. The ADCP measured the flow velocity profile to within 5 to 15 cm of the bed at a frequency of ~1 Hz. We averaged about 100 to 1000 velocity profiles in the island sites and about 50 in the channel sites to obtain the representative velocity profiles at the concentration-depth profiles. We averaged data within a radius of 1.5 times the flow depth from the concentration-depth profile location and within 10 s of collecting a suspended sediment sample. For the deeper flows (>10 m) in Wax Lake Outlet and the delta apex, the velocity profiles contain about 50 bins in the vertical. The shallow channel profiles (3 to 4 m depth) have about 10 to 30 bins. The island profiles, with depths of 1 m or less, have about 5 bins. The bin height is about 10 to 20 cm for the deeper flows and about 5 to 10 cm for the shallower flows. We did not observe any clear wind or vegetation signatures in the representative velocity profiles (e.g., Baptist et al., 2007).

We estimated the total boundary shear velocity, u_* (m s^{-1}), by fitting each representative flow velocity profile to the law of the wall (e.g., García, 2008). The law of the wall is reasonable because the representative velocity profiles visually show a clear linear trend between flow velocity and the logarithm of height. However, some data above 50% of the flow depth deviate from the linear trend likely due to tide and wake effects (Soulsby and Dyer, 1981; Nezu and Nakagawa, 1993). We excluded this upper data and fitted the law of the wall using a weighted least squares regression with weights equal to the reciprocal of the square of the velocity standard error. The coefficients of determination have a median of 0.89 and range from 0.06 to 0.99. We used the shear velocity to calculate the near-bed Kolmogorov microscale. The Kolmogorov microscale varies with height above the bed as $\eta(z) = (\nu^3/\varepsilon)^{1/4}$, where ε (m^2 s^{-3}) is the dissipation rate of turbulence kinetic energy per unit mass, and $\varepsilon = (u_*^3/\kappa)(1/z - 1/h)$, where κ (dimensionless) is the von Kármán constant (0.41), z (m) is height above the bed, and h (m) is the water depth (Nezu and

Nakagawa, 1993). Following Nghiem et al. (2022), we chose η as the value at 10% of the flow depth (i.e., the near-bed value; Sect. 4.5).

3.4.2 Geochemical Measurements for Semi-Empirical Model

We measured sediment Al/Si using X-ray fluorescence (XRF) for 33 suspended, bed, and core sediment samples for the semi-empirical model. Due to sample mass limitations, we measured quantitative Al/Si using glass pellet fusion on a 4 kW Zetium Panalytical XRF analyzer for only 7 samples. For the remaining 26 samples, we measured semi-quantitative Al/Si using a Rigaku Primus IV XRF Spectrometer. We re-analyzed the samples that had been measured on the Zetium using the Rigaku to calibrate a linear equation ($R^2 = 0.91$) converting the semi-quantitative Al/Si to quantitative Al/Si. Using the converted quantitative Al/Si, we calibrated a linear equation between Al/Si and volume fraction finer than a certain grain size threshold so we could predict Al/Si for cases in which grain size distribution is known but we did not measure Al/Si. We calculated the coefficients of determination for many grain size thresholds and selected the model with the highest R^2 ($\mathrm{Al/Si} = 0.089 + 0.17[\text{volume fraction finer than } 23.1\ \mu\text{m}]$; $R^2 = 0.90$). We predicted Al/Si from the depth-averaged grain size distributions (Sect. 4.1) for all concentration-depth profiles using this equation.

We measured total organic carbon (TOC) concentration of suspended sediment samples to calculate θ in the semi-empirical model. Sediment aliquots were decarbonated by leaching with 2 M HCl at 80°C and dried. Samples were weighed before and after decarbonation to correct for the fraction of sediment mass lost during decarbonation. TOC concentration was measured using an Exeter Analytical CHN analyzer with uncertainties determined from repeat measurements of reference materials. We depth-averaged TOC concentrations for each concentration-depth profile using the trapezoidal rule on measured TOC concentrations weighted by sediment concentration. We assumed all organic matter was cellulose to convert depth-averaged TOC concentration to organic matter concentration (Nghiem et al., 2022). We calculated θ using the computed organic matter concentration and depth-averaged median primary particle diameter (Sect. 4.6.1; Nghiem et al., 2022).

We measured the major ion concentrations (cations: Na^+, K^+, Ca^{2+}, Mg^{2+}; anions: Cl^-, HCO_3^-, SO_4^{2-}) of water samples to calculate Φ for the semi-empirical model (Nghiem et al., 2022; Rommelfanger et al., 2022). We measured dissolved inorganic carbon (DIC) concentrations using a Picarro Cavity-Ring Down Spectroscopy G2131-*i* and assumed that all DIC was HCO_3^- to calculate HCO_3^- concentrations. For DIC, about 6 mL of filtered river water was injected through a 0.2 μm syringe filter into an evacuated and pre-weighed 12 mL exetainer. Samples were acidified with 10% phosphoric acid. The resulting CO_2 was carried in a nitrogen stream for total carbon measurements (Dong et al., 2018). DIC concentration was calibrated against weighed and acidified optical calcite standard reference materials. Concentrations of the rest of the ions were measured by ion chromatography at the Department of Geography, Durham University and checked by regular measurements of the LETHBRIDGE-03 standard. We solved for the HCO_3^-

concentration using charge balance for cases in which we had ion chromatography measurements but did not measure DIC concentration.

3.4.3 In Situ Particle Size Distribution and Concentration Measurements

We used a LISST instrument to measure in situ particle size distribution and concentration. We assumed that the particles measured by LISST were either flocs or unflocculated sediment. The LISST measures the particle volume concentration, including the pores within flocs, from 1 to 500 μm in 36 logarithmically spaced size bins using laser diffraction at a rate of 1 Hz (Sequoia Scientific, 2022). Unlike the Mastersizer, the LISST does not rely on particle optical properties because it uses an empirical calibration for natural particles to invert the angular light scattering intensity and calculate the particle size distribution (Agrawal et al., 2008). We deployed the LISST attached to a rope from a boat in drift and measured downcast profiles by lowering the LISST at a rate of about 0.1 m s^{-1}. Optical laser transmission during measurements was within recommended ranges (Sequoia Scientific, 2022). For each LISST cast, we averaged particle size distribution and concentration data into 12 bins uniformly spaced with height above the bed to improve data display in Fig. 5. We calculated the depth-averaged particle size distribution using the trapezoidal rule with the binned concentrations as described in Sect. 4.1. Further LISST methods are documented in Fichot and Harringmeyer (2021).

3.4.4 Floc Imaging

We measured floc diameters and settling velocities with a custom imaging device called the "floc cam" (Fig. 2a). The floc cam is a frame on which we mounted a camera and a modified 2.2 L Van Dorn sampler. We installed a 7 cm diameter window on the side of the sampler through which a backlight illuminates the interior. On the opposite side, we installed a 3 cm diameter window through which a camera takes photos. For each floc cam sample, we followed the same procedure for suspended sediment sampling up until the sample was retrieved from depth. We then mounted the sampler in the floc cam frame and took photos of backlit particles within the sampler using a Nikon D750 camera equipped with an AF-S Micro NIKKOR 60 mm f/2.8G ED lens (Fig. 2a). We programmed the camera to take photos at a rate of 4 Hz. Once the sampler and camera were in place, we covered the frame with a black tarp to shield the floc cam from ambient light. The time between sample collection and the start of image collection was about 1 min. We allowed the camera to take photos for a few minutes, yielding an image time series for each floc cam sample. We measured a resolution of 6 μm per pixel in the focal plane of the camera by photographing a ruler.

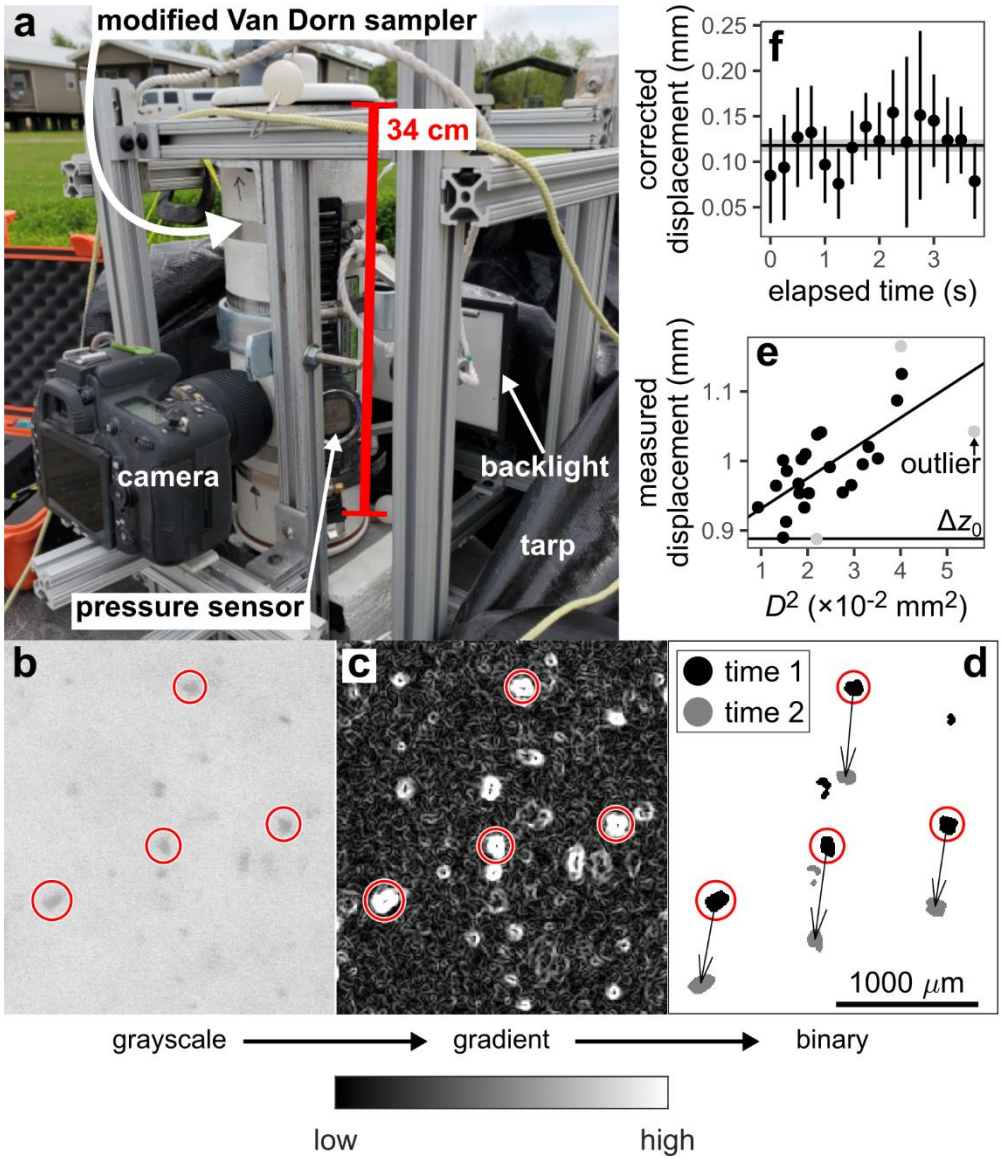

Figure 2: Floc cam data collection and processing. (a) Floc cam setup. During image collection, the black tarp covered the sampler and frame to block external light. (b) Example floc cam grayscale image. (c) 2D gradient of the grayscale image. High-gradient pixels correspond to particle borders. (d) Binarized particles showing particle displacement between an image pair. Scale in panel d also applies to panels b and c. (e) Example scatterplot of squared diameter, D^2, and measured displacement. Δz_0 indicates the fitted background correction. (f) Time series of corrected displacement for a single tracked particle across multiple image pairs. The corrected displacement isolates the displacement due to gravitational settling from that due to background currents.

We detected particles in each image with the MATLAB Image Processing Toolbox following Keyvani and Strom (2013). We converted each image to grayscale and cropped the image to a smaller area of interest. We rescaled the pixel values in the cropped image

and applied a Gaussian smoothing filter (Fig. 2b). We took the gradient of the image with a central difference method (Fig. 2c). We binarized the gradient image using a gradient cutoff, determined by trial-and-error, to exclude any particles where the gradient was too small (i.e., the particle was out-of-focus; Fig. 2d) but retain a sufficient number of detected particles. We applied morphological erosion and dilation on the binary image to remove noise speckles and connect fragments belonging to the same particle. Finally, we filled any holes within detected particles.

To calculate settling velocity, we tracked particles manually between successive frames in each binary image time series of in-focus particles (Fig. 2d). We identified the same particle across frames according to particle size, shape, and displacement. We tracked 100 unique particles for each time series over an image time span of 10 to 20 s and only recorded particles that could be tracked for at least three consecutive frames. The mean number of frames over which we tracked particles is 7.4. For each tracked particle, we calculated the diameter as the diameter of an equal-area circle using the second-largest measured particle area to exclude outliers. We used a regression method to remove the effect of background currents on observed particle motion and isolate particle displacement due to gravitational settling only. We assumed that background currents perfectly advected particles (Smith and Friedrichs, 2015). The particle displacement between an image pair is $\Delta\hat{z} = \Delta z + \Delta z_0$ where $\Delta\hat{z}$ (m) is the observed vertical displacement of the particle, Δz (m) is the displacement due to gravitational settling, and Δz_0 (m) is the displacement due to background currents. For a given time interval, Stokes law predicts that the gravitational displacement scales with the square of particle diameter, *D*. We assumed that Δz_0 is independent of particle size because the particles were sufficiently small. Using the data of all tracked particles in an image pair, we regressed $\Delta\hat{z}$ against D^2 according to $\Delta\hat{z} = cD^2 + \Delta z_0$ (Fig. 2e). We recovered Δz_0 as the intercept and solved for Δz (Fig. 2f) for all particles and image pairs. We discarded the data for which $\Delta\hat{z}$ fell into the 95% confidence interval of the estimated Δz_0. This filtering retained 222 out of an initial 400 total tracked particles (56%). We calculated settling velocity for each particle as the mean of Δz divided by the time interval (0.25 s).

3.4.5 Rouse-Vanoni Equation Analysis of Sediment Concentration-Depth Profiles

Rouse-Vanoni equation fits to grain size-specific concentration-depth profiles provide inferred floc cutoff diameter and depth-averaged floc settling velocity (Lamb et al., 2020; Nghiem et al., 2022). The Rouse-Vanoni equation models the suspended sediment concentration as a function of height from the bed, *z*, in a flow of depth *h* assuming a balance of gravitational sediment settling and upward turbulent sediment fluxes (Rouse, 1937):

$$C_i = C_{bi}\left(\frac{\frac{h-z}{z}}{\frac{h-h_b}{h_b}}\right)^{p_i} \quad (8)$$

where C_i (dimensionless) is the sediment volume concentration, C_{bi} (dimensionless) is the sediment volume concentration at the near-bed height h_b (m), p_i (dimensionless) is the Rouse number, and the subscript i denotes the ith grain size class. Vertical concentration stratification increases with Rouse number, $p_i = w_{si}/(\kappa\beta u_*)$, where w_{si} (m s^{-1}) is the in situ grain size-specific settling velocity. The diffusivity ratio, β (dimensionless), is the ratio of turbulent sediment diffusivity and turbulent momentum diffusivity and accounts for the fact that sediment does not exactly follow turbulent eddies (e.g., García, 2008). Flux Richardson numbers, calculated using the settling velocities of flocs and unflocculated sediment (Sect. 5.8), have a median of 1.5×10^{-4} and maximum of 6.6×10^{-2}, indicating limited sediment-induced turbulence damping effects on flow velocity and concentration-depth profiles (Smith and McLean, 1977; Wright and Parker, 2004).

If β and u_* are known, then w_{si} can be calculated from the fitted p_i. Past studies using this method interpreted the inferred settling velocity for fine silt and clay grain sizes as the floc settling velocity because it is much faster than the settling velocity theory prediction for individual grains (Lamb et al., 2020; Nghiem et al., 2022). β is an obstacle to calculating w_{si} because predicting β is still an open question (De Leeuw et al., 2020; Lamb et al., 2020). β is often assumed to be unity. Deviations from unity have been attributed to sediment-induced density stratification (Wright and Parker, 2004; Moodie et al., 2020) and grain size-dependent momentum effects (Carstens, 1952; Csanady, 1963; Graf and Cellino, 2002). Limited evidence shows that the diffusivity ratio for flocs, β_{fl}, might follow an existing formulation for solid grains (Izquierdo-Ayala et al., 2021, 2023), but still requires more investigation. For simplicity, we first assumed $\beta = 1$ for flocs and sediment grains. We re-evaluate β_{fl} with independent floc settling velocity data in Sect. 5.9.

Following Lamb et al. (2020) and Nghiem et al. (2022), we fitted the log-linearized Rouse-Vanoni equation to grain size-specific concentration-depth profiles (e.g., profiles of the dispersed grains), an example of which is depicted in Fig. 3a. We converted the sediment mass concentrations to volume concentrations assuming a sediment density of 2650 kg m^{-3} and used $h_b = 0.1h$ (De Leeuw et al., 2020). For each grain size class, the grain size-specific concentration is the total sediment concentration times the volume fraction from the grain size distribution (Sect. 4.1). In order to fit the Rouse-Vanoni equation, we required the grain size-specific concentration-depth profile to have a nonzero concentration for all suspended sediment samples in the profile. We estimated the grain size-specific Rouse number, p_i, from the Rouse-Vanoni equation fits. We used shear velocity estimates (Sect. 4.1) and $\beta = 1$ to calculate w_{si}. Figure 3b shows grain diameter, D_g (m), and w_{si} for the concentration-depth profiles with corresponding LISST measurements (Sect. 3). We identified the floc cutoff diameter, D_t, by eye for each concentration-depth profile as the diameter below which the inferred settling velocity begins to depart significantly from conventional settling velocity theory (grain settling velocity, $w_{sg} = \left(R_s g D_g^2\right)/\left(c_1\nu + \sqrt{0.75 c_2 R_s g D_g^3}\right)$ for $c_1 = 20$, and $c_2 = 1.1$; Ferguson and Church, 2004). We calculated the Rouse-estimated floc settling velocity as the median w_{si} within grain diameters finer than D_t (Nghiem et al., 2022).

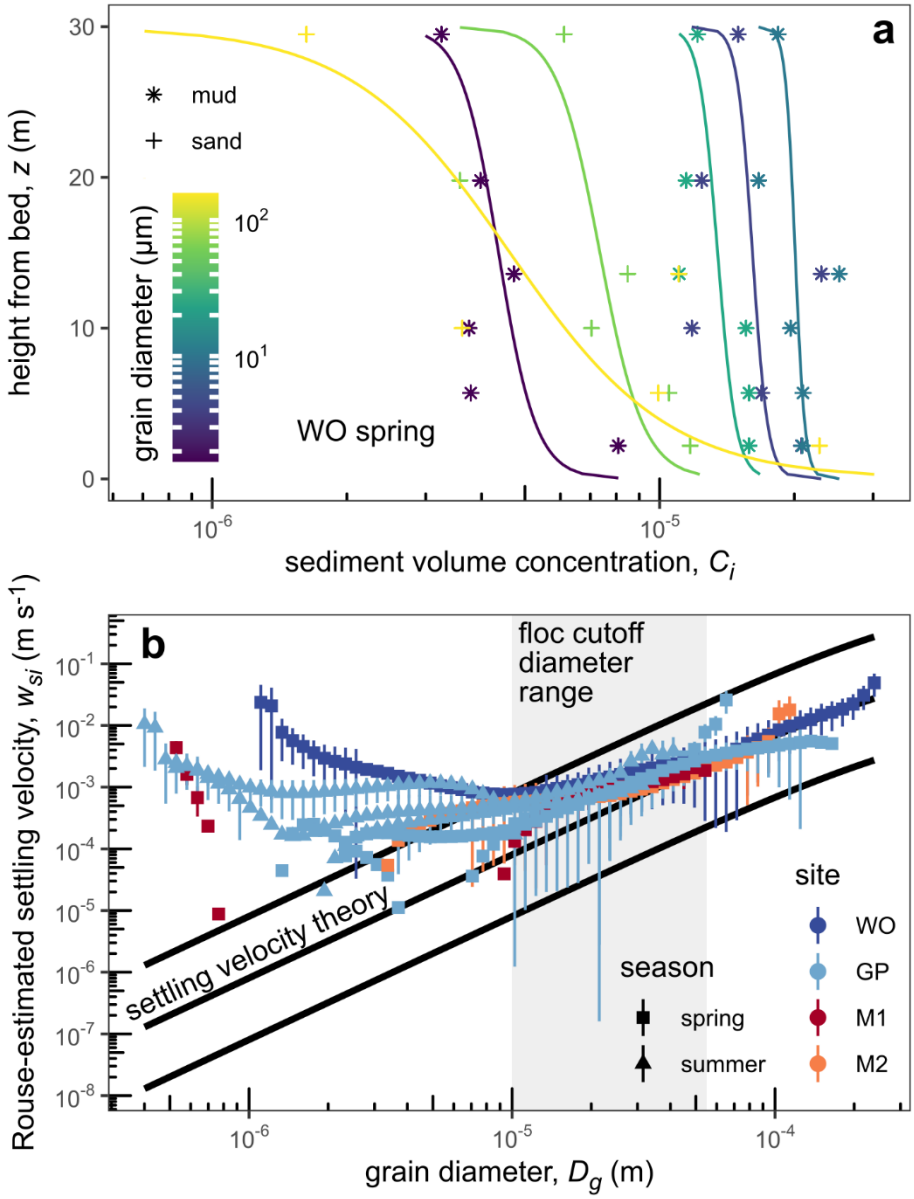

Figure 3: Rouse-Vanoni equation results. (a) Example of sediment volume concentration as a function of height above bed for profile WO spring. We used the full 100 grain size classes in all calculations, but reclassified the data into 6 classes for this panel only to improve readability. Curves represent the best-fit Rouse-Vanoni profiles (Eq. 8). Data scatter likely represents spatiotemporal variations in turbulence, bedforms, and/or other natural sources of variability. (b) Grain diameter and Rouse-estimated in situ settling velocity assuming $\beta = 1$ for concentration-depth profiles with LISST measurements. Black settling velocity theory curves indicate the Ferguson and Church (2004) model with an order-of-magnitude above and below. Floc cutoff diameter varies between concentration-depth profiles and ranges between 10 and 55 μm for the displayed profiles.

Vertical bars represent the propagated 68% confidence interval on the Rouse number estimates. Points without vertical bars have confidence intervals that overlap with 0.

3.4.6 Estimating Floc Properties

Here we describe how we combined our grain size distributions (Sect. 4.1) and floc data (Sect. 4.3-4.5) to calculate floc properties.

3.4.6.1 Floc and Primary Particle Size Distribution and Concentration

Our first goal was to delineate the size distribution and concentration of flocs and primary particles. To do this, we paired LISST and sediment sample data because they record mixtures of different types of particles (Fig. 4). LISST measured the size distribution and concentration of flocs and unflocculated sediment grains together (i.e., in situ particles; Sect. 4.3). LISST particle volume concentration includes the volumes of mineral sediment and pores between primary particles within flocs (Mikkelsen and Pejrup, 2001; Livsey et al., 2022). On the other hand, suspended sediment data represent the size distribution and concentration of fully dispersed sediment grains, which might have been flocculated in situ. We paired each suspended sediment sample from the concentration-depth profiles to a corresponding set of measurements from the concurrent LISST cast. LISST measurements were assigned when collected within 0.1 m (the sampler radius) of the sample collection depth. If there were no LISST measurements in this range, then we assigned the 3 measurements closest in depth. We assumed that paired LISST and sediment data statistically represent the same suspended material, allowing direct comparison between the distributions and volume concentrations.

Figure 4 illustrates how we divided LISST particle sizes into three zones that either contain flocs only or both flocs and unflocculated grains to help isolate the floc and primary particle size distribution and concentration. Zone 1 is defined as particles measured by the LISST that were coarser than the maximum grain diameter of the dispersed sediment. We assumed that all particles in zone 1 are flocs because they are larger than any dispersed sediment grains we measured. Zone 2 is defined as particles measured by the LISST that are finer than the floc cutoff diameter (Sect. 4.5; Fig. 3b). We inferred that particles in zone 2 were also all flocs under the assumption that all sediment finer than the floc cutoff diameter was flocculated (Fig. 3b). In reality, some sediment finer than the floc cutoff diameter might have been unflocculated. However, the enhanced settling velocities inferred from the concentration-depth profiles imply significant flocculation in these sizes (Fig. 3b), making complete flocculation a reasonable assumption. Finally, zone 3 lies between zones 1 and 2 and is defined as particles measured by LISST with sizes between the floc cutoff diameter and maximum grain diameter (Fig. 4). As such, zone 3 likely consists of a mixture of flocs and unflocculated grains.

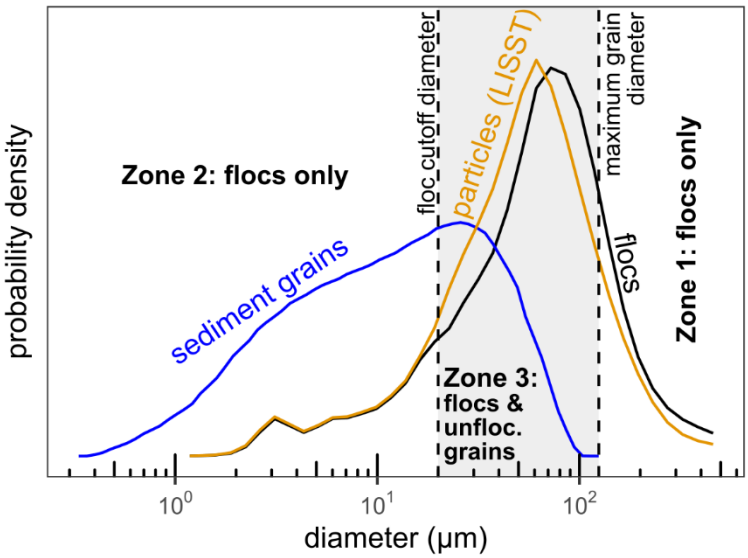

Figure 4: Example of calculating floc size distribution (black) from suspended sediment grain size distribution (blue) and LISST in situ particle size distribution (orange). Particles include flocs and unflocculated grains. Zones describe the particles in the LISST particle size distribution and are demarcated by the floc cutoff and maximum grain diameters. We identified floc cutoff diameter as the grain diameter at which the Rouse-estimated settling velocity departs from settling velocity theory for single grains (Sect. 4.5; Fig. 3b). Maximum grain diameter is the maximum diameter of sediment grains measured by grain size analysis of fully dispersed sediment (Sect. 4.1). Data correspond to a suspended sediment sample collected at 1.9 m depth out of 3.8 m total depth from the GP spring 1 profile (Table 2).

We calculated the floc size distribution and concentration according to the LISST particle zones (Fig. 4). Floc concentration is the combined volume of primary particles and pores within flocs divided by the total measured volume. We compared sediment and LISST volume concentrations. We calculated the LISST particle volume concentration in each LISST size class by multiplying the particle size fraction and the total particle concentration. We then calculated the corresponding sediment volume concentration by interpolating the grain size fraction to match the LISST size class and multiplying the fraction by the total sediment concentration. According to our assumptions, LISST particle concentrations in zones 1 and 2 already represent floc concentrations and thus do not require any adjustment. This is not true in zone 3, so we calculated the floc concentration in each zone 3 size class by subtracting the particle and sediment volume concentrations. Finally, we renormalized the floc concentrations across size classes to compute the floc size distribution (Fig. 4). We calculated floc size distribution and concentration from each assigned LISST measurement and averaged them to obtain the representative floc size distribution and concentration for each sediment sample. We took the floc diameter for each size class, D_{fi}, to be the geometric mean of the floc diameter at the lower and upper boundaries of the size class. For each concentration-depth profile, we calculated the depth-averaged floc size distribution using the trapezoidal rule as described in Sect. 4.1.

We computed the primary particle size distribution and concentration by truncating the sediment grain size distribution to the fractions finer than the floc cutoff diameter (Table 1). Median primary particle diameter, $D_{p,50}$ (m), is the median of the primary particle size distribution associated with each sediment sample. For the semi-empirical model (Eq. 7), we calculated the depth-averaged median primary particle diameter, $\widetilde{D}_{p,50}$, as the median grain size of the depth-averaged grain size distribution (Sect. 4.1) truncated with the floc cutoff diameter. We calculated the floc bulk solid fraction, $\bar{\varphi}$ (dimensionless), as the ratio of the primary particle and floc volume concentrations (e.g., Mikkelsen and Pejrup, 2001; Guo and He, 2011).

3.4.6.2 Fractal Dimension and Effective Primary Particle Diameter

Our next goal was to estimate the fractal-related terms in the explicit model: fractal dimension, n_f, and effective primary particle diameter, D_p. Our strategy was to link the explicit model (Eq. 1) and solid fraction theory (Eq. 2), in which n_f and D_p appear, to mean settling velocity and bulk solid fraction estimated from data. As follows, we solved for the n_f and D_p that ensure consistency between the bulk solid fraction and mean settling velocity over the floc size distribution (Sect. 4.6.1).

Estimating n_f and D_p requires two equations to calculate those two unknowns. The first equation is the bulk solid fraction over the floc size distribution using solid fraction theory (Eq. 2):

$$\bar{\varphi} = \sum_{i=1}^{n} \varphi_i = \sum_{i=1}^{n} f_i \left(\frac{D_{fi}}{D_p}\right)^{n_f-3} \quad (9)$$

where f_i is the volume fraction in the ith floc size class from the floc size distribution and n is the number of floc size classes (36). We assumed that a single D_p applies across the floc size distribution, but primary particle diameter might vary with floc diameter (Nicholas and Walling, 1996). The second equation is the mean settling velocity over the floc size distribution using the explicit model (Eq. 1):

$$\overline{w_s} = \sum_{i=1}^{n} w_{si} = \sum_{i=1}^{n} f_i \frac{R_s g D_p^2}{b_1 \Omega_i \nu} \left(\frac{D_{fi}}{D_p}\right)^{n_f-1} \quad (10a)$$

which we set equal to the explicit model settling velocity with mean values of input variables:

$$\overline{w_s} = \frac{R_s g \bar{\varphi} \overline{D_f}^2}{b_1 \bar{\Omega} \nu} \quad (10b)$$

where $\overline{D_f}$ (m) is the geometric mean floc diameter calculated from the floc size distribution and $\overline{\Omega}$ is the mean drag ratio. Although Eq. (9) and (10a) both use fractal solid fraction theory (Eq. 2), they are distinct constraints because they integrate over different parameters (solid fraction in Eq. 9; settling velocity in Eq. 10). We substituted $\bar{\varphi}$ in Eq. (10b) with Eq. (9), set the resulting $\overline{w_s}$ equal to Eq. (10a), and rearranged terms to obtain:

$$\frac{\sum f_i \frac{\overline{\Omega}}{\Omega_i} D_{fi}^{n_f-1}}{\sum f_i D_{fi}^{n_f-3}} = \overline{D_f}^2 \quad (11)$$

We assumed that the effect of $\overline{\Omega}/\Omega_i$ on the summation in Eq. (11) is small and neglected it (i.e., $\sum f_i \, (\overline{\Omega}/\Omega_i) D_f^{n_f-1} = \sum f_i D_f^{n_f-1}$). This assumption is justified because n_f estimates align well with typical n_f for natural flocs (Sect. 5.6). As such, n_f remains as the only unknown in Eq. (11) because the rest of the variables, f_i, D_{fi}, and $\overline{D_f}$, are all known from the floc size distribution (Sect. 4.6.1). We numerically solved Eq. (11) to calculate n_f for each sediment sample. We then solved Eq. (9) for D_p using f_i, n_f, and the known bulk solid fraction, $\bar{\varphi}$ (Sect. 4.6.1). We estimated uncertainty on floc concentration, n_f, and D_p as the 95% bounds on the bootstrap distribution from 1000 bootstrap replicates of resampling the assigned LISST measurements that go into the floc size distribution and concentration (Sect. 4.6.1).

To test the fractal D_p model (Eq. 5), we compared its predictions at different values of the weighting dimension, n_w, to our effective primary particle diameter estimates. We used the number distribution of primary particle size, rather than the volume distribution, to calculate the moments in Eq. (5) because primary particles are added one-by-one as flocs grow. We constructed the number distribution by dividing the volume fraction in each size class by the cube of the grain diameter and renormalizing the distribution. We also calculated the number-based median primary particle diameter using the number distribution to compare with effective primary particle diameter estimates.

3.4.6.3 Drag Ratio

The remaining parameter in the explicit model is the drag ratio, Ω. We solved the explicit model (Eq. 1) for Ω using n_f, D_p, and floc cam-measured floc diameter and settling velocity for each floc cam observation (Sect. 4.4). We used these Ω estimates to test permeability models presented in Sect. 2.1. For each permeability model, we identified the range of all possible Ω predictions as a function of fractal dimension, n_f, to test whether our Ω estimates fall within the range. If $D_f = D_p$, then the solid fraction is unity (Eq. 2) for all n_f leading to a maximum $\Omega = 1$ (i.e., impermeable floc). The minimum Ω, $\Omega_{\min}$, at a given n_f occurs at the maximal dimensionless permeability, $\xi_{\max}^{-2}$, because Ω and ξ^{-2} are inversely related (Eq. 3). Although $\xi_{\max}^{-2}$ depends on the permeability model, we present the Davies model only because the Brinkman model yielded similar results (Sect. 5.7). We differentiated the

Davies model (Eq. 6) with respect to φ to find $\xi_{\max}^{-2}$ and, in turn, $\Omega_{\min} = \Omega(\xi^{-2} = \xi_{\max}^{-2})$ using Eq. (3):

$$\xi_{\max}^{-2} = \frac{1}{16}\left(\frac{1}{56}\frac{3n_f - 5}{23 - 9n_f}\right)^{\frac{1}{3}\left(\frac{2}{3-n_f}-\frac{3}{2}\right)} \quad (12)$$

3.4.6.4 Floc Settling Velocity Distribution

To find the floc settling velocity distribution associated with each sediment sample, we used n_f, D_p, and Ω in the explicit model (Eq. 1) to convert the floc diameters in the floc size distribution into floc settling velocities. In this calculation, we used a best-fit constant drag ratio (Sect. 5.7), $\Omega = 0.48$, because we were unable to constrain Ω for concentration-depth profiles that lack floc cam observations. For the bins at the fine tail in which $D_{fi} < D_p$, we capped the solid fraction at 1 (Eq. 2). We took the floc settling velocity for each class, w_{si}, to be the geometric mean of the floc settling velocity at the lower and upper boundaries of the class. For each concentration-depth profile, we calculated the depth-averaged floc settling velocity distribution using the trapezoidal rule as described in Sect. 4.1.

3.5 Results

First, we describe the basic hydrodynamics, sediment properties, and floc observations from the individual measurement methods (Sect. 5.1-5.4). We then present floc variables derived from combining data sources (Sect. 5.5-5.8). We compare effective primary particle diameter and drag ratio to theory and validate them using floc settling velocity inferred from the Rouse-Vanoni equation fitting (Sect. 5.6-5.9). Finally, we validate the semi-empirical model and use it to examine environmental controls on floc properties (Sect. 5.10).

3.5.1 Hydrodynamics

The sampled profiles span a wide hydrodynamic range in WLD because of discharge seasonality and environment (Fig. 1d; Table 2). The fastest flow occurred at site WO in the spring (~1.5 m s^{-1} depth-averaged) upstream of the delta apex in the Wax Lake Outlet, where the water depth was greatest (30 m) among the sites. Further down the delta, the distributary channel site GP had slower flow velocity (~0.56 m s^{-1} depth-averaged in the spring) and shallower depth (~3.7 m). At site GP, depth-averaged flow velocity in summer was about half (~0.2 to 0.3 m s^{-1}) of that in spring (Fig. 1d). The island sites were sampled in the spring only. These sites had the slowest flow velocities (0.024 and 0.12 m s^{-1}) out of the sampled sites with water depths of ~0.6 m. Shear velocity generally increased with flow velocity, ranging from ~0.006 (in the island) to ~0.1 m s^{-1} (in Wax Lake Outlet). Near-bed Kolmogorov microscale varied inversely with the shear velocity from 150 to 600 μm. Water chemistry measurements show a median salinity of 0.25 ppt and a maximum of 0.29 ppt, confirming that the water was fresh (< 0.5 ppt).

Table 2: Metadata and hydrodynamic data of sediment concentration-depth profiles with paired LISST data (Sect. 3). Boldface profile name indicates that we collected floc cam images for the profile. Shear velocity uncertainty indicates the 95% confidence interval on the law of the wall fit (Sect. 4.1).

Profile name (Site + season + index)	Date (yyyy-mm-dd)	Number of suspended sediment samples	Water depth (m)	Depth-averaged flow velocity (m s^{-1})	Shear velocity (m s^{-1})	Near-bed Kolmogorov microscale (μm)	Depth-averaged suspended sediment volume concentration ($\times 10^{-5}$)	Floc cutoff diameter (μm)
GP spring 1	2021-03-27	9	3.8	0.55	0.071 ± 0.011	150	5.2	20
WO spring	2021-03-30	6	30	1.5	0.092 ± 0.0072	220	6.9	55
M2 spring	2021-04-02	5	0.64	0.12	0.031 ± 0.018	180	5.5	30
M1 spring	2021-04-02	5	0.59	0.024	0.0061 ± 0.0026	600	4.7	35
GP spring 2	2021-04-02	6	3.5	0.57	0.054 ± 0.014	180	6.2	10
GP summer 1	2021-08-18	6	3.4	0.22	0.025 ± 0.013	330	0.69	20
GP summer 2	2021-08-20	8	3.4	0.34	0.022 ± 0.0065	360	0.54	20
GP summer 3	2021-08-22	10	3.2	0.25	0.019 ± 0.0070	390	0.54	25

3.5.2 Sediment Concentration-Depth Profiles

Depth-averaged suspended sediment was muddy (~90% mud) and more concentrated in the spring (~6×10^{-5} volume concentration) than in the summer (~6×10^{-6}) because of discharge seasonality (Table 2). The grain size-specific concentration-depth profiles reveal higher concentration closer to the bed for sand, a pattern consistent with Rouse-Vanoni theory (Eq. 8; Fig. 3a). Mud was also stratified despite the expectation of a uniform concentration-depth profile if mud settled as individual grains (Eq. 8), indicating likely flocculation.

The grain diameter versus in situ settling velocity trend from the Rouse-Vanoni equation fitting shows that sediment finer than 10 to 55 μm (i.e., the floc cutoff diameter) was appreciably flocculated at the eight main sample profiles (Fig. 3b; Table 2). Enhanced settling velocity in the grain sizes finer than the floc cutoff diameter is consistent with Lamb et al. (2020) and Nghiem et al. (2022) and indicates the presence of flocculation. Conversely, in situ settling velocity follows theory well for grain diameters coarser than the floc cutoff diameter and indicates the absence of flocculation. Although the $\beta = 1$ assumption makes the precise in situ settling velocity values inaccurate, we expect the floc cutoff diameter to be robust because it marks an abrupt change in the settling velocity pattern.

3.5.3 LISST Particle Size Distribution and Concentration

To demonstrate results prior to additional processing (Sect. 4.6.1), Figure 5 shows the raw LISST-measured in situ particle concentration and size distribution observations. The concentration profiles of flocs and unflocculated sediment (i.e., in situ particles) measured by LISST had little systematic vertical variation except for the site GP profiles in the spring in which the concentration increased slightly closer to the bed (Fig. 5a). In the spring, the particle volume concentration was ~3×10^{-4} to 5×10^{-4} for all sites except for site M1, which had a slightly smaller concentration of ~2×10^{-4} to 3×10^{-4}. In the summer, particle volume concentration at site GP was much smaller at ~5×10^{-5} to 8×10^{-5} because of the relatively lower discharge.

Channel sites (WO and GP) had median particle diameters of ~50 to 90 μm, while island sites (M1 and M2) had median particle diameters of ~35 μm, all with minimal vertical variation (Fig. 5b). Depth-averaged particle size distributions were similar across the channel sites for both the spring and summer while the island distributions were skewed toward finer particles (Fig. 5c). The fraction of particles coarser than the floc cutoff diameter ranged from ~0.10 to 0.50. The median depth-averaged particle diameter from the LISST ranges from about 3 to 15 times larger than the median grain diameter of the dispersed sediment (Fig. 5d), implying the presence of flocculation.

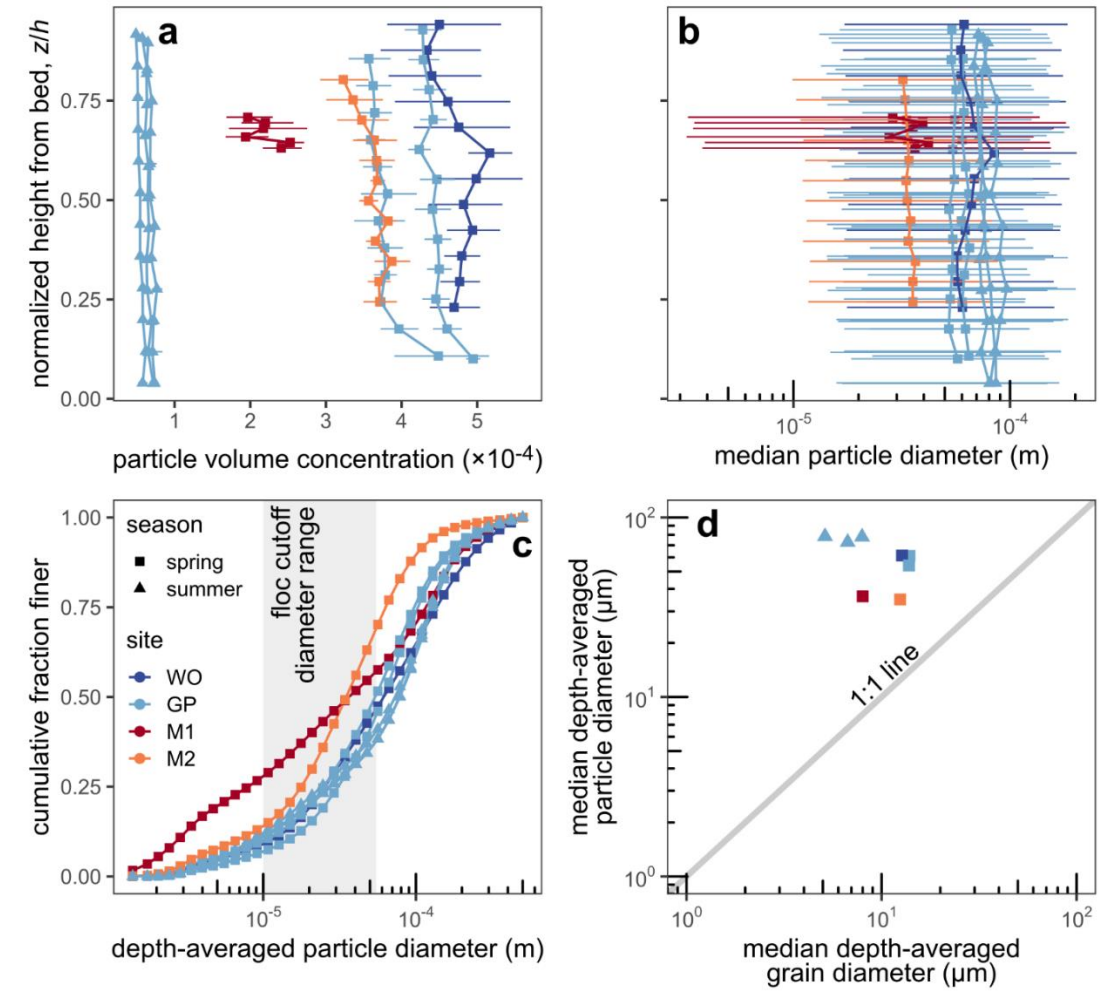

Figure 5: LISST results for in situ particles, which include flocs and unflocculated sediment. (a) Profiles of in situ particle volume concentration from LISST, binned into 12 vertical classes (Sect. 4.3). Horizontal bars represent the 95% bootstrap uncertainty. (b) Profiles of median in situ particle diameter from LISST, binned into 12 vertical classes. Horizontal bars represent the span of the D_{16} and D_{84} particle diameters, the diameters for which 16% and 84% of particles are finer, respectively. (c) Cumulative distribution functions of depth-averaged particle diameter from LISST. (d) Median depth-averaged grain diameter from sediment samples and median depth-averaged particle diameter from LISST. The legend in panel c applies for all panels.

3.5.4 Floc Cam

Tracked particles imaged by floc cam had diameters of ~70 to 200 μm and settling velocities of ~0.1 to 1 mm s^{-1} (Fig. 6), but we did not know a priori whether these particles were flocs because the image quality did not permit a visual determination. To test whether

tracked particles were flocs, Figure 6 compares diameter and settling velocity because, unlike flocs, solid non-cohesive grains follow conventional settling velocity theory (Ferguson and Church, 2004). We concluded that tracked particles were flocs because, for a given diameter, measured settling velocities are slower than settling velocity predictions of solid grains due to the fact that flocs are less dense than sediment grains. Measured settling velocities also are up to one order-of-magnitude faster than the predicted settling velocity of a typical 8-μm mud primary particle, also indicating flocculation.

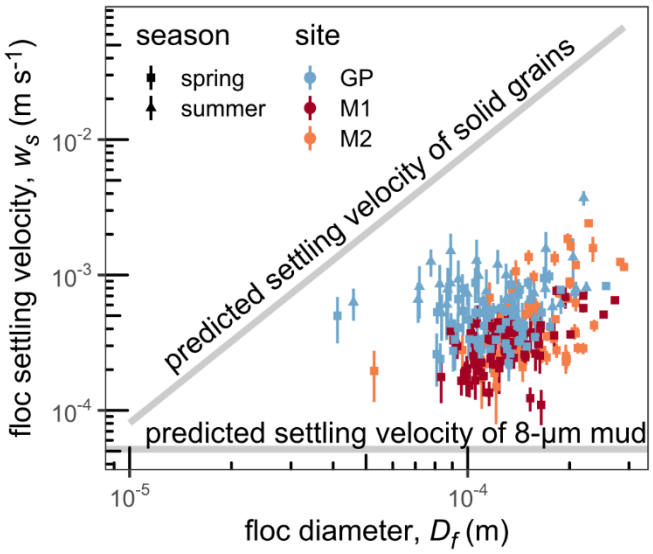

Figure 6: Diameters and settling velocities of floc cam-measured particles, which we inferred to be flocs. Vertical bars indicate the propagated mean standard error on the background displacement estimate (Sect. 4.4).

3.5.5 Floc Concentration, Size Distribution, and Bulk Solid Fraction

As described in Sect. 4.6.1, we paired concentration and size distribution data for sediment and in situ particles to isolate the floc concentration and size distribution (Table 1). Floc volume concentration was ~3×10^{-4} to 5×10^{-4} for the sites in the spring except for site M1, which had a smaller concentration of ~2×10^{-4} (Fig. 7a). All floc concentrations in the summer were far smaller than those in the spring at ~5×10^{-5} to 8×10^{-5} because of the relatively lower discharge. These concentration trends are similar to those for the particles (Sect. 5.3).

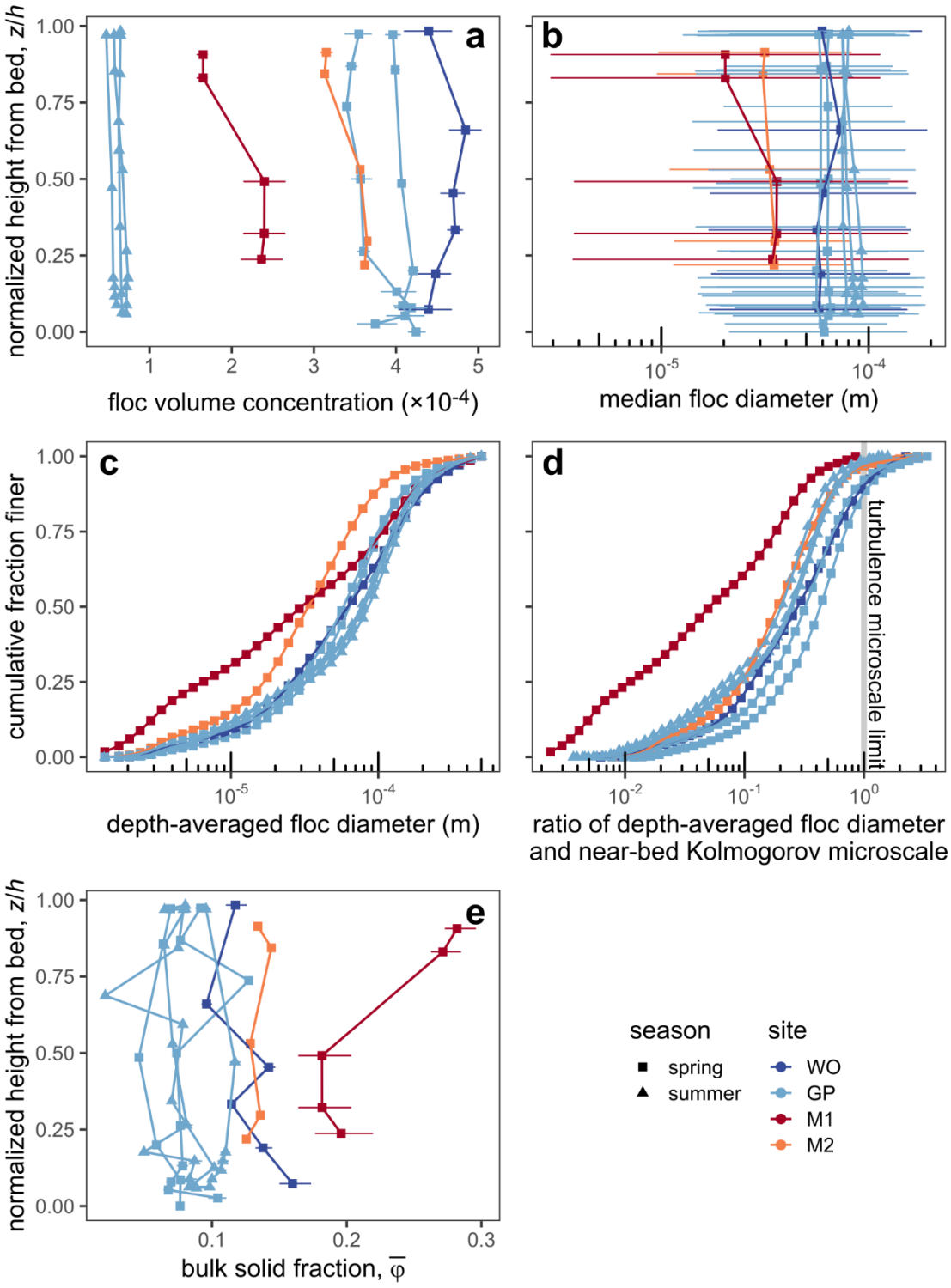
a
b
c
d
e
normalized height from bed, z/h
floc volume concentration (×10-4)
median floc diameter (m)
cumulative fraction finer
depth-averaged floc diameter (m)
ratio of depth-averaged floc diameter and near-bed Kolmogorov microscale
turbulence microscale limit
bulk solid fraction, φ
season
spring
summer
site
WO
GP
M1
M2

Figure 7: Floc concentration, size, and bulk solid fraction results. (a) Profiles of floc volume concentration. Horizontal bars represent the 95% bootstrap uncertainty. (b) Profiles of median floc diameter. Horizontal bars represent the span of the D_{16} and D_{84} floc diameters. (c) Cumulative distribution functions of depth-averaged floc diameter. (d) Cumulative distribution functions of the ratio of depth-averaged floc diameter and near-bed Kolmogorov microscale. (e) Profiles of bulk solid fraction. Horizontal bars represent the 95% bootstrap uncertainty.

Median floc diameter, $D_{f,50}$ (m), was ~50 to 90 μm for channel sites and ~20 to 30 μm for island sites with little vertical variation (Fig. 7b). Overall, flocs were ~1 to 100 μm in diameter (Fig. 7c). Depth-averaged floc size distributions at the channel sites were similar for spring and summer (Fig. 7c). In contrast, the floc size distributions at the island sites were enriched in finer flocs. ~88 to 100% of flocs by volume were smaller than the near-bed Kolmogorov microscale (Fig. 7d), consistent with the idea that the Kolmogorov microscale sets the maximum floc size (Van Leussen, 1988; Kuprenas et al., 2018). Flocs larger than the near-bed Kolmogorov microscale might either break up once they reach the elevated near-bed shear stress or, if they are sufficiently strong, withstand breakage and deposit on the bed (Mehta and Partheniades, 1975). Floc cam observations yield a median floc Reynolds number of 0.05, indicating minor inertial effects and justifying neglect of the inertial term in the explicit model (Strom and Keyvani, 2011).

After isolating the primary particle and floc volume concentrations (Sect. 4.6.1), we took the ratio of the concentrations as the floc bulk solid fraction. Bulk solid fraction ranged from ~0.05 to 0.3 and showed little systematic vertical variation (Fig. 7e). Bulk solid fraction in the island was typically higher (> 0.1) than that in the channel (< 0.1) because flocs in the island were finer (Fig. 7bc) and hence denser (Eq. 2) than those in the channel. Bulk solid fractions at WO spring were larger than those at GP because faster shear velocity at WO suspended coarser primary particles (Fig. 8; Table 2). Overall, these bulk solid fractions agree with prior floc density measurements (e.g., Van Leussen, 1988).

3.5.6 Fractal Dimension and Effective Primary Particle Diameter

Figure 8a displays fractal dimension, n_f, and effective primary particle diameter, D_p, two key explicit model parameters that we derived using the floc size distribution and bulk solid fraction (Sect. 4.6.2; Table 1). n_f is narrowly constrained to ~2 to 2.15, which is well within the expected range of 1.7 to 2.3 for natural flocs (Tambo and Watanabe, 1979; Winterwerp, 1998). We deemed $n_f = 2.1$ to be representative. Smaller n_f in the island compared to that in the channel might indicate floc response to changes in factors like turbulence, sediment concentration, organic matter, and water chemistry. Effective primary particle diameter, D_p, ranges from ~1 to 3 μm with a typical value of 2 μm. The range of D_p is similar across sampling sites except for at WO spring where all D_p exceeded 2 μm because of the faster shear velocity. No clear trend is apparent between n_f and D_p.

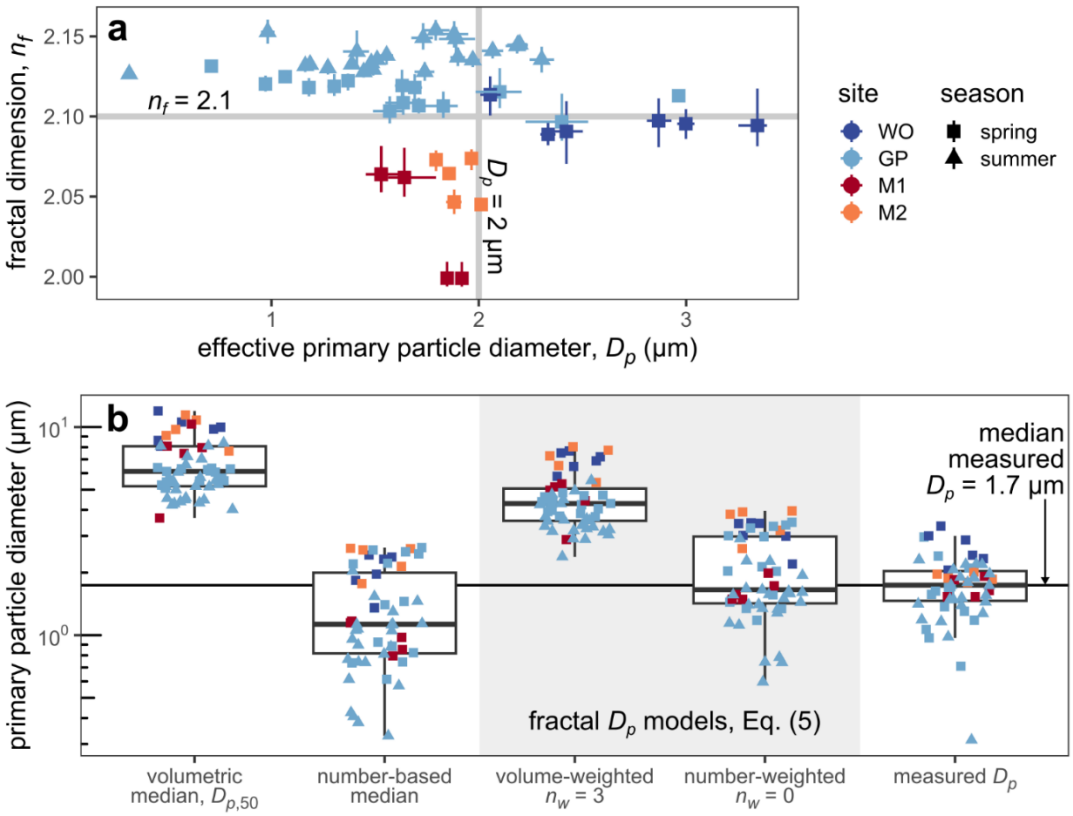

Figure 8: (a) Fractal dimension and effective primary particle diameter. Horizontal and vertical bars represent the 95% bootstrap uncertainty. Bars are smaller than the points where they are not visible. (b) Effective primary particle diameter, D_p, model comparison. We calculated median primary particle diameters from volumetric (Sect. 4.6.1) and number-based (Sect. 4.6.2) primary particle size distributions. We calculated fractal D_p using Eq. (5) on number-based primary particle size distributions (Sect. 4.6.2) and varied the weighting dimension, n_w, between 0 and 3. Measured D_p were estimated from data (Sect. 4.6.2).

Figure 8b shows that the median primary particle diameter, $D_{p,50}$, and the volume-weighted fractal D_p (Eq. 5 with $n_w = 3$) both overpredict our D_p estimates. Smaller values of n_w improve the comparison between Eq. (5) and measured D_p (not shown) until the best agreement is achieved at $n_w = 0$ (i.e., number weighting). The number-weighted fractal D_p (median = 1.6 µm) best predicts D_p (median = 1.7 µm) within a factor of about 3. Potential error in converting a volume-based size distribution to a number-based distribution might be responsible for the residual misfit between the number-weighted fractal D_p and measured D_p. In contrast, past studies used the median primary particle size diameter as the effective primary particle diameter (e.g., Syvitski et al., 1995; Strom and Keyvani, 2011). The volumetric median is biased a factor of about 2 to 6 larger than measured D_p. Conversely, the number-based median is biased low compared to measured D_p. These results indicate that the median is a poor representation of D_p.

3.5.7 Drag Ratio

We estimated the final unknown in the explicit model, the drag ratio, Ω, by solving the explicit model (Eq. 1) with n_f, D_p, and floc cam-measured diameter and settling velocity (Sect. 4.6.3; Table 1). Overall, Ω estimates span a wide range from ~0.15 to 1 with a mean of 0.48 (Fig. 9a), indicating that permeability enhances floc settling velocity and reduces floc drag force by up to a factor of 7. High variability in Ω exists even within the same floc cam deployment. Although some Ω values exceed 1, ~91% of the data fall between 0 and 1 indicating that our estimates are physically reasonable.

We used our Ω measurements to test the ability of permeability models to predict drag ratio. We first tested four existing models, the Brinkman and Davies models and their Li and Logan variants (Sect. 2.1), but only present the Davies model and its Li and Logan modification because the other models yielded similar results. Figure 9a shows fractal dimension and drag ratio for each floc cam observation against the field of all possible model predictions defined by the zone between Ω_{min} (Eq. 12) and 1 for the Davies model and its Li and Logan variant. The zone is the same for the two models because Ω_{min} only depends on fractal dimension (Eq. 3; Eq. 12). As a result, the Li and Logan strategy, replacing D_p with a larger cluster diameter, D_c, does not affect the range of Ω predictions. Both models are largely incompatible with the data because ~88% of the data (excluding $\Omega > 1$ data) lie below the zone of possible Ω.

The discordance between our measured values of Ω and the Davies model is probably because natural flocs violate the model assumptions of uniform porosity and a single primary particle size. However, a complete 3-D rendering of floc structure is generally impractical, making a full model of non-uniform flow paths difficult to implement. Instead, we explored an empirical approach to modify the Davies model (Eq. 6) by replacing φ with a permeable solid fraction, φ_r, but keeping the same D_p/D_f. That is,

$$\xi^{-2} = \left(\frac{D_p}{D_f}\right)^2 [16\varphi_r^{1.5}(1 + 56\varphi_r^3)]^{-1} \quad (13)$$

where the permeable solid fraction, $\varphi_r = \left(D_f/D_p\right)^{n_r-3}$, and n_r is the permeable fractal dimension (analogous to Eq. 2). This permeable solid fraction model gives another degree of freedom, φ_r or n_r, to capture potential impacts of non-uniform porosity and primary particle size distribution on permeability. Unfortunately, we could not predict φ_r independent of Ω. Instead, we inverted our Ω estimates for values of φ_r and n_r that yield a perfect match between Ω theory (Eq. 3, 6, and 13) and observations (Fig. 9a). Figure 9b shows these optimal values of φ_r. In most cases, φ_r is smaller than φ (median φ_r/φ = 0.10; IQR/2 = 0.08). We interpreted this result to indicate that φ_r represents the subset of primary particles that set the main through-flow conduits because not all primary particles contribute to through-flow and drag (see Sect. 6.3 for more discussion). n_r estimates range between 1.06 and 2.79 with a median of 1.53. The fact that all n_r values fall within the

physically meaningful range of 1 to 3 supports using the permeable solid fraction model (Eq. 13) to overcome the assumptions in the Davies model.

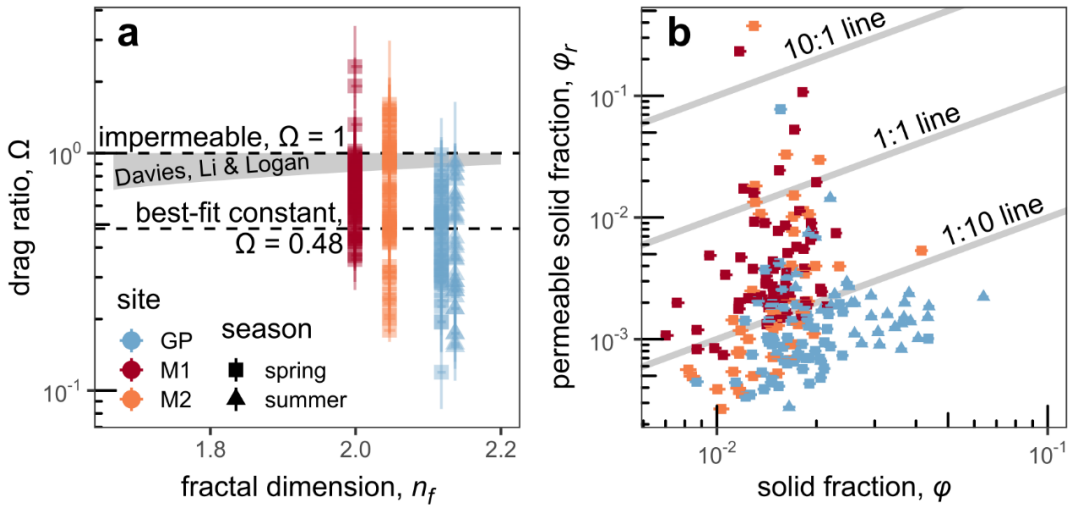

Figure 9: Drag ratio results from combining the explicit model and floc cam-measured floc settling velocity. (a) Fractal dimension and measured drag ratio. The shaded area indicates the field of all possible drag ratios under the Davies model (Eq. 6) and its Li and Logan modification. Drag ratio bars indicate the propagated mean standard error on the background displacement estimate (Sect. 4.4) and propagated 95% bootstrap uncertainty on n_f and D_p. (b) Solid fraction and permeable solid fraction according to the permeable solid fraction model based on the Davies model. Horizontal bars represent the propagated 95% bootstrap uncertainty on n_f and D_p. The legend in panel a applies for all panels.

3.5.8 Floc Settling Velocity

To calculate floc settling velocity distributions, we used the measured n_f, D_p, and Ω in the explicit model to convert the floc size distributions (Sect. 4.6.4). We used a best-fit constant $\Omega = 0.48$ because we only had Ω estimates for the four concentration-depth profiles with paired floc cam measurements (Fig. 9a; Table 2). Median floc settling velocities at the channel sites in spring and summer were ~0.1 to 0.5 mm s^{-1} (Fig. 10a). Island sites had median floc settling velocities of about 0.1 mm s^{-1}, with a substantial fraction of floc settling velocity of order 0.01 mm s^{-1}. No systematic vertical trends in median settling velocity are apparent. Depth-averaged floc settling velocity broadly ranged from ~0.1 to 1 mm s^{-1} (Fig. 10b). Finer floc sizes (Fig. 7c), despite larger bulk solid fractions (Fig. 7e), in the island caused slower floc settling velocity in the island compared to that in the channels (Fig. 10b).

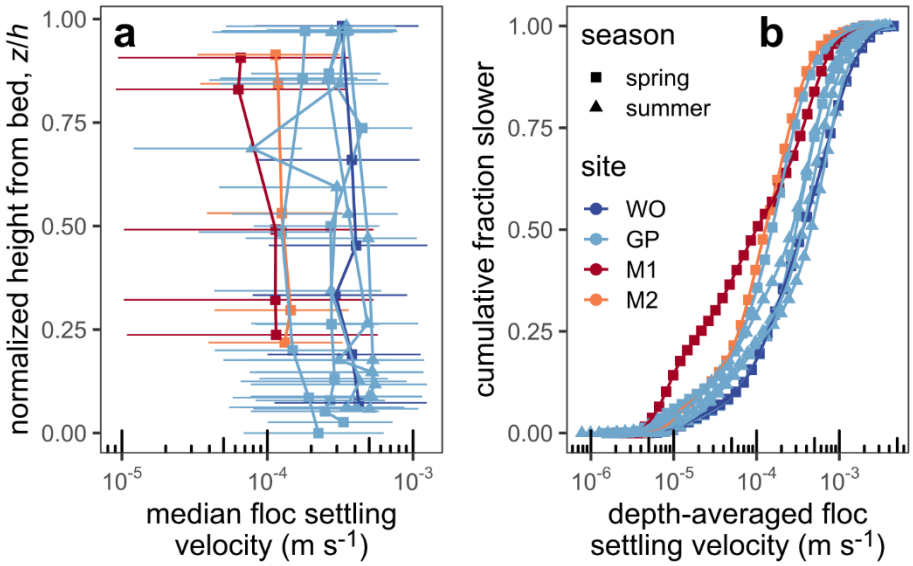

Figure 10: Floc settling velocity results. (a) Profiles of median floc settling velocity. Horizontal bars represent the span of the 0.16 and 0.84 quantile floc settling velocities. (b) Cumulative distribution functions of depth-averaged floc settling velocity. The legend in panel b applies for all panels.

3.5.9 Validating the Explicit Model

We compared Rouse-estimated floc settling velocities (Sect. 4.5) and explicit model predictions as an integrated test of the estimated n_f, D_p (Sect. 5.6), and Ω (Sect. 5.7) because these settling velocity estimates are independent. Figure 11 shows that Rouse-estimated floc settling velocity displays a linear trend with the median from the explicit model albeit with some scatter largely from the non-GP sites. Although we assumed a floc diffusivity ratio, β_{fl}, of unity to calculate the Rouse-estimated floc settling velocities (Sect. 4.5), the data indicate that $\beta_{fl} = 0.65$ optimizes the correlation between the settling velocities. $\beta_{fl} = 0.65$ is realistic because it falls within the ranges of previously estimated diffusivity ratios (Nghiem et al., 2022) and diffusivity ratio models (e.g., De Leeuw et al., 2020). As a result, we concluded that the Rouse-estimated settling velocity validates well our explicit model parameter estimates.

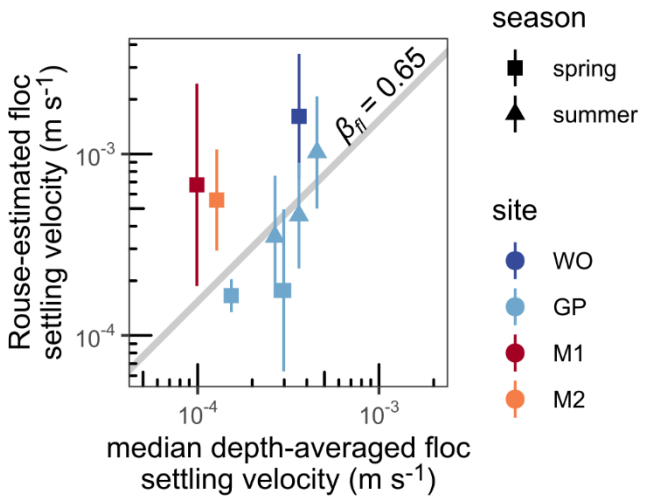

Figure 11: Rouse-estimated floc settling velocity, using $\beta_{fl} = 1$, and median depth-averaged floc settling velocity computed using estimates of n_f, D_p, and Ω in the explicit model. $\beta_{fl} = 0.65$ indicates the best-fit floc diffusivity ratio. Vertical bars indicate the 95% confidence interval on shear velocity (Sect. 4.1) and standard deviation of Rouse-estimated floc settling velocity (Sect. 4.5).

3.5.10 Validating the Semi-Empirical Model

Figure 12 shows the validation of the semi-empirical model. We compared the semi-empirical model predictions (Eq. 7; Nghiem et al., 2022) and the observed floc cutoff diameter (sediment concentration-depth profiles, Rouse-Vanoni theory; Sect. 4.5), floc settling velocity (floc cam, Sect. 4.4; LISST combined with sediment sample data, Sect. 4.6.4), and floc diameter (LISST combined with sediment sample data; Sect. 4.6.1). We used the median of the depth-averaged distribution for floc settling velocity and floc diameter in the comparison because the semi-empirical model was calibrated on depth-averaged data (Nghiem et al., 2022). The semi-empirical model predicts the floc cutoff diameter well within a factor of ~2 of measurements and captures the overall data trend (Fig. 12a). Floc settling velocity predictions of the semi-empirical model agree well in a factor of 2 with the floc cam and LISST-based floc settling velocity measurements (Fig. 12b). Since we used the explicit model to calculate floc settling velocity distribution (Sect. 4.6.4), Fig. 12b also confirms the consistency between the semi-empirical and explicit models. The floc diameter results indicate that the semi-empirical model predicts adequately within a factor of 2, albeit with a limited number of data points (Fig. 12c). The reasonable performance of the semi-empirical model against direct measurements in WLD validates the model.

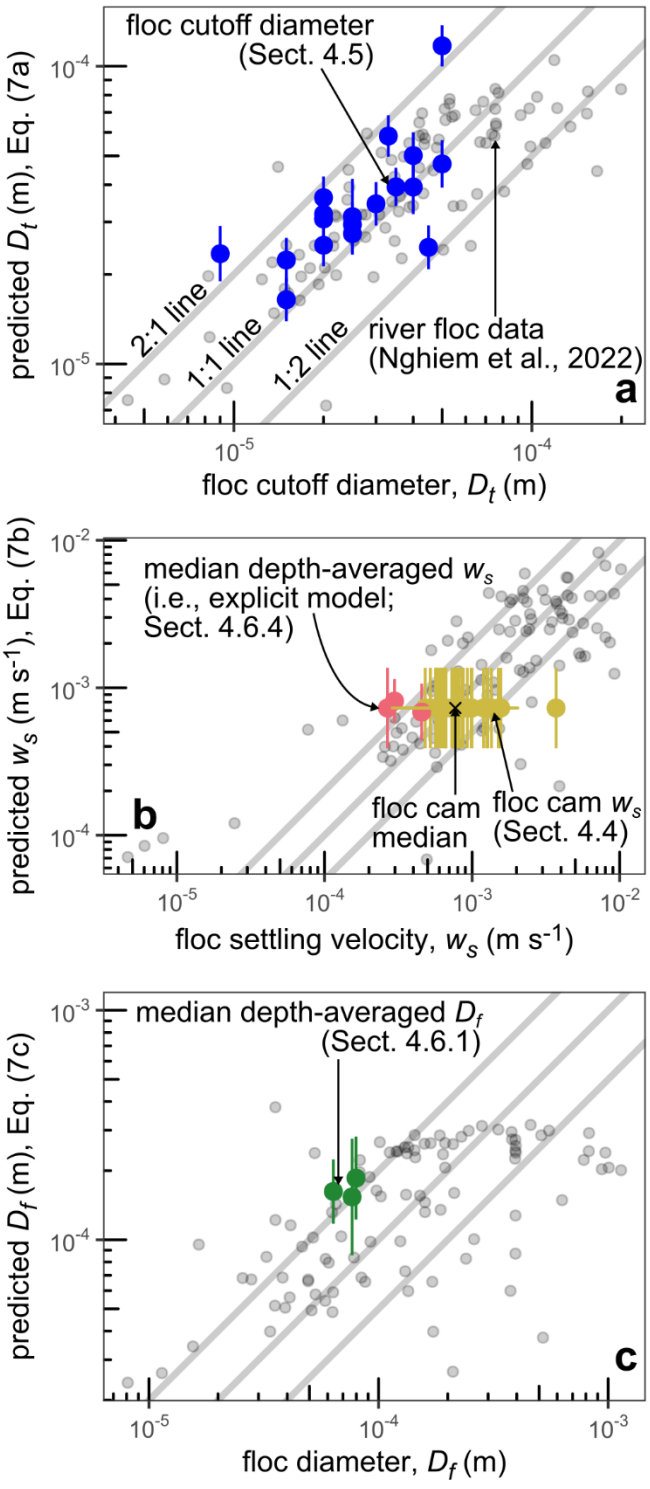

Figure 12: Measured and semi-empirical model predictions of (a) floc cutoff diameter (Eq. 7a), (b) floc settling velocity (Eq. 7b), and (c) floc diameter (Eq. 7c). Gray points are the river floc data that Nghiem et al. (2022) used to calibrate the semi-empirical

model. Vertical bars represent the 95% confidence interval of predictions. The floc cam data have the same predicted floc settling velocity because they represent a single floc cam deployment. Data for which water chemistry was not measured are omitted because they lack semi-empirical model predictions, which explains the absence of floc cam data in panel c.

To demonstrate environmental effects on flocculation, we followed Nghiem et al. (2022) and plotted the predictors in the semi-empirical model against the floc cutoff diameter (normalized to remove the effects of other variables and by the median) because the floc cutoff diameter model (Eq. 7a) displays the best correlation with measurements (Fig. 12). We expect similar patterns for floc settling velocity and diameter because the floc variables correlate with each other (Nghiem et al., 2022). Turbulence, through the Kolmogorov microscale, limits floc size and settling velocity (Fig. 13a; Fig. 7d) because the semi-empirical model assumes that floc growth and breakage rates are balanced (Nghiem et al., 2022). As depth-averaged median primary particle diameter increases, coarser and faster settling grains can be added to flocs (Fig. 13b). Higher sediment concentration enhances flocculation by increasing particle collision rate (Fig. 13c). The effect of organic matter, as quantified by the organic cover fraction, θ, promotes flocculation at low values, but is predicted to have an opposite effect once $\theta > 0.5$ because high organic coverage stabilizes sediment surfaces from aggregation (Fig. 13d). Sediment Al/Si and relative charge density, Φ, vary inversely with floc properties because they might preferentially cause clay flocculation and exclude faster settling silt grains from flocs (Fig. 13ef). These trends for WLD are similar to those found for global rivers (Nghiem et al., 2022).

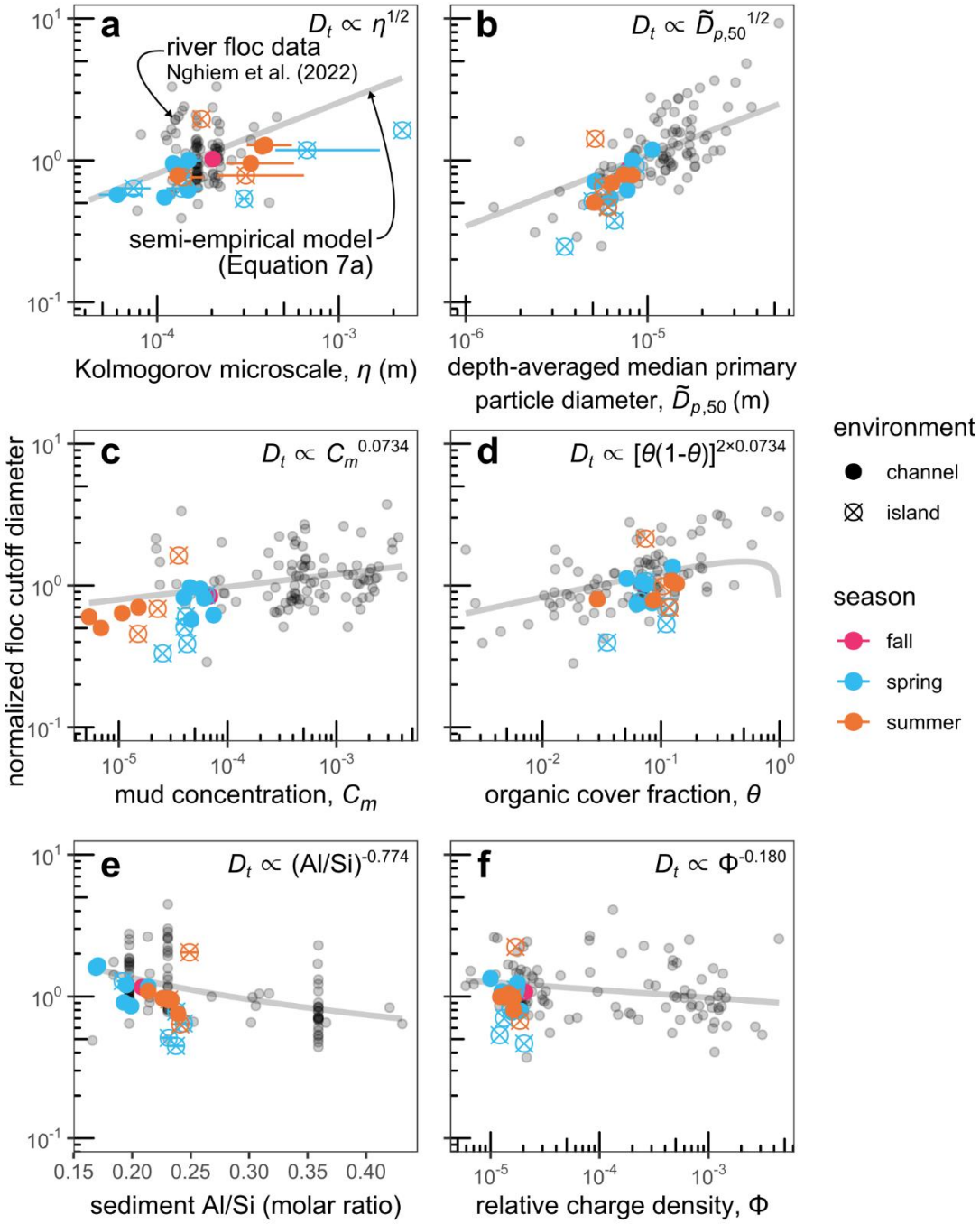

Figure 13: Semi-empirical model predictors plotted against floc cutoff diameter, D_t, normalized by the effects of all other predictors in the floc model (Eq. 7a). Gray curves indicate the model prediction. Horizontal bars indicate the (a) 95% confidence interval on shear velocity, (d) 1-σ error on percent weight organic carbon, or (e) 95% confidence interval on Al/Si estimates.

3.6 Discussion

3.6.1 Leveraging Multiple Floc Data Sources

By combining three floc data sources (in situ laser diffraction, camera, sediment concentration-depth profiles), we overcame the limitations of the individual data sources and derived a nearly complete accounting of floc properties, including floc diameter, solid fraction, floc settling velocity, fractal dimension, effective primary particle diameter, and drag ratio. In situ laser diffraction data alone are limited because they record a mixture of flocs and unflocculated sediment grains (e.g., Livsey et al., 2022). We developed a technique to isolate floc concentration and size distribution by separating flocs and unflocculated grains (Fig. 4) using in situ laser diffraction data and sediment concentration-depth profiles (Sect. 4.6.1). From this technique, we also computed primary particle concentration and size distribution and floc bulk solid fraction (i.e., ratio of primary particle and floc concentrations).

In past studies, a key knowledge gap was the role of effective primary particle diameter and drag ratio on floc settling velocity in the explicit model (e.g., Strom and Keyvani, 2011) because camera-measured floc diameter and settling velocity data alone were insufficient to separate those variables. We leveraged floc size distribution and bulk solid fraction to compute fractal dimension and effective primary particle diameter (Sect. 4.6.2). With an independent estimate of effective primary particle diameter, we could then use fractal dimension and floc cam-measured floc diameter and settling velocity to estimate drag ratio (Sect. 4.6.3). Our ability to disentangle effective primary particle diameter and drag ratio thus paved the way to test theory.

Although our data synthesis proved successful at furnishing many floc properties and holds good potential for future field studies, it still has limitations. We could only estimate a single effective primary particle diameter for each floc size distribution, but the effective primary particle diameter might vary within the floc size distribution especially at the fine tail where floc and effective primary particle diameters might be on a similar scale. There is some uncertainty combining LISST and suspended sediment sample data. We assumed that they measured statistically equivalent material because they did not strictly measure the exact same material. We assumed that all sediment finer than the floc cutoff diameter was flocculated across the water column (Sect. 4.5), but some fraction of this sediment could actually be unflocculated. We could not determine this fraction with our data.

3.6.2 Predicting Floc Settling Velocity

The explicit and semi-empirical floc settling velocity models are consistent with each other (Fig. 12b), indicating that model choice depends on the scale of interest and data availability. The explicit model is at the scale of the individual floc whereas the semi-empirical model is depth-averaged. We were able to compare the models because the depth-averaged floc settling velocity distributions represent a depth-averaging of the

explicit model, which was used to calculate floc settling velocity distributions (Sect. 4.6.4). The semi-empirical model has the advantage of relying on geochemical data that can be easier to measure compared to the floc parameters in the explicit model.

Although we used joint camera, in situ particle sizing, and suspended sediment concentration and grain size distribution profiles to constrain effective primary particle diameter and drag ratio in the explicit model, we suggest that the explicit model can still be used to predict floc settling velocity given only suspended sediment grain size distribution and floc diameter (e.g., through camera or in situ particle sizing data). The primary particle size distribution can be obtained from the suspended sediment grain size distribution by choosing a floc cutoff diameter (in the range of ~10 to 50 μm; Nghiem et al., 2022) and removing coarser sediment from the distribution (Sect. 4.6.1). The fractal dimension of natural flocs can be assumed to be 2 (Winterwerp, 1998). The fractal dimension and primary particle size distribution feed into Eq. (5) with $n_w = 0$ to predict effective primary particle diameter. Predicting drag ratio remains a challenge because prior analytical permeability models were inconsistent with our drag ratio estimates (Fig. 9a). Ω can be constrained based on additional field measurements, as done here, or left as a tuning parameter.

The semi-empirical model predicts floc cutoff diameter, diameter, and settling velocity as a function of water chemistry, organic matter, sediment mineralogy and concentration, and turbulence in the absence of a purely mechanistic theory to link these factors. The full unsteady form of the semi-empirical model, along with existing dynamic flocculation models (e.g., Xu et al., 2008; Son and Hsu, 2011; Shen et al., 2018), can be used to predict floc settling velocity through time and space in a sediment transport model. However, this approach can be computationally expensive and require parameters that are difficult to constrain. Our analysis suggests the assumption of local equilibrium is a reasonable simplification to predict floc properties because our observations are consistent with the equilibrium semi-empirical model (Fig. 12). This fact implies that flocs quickly adjust to their local conditions, a behavior that has some experimental evidence (Tran et al., 2018). In fact, we suggest that using a single constant floc settling velocity for the mud settling velocity (Roberts et al., 2000; Braat et al., 2017) might be reasonable in alluvial channels because tradeoffs between turbulence, sediment concentration, and primary particle size and mineralogy might offset each other (Sect. 6.4).

3.6.3 Role of Effective Primary Particle Diameter and Drag Ratio on Floc Settling Velocity

Our results indicate that the effective primary particle diameter best follows the number-weighted fractal D_p model (Eq. 5 with $n_w = 0$; Fig. 8b). In contrast, the volume-weighted fractal D_p ($n_w = 3$) is biased high compared to measured D_p. Regardless of n_w, the fractal D_p model (Eq. 5) ensures that the effective primary particles occupy the same n_f-dimensional space as the original primary particles. The choice of n_w relies on the relevant physical dimension (Bushell and Amal, 2000). The number-weighted version ($n_w = 0$)

indicates that the number of effective primary particles matches the number of original primary particles in the floc under fractal theory (Bushell and Amal, 2000). On the other hand, $n_w = 3$ means that the total primary particle volume is conserved. The fact that the number-weighted fractal D_p outperforms the volume-weighted version implies that conserving the number of primary particles, rather than the primary particle volume, is critical for the effective primary particle diameter. This conclusion is counterintuitive because we calculated D_p using fractal theory for solid fraction (Eq. 9), which is a volume-based metric. However, the number of primary particles might be more important because the fractal solid fraction theory (Eq. 2) assumes that the number of primary particles follows fractal scaling (Kranenburg, 1994). In contrast, past work treated D_p as an average length scale of primary particles (Syvitski et al., 1995; Strom and Keyvani, 2011). If one assumed D_p is the volumetric median, then one would overestimate the solid fraction and floc settling velocity by a factor dependent on the fractal dimension (Eq. 1 and 2). In our data, this factor ranges from ~1.7 to 15 and has a median of 3.3.

We used a new permeable solid fraction model to determine the physical reason our drag ratio estimates are incompatible with existing permeability models. Natural flocs are distinct because they have non-uniform porosity (Eq. 2) and a primary particle size distribution. These features probably caused the much smaller drag ratios (higher permeability) than could be predicted by prior permeability models (Fig. 9a). The Li and Logan strategy attempts to account for non-uniform porosity by replacing the effective primary particle diameter with a larger cluster diameter representing the clusters that form the main flow paths through the floc. However, this approach is very limited, as recognized by Kim and Stolzenbach (2002). The increase in permeability caused by the Li and Logan modification is small because an effective increase in the solid fraction partially offsets larger pores caused by primary particle clustering. Kim and Stolzenbach (2002) found that the original Davies model (Eq. 6) performed well at predicting the hydrodynamic drag on fractal aggregates with non-uniform porosity, suggesting that the Davies model is suitable for flocs in contrast to our findings (Fig. 9a). If non-uniform porosity caused by fractal structure is not the source of the discrepancy between our drag ratio estimates and the Davies model, then it is likely the primary particle size distribution because Kim and Stolzenbach (2002) did not test aggregates containing many primary particle sizes. The permeable solid fraction model offers a physical explanation because the permeable solid fraction is, on average, 10% of the true solid fraction (Fig. 9b). This result suggests that a subset of the primary particles composes the portion of the floc structure (characterized by the permeable fractal dimension) responsible for conducting flow through the floc. The rest of the primary particles might be shielded from the flow because of their configuration with respect to adjacent larger particles and do not contribute to permeability. The configuration of organic matter within flocs might also affect permeability by controlling flow paths. It is difficult to study all these effects because the complete floc structure must be known, but recent advances in 3-D floc imaging might facilitate more detailed studies (Lawrence et al., 2022; Lawrence et al., 2023).

Although the drag ratio estimates depend on the assumed floc shape, floc shape is not responsible for the inability of existing permeability models to reproduce the drag ratio. Floc shape affects the shape factor, b_1, in the explicit model. Larger values of b_1 cause smaller drag ratio estimates (Sect. 4.6.3). Stokes law shows that $b_1 = 18$ (Stokes, 1851) for an impermeable sphere ($\Omega = 1$). Strom and Keyvani (2011) suggested that $b_1 \sim 20$ is suitable for flocs with $n_f < 2$, but $b_1 = 120$ for flocs with $n_f \geq 2.5$. Regardless of the precise value of b_1, particle shape effects only cause $b_1 > 18$ because shape irregularities induce more drag (McNown and Malaika, 1950; Dietrich, 1982). We used a relatively low value of $b_1 = 20$ (Ferguson and Church, 2004) to calculate the drag ratio. Higher b_1 would only further amplify floc permeability and widen the discrepancy with theory.

3.6.4 Environmental Controls on Flocculation

The semi-empirical model trends in Fig. 13 show the major environmental controls on flocs in WLD and globally. However, these variables are not independent. We hypothesize that turbulence causes correlation and feedbacks between these factors through sediment entrainment and settling dynamics in alluvial systems. To test this hypothesis, Figure 14 compares Kolmogorov microscale, which scales inversely with turbulence intensity, and semi-empirical model parameters. For rivers and WLD channels, Kolmogorov microscale correlates with finer primary particle diameter and higher Al/Si because more turbulent flows (smaller microscale and higher shear velocity) entrain and suspend coarser sediment (Fig. 14ab). Coarser primary particles have distinct mineralogy (lower Al/Si) than finer grains. Higher mud concentration corresponds to smaller Kolmogorov microscale because higher fluid stress entrains more sediment from the bed (Fig. 14c). Flows with higher turbulent energy can also maintain faster-settling flocs, if conditions permit their formation, in the water column (Eq. 8; Dunne et al., 2024). All else equal, these interactions indicate that higher turbulence intensity correlates with larger floc cutoff diameter, faster floc settling velocity, and larger floc diameter (Eq. 7) in alluvial channels. However, increases in turbulence intensity offset these effects because they cause floc breakage at equilibrium, leading to a negative feedback. These patterns are not evident in the WLD island because variables are poorly correlated with Kolmogorov microscale (Fig. 14) potentially owing to more complicated two-dimensional and unsteady effects on sediment transport (Geleynse et al., 2015; Bevington et al., 2017).

We argue that turbulence is the overriding variable controlling flocculation in global rivers and the channels of WLD because it not only directly affects particle collisions, floc breakage (Winterwerp, 1998), and flow competence with respect to flocs, but also sets concentration and primary particle size and mineralogy. The negative feedback demonstrates that flocculation can buffer partially against spatiotemporal changes in turbulence, a mechanism that might explain observations of limited floc settling velocity variation (~0.2 to 0.6 mm s^{-1}) across seasons in the Mississippi River (Osborn et al., 2023) and, more broadly, the limited global variation of ~0.1 to 1 mm s^{-1} (e.g., Hill et al., 2000; Mikkelsen et al., 2007; Nghiem et al., 2022).

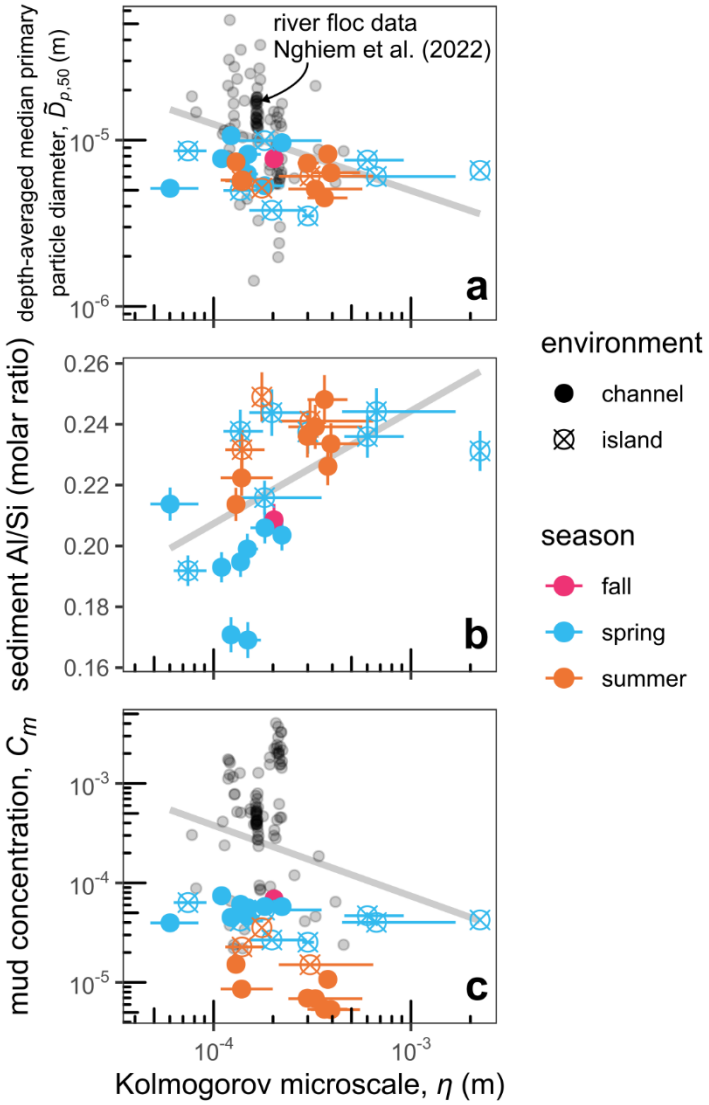

Figure 14: Kolmogorov microscale and (a) depth-averaged median primary particle diameter, (b) sediment Al/Si, and (c) mud volume concentration. In each panel, the gray line indicates the trend line. Horizontal error bars indicate the 95% confidence interval on shear velocity. In panel b, vertical error bars indicate the 95% confidence interval on Al/Si estimates. River floc data are omitted in panel b because most Al/Si data compiled by Nghiem et al. (2022) were not concurrent with the sediment concentration-depth profile and hydrodynamic surveys.

In contrast to the other semi-empirical model inputs, organic cover fraction and relative charge density vary less and are not responsible for the bulk of the variability in floc parameters (Fig. 13). This does not imply that they are unimportant for flocculation. Instead, we propose that they are allogenic catchment-wide controls on flocculation and vary over longer time scales. For example, tectonic activity and climate change can alter

biological productivity and chemical weathering intensity on the catchment scale (Geider et al., 2001; West et al., 2005), altering the organic cover fraction and relative charge density through changes in organic carbon loading on sediment and water chemistry (e.g., Galy et al., 2008). These effects are not directly linked to turbulence feedbacks, implying that they can cause persistent changes in floc properties that are not simultaneously offset. In fact, organic matter might modulate turbulence and force a positive feedback that increases floc size and settling velocity because biological cohesion can limit bedform size and hence reduce the turbulent shear (i.e., increase Kolmogorov microscale) associated with bedforms (Malarkey et al., 2015; Parsons et al., 2016). In contrast, Kolmogorov microscale, sediment concentration, Al/Si, and primary particle size vary autogenically on shorter flood-to-seasonal discharge time scales because they adjust together in response to discharge and sediment dynamics within the alluvial system (e.g., Phillips et al., 2022).

3.7 Conclusion

Flocculation controls the transport and distribution of mud across rivers and wetlands by increasing the effective mud settling velocity. To test theory controlling floc settling velocity, we combined multiple floc data sources—a camera, in situ LISST particle size and concentration, and sediment concentration-depth profiles—in the freshwater Wax Lake Delta, LA. We not only calculated commonly constrained floc properties like diameter, settling velocity, and fractal dimension, but also made novel field measurements. Key advances of the data synthesis include isolating floc concentration and size distribution in in situ laser diffraction data and computing hitherto poorly constrained variables: effective primary particle diameter and drag ratio. We observed flocs in WLD with median diameters of 30 to 90 μm, bulk solid fraction of 0.05 to 0.3, and settling velocities on the order of 0.1 to 1 mm s^{-1} with little vertical variation. Flocs included grains up to 10 to 55 μm in diameter. Flocs in channels tended to be larger and lighter, while flocs in an island wetland tended to be smaller and denser. On average, floc diameter and settling velocity were an order-of-magnitude larger than those of primary particles. We used this data to validate and calibrate an explicit floc settling velocity model based on Stokes law and a semi-empirical model, which relies on hydrodynamic and geochemical data.

Using the new complete dataset of floc attributes, we tested theory for two key unknowns, effective primary particle diameter and drag ratio, in the explicit model. Effective primary particle diameter varied between 1 and 3 μm and had a typical value of 2 μm. We verified a fractal model for effective primary particle diameter that conserves the number and fractal space of the original primary particles (Fig. 8b), demonstrating that the effective primary particle diameter is not a simple characteristic length scale (i.e., median) as previous studies assumed. The volumetric median primary particle diameter systematically overestimates the effective primary particle diameter by an average factor of 2 and up to a factor of 6, leading to overestimates of floc solid fraction and settling velocity. Floc permeability, quantified by the drag ratio, has been little explored for natural flocs. The mean drag ratio was 0.48, but drag ratio ranged between 0.15 and 1 (Fig. 9a). These drag ratios indicate

enhanced floc settling velocity by a mean factor of 2 and up to a factor of 7. The drag ratio estimates do not conform to prior permeability theory because the theory does not consider a primary particle size distribution. Instead, a new permeable solid fraction model suggests that only some primary particles are relevant for permeability because primary particle size interactions might shield other primary particles from the main flow paths (Fig. 9b).

We tested the semi-empirical model for the first time using direct measurements of flocs. Our data validate the semi-empirical model because it predicts floc cutoff diameter, floc settling velocity, and floc diameter all within a factor of 2 of the measured field data. We also showed that its floc settling velocity predictions are consistent with those of the explicit model. The semi-empirical model reveals that turbulence, sediment concentration and mineralogy, organic matter, and water chemistry control flocculation in WLD and suggests that flocs can be reasonably modeled in local equilibrium. Results indicate that turbulence controls a negative feedback on floc settling velocity because higher turbulence intensity causes higher sediment concentration, lower Al/Si (a sediment mineralogy proxy), and higher primary particle diameter through sediment entrainment dynamics (Sect. 6.4). These factors correlate with faster floc settling velocity, but are offset by shear breakage of flocs. This feedback might mitigate changes in floc settling velocity in alluvial channels on the flood and seasonal time scales over which flow turbulence typically varies. Organic matter binding and sediment surface charge interactions might affect flocculation at longer time scales because they are set by allogenic catchment-to-continental scale processes like biological productivity and chemical weathering of rock. Overall, the semi-empirical and explicit models are both viable options for predicting floc settling velocity in rivers and freshwater wetlands but require knowledge of different predictors and operate at different scales.

Finally, we emphasize that the workflow of combining multiple floc methods (camera, in situ laser diffraction, sediment concentration-depth profiles) presented in this study is a powerful tool that can provide a more complete description of flocs than previously done with only one or two of the individual methods.

3.8 Notation

Al/Si	Sediment Al-Si molar ratio
b_1	Settling velocity model constant (20), dimensionless
C_{fl}	Floc volume concentration, dimensionless
C_i	Sediment volume concentration for *i*th grain size class, dimensionless
C_{bi}	Near-bed sediment volume concentration for *i*th grain size class, dimensionless

C_m	Depth-averaged mud volume concentration, dimensionless
D_c	Cluster diameter, m
D_f	Floc diameter, m
$D_{f,50}$	Median floc diameter, m
D_p	Effective primary particle diameter, m
$D_{p,50}$	Median primary particle diameter, m
$\widetilde{D}_{p,50}$	Depth-averaged median primary particle diameter, m
D_t	Floc cutoff diameter, m
g	Gravitational acceleration (9.81), m s^{-2}
h	Local water depth, m
h_b	Near-bed height ($0.1h$), m
k	Floc permeability, m^2
n_f	Floc fractal dimension, dimensionless
n_r	Permeable fractal dimension, dimensionless
n_w	Weighting dimension, dimensionless
p_i	Rouse number for *i*th grain size class, dimensionless
R_s	Submerged specific gravity of sediment (1.65), dimensionless
u_*	Shear velocity, m s^{-1}
w_s	Floc settling velocity, m s^{-1}
w_{si}	In situ particle settling velocity for *i*th grain size class, m s^{-1}
β	Sediment diffusivity ratio, dimensionless
β_{fl}	Floc diffusivity ratio, dimensionless

η	Kolmogorov microscale, m
θ	Organic cover fraction, dimensionless
κ	Von Kármán constant (0.41), dimensionless
ν	Kinematic viscosity of water (10^{-6}), $m^2\ s^{-1}$
ξ^{-2}	Dimensionless floc permeability, dimensionless
ρ	Water density (1000), kg m^{-3}
ρ_s	Sediment density (2650), kg m^{-3}
Φ	Relative charge density, dimensionless
φ	Floc solid fraction, dimensionless
$\bar{\varphi}$	Bulk floc solid fraction, dimensionless
φ_r	Permeable solid fraction, dimensionless
Ω	Drag ratio, dimensionless

3.9 Data availability

Sediment sample grain size distribution data are available online in the NASA Delta-X data repository at https://daac.ornl.gov/cgi-bin/dataset_lister.pl?p=41. The remainder of the data is available online at https://doi.org/10.22002/w4ave-nrg52.

3.10 Author contribution

JAN and MPL conceived the study. JAN, GKL, JPH, GS, CGF, and MPL collected samples and made measurements in the field. JAN, GKL, and GS analyzed samples in the lab. JAN analyzed data and wrote the original paper with supervision by MPL. All authors contributed to data interpretation, review, and editing.

3.11 Acknowledgements

The NASA Delta-X project is funded by the Science Mission Directorate's Earth Science Division through the Earth Venture Suborbital-3 Program NNH17ZDA001N-EVS3. JAN acknowledges funding from NASA FINESST Grant 80NSSC20K1645. The authors thank Mathieu Dellinger and Amanda Hayton for conducting the ion chromatography at Durham University. We thank Sijia Dong for measuring DIC concentrations. We thank Claire

Bucholz, Youli Li, Juliet Ryan-Davis, and Miguel Zepeda-Rosales for assistance with XRF analysis. We thank John Bourg, Madison Douglas, Paola Passalacqua, Eric Prokocki, Maryn Sanders, Adam Songy, Kyle Wright, and Caltech's fall 2019 Ge 121a class for field assistance.

3.12 References

Agrawal, Y. C. and Pottsmith, H. C.: Instruments for particle size and settling velocity observations in sediment transport, Marine Geology, 168, 89–114, https://doi.org/10.1016/S0025-3227(00)00044-X, 2000.

Agrawal, Y. C., Whitmire, A., Mikkelsen, O. A., and Pottsmith, H. C.: Light scattering by random shaped particles and consequences on measuring suspended sediments by laser diffraction, Journal of Geophysical Research: Oceans, 113, https://doi.org/10.1029/2007JC004403, 2008.

Baptist, M. J., Babovic, V., Rodríguez Uthurburu, J., Keijzer, M., Uittenbogaard, R. E., Mynett, A., and Verwey, A.: On inducing equations for vegetation resistance, Journal of Hydraulic Research, 45, 435–450, https://doi.org/10.1080/00221686.2007.9521778, 2007.

Benson, T. and French, J. R.: InSiPID: A new low-cost instrument for in situ particle size measurements in estuarine and coastal waters, Journal of Sea Research, 58, 167–188, https://doi.org/10.1016/j.seares.2007.04.003, 2007.

Bevington, A. E., Twilley, R. R., Sasser, C. E., and Holm Jr, G. O.: Contribution of river floods, hurricanes, and cold fronts to elevation change in a deltaic floodplain, northern Gulf of Mexico, USA, Estuarine, Coastal and Shelf Science, 191, 188–200, https://doi.org/10.1016/j.ecss.2017.04.010, 2017.

Blair, N. E. and Aller, R. C.: The Fate of Terrestrial Organic Carbon in the Marine Environment, Annual Review of Marine Science, 4, 401–423, https://doi.org/10.1146/annurev-marine-120709-142717, 2012.

Blum, M. D. and Roberts, H. H.: Drowning of the Mississippi Delta due to insufficient sediment supply and global sea-level rise, Nature Geoscience, 2, 488–491, https://doi.org/10.1038/NGEO55, 2009.

Bouchez, J., Galy, V., Hilton, R. G., Gaillardet, J., Moreira-Turcq, P., Pérez, M. A., France-Lanord, C., and Maurice, L.: Source, transport and fluxes of Amazon River particulate organic carbon: Insights from river sediment depth-profiles, Geochimica et Cosmochimica Acta, 133, 280–298, https://doi.org/10.1016/j.gca.2014.02.032, 2014.

Braat, L., van Kessel, T., Leuven, J. R., and Kleinhans, M. G.: Effects of mud supply on large-scale estuary morphology and development over centuries to millennia, Earth Surface Dynamics, 5, 617–652, https://doi.org/10.5194/esurf-5-617-2017, 2017.

Brinkman, H. C.: A calculation of the viscous force exerted by a flowing fluid on a dense swarm of particles, Applied Scientific Research, A1, 27–34, https://doi.org/10.1007/BF02120313, 1947.

Bushell, G. and Amal, R.: Fractal aggregates of polydisperse particles, Journal of colloid and interface science, 205, 459–469, https://doi.org/10.1006/jcis.1998.5667, 1998.

Bushell, G. and Amal, R.: Measurement of fractal aggregates of polydisperse particles using small-angle light scattering, Journal of colloid and interface science, 221, 186–194, https://doi.org/10.1006/jcis.1999.6532, 2000.

Carstens, M. R.: Accelerated motion of a spherical particle, Eos, Transactions American Geophysical Union, 33, 713–721, https://doi.org/10.1029/TR033i005p00713, 1952.

Chase, R. R.: Settling behavior of natural aquatic particulates, Limnology and Oceanography, 24, 417–426, https://doi.org/10.4319/lo.1979.24.3.0417, 1979.

Cohen, S., Syvitski, J., Ashley, T., Lammers, R., Fekete, B., and Li, H.-Y.: Spatial trends and drivers of bedload and suspended sediment fluxes in global rivers, Water Resources Research, 58, e2021WR031583, https://doi.org/10.1029/2021WR031583, 2022.

Craig, M. J., Baas, J. H., Amos, K. J., Strachan, L. J., Manning, A. J., Paterson, D. M., Hope, J. A., Nodder, S. D., and Baker, M. L.: Biomediation of submarine sediment gravity flow dynamics, Geology, 48, 72–76, https://doi.org/10.1130/G46837.1, 2020.

Csanady, G. T.: Turbulent diffusion of heavy particles in the atmosphere, Journal of Atmospheric Sciences, 20, 201–208, https://doi.org/10.1175/1520-0469(1963)020%3C0201:TDOHPI%3E2.0.CO;2, 1963.

Davies, C. N.: The separation of airborne dust and particles, Proceedings of the Institution of mechanical engineers, 167, 185–213, https://doi.org/10.1177/002034835316701b13, 1953.

De Leeuw, J., Lamb, M. P., Parker, G., Moodie, A. J., Haught, D., Venditti, J. G., and Nittrouer, J. A.: Entrainment and suspension of sand and gravel, Earth Surface Dynamics, 8, 485–504, https://doi.org/10.5194/esurf-8-485-2020, 2020.

Deng, Z., He, Q., Manning, A. J., and Chassagne, C.: A laboratory study on the behavior of estuarine sediment flocculation as function of salinity, EPS and living algae, Marine Geology, 459, 107029, https://doi.org/10.1016/j.margeo.2023.107029, 2023.

Derjaguin, B. V. and Landau, L.: Theory of the stability of strongly charged lyophobic sol and of the adhesion of strongly charged particles in solutions of electrolytes, Acta Physico Chimica URSS, 14, 633, 1941.

Dietrich, W. E.: Settling velocity of natural particles, Water Resources Research, 18, 1615–1626, https://doi.org/10.1029/WR018i006p01615, 1982.

Dong, S., Subhas, A. V., Rollins, N. E., Naviaux, J. D., Adkins, J. F., and Berelson, W. M.: A kinetic pressure effect on calcite dissolution in seawater, Geochimica et Cosmochimica Acta, 238, 411–423, https://doi.org/10.1016/j.gca.2018.07.015, 2018.

Douglas, M. M., Li, G. K., Fischer, W. W., Rowland, J. C., Kemeny, P. C., West, A. J., Schwenk, J., Piliouras, A. P., Chadwick, A. J., and Lamb, M. P.: Organic carbon burial by river meandering partially offsets bank-erosion carbon fluxes in a discontinuous permafrost floodplain, Earth Surface Dynamics, 10, 421–435, https://doi.org/10.5194/esurf-10-421-2022, 2022.

Droppo, I. G. and Ongley, E. D.: Flocculation of suspended sediment in rivers of southeastern Canada, Water Research, 28, 1799–1809, https://doi.org/10.1016/0043-1354(94)90253-4, 1994.

Dunne, K. B. J., Nittrouer, J. A., Abolfazli, E., Osborn, R., and Strom, K. B.: Hydrodynamically-driven deposition of mud in river systems, Geophysical Research Letters, 51, e2023GL107174, https://doi.org/10.1029/2023GL107174, 2024.

Dyer, K. R. and Manning, A. J.: Observation of the size, settling velocity and effective density of flocs, and their fractal dimensions, Journal of sea research, 41, 87–95, https://doi.org/10.1016/S1385-1101(98)00036-7, 1999.

Edwards, T. K. and Glysson, G. D.: Field methods for measurement of fluvial sediment, US Geological Survey Denver, CO, 1999.

Eisma, D.: Flocculation and de-flocculation of suspended matter in estuaries, Netherlands Journal of sea research, 20, 183–199, https://doi.org/10.1016/0077-7579(86)90041-4, 1986.

Eisma, D., Cadée, G. C., Laane, R., and Kalf, J.: Preliminary results of AURELIA-and NAVICULA Cruises in the Rhine-and Ems-estuaries, January-February, 1982, Mitteilungen aus dem Geologisch-Paläontologischen Institut der Universität Hamburg, 633–654, 1982.

Ferguson, R. I. and Church, M.: A Simple Universal Equation for Grain Settling Velocity, Journal of Sedimentary Research, 74, 933–937, https://doi.org/10.1306/051204740933, 2004.

Fichot, C. and Harringmeyer, J.: Delta-X: In situ Beam Attenuation and Particle Size from LISST-200X, 2021, ORNL DAAC, https://doi.org/10.3334/ORNLDAAC/2077, 2021.

Galy, V., Beyssac, O., France-Lanord, C., and Eglinton, T.: Recycling of graphite during Himalayan erosion: a geological stabilization of carbon in the crust, Science, 322, 943–945, https://doi.org/10.1126/science.1161408, 2008.

Garcia, M.: Sedimentation Engineering: Processes, Measurements, Modeling, and Practice, https://doi.org/10.1061/9780784408148, 2008.

Geider, R. J., Delucia, E. H., Falkowski, P. G., Finzi, A. C., Grime, J. P., Grace, J., Kana, T. M., La Roche, J., Long, S. P., and Osborne, B. A.: Primary productivity of planet earth: biological determinants and physical constraints in terrestrial and aquatic habitats, Global Change Biology, 7, 849–882, https://doi.org/10.1046/j.1365-2486.2001.00448.x, 2001.

Geleynse, N., Hiatt, M., Sangireddy, H., and Passalacqua, P.: Identifying environmental controls on the shoreline of a natural river delta, Journal of Geophysical Research: Earth Surface, 120, 877–893, https://doi.org/10.1002/2014JF003408, 2015.

Gibbs, R. J.: Estuarine flocs: their size, settling velocity and density, Journal of Geophysical Research: Oceans, 90, 3249–3251, https://doi.org/10.1029/JC090iC02p03249, 1985.

Gmachowski, L.: Mass–radius relation for fractal aggregates of polydisperse particles, Colloids and Surfaces A: Physicochemical and Engineering Aspects, 224, 45–52, https://doi.org/10.1016/S0927-7757(03)00318-2, 2003.

Graf, W. H. and Cellino, M.: Suspension flows in open channels; experimental study, Journal of Hydraulic Research, 40, 435–447, https://doi.org/10.1080/00221680209499886, 2002.

Graham, G. W., Davies, E. J., Nimmo-Smith, W. A. M., Bowers, D. G., and Braithwaite, K. M.: Interpreting LISST-100X measurements of particles with complex shape using digital in-line holography, Journal of Geophysical Research: Oceans, 117, https://doi.org/10.1029/2011JC007613, 2012.

Gregory, J. and Barany, S.: Adsorption and flocculation by polymers and polymer mixtures, Advances in colloid and interface science, 169, 1–12, https://doi.org/10.1016/j.cis.2011.06.004, 2011.

Guo, L. and He, Q.: Freshwater flocculation of suspended sediments in the Yangtze River, China, Ocean Dynamics, 61, 371–386, https://doi.org/10.1007/s10236-011-0391-x, 2011.

Hill, P. S., Milligan, T. G., and Geyer, W. R.: Controls on effective settling velocity of suspended sediment in the Eel River flood plume, Continental Shelf Research, 20, 2095–2111, https://doi.org/10.1016/S0278-4343(00)00064-9, 2000.

Hill, P. S., Voulgaris, G., and Trowbridge, J. H.: Controls on floc size in a continental shelf bottom boundary layer, Journal of Geophysical Research: Oceans, 106, 9543–9549, https://doi.org/10.1029/2000JC900102, 2001.

Holm, G. O. and Sasser, C. E.: Differential salinity response between two Mississippi River subdeltas: implications for changes in plant composition, Estuaries, 24, 78–89, https://doi.org/10.2307/1352815, 2001.

Izquierdo–Ayala, K., Garcia–Aragon, J. A., Castillo–Uzcanga, M. M., and Salinas-Tapia, H.: Freshwater flocculation dependence on turbulence properties in the Usumacinta river, Journal of Hydraulic Engineering, 147, 05021009, https://doi.org/10.1061/(ASCE)HY.1943-7900.0001940, 2021.

Izquierdo-Ayala, K., García-Aragón, J. A., Castillo-Uzcanga, M. M., Díaz-Delgado, C., Carrillo, L., and Salinas-Tapia, H.: Flocculation Patterns Related to Intra-Annual Hydrodynamics Variability in the Lower Grijalva-Usumacinta System, Water, 15, 292, https://doi.org/10.3390/w15020292, 2023.

Jarvis, P., Jefferson, B., and Parsons, S. A.: Measuring floc structural characteristics, Reviews in Environmental Science and Bio/Technology, 4, 1–18, https://doi.org/10.1007/s11157-005-7092-1, 2005.

Jensen, D. J., Cavanaugh, K. C., Thompson, D. R., Fagherazzi, S., Cortese, L., and Simard, M.: Leveraging the historical Landsat catalog for a remote sensing model of wetland accretion in coastal Louisiana, Journal of Geophysical Research: Biogeosciences, 127, e2022JG006794, https://doi.org/10.1029/2022JG006794, 2022.

Johnson, C. P., Li, X., and Logan, B. E.: Settling velocities of fractal aggregates, Environmental science & technology, 30, 1911–1918, https://doi.org/10.1021/es950604g, 1996.

Keyvani, A. and Strom, K.: A fully-automated image processing technique to improve measurement of suspended particles and flocs by removing out-of-focus objects, Computers & Geosciences, 52, 189–198, https://doi.org/10.1016/j.cageo.2012.08.018, 2013.

Kim, A. S. and Stolzenbach, K. D.: The permeability of synthetic fractal aggregates with realistic three-dimensional structure, Journal of colloid and interface science, 253, 315–328, https://doi.org/10.1006/jcis.2002.8525, 2002.

Kranck, K.: The role of flocculation in the filtering of particulate matter in estuaries, The estuary as a filter, 159–175, https://doi.org/10.1016/B978-0-12-405070-9.50014-1, 1984.

Kranck, K. and Milligan, T.: Macroflocs: production of marine snow in the laboratory, Marine Ecology - Progress Series, 3, 19–24, 1980.

Kranenburg, C.: The fractal structure of cohesive sediment aggregates, Estuarine, Coastal and Shelf Science, 39, 451–460, https://doi.org/10.1016/S0272-7714(06)80002-8, 1994.

Krishnappan, B. G.: In situ size distribution of suspended particles in the Fraser River, Journal of Hydraulic Engineering, 126, 561–569, https://doi.org/10.1061/(ASCE)0733-9429(2000)126:8(561), 2000.

Kuprenas, R., Tran, D., and Strom, K.: A Shear-Limited Flocculation Model for Dynamically Predicting Average Floc Size, Journal of Geophysical Research: Oceans, 123, 6736–6752, https://doi.org/10.1029/2018JC014154, 2018.

Lamb, M. P., De Leeuw, J., Fischer, W. W., Moodie, A. J., Venditti, J. G., Nittrouer, J. A., Haught, D., and Parker, G.: Mud in rivers transported as flocculated and suspended bed material, Nature Geoscience, 13, 566–570, https://doi.org/10.1038/s41561-020-0602-5, 2020.

Larsen, L. G., Harvey, J. W., and Crimaldi, J. P.: Morphologic and transport properties of natural organic floc, Water Resources Research, 45, https://doi.org/10.1029/2008WR006990, 2009.

Latimer, R. A. and Schweizer, C. W.: The Atchafalaya River Study: a report based upon engineering and geological studies of the enlargement of Old and Atchafalaya Rivers, 1951.

Lawrence, T. J., Carr, S. J., Wheatland, J. A. T., Manning, A. J., and Spencer, K. L.: Quantifying the 3D structure and function of porosity and pore space in natural sediment flocs, Journal of Soils and Sediments, 22, 3176–3188, https://doi.org/10.1007/s11368-022-03304-x, 2022.

Lawrence, T. J., Carr, S. J., Manning, A. J., Wheatland, J. A. T., Bushby, A. J., and Spencer, K. L.: Functional behaviour of flocs explained by observed 3D structure and porosity, Frontiers in Earth Science, 11, 1264953, https://doi.org/10.3389/feart.2023.1264953, 2023.

Lee, B. J., Kim, J., Hur, J., Choi, I. H., Toorman, E. A., Fettweis, M., and Choi, J. W.: Seasonal Dynamics of Organic Matter Composition and Its Effects on Suspended Sediment

Flocculation in River Water, Water Resources Research, 55, 6968–6985, https://doi.org/10.1029/2018WR024486, 2019.

Li, X. and Logan, B. E.: Collision frequencies of fractal aggregates with small particles by differential sedimentation, Environmental science & technology, 31, 1229–1236, https://doi.org/10.1021/es960771w, 1997.

Li, X.-Y. and Logan, B. E.: Permeability of fractal aggregates, Water research, 35, 3373–3380, https://doi.org/10.1016/S0043-1354(01)00061-6, 2001.

Livsey, D. N., Crosswell, J. R., Turner, R. D. R., Steven, A. D. L., and Grace, P. R.: Flocculation of Riverine Sediment Draining to the Great Barrier Reef, Implications for Monitoring and Modeling of Sediment Dispersal Across Continental Shelves, Journal of Geophysical Research: Oceans, 127, e2021JC017988, https://doi.org/10.1029/2021JC017988, 2022.

Malarkey, J., Baas, J. H., Hope, J. A., Aspden, R. J., Parsons, D. R., Peakall, J., Paterson, D. M., Schindler, R. J., Ye, L., and Lichtman, I. D.: The pervasive role of biological cohesion in bedform development, Nature communications, 6, 6257, https://doi.org/10.1038/ncomms7257, 2015.

Malvern Panalytical: Mastersizer User Guide, 2024.

Manning, A. J., Baugh, J. V., Spearman, J. R., and Whitehouse, R. J.: Flocculation settling characteristics of mud: sand mixtures, Ocean dynamics, 60, 237–253, https://doi.org/10.1007/s10236-009-0251-0, 2010.

Mayer, L. M.: Surface area control of organic carbon accumulation in continental shelf sediments, Geochimica et Cosmochimica Acta, 58, 1271–1284, https://doi.org/10.1016/0016-7037(94)90381-6, 1994.

McCave, I. N.: Size spectra and aggregation of suspended particles in the deep ocean, Deep Sea Research Part A. Oceanographic Research Papers, 31, 329–352, https://doi.org/10.1016/0198-0149(84)90088-8, 1984.

McNown, J. S. and Malaika, J.: Effects of particle shape on settling velocity at low Reynolds numbers, Eos, Transactions American Geophysical Union, 31, 74–82, https://doi.org/10.1029/TR031i001p00074, 1950.

Mehta, A. J. and Partheniades, E.: An investigation of the depositional properties of flocculated fine sediments, Journal of Hydraulic Research, 13, 361–381, https://doi.org/10.1080/00221687509499694, 1975.

Mietta, F., Chassagne, C., Manning, A. J., and Winterwerp, J. C.: Influence of shear rate, organic matter content, pH and salinity on mud flocculation, Ocean Dynamics, 59, 751–763, https://doi.org/10.1007/s10236-009-0231-4, 2009.

Mikkelsen, O. and Pejrup, M.: The use of a LISST-100 laser particle sizer for in-situ estimates of floc size, density and settling velocity, Geo-Marine Letters, 20, 187–195, https://doi.org/10.1007/s003670100064, 2001.

Mikkelsen, O. A., Milligan, T. G., Hill, P. S., and Moffatt, D.: INSSECT—an instrumented platform for investigating floc properties close to the seabed, Limnology and Oceanography: Methods, 2, 226–236, https://doi.org/10.4319/lom.2004.2.226, 2004.

Mikkelsen, O. A., Hill, P. S., Milligan, T. G., and Chant, R. J.: In situ particle size distributions and volume concentrations from a LISST-100 laser particle sizer and a digital floc camera, Continental Shelf Research, 25, 1959–1978, https://doi.org/10.1016/j.csr.2005.07.001, 2005.

Mikkelsen, O. A., Hill, P. S., and Milligan, T. G.: Seasonal and spatial variation of floc size, settling velocity, and density on the inner Adriatic Shelf (Italy), Continental Shelf Research, 27, 417–430, https://doi.org/10.1016/j.csr.2006.11.004, 2007.

Moodie, A. J., Nittrouer, J. A., Ma, H., Carlson, B. N., Wang, Y., Lamb, M. P., and Parker, G.: Suspended-sediment induced stratification inferred from concentration and velocity profile measurements in the lower Yellow River, China, Water Resources Research, e2020WR027192, https://doi.org/10.1029/2020WR027192, 2020.

Neale, G., Epstein, N., and Nader, W.: Creeping flow relative to permeable spheres, Chemical Engineering Science, 28, 1865–1874, https://doi.org/10.1016/0009-2509(73)85070-5, 1973.

Nelson, C. H. and Lamothe, P. J.: Heavy metal anomalies in the Tinto and Odiel river and estuary system, Spain, Estuaries, 16, 496–511, https://doi.org/10.2307/1352597, 1993.

Nezu, I. and Nakagawa, H.: Turbulence in open-channel flows, AA Balkema, Rotterdam, 1–281, 1993.

Nghiem, J., Salter, G., and Lamb, M. P.: Delta-X: Bed and Suspended Sediment Grain Size, MRD, LA, USA, 2021, Version 2, ORNL DAAC, https://doi.org/10.3334/ORNLDAAC/2135, 2021.

Nghiem, J. A., Fischer, W. W., Li, G. K., and Lamb, M. P.: A Mechanistic Model for Mud Flocculation in Freshwater Rivers, Journal of Geophysical Research: Earth Surface, e2021JF006392, https://doi.org/10.1029/2021JF006392, 2022.

Nicholas, A. P. and Walling, D. E.: The significance of particle aggregation in the overbank deposition of suspended sediment on river floodplains, Journal of Hydrology, 186, 275–293, https://doi.org/10.1016/S0022-1694(96)03023-5, 1996.

Osborn, R., Dillon, B., Tran, D., Abolfazli, E., Dunne, K. B., Nittrouer, J. A., and Strom, K.: FlocARAZI: an in-situ, image-based profiling instrument for sizing solid and flocculated suspended sediment, Journal of Geophysical Research: Earth Surface, e2021JF006210, https://doi.org/10.1029/2021JF006210, 2021.

Osborn, R., Dunne, K. B., Ashley, T., Nittrouer, J. A., and Strom, K.: The flocculation state of mud in the lowermost freshwater reaches of the Mississippi River: spatial distribution of sizes, seasonal changes, and their impact on vertical concentration profiles, Journal of Geophysical Research: Earth Surface, e2022JF006975, https://doi.org/10.1029/2022JF006975, 2023.

Özer, M., Orhan, M., and Işik, N. S.: Effect of particle optical properties on size distribution of soils obtained by laser diffraction, Environmental & Engineering Geoscience, 16, 163–173, https://doi.org/10.2113/gseegeosci.16.2.163, 2010.

Parsons, D. R., Schindler, R. J., Hope, J. A., Malarkey, J., Baas, J. H., Peakall, J., Manning, A. J., Ye, L., Simmons, S., and Paterson, D. M.: The role of biophysical cohesion on subaqueous bed form size, Geophysical research letters, 43, 1566–1573, https://doi.org/10.1002/2016GL067667, 2016.

Partheniades, E.: Erosion and deposition of cohesive soils, Journal of the Hydraulics Division, 91, 105–139, https://doi.org/10.1061/JYCEAJ.0001165, 1965.

Phillips, C. B., Masteller, C. C., Slater, L. J., Dunne, K. B., Francalanci, S., Lanzoni, S., Merritts, D. J., Lajeunesse, E., and Jerolmack, D. J.: Threshold constraints on the size, shape and stability of alluvial rivers, Nature Reviews Earth & Environment, 3, 406–419, https://doi.org/10.1038/s43017-022-00282-z, 2022.

Pizzuto, J. E.: Long-term storage and transport length scale of fine sediment: Analysis of a mercury release into a river, Geophysical Research Letters, 41, 5875–5882, https://doi.org/10.1002/2014GL060722, 2014.

Rawle, A. F.: Best practice in laser diffraction–a robustness study of the optical properties of silica, Procedia engineering, 102, 182–189, https://doi.org/10.1016/j.proeng.2015.01.124, 2015.

Roberts, H. H., Adams, R. D., and Cunningham, R. H. W.: Evolution of sand-dominant subaerial phase, Atchafalaya Delta, Louisiana, AAPG Bulletin, 64, 264–279, https://doi.org/10.1306/2F918964-16CE-11D7-8645000102C1865D, 1980.

Roberts, W., Le Hir, P., and Whitehouse, R. J. S.: Investigation using simple mathematical models of the effect of tidal currents and waves on the profile shape of intertidal mudflats, Continental Shelf Research, 20, 1079–1097, https://doi.org/10.1016/S0278-4343(00)00013-3, 2000.

Rommelfanger, N., Vowinckel, B., Wang, Z., Dohrmann, R., Meiburg, E., and Luzzatto-Fegiz, P.: A simple criterion and experiments for onset of flocculation in kaolin clay suspensions, arXiv preprint arXiv:2203.15545, https://doi.org/10.48550/arXiv.2203.15545, 2022.

Rouse, H.: Modern conceptions of the mechanics of fluid turbulence, Transactions of the American Society of Civil Engineers, 102, 463–505, https://doi.org/10.1061/TACEAT.0004872, 1937.

Schindler, R. J., Parsons, D. R., Ye, L., Hope, J. A., Baas, J. H., Peakall, J., Manning, A. J., Aspden, R. J., Malarkey, J., and Simmons, S.: Sticky stuff: Redefining bedform prediction in modern and ancient environments, Geology, 43, 399–402, https://doi.org/10.1130/G36262.1, 2015.

Sequoia Scientific: LISST-200X Particle Size Analyzer User's Manual, 2022.

Shen, X., Lee, B. J., Fettweis, M., and Toorman, E. A.: A tri-modal flocculation model coupled with TELEMAC for estuarine muds both in the laboratory and in the field, Water research, 145, 473–486, https://doi.org/10.1016/j.watres.2018.08.062, 2018.

Smellie, R. H. and La Mer, V. K.: Flocculation, subsidence and filtration of phosphate slimes: VI. A quantitative theory of filtration of flocculated suspensions, Journal of Colloid Science, 13, 589–599, https://doi.org/10.1016/0095-8522(58)90071-0, 1958.

Smith, J. D. and McLean, S. R.: Spatially averaged flow over a wavy surface, Journal of Geophysical Research, 82, 1735–1746, https://doi.org/10.1029/JC082i012p01735, 1977.

Smith, S. J. and Friedrichs, C. T.: Image processing methods for in situ estimation of cohesive sediment floc size, settling velocity, and density, Limnology and Oceanography: Methods, 13, 250–264, https://doi.org/10.1002/lom3.10022, 2015.

Son, M. and Hsu, T.-J.: The effects of flocculation and bed erodibility on modeling cohesive sediment resuspension, Journal of Geophysical Research: Oceans, 116, https://doi.org/10.1029/2010JC006352, 2011.

Soulsby, R. L. and Dyer, K. R.: The form of the near-bed velocity profile in a tidally accelerating flow, Journal of Geophysical Research: Oceans, 86, 8067–8074, https://doi.org/10.1029/JC086iC09p08067, 1981.

Soulsby, R. L., Manning, A. J., Spearman, J., and Whitehouse, R. J. S.: Settling velocity and mass settling flux of flocculated estuarine sediments, Marine Geology, 339, 1–12, https://doi.org/10.1016/j.margeo.2013.04.006, 2013.

Spencer, K. L., Wheatland, J. A., Bushby, A. J., Carr, S. J., Droppo, I. G., and Manning, A. J.: A structure–function based approach to floc hierarchy and evidence for the non-fractal nature of natural sediment flocs, Scientific reports, 11, 1–10, https://doi.org/10.1038/s41598-021-93302-9, 2021.

Stokes, G. G.: On the effect of the internal friction of fluids on the motion of pendulums, Transactions of the Cambridge Philosophical Society, 1851.

Strom, K. and Keyvani, A.: An explicit full-range settling velocity equation for mud flocs, Journal of Sedimentary Research, 81, 921–934, https://doi.org/10.2110/jsr.2011.62, 2011.

Syvitski, J. P., Asprey, K. W., and Leblanc, K. W. G.: In-situ characteristics of particles settling within a deep-water estuary, Deep Sea Research Part II: Topical Studies in Oceanography, 42, 223–256, https://doi.org/10.1016/0967-0645(95)00013-G, 1995.

Syvitski, J. P., Kettner, A. J., Overeem, I., Hutton, E. W., Hannon, M. T., Brakenridge, G. R., Day, J., Vörösmarty, C., Saito, Y., and Giosan, L.: Sinking deltas due to human activities, Nature Geoscience, 2, 681–686, https://doi.org/10.1038/ngeo629, 2009.

Tambo, N. and Watanabe, Y.: Physical characteristics of flocs—I. The floc density function and aluminium floc, Water Research, 13, 409–419, https://doi.org/10.1016/0043-1354(79)90033-2, 1979.

Tennekes, H. and Lumley, J. L.: A first course in turbulence, MIT Press, 1972.

Tran, D. and Strom, K.: Floc sizes and resuspension rates from fresh deposits: Influences of suspended sediment concentration, turbulence, and deposition time, Estuarine, Coastal and Shelf Science, 229, 106397, https://doi.org/10.1016/j.ecss.2019.106397, 2019.

Tran, D., Kuprenas, R., and Strom, K.: How do changes in suspended sediment concentration alone influence the size of mud flocs under steady turbulent shearing?, Continental Shelf Research, 158, 1–14, https://doi.org/10.1016/j.csr.2018.02.008, 2018.

Van Leussen, W.: Aggregation of Particles, Settling Velocity of Mud Flocs A Review, in: Physical Processes in Estuaries, Berlin, Heidelberg, 347–403, https://doi.org/10.1007/978-3-642-73691-9_19, 1988.

Verwey, E. J. W.: Theory of the stability of lyophobic colloids., The Journal of Physical Chemistry, 51, 631–636, https://doi.org/10.1021/j150453a001, 1947.

Walling, D. E. and Fang, D.: Recent trends in the suspended sediment loads of the world's rivers, Global and planetary change, 39, 111–126, https://doi.org/10.1016/S0921-8181(03)00020-1, 2003.

West, A. J., Galy, A., and Bickle, M.: Tectonic and climatic controls on silicate weathering, Earth and Planetary Science Letters, 235, 211–228, https://doi.org/10.1016/j.epsl.2005.03.020, 2005.

Whitehouse, R., Soulsby, R., Roberts, W., and Mitchener, H.: Dynamics of estuarine muds, Thomas Telford, 2000.

Winterwerp, J. C.: A simple model for turbulence induced flocculation of cohesive sediment, Journal of Hydraulic Research, 36, 309–326, https://doi.org/10.1080/00221689809498621, 1998.

Woodfield, D. and Bickert, G.: An improved permeability model for fractal aggregates settling in creeping flow, Water research, 35, 3801–3806, https://doi.org/10.1016/S0043-1354(01)00128-2, 2001.

Wright, S. and Parker, G.: Density stratification effects in sand-bed rivers, Journal of Hydraulic Engineering, 130, 783–795, https://doi.org/10.1061/(ASCE)0733-9429(2004)130:8(783), 2004.

Xu, F., Wang, D.-P., and Riemer, N.: Modeling flocculation processes of fine-grained particles using a size-resolved method: comparison with published laboratory experiments, Continental Shelf Research, 28, 2668–2677, https://doi.org/10.1016/j.csr.2008.09.001, 2008.

Yu, X. and Somasundaran, P.: Role of polymer conformation in interparticle-bridging dominated flocculation, Journal of Colloid and Interface Science, 177, 283–287, https://doi.org/10.1006/jcis.1996.0033, 1996.

Zeichner, S. S., Nghiem, J., Lamb, M. P., Takashima, N., De Leeuw, J., Ganti, V., and Fischer, W. W.: Early plant organics increased global terrestrial mud deposition through enhanced flocculation, Science, 371, 526–529, https://doi.org/10.1126/science.abd0379, 2021.

Chapter 4

EVIDENCE FOR MUD AS FLOCCULATED BED-MATERIAL LOAD VERSUS WASHLOAD IN A RIVER DELTA

Justin A. Nghiem, Gen K. Li, Joshua P. Harringmeyer, Gerard Salter, Cédric G. Fichot, Kyle Wright, Paola Passalacqua, and Michael P. Lamb

Chapter 4 is modified from a submitted manuscript: Nghiem, J. A., Li, G. K., Harringmeyer, J. P., Salter, G., Fichot, C. G., Wright, K., Passalacqua, P., & Lamb, M. P. Evidence for Mud as Flocculated Bed-Material Load versus Washload in a River Delta. Submitted.

Abstract

Mud dominates the particulate load of sediment and organic carbon from continents to oceans, but mud concentration and transport rate remain notoriously difficult to predict. In rivers, mud is thought to be transported as washload—particles so small that they are absent from the riverbed, washed through the river like passive tracers, and controlled by far upstream inputs rather than local sediment entrainment from the bed. However, freshwater flocculation in rivers can aggregate mud grains into larger particles that behave hydrodynamically more like sand. If correct, this finding opens the door to describe mud transport as bed-material load—particles in dynamic interchange between the bed and water column—for which robust theory exists. Here we present evidence that mud behaves as flocculated bed-material load, rather than washload, in the freshwater Wax Lake Delta (WLD), a major distributary of the Mississippi River Delta. Grain size-specific concentration-depth profiles indicate that mud is flocculated in WLD. In situ turbidity sensors, airborne hyperspectral imaging (AVIRIS-NG), and concentration-depth profiles show that mud concentration varies temporally and spatially in response to shear stress variations, consistent with bed-material load dynamics. Furthermore, mud exists in the channel bed (median 14% mud by volume) and dominates the bed on deltaic islands (median 90%). Bed-material entrainment theory explains observed near-bed mud concentrations using a formulation that accounts for floc growth and densification near the bed. Together, these findings support a unified treatment of sand and flocculated mud as bed-material load in lowland rivers and deltas.

Plain Language Summary

Understanding the transport of fine-grained sediment (i.e., mud) in rivers and deltas is important for predicting land building and the fate of mud-bound organic matter and pollutants. Past studies have often assumed that sediment supply alone sets the mud concentration because the turbulent energy of flowing water flushes out mud downstream with minimal deposition on the riverbed owing to the very slow settling rates of small mud

particles. To test this idea, we conducted a study in the Wax Lake Delta (WLD), a freshwater river delta near the Mississippi River Delta. Evidence in WLD from sediment size and concentration, remote sensing sediment concentration maps, and time series of sediment concentration and water depth indicates that mud particles settled faster than expected because they aggregated into larger particles. The enhanced settling of mud promoted active exchange of mud between the bed and flow following theory for bed sediment erosion and growth of mud aggregates near the bed. This finding improves the ability to predict mud transport in rivers and deltas because it shows that mud is linked to the local flow and bed via mud settling and erosion dynamics and not passively washed away as often assumed.

4.1 Introduction

Mud, defined as sediment with diameter finer than 62.5 μm, constitutes most of the sediment load in lowland rivers (e.g., Baronas et al., 2020; Bouchez et al., 2011; Lupker et al., 2011). Mud is important because it can control channel morphology through cohesion (Dunne and Jerolmack, 2020), carry organic carbon (Bianchi et al., 2024; Galy et al., 2008), and build land (Kim et al., 2009). Yet mud concentration and transport rate have been notoriously difficult to predict. The Exner equation expresses land accretion or erosion via sediment mass balance (e.g., García, 2008):

$$(1-\lambda)\frac{\partial \eta}{\partial t} = -\frac{\partial (h\bar{C})}{\partial t} - \bar{u}h\frac{\partial \bar{C}}{\partial x} \quad (1)$$

The left side of Eq. (1), the land accretion rate, is the change of elevation, η (m), with time, accounting for deposit porosity, λ. On the right side, the accretion rate depends on the water depth, h (m), depth-averaged flow velocity, $\bar{u}$ (m s^{-1}), and depth-averaged sediment volume concentration, $\bar{C}$. The right side shows that temporal and spatial gradients in sediment concentration due to settling and entrainment dynamics drive accretion rate.

However, mud in rivers is commonly assumed to be washload that is passively transported and does not participate in the sediment balance (Eq. 1) because of its small grain size and slow settling velocity. The features of washload mud are all tied to the slow settling velocity of mud relative to the turbulent shear velocity of the flow. Washload mud is uniformly well-mixed in rivers vertically and laterally in the water column like a passive tracer (Dunne et al., 2024; Ganti et al., 2014; Komar, 1980). Washload mud is expected to remain suspended for extraordinarily long distances because the vertical settling velocity is very small compared to the horizontal flow velocity (Ganti et al., 2014; Venditti et al., 2015). As a result, mud "washes out" of the reach of interest (Einstein et al., 1940; Einstein, 1950), leading to a distinct deficiency, if not absence, of mud in the bed (Church, 2006; Lane, 1947; Eq. 1). At the same time, shear velocity drives high potential entrainment rates of washload mud from the bed and prevents mud accumulation in the bed (De Leeuw et al., 2020; Lamb et al., 2020). Additionally, the fact that washload mud already experiences such high shear stress relative to that required for full suspension implies that the washload mud concentration is insensitive to fluctuations in entrainment rate caused by shear velocity fluctuations. In sum, washload mud implies that the local flow and bed grain size distribution bear no relation to the mud

supply, which is solely set by upstream inputs like hillslope soil erosion, and thus cannot be used to predict the concentration and transport rate of washload mud.

Unlike mud, sand in lowland rivers and deltas is typically treated as bed-material load because its faster settling velocity establishes active exchange between the bed and flow. Fast settling velocity increases the deposition flux (Parker, 1978), making sand well-represented in the bed and available for entrainment. Simultaneously, fast settling velocity decreases the entrainment flux (De Leeuw et al., 2020; García and Parker, 1991), preventing sand from being winnowed away. These feedbacks dynamically adjust the local bed grain size distribution and sediment concentration and bring the fluxes into equilibrium. Thus, if the bed-material entrainment equation is known (e.g., De Leeuw et al., 2020), then the sand concentration can be predicted from the local flow conditions and bed grain size distribution. Unlike washload, bed-material load is determined by supply and local entrainment and deposition and varies in space and time following bed-material entrainment theory (Eq. 1).

Although bed-material theory is typically applied to sand, Lamb et al. (2020) showed that it too could predict mud concentrations in a global river data compilation because flocculation enhances mud settling velocity and the interchange of mud between the bed and flow. Flocculation occurs when sediment (usually mud) coheres into larger fragile particles called flocs with the aid of salinity or organic matter (Van Leussen, 1988; Winterwerp, 1998). Flocculation can increase in situ mud settling velocity by orders of magnitude because flocs are larger than their constituent primary particles (Strom and Keyvani, 2011). However, the treatment of mud as flocculated bed-material load has not yet been evaluated in deltas, which typically have muddier beds than rivers. Cohesive entrainment equations are typically used for mud-dominated beds like in coastal wetlands and marshes and have the form of a power law function of shear stress and cohesive bed strength (Mehta, 1993; Partheniades, 1965). However, the input parameters are uncertain because they must be calibrated for each specific case to handle the wide natural heterogeneity in cohesion due to organic matter (Gerbersdorf et al., 2008), bed porosity and grain size (Jacobs et al., 2011; Van Ledden et al., 2004), rheology (Winterwerp et al., 2012), and water chemistry (Arulanandan, 1975). It is unknown whether theory for cohesive entrainment, flocculated bed-material load, or some combination of them best describes mud transport in deltas.

We conducted fieldwork in the Wax Lake Delta (WLD), Louisiana as part of the NASA Delta-X project to test the hypothesis that flocculation causes mud in deltas to behave as bed-material load rather than washload using a series of field comparisons. First, we introduce WLD and the general field sampling strategy (Section 2). We then report our field and data methods for sediment concentration-depth profiles, bed grain size distributions, in situ time series of water depth and sediment concentration, and sediment concentration maps (Section 3). In the Results, we first report field data to describe the flow and sediment conditions in WLD (Sections 4.1-4.2). Next, we present evidence from five comparisons to evaluate whether mud behaved as washload or flocculated bed-material load. We first test whether flocculation enhanced the in situ mud settling velocity toward bed-material load (Section 4.3). Second (Section 4.4), we use sediment concentration maps to evaluate whether mud was well-mixed and spatially uniform (i.e., washload) or spatially heterogeneous (i.e., bed-

material load). For the third comparison, we determine whether mud was present in the channel and island bed sediment because bed-material entrainment must source mud from the bed (Section 4.5). Fourth (Section 4.6), we compare in situ time series of sediment concentration and water depth, which is a shear stress proxy, to determine whether sediment concentration is insensitive to tidally forced stress fluctuations (i.e., washload) or responds to fluctuations through settling and entrainment dynamics (i.e., bed-material load). The final comparison evaluates whether bed-material entrainment theory explains observed flocculated sediment concentrations (Section 4.7). Finally, we discuss the physical meaning of mud as flocculated bed-material load, modeling mud entrainment and transport rate in practice, and the criteria for washload versus bed-material load (Section 5).

4.2 Study Site and Approach Overview

We conducted fieldwork in the Wax Lake Delta, Louisiana, a sub-delta in the Mississippi River Delta complex (Fig. 1ab). WLD is a ~100-km^2 river-dominated freshwater delta and receives water and sediment from the Wax Lake Outlet, which was dredged in 1942 and connects WLD to the Atchafalaya River (Latimer and Schweizer, 1951). In recent decades, WLD has been aggrading and prograding into the Gulf of Mexico (Jensen et al., 2022; Roberts et al., 1980). Large distributary channels separate several delta islands, which host shallow wetlands because they are typically flooded (Fig. 1b). In some places, secondary channels cut across the edge of the island and facilitate flow between the large distributary channel and island interior (Hiatt and Passalacqua, 2015; Salter and Lamb, 2022).

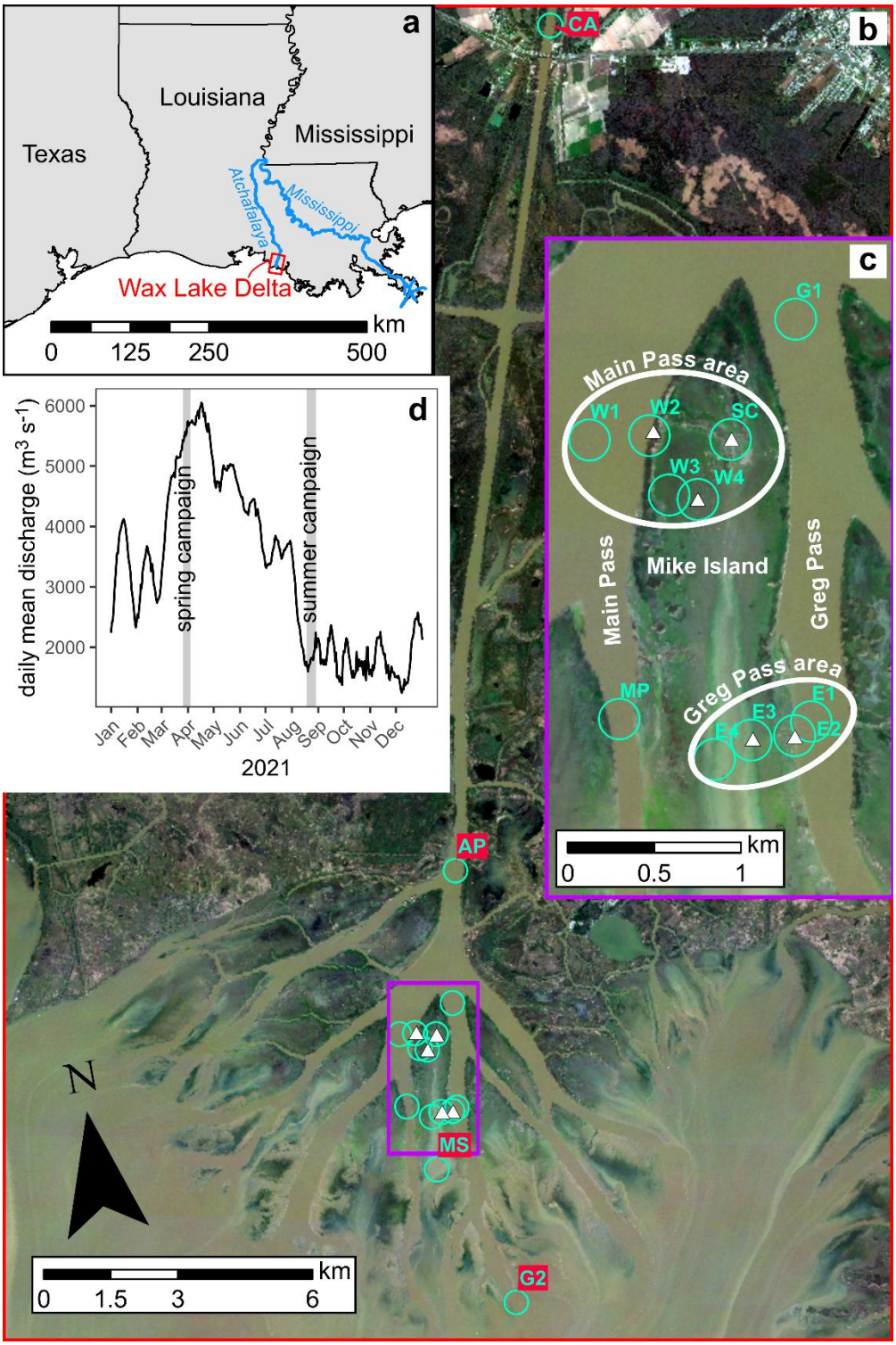

Figure 1. Wax Lake Delta study site. (a) Location of WLD in Louisiana. (b) Map of WLD indicating sample and data collection sites. Circles indicate sediment concentration-depth profile sites. Triangles indicate turbidity stations. Satellite image is from January 2021,

Image © 2021 Planet Labs PBC. (c) Zoom-in map of (b) focusing on Mike Island. (d) 2021 daily hydrograph at Calumet (USGS stream gauge 07381590).

Our approach to evaluate mud transport follows our five comparisons (Section 1). Grain size-specific sediment concentration-depth profiles show which suspended grain sizes were flocculated and the floc settling velocity. Sediment concentration maps reveal whether mud concentration was spatially uniform akin to washload. The grain size distribution of bed sediment quantifies the amount of mud in the bed available to be entrained for bed-material load. Concurrent time series of sediment concentration and water depth demonstrate the degree to which mud concentration correlates with the tidally driven stress fluctuations due to settling and entrainment.

We conducted the field comparisons across two field campaigns in spring (March to April) and summer (August) 2021 as part of the NASA Delta-X project. We sampled 26 suspended sediment profiles (i.e., sediment concentration-depth profiles) and bed material (Fig. 1bc). For each concentration-depth profile, we used a Teledyne RiverPro acoustic Doppler current profiler (ADCP) to measure flow velocity profiles and calculate shear velocity. Harringmeyer et al. (2024) calibrated WLD sediment concentration maps for the same field campaigns using AVIRIS-NG hyperspectral imaging. During each campaign, we installed turbidity stations (5 in spring, 4 in summer) at which we measured turbidity and water depth using in situ turbidity and pressure sensors. The stations were clustered into the Main Pass and Greg Pass areas (Fig. 1c). The Main Pass area corresponds to northwestern Mike Island and consists of site W2 (edge of Main Pass channel), site SC (in a small secondary channel branch), and site W4 (in island wetland; only installed in the spring). The Greg Pass area corresponds to southeastern Mike Island and consists of site E2 (edge of Greg Pass channel) and site E3 (in island wetland). We sampled suspended sediment at the turbidity sensors to develop an in situ calibration between turbidity and sediment concentration (Nghiem, Salter, et al., 2022).

4.3 Methods

4.3.1 Suspended sediment concentration-depth profiles

We briefly summarize our suspended sediment concentration-depth profile methods, which are reported in full in Nghiem, Salter, and Lamb (2024), Nghiem et al. (2024), and Nghiem, Salter, and Lamb (2025). For each profile, we collected suspended sediment samples at multiple heights above the bed from a boat using a Van Dorn sampler. We sampled bed sediment using a Ponar grab sampler or, where sufficiently shallow, a piston core. We filtered each sample through 0.2-μm pore size polyethersulfone filter paper (Sterlitech). In the lab, we dried and weighed the samples and, for the suspended samples, calculated the concentration. We decarbonated, oxidized, and chemically deflocculated an aliquot of each sample for grain size analysis using a Malvern Mastersizer 3000E laser diffraction instrument, which measured the volume distribution from 0.2 to 2100 μm in 100 logarithmically spaced bins.

For each concentration-depth profile, we partitioned the sediment concentrations into the 100 grain size classes using the measured grain size distributions and calculated the grain size-specific sediment concentration-depth profiles (Fig. 2a). As documented in Nghiem et al. (2024), we used ADCP data to estimate the water temperature, flow depth, depth-averaged flow velocity, and shear velocity for each concentration-depth profile. We integrated the flow velocity profile to obtain the depth-averaged flow velocity. We estimated shear velocity by fitting the law of the wall theory for turbulent flow velocity profiles to the measured flow velocity profile. We discarded data in the top half of the flow due to potential tide and wake effects (Nezu and Nakagawa, 1993; Soulsby and Dyer, 1981). We calculated the skin friction shear velocity, $u_{*\mathrm{sk}}$, using the Manning-Strickler relation following De Leeuw et al. (2020).

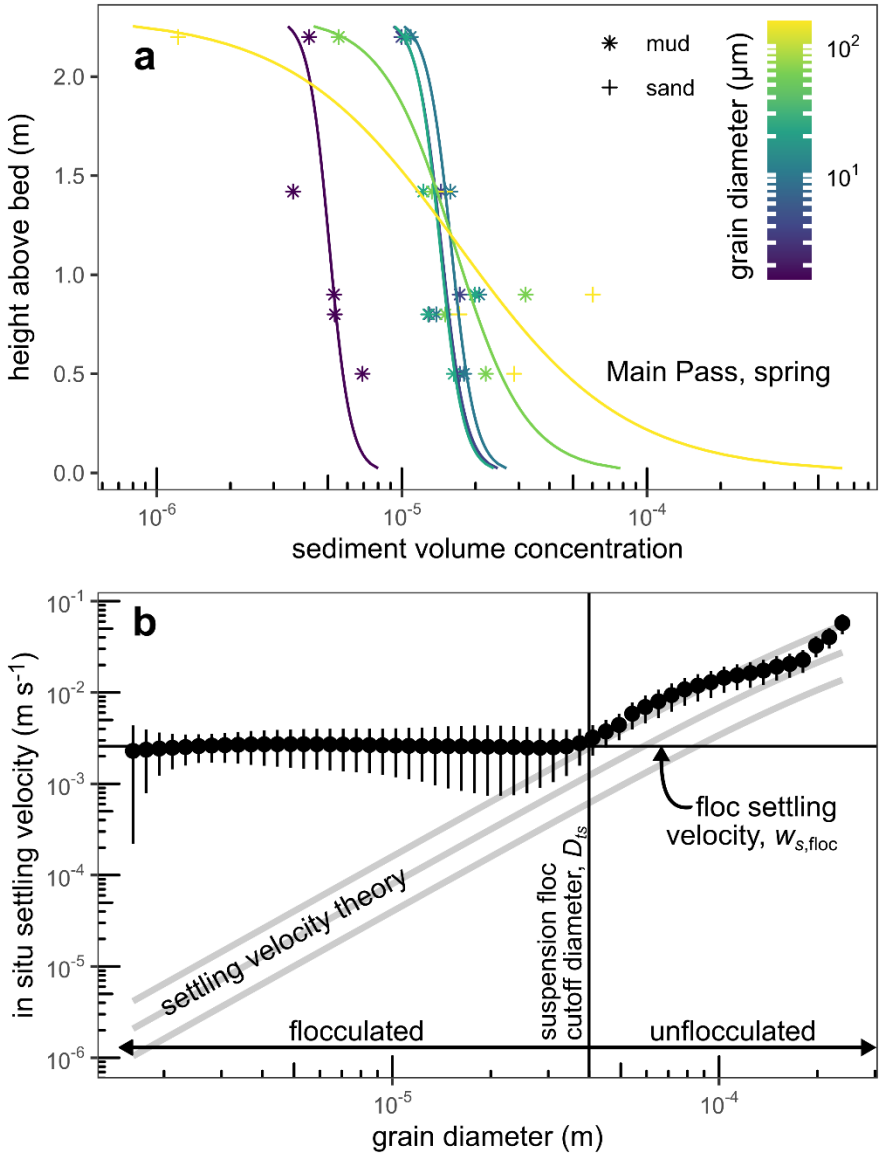

Figure 2. Suspended sediment concentration-depth profile methods illustrated by a profile in Main Pass in spring (March 25, 2021, 8:33-9:26 CDT). (a) Grain size-specific sediment concentration-depth profiles. Suspended sediment is grouped into 6 classes here for display purposes only. (b) Grain diameter versus in situ settling velocity for the same concentration-depth profile inferred from fitting the Rouse-Vanoni equation with $\beta = 1$. Theory curves show the settling velocity prediction for single grains according to Ferguson and Church (2004) with a factor of 2 above and below. The suspension floc cutoff diameter, D_{ts} (m), indicates the grain size below which all suspended sediment is effectively flocculated based on the plateau at the floc settling velocity, $w_{s,\mathrm{floc}}$ (Nghiem, Fischer, et al., 2022). The bias between calculated and predicted settling velocity for grains coarser than D_{ts} is probably due to uncertainty in β. Error bars indicate the propagated 95% confidence intervals on shear velocity and Rouse number.

4.3.2 Calculating suspension floc cutoff diameter, near-bed concentration, and settling velocity

We fitted the Rouse-Vanoni equation to grain size-specific concentration-depth profiles (Section 3.1) and identified the suspended grain sizes that were flocculated using the suspension floc cutoff diameter, D_{ts}. In previous work, the suspension floc cutoff diameter was simply called "floc cutoff diameter" (Nghiem, Fischer, et al., 2022; Nghiem et al., 2024). Nghiem et al. (2024) already reported D_{ts} for our concentration-depth profiles. Assuming a balance between gravitational and turbulent fluxes of sediment, the Rouse-Vanoni equation is:

$$\frac{C_i}{C_{bi}} = \left(\frac{\frac{h - z}{z}}{\frac{h - h_b}{h_b}} \right)^{p_i} \quad (2)$$

in which C is the sediment volume concentration at height z (m) from the bed (Rouse, 1937). The subscript i denotes quantities specific to the ith sediment class. The class-specific Rouse number, $p_i = w_{si}/(\kappa \beta_i u_*)$ with von Kármán constant $\kappa = 0.41$, shows that faster settling velocity relative to shear velocity causes greater concentration near the bed relative to that near the water surface. The near-bed concentration, C_b, is the concentration at the near-bed height, h_b (m), which is typically selected as a small fraction of the flow depth, $\alpha = h_b/h$. We used $\alpha = 0.1$ following De Leeuw et al. (2020). We fitted the Rouse-Vanoni equation (Eq. 2) to the grain size-specific concentration-depth profiles, yielding estimates of p_i and C_{bi} for each sediment class. We inverted the p_i for in situ settling velocity, w_{si}, using the Rouse number definition, shear velocity (Section 3.1), and diffusivity ratio $\beta = 1$. We calculated D_{ts} for each concentration-depth profile as the grain diameter at which the in situ settling velocity deviates from settling velocity theory for single grains (Fig. 2b). Suspended sediment finer than D_{ts} is significantly flocculated because inferred in situ settling velocity exceeded the predicted settling velocity of single grains. Although the diffusivity ratio is uncertain (e.g., De Leeuw et al., 2020), estimates of D_{ts} are insensitive to different treatments

of β because the change in settling velocity with grain diameter is abrupt (Nghiem et al., 2024).

Following Lamb et al. (2020), we grouped the concentration of sediment finer than D_{ts} into a single floc class and re-fitted the Rouse-Vanoni equation to estimate p_i and C_{bi} for flocculated sediment. This concentration represents only sediment grains, and not floc porosity, because we measured grain size distributions of fully dispersed grains (Section 3.1). We also regrouped the unflocculated sediment classes (i.e., sediment coarser than D_{ts}) into 49 classes and re-fitted the Rouse-Vanoni equation on these new classes to obtain p_i and C_{bi}. We re-calculated the sediment volume fraction in the bed, f_i, following these new grain size classifications. We filtered out low quality data following De Leeuw et al. (2020).

For each concentration-depth profile, we calculated w_{si} in the floc class as the floc settling velocity, $w_{s,\mathrm{floc}}$, in which $w_{s,\mathrm{floc}}$ is the settling velocity at a grain size of D_{ts} following theory for single grains (Fig. 2b; Ferguson and Church, 2004) as done in prior work (Lamb et al., 2020; Nghiem, Fischer, et al., 2022; Zeichner et al., 2021). For all unflocculated classes, we calculated w_{si} at the corresponding grain size (Ferguson and Church, 2004). We used a submerged specific gravity of sediment, $R = 1.65$, and a temperature-dependent kinematic viscosity (Lamb, 1945) in the settling velocity equation.

4.3.3 AVIRIS-NG Sediment Concentration Maps

We used the suspended sediment mass balance as the conceptual framework for interpreting sediment concentration maps, time series, and entrainment rates when testing the washload versus bed-material load criteria. The one-dimensional depth-averaged suspended sediment mass balance, neglecting sediment diffusion, is (Spasojevic and Holly, 1990):

$$\frac{\partial(h\bar{C}_i)}{\partial t} + \bar{u}h\frac{\partial \bar{C}_i}{\partial x} = w_{si}(f_i E_i - C_{bi}) \quad (3)$$

in which h (m) is the flow depth, $\bar{u}$ (m s^{-1}) is the depth-averaged flow velocity, $\bar{C}_i$ is the class-specific depth-averaged suspended sediment volume concentration, and E_i is the class-specific dimensionless entrainment rate. Physically, Eq. (3) shows that the time rate of change of the sediment concentration through the water column depends on the divergence of the sediment flux and the local sediment source (entrainment) and sink (settling). The bed fraction, f_i, linearly weights the class-specific entrainment rate (García and Parker, 1991). The sediment entrainment flux from the bed, $w_{si}f_iE_i$, counteracts the deposition flux from the flow, $w_{si}C_{bi}$. The difference is the net rate at which suspended sediment is locally eroded or deposited (Eq. 1).

We evaluated spatial patterns of sediment concentration using the AVIRIS-NG sediment concentration maps of Harringmeyer et al. (2024) because sediment mass balance (Eq. 3) shows that spatial concentration gradients are linked to deposition and entrainment for bed-material load. AVIRIS-NG is an airborne imaging spectrometer and was deployed at WLD during the Delta-X field campaigns. A partial least squares algorithm, developed and

validated using a large set of in situ reflectance spectra and near-surface sediment concentrations sampled at ~0.5 m depth, was used to retrieve WLD sediment concentration maps from AVIRIS-NG images (Fichot and Harringmeyer, 2023; Harringmeyer et al., 2024). We used two concentration maps, one for each season (April 2 and August 22, 2021), that had the best data quality (Harringmeyer et al., 2024). Harringmeyer et al. (2024) also showed that water depths and sediment concentrations were sufficiently high such that bottom reflectance did not significantly affect the retrieved suspended sediment concentration in the shallow islands.

4.3.4 Turbidity Stations

We used in situ sediment concentration and water depth time series, documented fully in Nghiem, Salter, et al. (2022), to evaluate the extent to which mud settling and entrainment responded to tidally forced shear velocity fluctuations following Eq. (3). We measured time series of turbidity and water pressure at each turbidity station using in situ turbidity and pressure sensors. Pressure sensors measured water pressure at a 1-minute interval. We converted the water pressure time series into a local water depth time series assuming hydrostatic pressure and correcting for atmospheric pressure using a co-located air pressure sensor.

We used two types of optical backscatter turbidity sensors, Observator Analite NEP-595 (at 90°) and Campbell Scientific OBS-3+ (from 90 to 165°). We cross-calibrated them in the field to correct for instrument differences (Nghiem, Salter, et al., 2022). The Campbell Scientific sensors measured turbidity at an interval of 30 or 60 s. The Observator sensors measured turbidity at a 10-minute interval. We developed a turbidity-sediment concentration relation using suspended sediment samples collected near the sensors and converted the turbidity time series into sediment concentration (Nghiem, Salter, et al., 2022). We smoothed the concentration time series using a smoothing spline to reduce noise. We supplemented the local time series data with the time series of discharge entering WLD measured at the USGS Calumet stream gauge (Fig. 1b) and mean hourly wind speed from the offshore NOAA Eugene Island station (ID 8764314) located approximately 17 km from the northern tip of Mike Island.

4.3.5 Predicting equilibrium entrainment rate and near-bed concentration

Assuming equilibrium between erosion and deposition, we predicted the class-specific entrainment rate, E_i, and near-bed concentration, C_{bi}, for each concentration-depth profile to evaluate whether bed-material entrainment theory could predict the observed near-bed concentrations of flocculated mud. At equilibrium, the suspended sediment mass balance (Eq. 3) simplifies to $C_{bi} = f_i E_i$ because the derivatives go to zero. To predict C_{bi}, we measured f_i from bed grain size distributions (Sections 3.1 and 3.2) and calculated E_i using the De Leeuw et al. (2020) empirical entrainment rate equation calibrated on a global river sand data compilation:

$$E_i = 4.74 \times 10^{-4} \left(\frac{u_{*\mathrm{sk}}}{w_{si}}\right)^{1.77} \mathrm{Fr}^{1.18} \quad (4)$$

where $u_{*\mathrm{sk}}$ (m s^{-1}) is the skin friction shear velocity, $\mathrm{Fr} = \bar{u}/\sqrt{gh}$ is the Froude number, and g is gravitational acceleration (= 9.81 m s^{-2}). We used $u_{*\mathrm{sk}}$, $\bar{u}$, and h from the concentration-depth profile measurements (Section 3.1) and w_{si}, which we set to $w_{s,\mathrm{floc}}$ for each floc class (Section 3.2). We compared the predicted C_{bi} to the measured C_{bi} from the Rouse-Vanoni equation fitting (Section 3.2).

4.4 Results

First, we report the time series observations, hydrodynamics, and suspended sediment grain size distribution and concentration to characterize the flow and sediment in WLD (Sections 4.1 and 4.2). We then present five field comparisons of whether mud in WLD behaves more like washload or bed-material load (Sections 4.3-4.7).

4.4.1 Discharge, water surface elevation, and sediment concentration time series

The time series data demonstrate that WLD, despite being nominally river-dominated and microtidal, experiences regular tide and occasional wind forcing that affect local water level, sediment concentration, and dynamics of sediment and water flux between channels and islands (Geleynse et al., 2015). In the spring campaign, discharge entering WLD was ~5500 m^3 s^{-1}, close to the peak discharge for 2021 (Fig. 3a), with a slight increasing trend and limited tidal influence. As measured from the offshore Eugene Island station, the typical wind speed was a gentle breeze (~5 m s^{-1}) but occasionally reached strong breeze (~10 m s^{-1}) (Fig. 3b). The local water depth fluctuated according to the tidal cycle (Fig. 3c). At both Main and Greg Pass areas, the time series in the channel and in the island were relatively well in phase. Sediment volume concentration, calibrated from turbidity data, was relatively constant in both areas at ~5×10^{-5} (Fig. 3d). Within Mike Island (island and secondary channel), tides were probably responsible for the low oscillations in concentration. A high wind event on March 31-April 1, with hourly wind speed peaking at ~14 m s^{-1} (moderate gale), correlated with a drop in water depth (by ~0.4 m; Fig. 4bc) and a spike in sediment concentration (by a factor of ~6, 5×10^{-5} to 3×10^{-4}; Fig. 3d) at site E3, a shallow wetland in Mike Island. We interpreted this behavior as a wind setup toward the Gulf of Mexico pushing water out of WLD (i.e., drawdown for the delta). The accompanying wind stress likely generated waves that enhanced sediment entrainment and increased concentration. This phenomenon likely occurred at other stations too, but was not recorded because the water surface dropped below the sensors. The reason for the brief rise in concentration in the secondary channel (SC) on March 29 is unclear, but could be an error due to debris interference.

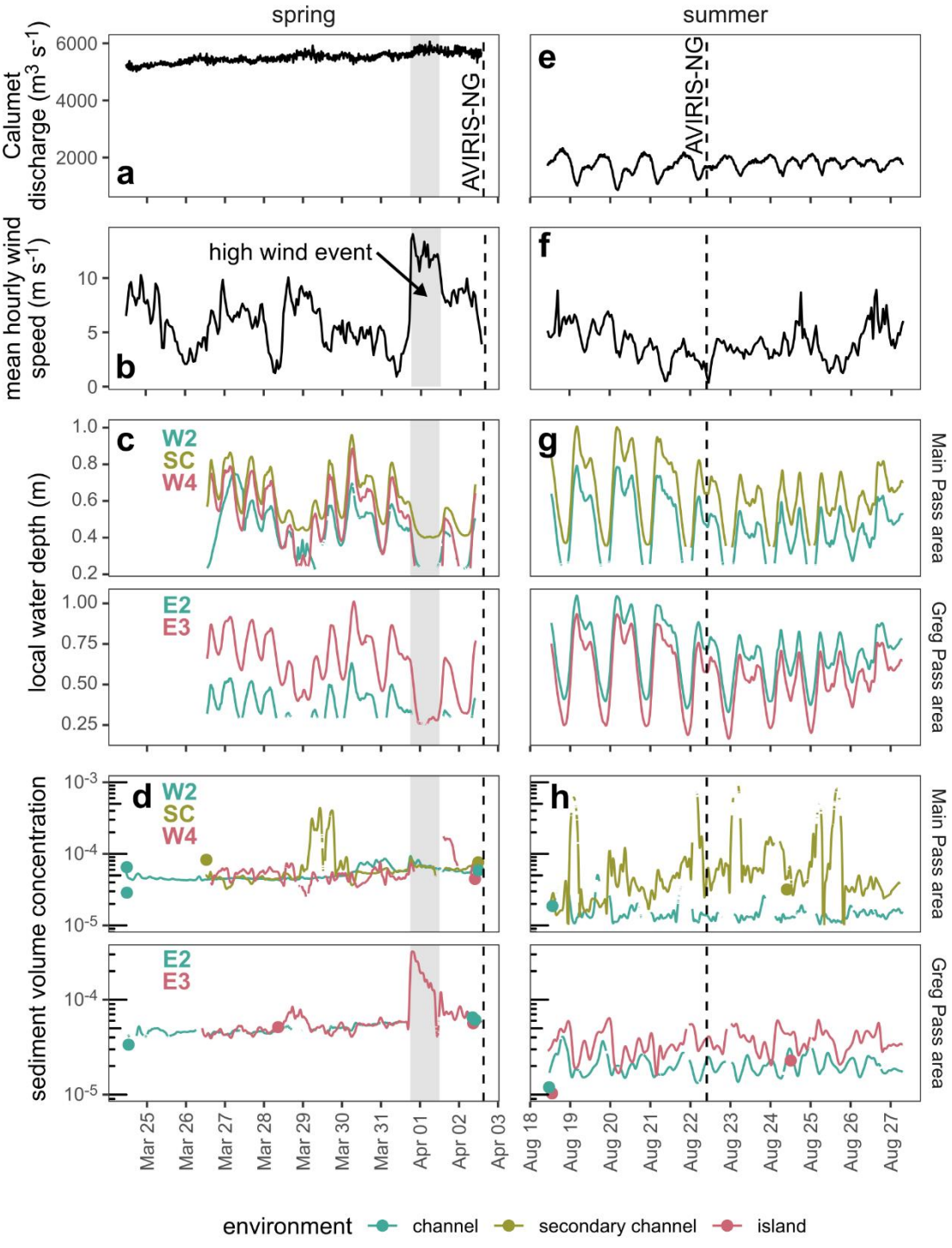

Figure 3. Wax Lake Delta time series observations during spring and summer 2021 field campaigns. (a) and (e): Hydrograph at the USGS Calumet stream gauge. (b) and (f): (b) Mean hourly wind speed time series measured at Eugene Island. (c) and (g): Water depth time

series at the turbidity stations measured by pressure sensors. (d) and (h): Sediment volume concentration at the turbidity stations measured by turbidity sensors and calibrated to sediment concentration. Points in the concentration time series indicate calibration or concentration-depth profile sediment concentrations measured near the turbidity sensor. Gaps indicate periods in which the water surface was below the sensor. Refer to Fig. 1 for measurement locations. AVIRIS-NG data collection times for the two selected sediment concentration maps are marked as vertical dashed lines.

In the summer campaign, the discharge entering WLD oscillated between ~1000 and 2000 $m^3 s^{-1}$ (Fig. 3e) because of tidal effects but was otherwise stationary, indicating a constant upstream river discharge. The wind speed was ~4 m s^{-1} (gentle breeze), did not exceed 9 m s^{-1} (fresh breeze; Fig. 3f), and was not fast enough to affect water level. In the Main Pass area, water depth fluctuations in the secondary channel in the island (site SC) lagged slightly behind those in Main Pass, site W2 (Fig. 3g). The island station was not installed in the summer. In the Greg Pass area, water depth fluctuations between channel (site E2) and island wetland (site E3) were well in phase, likely reflecting greater hydrological connectivity potentially due to lower vegetation density downstream where the more recently accreted island surface has had less time for vegetation colonization (Hiatt and Passalacqua, 2015; Sendrowski et al., 2021). Overall, the sediment volume concentration was ~2 to 5×10^{-5} and tended to be smaller than in the spring (Fig. 3h). Fluctuations in sediment concentration suggest a tidal influence, which is apparent even in the channel (unlike the spring). Notably, the sediment concentration in the island and secondary channel sites typically exceeded that in the corresponding channel site, whereas there was little difference in the spring. The higher hydrological and sediment connectivity between island and channel in the spring compared to that in the summer probably caused this seasonal concentration trend (Sendrowski et al., 2021).

4.4.2 Local flow conditions, sediment concentration, and grain size

Next, we turn to ADCP and suspended sediment concentration-depth profile data to characterize local flow conditions, sediment concentration, and grain size distributions.

Flow velocities near the centers of channels were on the order of 0.1 m s^{-1}, only reaching ~1 m s^{-1} in the upstream Wax Lake Outlet (spring and summer) and at the delta apex (spring only) where the flow depth exceeded 10 m (Fig. 4a). Center depths ranged from ~30 m in Wax Lake Outlet near Calumet to ~10 to 15 m at the delta apex and ~3 m in Greg and Main Passes with little seasonal difference. Flow velocities were faster near the water surface and slower near the bed as expected (Fig. 4b). The linearity between flow velocity and the logarithm of height in the lower half of the flow shows that the flow velocity profiles conform well to the law of the wall. For the same location (i.e., Greg Pass and apex), depth-averaged flow velocities and shear velocities were faster in the spring than in the summer because the spring discharge exceeded the summer discharge. Across both seasons, the local friction coefficient ranged approximately from 0.0030 to 0.020 with a best fit of 0.0082 (Fig. 4c).

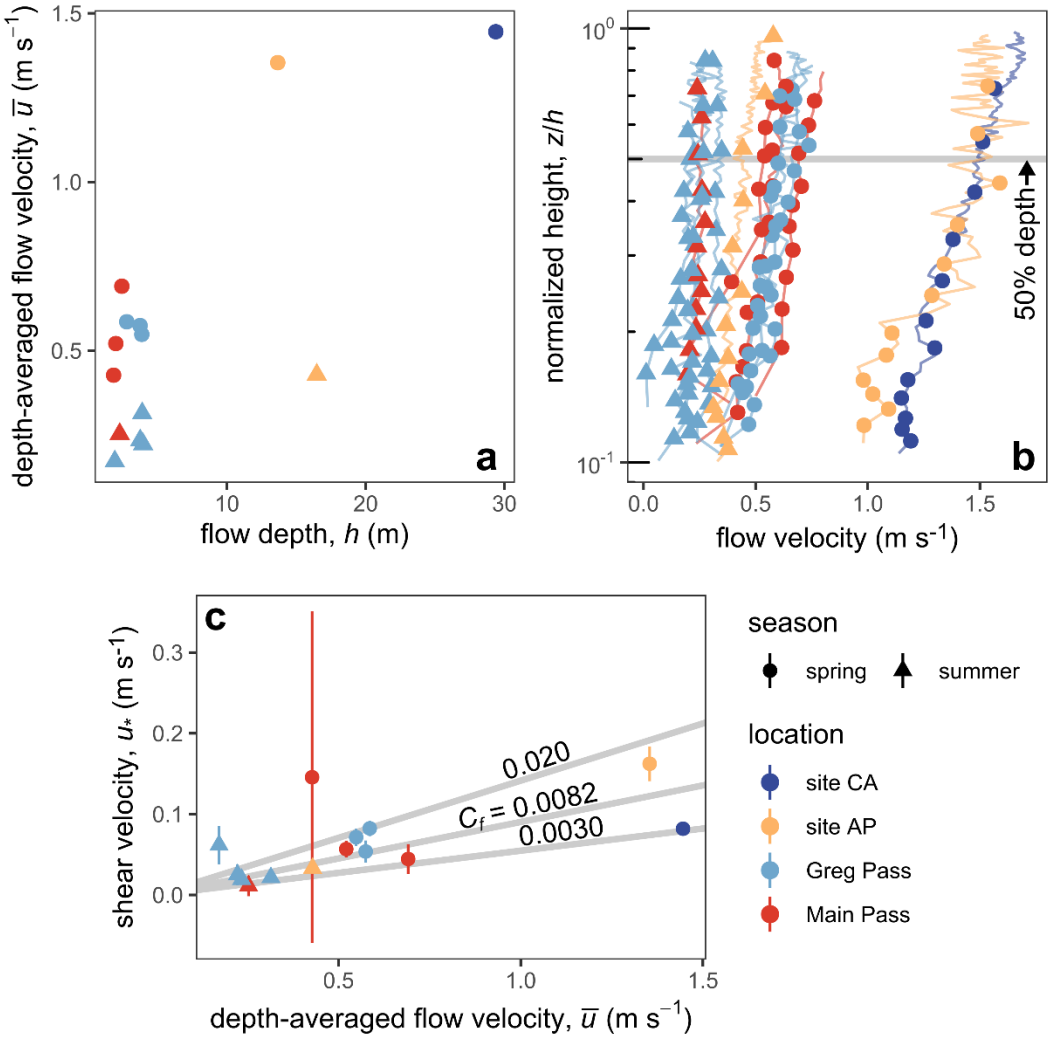

Figure 4. Channel center flow conditions from ADCP measurements. (a) Flow depth and depth-averaged flow velocity. (b) Flow velocity profiles. (c) Depth-averaged flow velocity and shear velocity. The bars on shear velocity indicate the 95% confidence interval of the law of the wall fit. Greg Pass includes sites G1, G2, and E1 (Fig. 1b). Main Pass includes sites W1 and MP.

In the island, depth-averaged flow velocities were typically faster in a secondary channel branch (site SC; faster than ~0.2 m s^{-1}) than in the shallow wetland (sites W4 and E3; slower than 0.2 m s^{-1}) because channelization limits lateral flow spreading (Fig. 5a). Flow depths ranged from ~0.4 to 0.8 m. Site E3, the shallow wetland in the Greg Pass area (Fig. 1c), showed faster flow velocity in the spring than in the summer (~0.1 versus 0.05 m s^{-1}) and deeper flow (~0.6 to 0.8 m versus ~0.4 to 0.7 m), but the precise difference depended on the tidal cycle (Fig. 3cg). Island flow velocity profiles are reasonably linear in the lower half of the flow (in log space), indicating the law of the wall is appropriate for this portion (Fig. 5b). A friction coefficient of 0.047 describes the island data well (Fig. 5c) except for the data at

site SC in the spring. Vegetation and shallower flow probably caused the island friction coefficient to be larger than that in the channel (Fig. 4c).

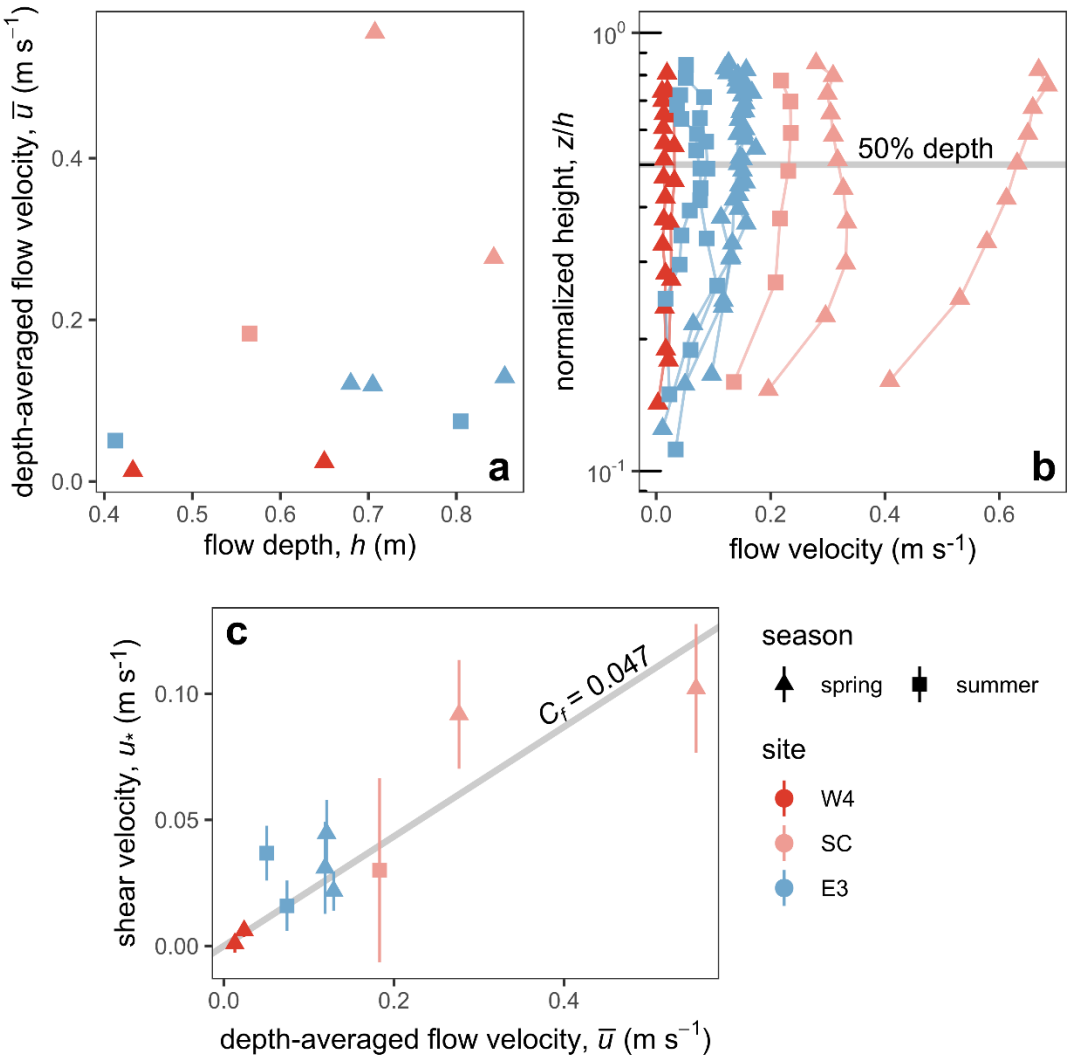

Figure 5. Island flow conditions from ADCP measurements. (a) Flow depth and depth-averaged flow velocity. (b) Flow velocity profiles. (c) Depth-averaged flow velocity and shear velocity. The bars on shear velocity indicate the 95% confidence interval of the law of the wall fit.

Suspended sediment grain size and concentration trends broadly reflected differences in flow seasonally and between environments. Suspended sediment was ubiquitously muddy across the channel and island with most of the depth-averaged sediment concentrations exceeding 90% mud by volume (Fig. 6a). The depth-averaged median grain diameter, D_{50}, generally has a positive correlation with shear velocity for shear velocity exceeding 0.01 m s^{-1} and is relatively constant at slower shear velocities albeit with limited data (Fig. 6b). D_{50} varied

little seasonally in the shallow island wetlands (~5 to 10 μm). In contrast, D_{50} in channels was generally finer than ~10 μm in the summer and coarser than 10 μm in the spring. The depth-averaged suspended sediment concentration broadly increased with shear velocity from 10^{-5} to 10^{-4} (Fig. 6c). However, channel concentrations in the summer were disproportionately smaller of order 10^{-6} to 10^{-5}.

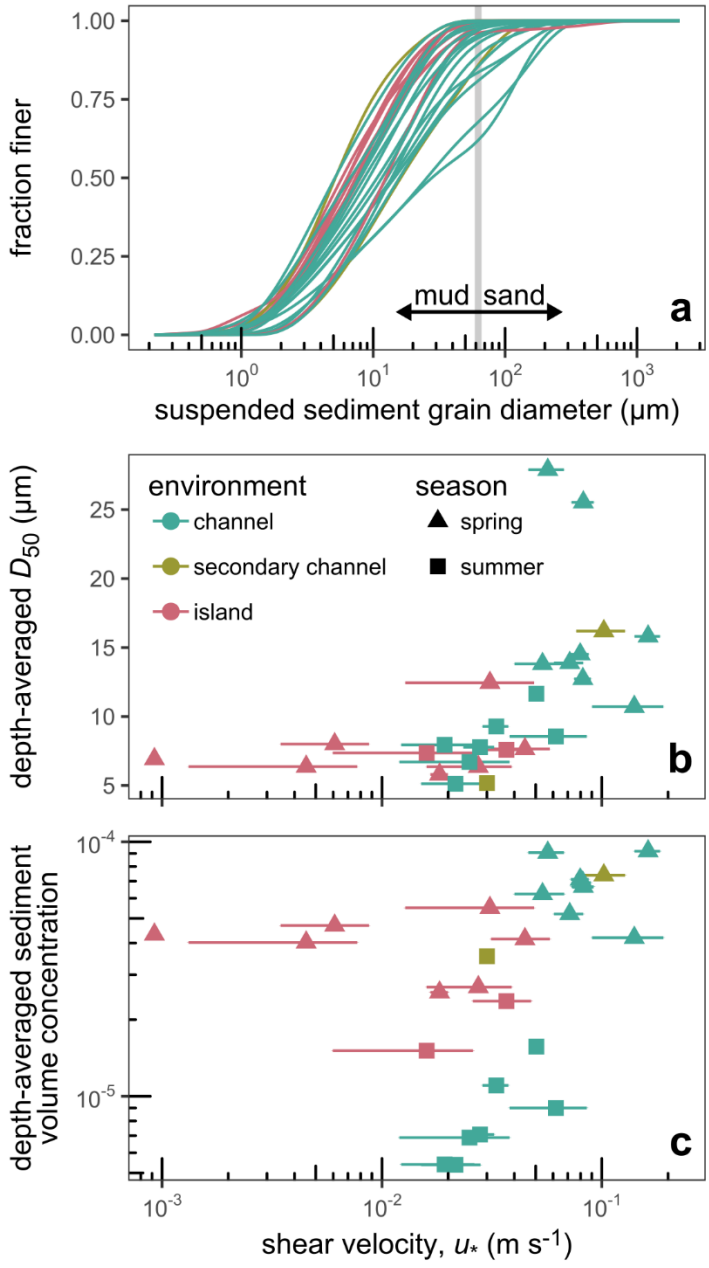

Figure 6. Suspended sediment grain size and concentration. (a) Cumulative distribution function of depth-averaged suspended sediment grain size. Shear velocity versus (b) median grain size, D_{50}, of the depth-averaged suspended sediment grain size distribution and (c)

depth-averaged sediment volume concentration. The bars on shear velocity indicate the 95% confidence interval of the law of the wall fit. The legend in panel b applies for all panels.

4.4.3 Comparison 1: Is suspended mud flocculated?

The first comparison of mud as washload versus flocculated bed-material load evaluates whether suspended mud in WLD is flocculated. If mud is washload, then we expect mud to settle at slower rates typical of individual mud grains. If mud is flocculated bed-material load, then we expect flocculation to increase mud settling velocity. The Rouse-Vanoni equation (Eq. 2) shows that the difference in settling velocity is expressed in the shape of the sediment concentration-depth profile. Washload mud is uniformly mixed in the vertical because of its slow settling velocity (i.e., lower Rouse number). Bed-material mud is more concentrated closer to the bed, relative to the water surface, because of its faster settling velocity (i.e., higher Rouse number). Based on this expectation, some authors have defined washload criteria using the Rouse number. Komar (1980) surmised that $w_s/u_* = 0.03$ (equivalently $p = 0.07$ assuming $\beta = 1$) separates washload and bed-material load. Classifying washload as $p < 0.8$ is also common (e.g., Dunne et al., 2024).

Concentration-depth profiles of mud grain sizes typically show slight concentration stratification (i.e., higher Rouse number; Fig. 2a). Rouse-Vanoni equation fits to the full 100 grain size classes (Section 3.1) yield a median Rouse number for mud of 0.051 and a median Rouse number for sand of 0.29. According to Rouse number washload thresholds (i.e., p = 0.07, 0.8), our median mud Rouse number in WLD indicates that mud behaved as washload. However, this conclusion lacks support because the precise threshold does not have a clear physical rationale. Furthermore, the Rouse number does not fully address washload because it fails to account for sediment exchange between the bed and flow. For example, a high near-bed concentration can compensate for a slow settling velocity (i.e., low Rouse number) in the deposition flux, $w_{si}C_{bi}$ (Eq. 3).

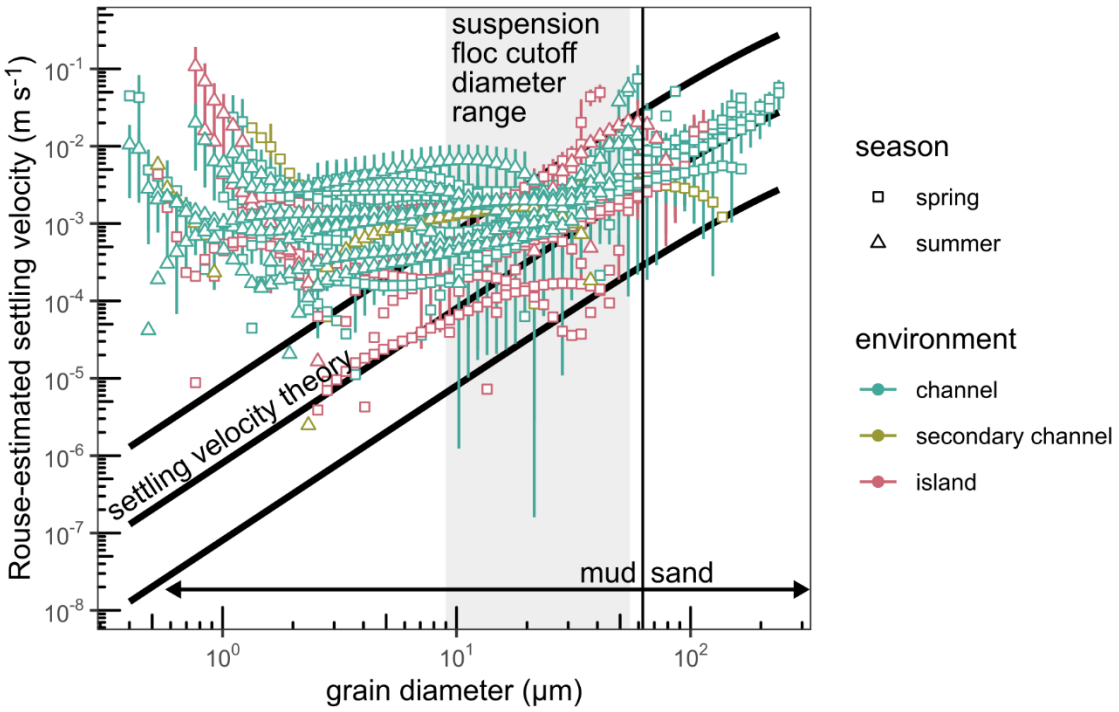

Figure 7. Grain diameter and in situ settling velocity calculated from Rouse-Vanoni equation fits assuming $\beta = 1$. Settling velocity theory represents the modified Stokes settling model of Ferguson and Church (2004) for individual grains. Curves above and below theory indicate an order-of-magnitude deviation. Vertical bars represent the propagated 68% confidence interval on the Rouse number estimates. Points without vertical bars have confidence intervals that overlap with 0.

Inferred in situ settling velocities from fitting the Rouse-Vanoni equation to the full 100 grain size classes (Section 3.2) reveal widespread flocculation in WLD (Fig. 7). The suspension floc cutoff diameter, D_{ts}, ranges between 9 and 55 μm depending on the concentration-depth profile. Sediment coarser than D_{ts} follows settling velocity theory albeit with some scatter about the curve due to uncertainty with β, which is assumed to be 1. Sediment finer than D_{ts} deviates to much faster settling velocities, which we interpreted to be enhanced settling velocity due to flocculation (e.g., Lamb et al., 2020). However, the settling velocities for sediment finer D_{ts} likely do not reflect precise floc settling velocities because of uncertainty with β. The fact that D_{ts} is finer than 62.5 μm, the mud-sand grain size boundary, means that some of the coarser mud was unflocculated. However, this mud would settle faster than flocs following the theoretical settling curve (Fig. 2b; Fig. 7).

We concluded that suspended mud is commonly flocculated in WLD because the inferred in situ settling velocities are faster than settling velocity predictions for grains finer than the suspension floc cutoff diameter. The presence of flocculation supports the idea that mud behaves more like bed-material load than washload because flocculation increases the mud settling velocity and deposition flux (Eq. 3).

4.4.4 Comparison 2: Is mud concentration spatially heterogeneous?

The second comparison assesses whether mud concentration was uniform or heterogeneous in space throughout the delta. Akin to the expectations for the vertical sediment distribution (Section 4.3), mud is uniformly distributed under the washload paradigm because it is well-mixed with negligible entrainment and deposition to alter its concentration, set by the upstream input, in space. Conversely, mud as bed-material load produces spatially heterogeneous patterns in concentration due to spatially varying entrainment and deposition rates. These variations stem from differences in concentration (for deposition), local flow conditions, and bed grain size distribution (for entrainment) according to the sediment mass balance and entrainment equations (Eq. 3 and 4).

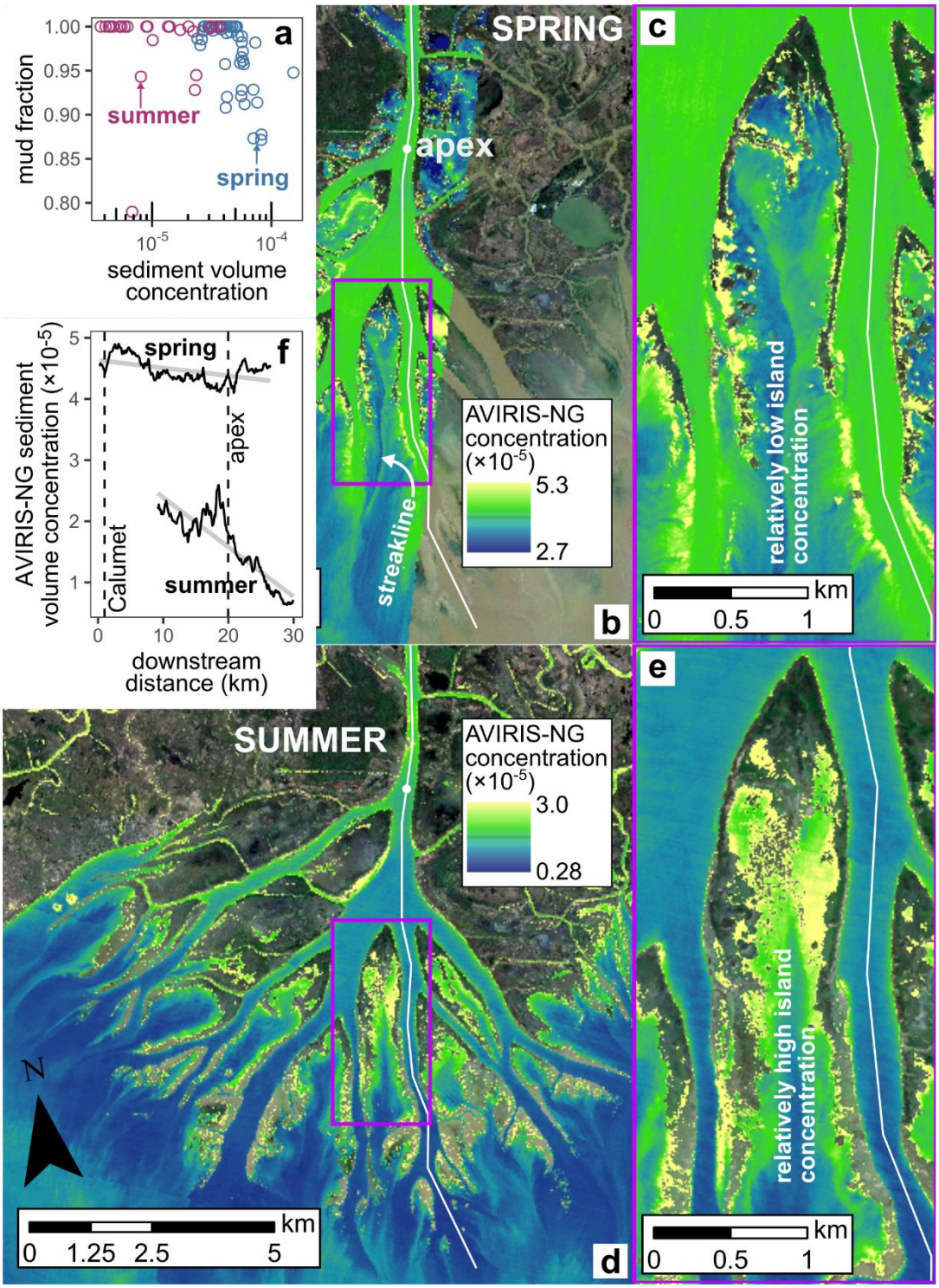

Figure 8. AVIRIS-NG sediment concentration maps. (a) Sediment concentration and mud fraction for suspended sediment samples collected within the top 0.5 m of the water surface. (b) AVIRIS-NG sediment concentration map for the spring campaign, April 2, 2021. (c) Zoom-in map of panel b. (d) AVIRIS-NG sediment concentration map for the summer

campaign, August 22, 2021. (e) Zoom-in map of panel d. (f) Longitudinal profiles of sediment concentration extracted from AVIRIS-NG sediment concentration maps. We extracted the profile along the white path shown in all the map panels.

AVIRIS-NG sediment concentration maps show spatial heterogeneity in both spring and summer (Fig. 8). AVIRIS-NG sediment concentration nominally represents the near-surface total sediment concentration (Harringmeyer et al., 2024; Section 3.3). However, it is a good proxy for depth-averaged mud concentration because the relatively small measured Rouse numbers (Section 4.3) indicate a modest difference between near-surface and depth-averaged concentrations and our near-surface suspended sediment samples have very high mud fractions of ~0.9 (Fig. 8a). The spring map reveals concentration streaklines inside and extending out of islands (Fig. 8bc) and lower island concentrations compared to those in channels (Fig. 8c). The summer map reveals streaklines coming off the downstream island edges (Fig. 8d) and higher island concentrations compared to those in channels (Fig. 8e). Longitudinal profiles of sediment concentration extracted from the AVIRIS-NG maps show a general downstream decrease in the channel-bound sediment concentration that is steeper in the summer than in the spring (Fig. 8f). The presence of spatial structure in the AVIRIS-NG concentration maps points to mud as bed-material load because washload would be spatially uniform.

4.4.5 Comparison 3: Is mud found in the bed?

The third comparison assesses whether mud is in the island and channel beds in WLD. If mud is bed-material load, then mud needs to be present in the bed as the source for the mud entrainment flux (i.e., $f_i > 0$; Eq. 3). However, the presence of mud in the bed does not rule out washload because mud might be hosted in the bed through interstitial trapping (Einstein, 1968; Hill et al., 2017; Mooneyham and Strom, 2018) or hyporheic exchange (Packman and Brooks, 2001; Shrivastava et al., 2020). On the other hand, the absence of mud in the bed is a sufficient condition for mud to be washload because the suspended mud must then be entirely supplied from upstream without any local entrainment or deposition.

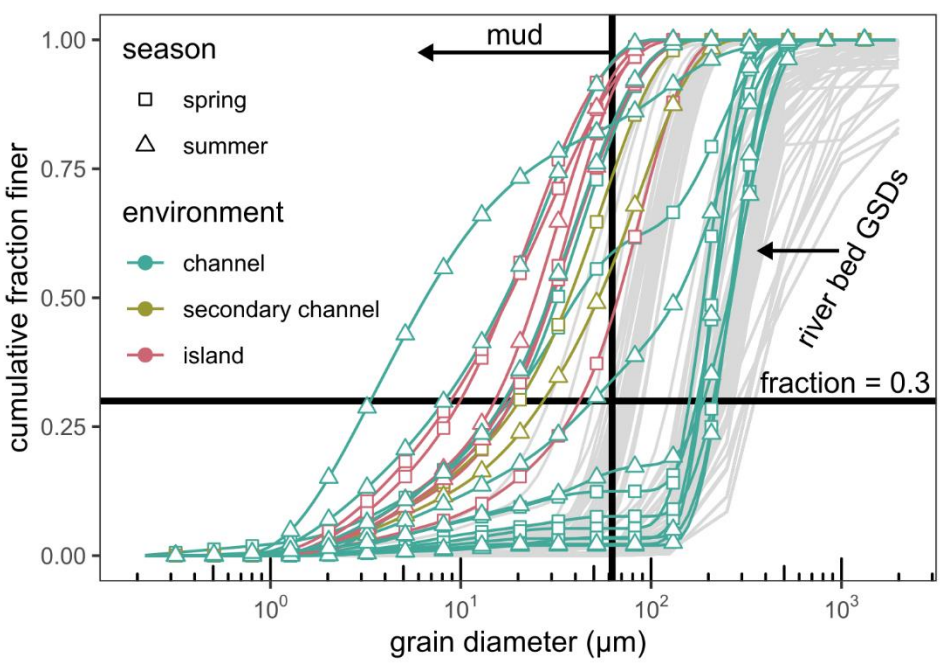

Figure 9. Cumulative distribution functions of bed grain size in WLD. River bed GSDs are from the data compilation of De Leeuw et al. (2020).

Bed sediment tended to be sandy in the channel and muddy in the island, including the secondary channel branch (Fig. 9). Muddier islands are probably because the sediment supply from the channel to the island is mud-dominated (Fig. 6a) and the lateral spreading of the flow over the shallow island wetland promotes a sediment convergence and hence deposition (Eq. 3). Despite the very low mud fractions in some channel beds (minimum mud fraction ~ 0.02), mud was present in the bed at all concentration-depth profile locations. Most of the sampled channel beds had mud fraction smaller than 0.3, which is a typical threshold between non-cohesive and cohesive bed behavior (e.g., Van Ledden et al., 2004; Van Rijn, 2020). In contrast to the bed sediment, the suspended sediment was mud-dominated for both channels and islands (Fig. 6a).

The presence of mud in the bed in the channels and islands of WLD implies that mud might be transported as bed-material load because mud must be in the bed to supply entrainment (Eq. 3), but washload also cannot be ruled out. Although the precise amount of mud in the bed that distinguishes washload and bed-material load is unclear, Lamb et al. (2020) showed that mud entrainment from mud-poor beds in global rivers could still sustain high suspended mud concentrations because the relatively slower floc settling velocities cause faster entrainment rates (Eq. 4).

4.4.6. Comparison 4: Does mud concentration respond to shear stress fluctuations?

The fourth comparison examines whether mud concentration changes with shear stress. If mud is bed-material load, then an increase in shear stress increases entrainment rate (Eq. 4) and concentration and vice versa. In contrast, the concentration of washload mud should be

insensitive to shear stress because washload mud is well-mixed in the water column at all typical transport conditions. This comparison is difficult to interpret in rivers because discharge typically drives higher sediment concentration by increasing sediment supply (i.e., through bank erosion and hillslope input) and shear stress (i.e., greater entrainment rate). Thus, the observed sediment concentration in rivers conflates the effects of washload supply and bed-material load entrainment. However, tidally influenced systems like WLD solve this issue because tides operate at shorter timescales than the incoming discharge. The input discharge and sediment supply can be relatively constant while the shear stress can change independently due to tides.

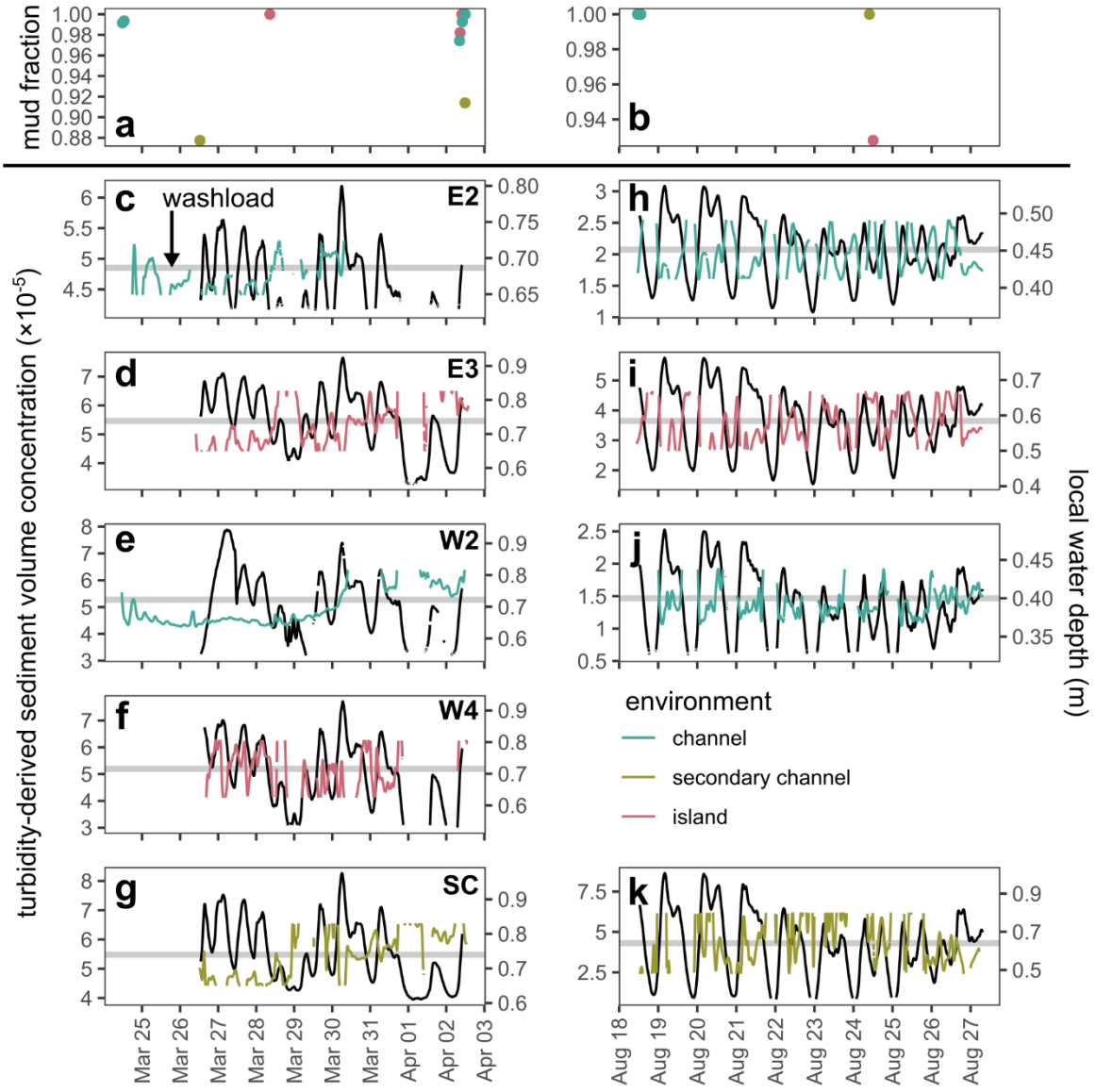

Figure 10. In situ turbidity and water depth time series results. (a) and (b): Mud fraction in suspended sediment samples taken to calibrate turbidity sensors. (c-k) Sediment

concentration and local water depth time series at the turbidity stations (Fig. 1bc). Colored curves correspond to the concentration time series. Black curves correspond to the local water depth time series. The data gaps are times in which the sensors were exposed to air.

Across all turbidity stations (Fig. 1), sediment concentration correlates inversely with the local water depth (Fig. 10). The turbidity-derived sediment concentration was calibrated to total sediment concentration (Nghiem, Salter, et al., 2022), but is a good proxy for mud concentration because the suspended sediment samples at the turbidity sensors show very high mud fractions of at least ~0.9 (Fig. 10ab). The anti-correlation between concentration and water depth is more apparent during the summer (Fig. 10h-k) than in the spring (Fig. 10c-g) because of the lower discharge (relative to tides) in the summer (Fig. 3e). Nonetheless, we interpreted the relationship of concentration and depth as the effect of tides altering the delta-wide water surface slope and shear stress. During falling tide, water surface elevation lowers first in the more offshore parts of the delta, thus drawing down the water surface slope from upstream. The steeper water surface slope causes higher shear stresses on the bed. Conversely, the onset of rising tide preferentially raises the water surface elevation in the more offshore waters and reduces the water surface slope and shear stress.

The inverse correlation between concentration and water depth suggests mud was transported as bed-material load in WLD because mud concentration was likely responding (Eq. 3) to shear stress-driven changes in local entrainment rate (Eq. 4) while the upstream discharge and coincident sediment supply were relatively constant (Fig. 3ae). Tides influenced the summer discharge because the lower discharge allowed the backwater zone to extend farther upstream (Fig. 3e), but discharge was otherwise steady averaging over tidal fluctuations. Although we installed the channel turbidity stations at the edges of channels (Fig. 1b), we expect that the same patterns held throughout the channels because they experienced to the same delta-wide hydraulics.

4.4.7 Comparison 5: Does flocculated mud follow bed-material entrainment theory?

The fifth comparison evaluates whether bed-material entrainment theory can predict the observed near-bed concentrations of flocculated mud. For each concentration-depth profile, we used the De Leeuw bed-material entrainment theory (Eq. 4) for the aggregated floc class and the unflocculated classes (Sections 3.2 and 3.5). We compared predictions with the measured floc near-bed concentrations from the Rouse-Vanoni equation fitting (Section 3.2). We found that bed-material entrainment theory agrees well with measurements for sand grain sizes (Fig. 11a), but tends to overpredict the mud concentrations (Fig. 11bc). We hypothesized that the overprediction for mud is because flocs on the bed might grow or densify by interacting with coarser bed sediment. For example, Tran and Strom (2019) found in experiments that deposited flocs tended to grow on the bed by aggregating with other flocs.

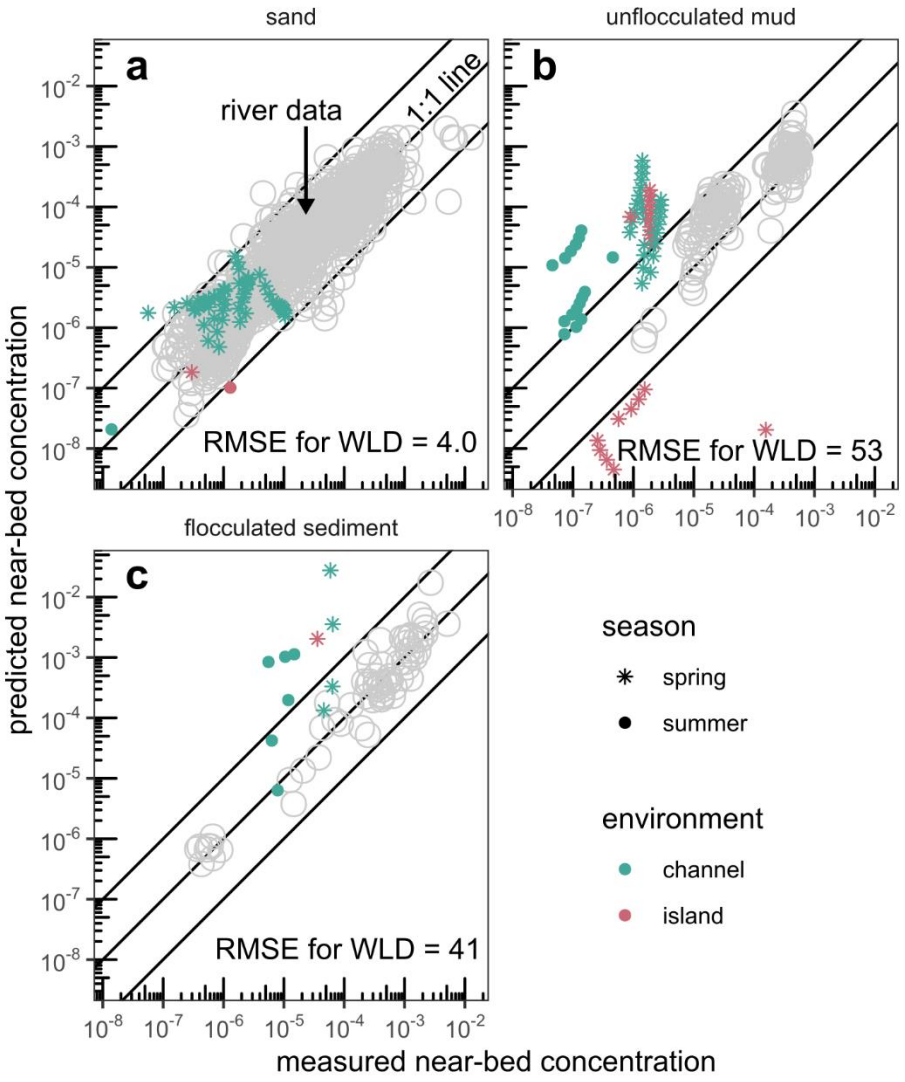

Figure 11. Near-bed concentration measurements from the Rouse-Vanoni equation fitting (Section 3.2) and predictions using the De Leeuw entrainment equation (Eq. 4). Gray circles represent the global river data compilation of De Leeuw et al. (2020) and Lamb et al. (2020).

To account for this possibility, we propose an entrainment floc cutoff diameter, D_{te} (m), which can be different from the floc cutoff diameter in the water column such that $D_{te} = \gamma D_{ts}$ and γ is the floc entrainment factor. We used the river concentration-depth profile and floc data compilation of Nghiem, Fischer, et al. (2022), to calibrate an empirical model for γ. For each concentration-depth profile, we calculated D_{te} as the floc cutoff diameter that produced an exact match between the predicted and measured near-bed concentrations for the floc class using Eq. (2) (Sections 3.2 and 3.5). We then calculated γ and regressed it against different possible controlling variables.

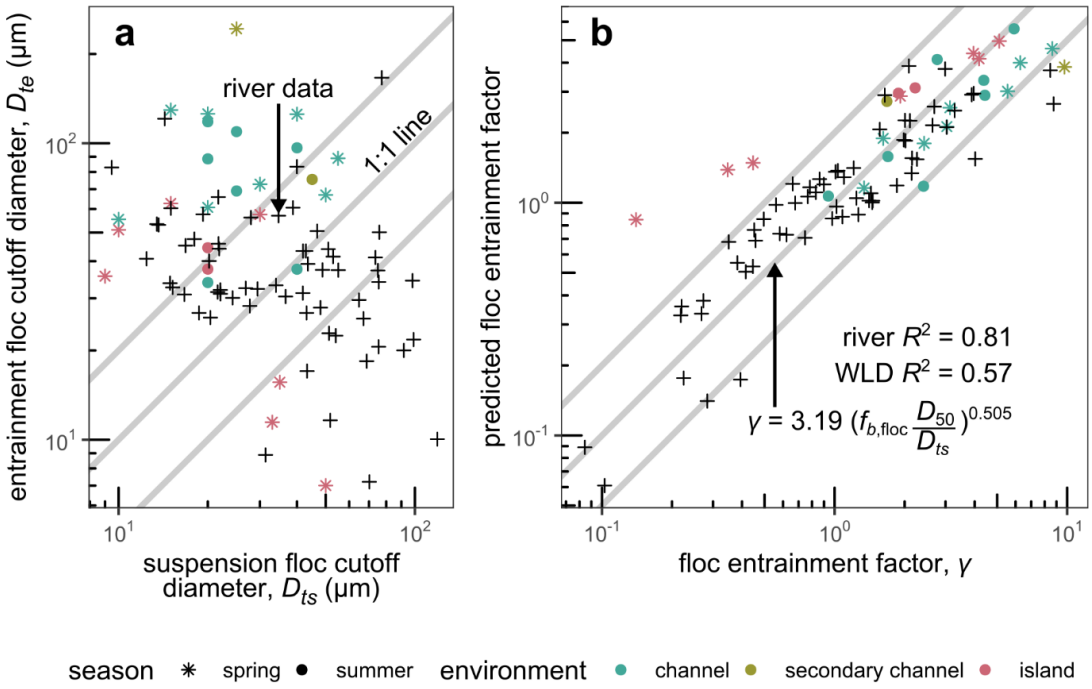

Figure 12. Floc cutoff diameter results. (a) Suspension and entrainment floc cutoff diameters. (b) Calculated and predicted floc entrainment factors. Crosses represent river floc data from Nghiem, Fischer, et al. (2022). River data were used to calibrate the γ model. In both panels, the lines about the 1:1 line represent a factor of 2.

Results show that the floc cutoff diameters for entrainment are typically larger than those in the water column for WLD data, whereas the two cutoff diameters are more similar, albeit scattered, for the river data compilation (Fig. 12a). One possible interpretation of the WLD data is that flocs cohere to coarser grains at the bed, causing them to become larger and/or denser (i.e., faster settling velocity) and more difficult to entrain. Through trial of many possible variables, we found a good correlation between γ and a proxy for the areal fraction of flocs on the bed, $f_{b,\mathrm{floc}}\,D_{50}/D_{ts}$ (Fig. 12b), where $f_{b,\mathrm{floc}}$ is the volume fraction of flocculated bed sediment (i.e., bed sediment finer than D_{ts}) and D_{50} (m) is the median bed grain size. $f_{b,\mathrm{floc}}\,D_{50}/D_{ts}$ represents the areal fraction of flocs on the bed because D_{ts} is a proxy for floc diameter and $f_{b,\mathrm{floc}} \sim D_{ts}^3/D_{50}^3$ is a volume fraction, meaning $f_{b,\mathrm{floc}}\,D_{50}/D_{ts} \sim D_{ts}^2/D_{50}^2$ is the areal fraction. We calibrated a power law using the Nghiem, Fischer, et al. (2022) river data compilation, leading to the empirical equation:

$$\gamma = 3.19\left(f_{b,\mathrm{floc}}\,D_{50}/D_{ts}\right)^{0.505} \quad (5)$$

with R^2 = 0.81 (Fig. 12b). Physically, Eq. (5) implies that flocs incorporate coarser grains (i.e., have a larger cutoff diameter) at or near the bed, compared to suspended flocs, as the areal fraction of flocs on the bed increases. Eq. (5) predicts well the floc cutoff factor in WLD

with R^2 = 0.57, especially considering that we did not train the model on the WLD data. We used Eq. (5) to calculate γ, which we multiplied by D_{ts} to predict D_{te}, and predict near-bed concentration (Sections 3.2 and 3.5).

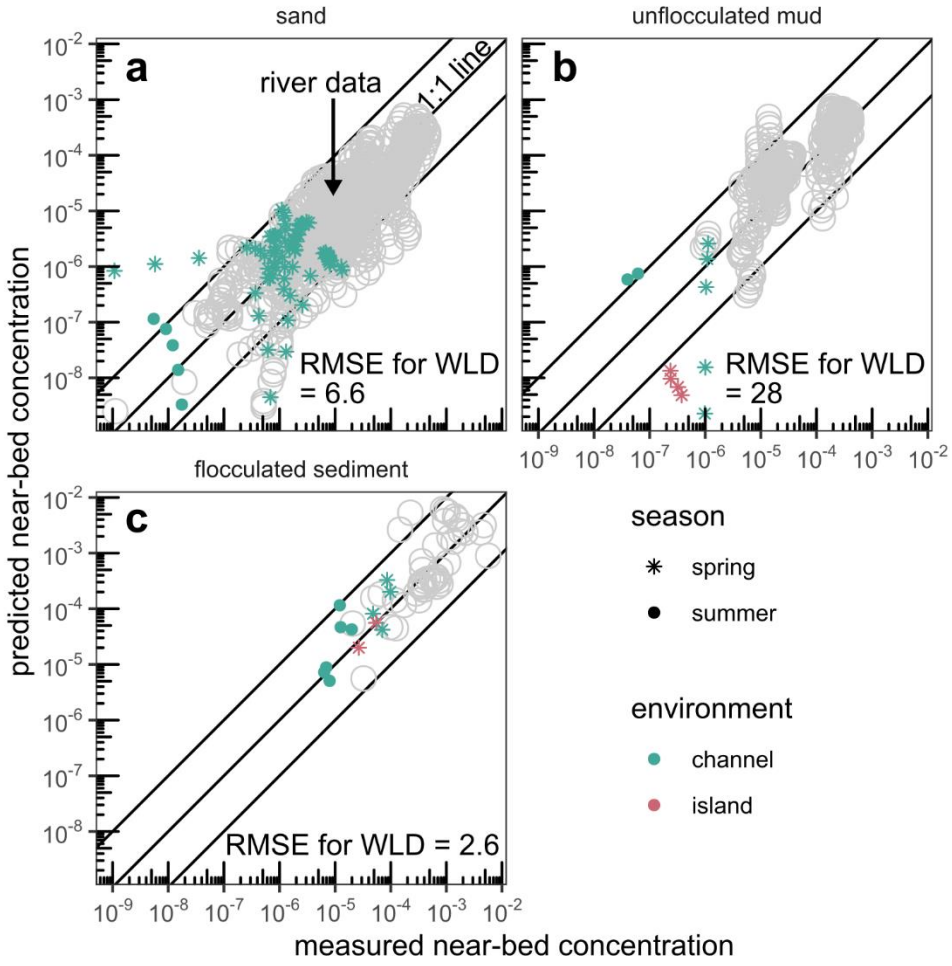

Figure 13. Near-bed concentration measurements from the Rouse-Vanoni equation fitting (Section 3.2) and predictions using the De Leeuw entrainment equation (Eq. 4) and Eq. (5) to account for the difference between the suspension and entrainment floc cutoff diameters. Gray circles represent the global river data compilation of Nghiem, Fischer, et al. (2022).

Using the new floc cutoff diameter for entrainment (i.e., combining Eq. 4 and 5) improves the agreement between the measured and predicted near-bed concentrations for the WLD flocculated sediment (Fig. 13). Since a larger cutoff diameter causes flocs to incorporate coarser grains, the agreements for all sediment types changed in Fig. 13 as compared to Fig. 11. The sand data in WLD shows slightly worse agreement (root mean square error, RMSE = 6.6 versus 4.0 in Fig. 11a), whereas the mud data are in greater agreement (RMSE = 53 to 28 for unflocculated mud in Fig. 11b; RMSE = 41 to 2.6 in Fig. 11c). For the WLD data, the entrainment floc cutoff diameter effectively increases the settling velocity and lowers the

entrainment rate for both unflocculated and flocculated mud (Eq. 4), thus compensating for the originally overestimated near-bed concentrations (Fig. 11bc).

4.5 Discussion

4.5.1 Is mud transported as washload or flocculated bed-material load in deltas?

We evaluated five comparisons of whether mud is transported as wash or bed-material load in a river delta (Sections 4.3-4.7). The comparisons are based on expectations that washload is well-mixed vertically and horizontally and controlled by upstream sediment supply due to its very slow settling velocity. All criteria showed that mud was more consistent with flocculated bed-material load than washload. First, we showed that mud finer than 9 to 55 μm, depending on the sampling site and time, is widely flocculated in WLD (Fig. 7) and thus has enhanced floc settling velocity. Second, remotely sensed sediment concentration maps of WLD suggests that mud concentration varies spatially in WLD again due to entrainment and deposition rather than being uniformly mixed as expected for washload (Fig. 8). Third, mud is present in the bed in non-negligible quantities in both channels and islands in WLD (Fig. 9). Fourth, in situ sediment concentration and water depth time series indicate that mud concentration varies in response to tidally driven shear stress changes due to entrainment and deposition dynamics (Fig. 10). Fifth, bed-material entrainment theory can match observed flocculated sediment concentration in WLD if a factor is used to enhance the sizes of primary particles incorporated into flocs near or at the bed (Fig. 11c). We interpret this fact to mean that flocs grow and densify by incorporating coarser bed sediment.

Based on these comparisons, we conclude that mud is transported as flocculated bed-material load for our measurement periods in WLD. We also expect this conclusion to hold in WLD generally because our data span the typical high and low annual discharges (Fig. 1d). Einstein and Chien (1953) postulated that the transport rate of fine sediment typically considered washload could theoretically be modeled using bed material entrainment, but the fine fraction in the bed is very sensitive to the flow conditions owing to its low amount and thus changes too quickly to be of any predictive value. Our results show that by increasing the settling velocity, flocculation increases the fine fraction in the bed and lengthens the time for the bed to respond to short fluctuations in sediment supply. Thus, we contend that the flocculated bed-material load treatment applies not only for rivers (Lamb et al., 2020), but also for deltas with muddier beds (Fig. 9).

4.5.2 Physical interpretation of near-bed flocs

The entrainment floc cutoff diameters are typically larger than the suspension floc cutoff diameters for WLD (Fig. 12a), meaning that floc growth at the bed, by incorporating coarser grains, is more common than floc break up. This idea is consistent with the experiments of Tran and Strom (2019) in which flocs on the bed tended to grow by cohering with other flocs by rolling and sliding, but rapidly returned to an equilibrium state with the local shear rate and sediment concentration once resuspended. Likewise, Lamb et al. (2020) identified two different floc settling velocities in a river data compilation: a median 0.34 mm s^{-1} for flocs

suspended in the water column and a faster 1.4 mm s^{-1}—corresponding to a floc cutoff diameter of 40 μm—for the floc entrainment rate near the bed. Although not described in their paper, the faster floc settling velocity produced better agreement between measured and predicted near-bed concentrations, consistent with our findings (Fig. 13c). Nonetheless, flocs in rivers are less sensitive, compared to WLD, to the use of a different entrainment floc cutoff diameter compared to that for suspension because lower areal fraction of flocs on the bed causes the cutoff diameters to scatter around a 1:1 correlation (Figure 12). For general cases, our results show that the entrainment floc cutoff diameter works for both rivers and the WLD (Fig. 13).

We found that the amount of growth or densification of flocs near the bed increased with the areal fraction of flocs on the bed possibly because greater floc concentration leads to higher collision and aggregation frequency between flocs and coarser bed sediment. However, this process has a limit as floc concentration increases. For a fully mud bed, the bed cohesive strength likely controls entrainment rather than floc deposition and entrainment (Winterwerp, 2002). The transition occurs when the floc concentration reaches the gelling concentration, upon which flocs form a space-filling network at the bed and transforms into a more consolidated fluid mud bed (Tran and Strom, 2019; Winterwerp, 2002). Using the theory of Winterwerp (2002), we calculated a typical gelling concentration in WLD of 0.04, which is about two orders of magnitude higher than observed floc concentrations (Nghiem et al., 2024). Thus, mud in WLD, as well as other rivers (Lamb et al., 2020; Nghiem et al., 2022), conforms to flocculated bed-material load theory without the need to invoke a critical cohesive bed strength as is typical for cohesive entrainment formulations (e.g., Partheniades, 1965).

4.5.3 Modeling mud as flocculated bed-material load

Bed-material entrainment theory provides a unified entrainment framework for mud and sand, which can streamline sediment transport models. This framework contrasts with most current approaches like Delft3D (Delft Hydraulics, 2025) that use different formulas for mud and sand. Although floc properties might change in space and time, these variations can be minimal within a given system because negative feedbacks between turbulence, sediment concentration, grain size, and sediment mineralogy can maintain floc settling velocity (Nghiem et al., 2024). Therefore, a single floc settling velocity, once adjusted to account for near-bed floc effects (Fig. 13), might be adequate to predict the entrainment rate of flocculated sediment.

4.5.4 The spectrum between washload and bed-material load

Although washload and bed-material load are often treated as two distinct transport modes, we stress that washload is actually a special case of bed-material load in the limit of very slow settling velocity. This idea is illustrated by the advection length, $l_a = \bar{u}h/w_s$, which is the typical horizontal distance that sediment travels before depositing on the bed (Ganti et al., 2014; Lamb et al., 2010). Ganti et al. (2014) showed that the advection length sets the minimum length scale of morphodynamic landforms because sediment mostly advects

through shorter length scales and reflects non-local supply. In the same vein, we argue that the advection length can be used to distinguish washload and bed-material load given the length scale of interest (Venditti et al., 2015). Regardless of settling velocity, sediment can be modeled as bed-material load so long as, for mud, the gelling concentration is not achieved and flocs do not coalesce into a cohesive bed layer (Fig. 14). But if the length scale of interest is much shorter than the advection length, then washload can be a justified simplification of bed-material load (Fig. 14) because the extremely slow settling velocity brings erosion and deposition fluxes to zero and precludes concentration gradients in time and space yielding uniformly mixed washload concentration (Eq. 3). Washload simply advects past shorter length scales without bed interaction because it settles too slowly to reach the bed.

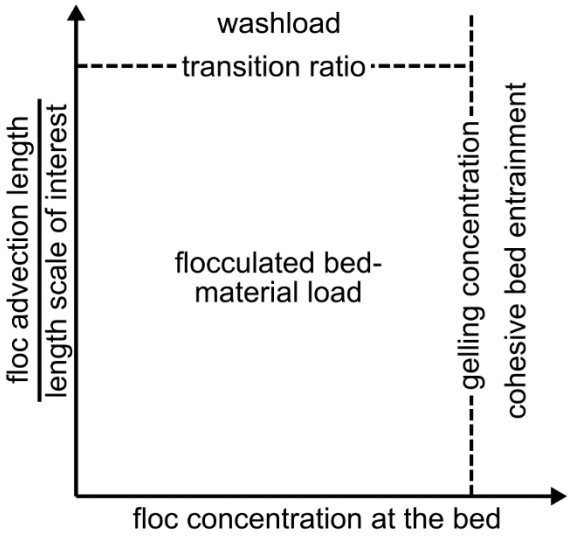

Figure 14. Conceptual diagram of the phase space for different treatments of flocculated mud transport.

In WLD, the differences between channel and island highlight the spectrum between washload and bed-material load according to the advection length (Fig. 14). In the channels, we measured typical values of $\bar{u}$ = 0.5 m s^{-1} and h = 3 m (Fig. 4). In Mike Island, we measured typical values of $\bar{u}$ = 0.1 m s^{-1} and h = 0.6 m (Fig. 5). Using a typical floc settling velocity of 0.3 mm s^{-1} in WLD (Nghiem et al., 2024) leads to floc advection lengths of 5000 m in the channels and 200 m in Mike Island. The kilometer-scale floc advection length in the channels is consistent with the kilometer-scale downstream decrease in concentration observed in the AVIRIS-NG concentration maps (Fig. 8f). The floc advection length in Mike Island is shorter than the width of Mike Island (~900 m). Accordingly, the bed in Mike Island contains abundant mud in contrast to the more modest amounts found in the channel bed (Fig. 9) because mud should behave more like bed-material load in the island than in the channel as predicted by the shorter floc advection length relative to island (or channel) length scale. Higher concentration gradients in the islands also point to mud behaving more like bed-material load in islands (Fig. 8ce). In general, given sediment and flow conditions, the

appropriateness of the washload simplification depends on the length scale of interest. For WLD, washload mud is probably a poor assumption for studying delta-wide sedimentation because the delta radius is ~10 km, which exceeds the typical floc advection length in channels. In contrast, the length scales of bars and dunes are much smaller than the floc advection length in channels, making washload a reasonable assumption.

4.6 Conclusion

Here we explored five consistency tests of whether mud is transported as washload or bed-material load in the Wax Lake Delta using suspended sediment concentration-depth profiles, bed sediment samples, in situ concentration and water depth time series, and remotely sensed sediment concentration maps. We concluded that mud behaves as flocculated bed-material load in WLD because it is flocculated, present in the bed, responds to shear stress fluctuations, is spatially heterogeneous, and can be predicted by bed-material entrainment theory. We found better agreement with bed-material entrainment theory by incorporating a larger near-bed floc cutoff diameter, implying that flocs are larger and/or denser near the bed surface, as compared to suspended flocs, because they incorporate coarser bed sediment. This modification affects entrainment rate by increasing floc settling velocity and fraction of flocculated bed sediment, at least up to the limit at which cohesive bed strength dominates mud entrainment. Together, these findings show that mud and sand can be modeled together under the unified framework of bed-material load in rivers and deltas.

4.7 Acknowledgments

The NASA Delta-X project is funded by the Science Mission Directorate's Earth Science Division through the Earth Venture Suborbital-3 Program NNH17ZDA001N-EVS3. We thank Mark Simard, Cathleen Jones, and staff at NASA/Caltech Jet Propulsion Lab for leading and administering the Delta-X project. We acknowledge funding from NASA FINESST Grant 80NSSC20K1645 to JAN and NSF Award 2136991 to MPL. We thank John Bourg, Madison Douglas, Eric Prokocki, Maryn Sanders, Adam Songy, and participants in Caltech's fall 2019 Ge 121a class for field assistance. We thank Michael Denbina for calibrating the water surface elevation time series data. We thank Alex Christensen and Dongchen Wang for helpful feedback and discussion.

4.8 Data Availability Statement

The WLD grain size distribution and suspended sediment concentration data are available online at the Oak Ridge National Laboratory Distributed Active Archive Center (ORNL DAAC) via https://doi.org/10.3334/ORNLDAAC/2379 (Nghiem, Salter, and Lamb, 2024) and https://doi.org/10.3334/ORNLDAAC/2382 (Nghiem, Salter, and Lamb, 2025). The AVIRIS-NG sediment concentration maps are available online at the ORNL DAAC via https://doi.org/10.3334/ORNLDAAC/2152 (Fichot and Harringmeyer, 2023). The in situ turbidity and water depth time series data are available online at the ORNL DAAC via https://doi.org/10.3334/ORNLDAAC/2241 (Nghiem, Salter, et al., 2022). The WLD floc

entrainment cutoff diameter data are available online at https://doi.org/10.22002/45yvp-xv214 (Nghiem, Li, et al., 2025).

4.9 References

Arulanandan, K. (1975). Fundamental aspects of erosion of cohesive soils. *Journal of the Hydraulics Division*, *101*(5), 635–639. https://doi.org/10.1061/JYCEAJ.0004366

Baronas, J. J., Stevenson, E. I., Hackney, C. R., Darby, S. E., Bickle, M. J., Hilton, R. G., Larkin, C. S., Parsons, D. R., Myo Khaing, A., & Tipper, E. T. (2020). Integrating suspended sediment flux in large alluvial river channels: Application of a synoptic Rouse-based model to the Irrawaddy and Salween rivers. *Journal of Geophysical Research: Earth Surface*, *125*(9), e2020JF005554. https://doi.org/10.1029/2020JF005554

Bianchi, T. S., Mayer, L. M., Amaral, J. H., Arndt, S., Galy, V., Kemp, D. B., Kuehl, S. A., Murray, N. J., & Regnier, P. (2024). Anthropogenic impacts on mud and organic carbon cycling. *Nature Geoscience*, 1–11. https://doi.org/10.1038/s41561-024-01405-5

Bouchez, J., Gaillardet, J., France-Lanord, C., Maurice, L., & Dutra-Maia, P. (2011). Grain size control of river suspended sediment geochemistry: Clues from Amazon River depth profiles. *Geochemistry, Geophysics, Geosystems*, *12*(3). https://doi.org/10.1029/2010GC003380

Church, M. (2006). Bed material transport and the morphology of alluvial river channels. *Annual Reviews of Earth and Planetary Science*, *34*, 325–354. https://doi.org/10.1146/annurev.earth.33.092203.122721

De Leeuw, J., Lamb, M. P., Parker, G., Moodie, A. J., Haught, D., Venditti, J. G., & Nittrouer, J. A. (2020). Entrainment and suspension of sand and gravel. *Earth Surface Dynamics*, *8*(2), 485–504. https://doi.org/10.5194/esurf-8-485-2020

Delft Hydraulics. (2025). Delft3D-FLOW user manual. *Delft, the Netherlands*.

Dunne, K. B. J., Nittrouer, J. A., Abolfazli, E., Osborn, R., & Strom, K. B. (2024). Hydrodynamically-driven deposition of mud in river systems. *Geophysical Research Letters*, *51*(4), e2023GL107174. https://doi.org/10.1029/2023GL107174

Dunne, K. B., & Jerolmack, D. J. (2020). What sets river width? *Science Advances*, *6*(41), eabc1505. https://doi.org/10.1126/sciadv.abc1505

Einstein, H. A. (1950). *The bed-load function for sediment transportation in open channel flows* (Issue 1026). US Department of Agriculture.

Einstein, H. A. (1968). Deposition of suspended particles in a gravel bed. *Journal of the Hydraulics Division*, *94*(5), 1197–1206. https://doi.org/10.1061/JYCEAJ.0001868

Einstein, H. A., Anderson, A. G., & Johnson, J. W. (1940). A distinction between bed-load and suspended load in natural streams. *Eos, Transactions American Geophysical Union, 21*(2), 628–633. https://doi.org/10.1029/TR021i002p00628

Einstein, H. A., & Chien, N. (1953). Can the rate of wash load be predicted from the bed-load function? *Eos, Transactions American Geophysical Union*, *34*(6), 876–882. https://doi.org/10.1029/TR034i006p00876

Ferguson, R. I., & Church, M. (2004). A Simple Universal Equation for Grain Settling Velocity. *Journal of Sedimentary Research*, *74*(6), 933–937. https://doi.org/10.1306/051204740933

Fichot, C. G., & Harringmeyer, J. (2023). Delta-X: AVIRIS-NG L3-derived Water Quality, TSS, and Turbidity, MRD, V3. *ORNL DAAC*. https://doi.org/10.3334/ORNLDAAC/2152

Galy, V., France-Lanord, C., & Lartiges, B. (2008). Loading and fate of particulate organic carbon from the Himalaya to the Ganga–Brahmaputra delta. *Geochimica et Cosmochimica Acta*, *72*(7), 1767–1787. https://doi.org/10.1016/j.gca.2008.01.027

Ganti, V., Lamb, M. P., & McElroy, B. (2014). Quantitative bounds on morphodynamics and implications for reading the sedimentary record. *Nature Communications*, *5*(1), 3298. https://doi.org/10.1038/ncomms4298

García, M. H. (2008). Sediment Transport and Morphodynamics. *Sedimentation Engineering: Processes, Measurements, Modeling, and Practice*, 21–163. https://doi.org/10.1061/9780784408148.ch02

Garcia, M., & Parker, G. (1991). Entrainment of Bed Sediment into Suspension. *Journal of Hydraulic Engineering*, *117*(4), 414–435. https://doi.org/10.1061/(ASCE)0733-9429(1991)117:4(414)

Geleynse, N., Hiatt, M., Sangireddy, H., & Passalacqua, P. (2015). Identifying environmental controls on the shoreline of a natural river delta. *Journal of Geophysical Research: Earth Surface*, *120*(5), 877–893. https://doi.org/10.1002/2014JF003408

Gerbersdorf, S. U., Jancke, T., Westrich, B., & Paterson, D. M. (2008). Microbial stabilization of riverine sediments by extracellular polymeric substances. *Geobiology*, *6*(1), 57–69. https://doi.org/10.1111/j.1472-4669.2007.00120.x

Harringmeyer, J. P., Ghosh, N., Weiser, M. W., Thompson, D. R., Simard, M., Lohrenz, S. E., & Fichot, C. G. (2024). A hyperspectral view of the nearshore Mississippi River Delta: Characterizing suspended particles in coastal wetlands using imaging spectroscopy. *Remote Sensing of Environment*, *301*, 113943. https://doi.org/10.1016/j.rse.2023.113943

Hiatt, M., & Passalacqua, P. (2015). Hydrological connectivity in river deltas: The first-order importance of channel-island exchange. *Water Resources Research, 51*(4), 2264–2282. https://doi.org/10.1002/2014WR016149

Hill, K. M., Gaffney, J., Baumgardner, S., Wilcock, P., & Paola, C. (2017). Experimental study of the effect of grain sizes in a bimodal mixture on bed slope, bed texture, and the transition to washload. *Water Resources Research, 53*(1), 923–941. https://doi.org/10.1002/2016WR019172

Jacobs, W., Le Hir, P., Van Kesteren, W., & Cann, P. (2011). Erosion threshold of sand–mud mixtures. *Continental Shelf Research, 31*(10), S14–S25. https://doi.org/10.1016/j.csr.2010.05.012

Jensen, D., Simard, M., Cavanaugh, K., Sheng, Y., Fichot, C. G., Pavelsky, T., & Twilley, R. (2019). Improving the Transferability of Suspended Solid Estimation in Wetland and Deltaic Waters with an Empirical Hyperspectral Approach. *Remote Sensing, 11*(13), 1629. https://doi.org/10.3390/rs11131629

Kim, W., Mohrig, D., Twilley, R., Paola, C., & Parker, G. (2009). Is It Feasible to Build New Land in the Mississippi River Delta? *Eos, Transactions American Geophysical Union, 90*(42), 373–374. https://doi.org/10.1029/2009EO420001

Komar, P. D. (1980). Modes of sediment transport in channelized water flows with ramifications to the erosion of the Martian outflow channels. *Icarus, 42*(3), 317–329. https://doi.org/10.1016/0019-1035(80)90097-4

Lamb, H. (1945). *Hydrodynamics* (6th ed). Dover publications; WorldCat.

Lamb, M. P., De Leeuw, J., Fischer, W. W., Moodie, A. J., Venditti, J. G., Nittrouer, J. A., Haught, D., & Parker, G. (2020). Mud in rivers transported as flocculated and suspended bed material. *Nature Geoscience, 13*(8), 566–570. https://doi.org/10.1038/s41561-020-0602-5

Lamb, M. P., McElroy, B., Kopriva, B., Shaw, J., & Mohrig, D. (2010). Linking river-flood dynamics to hyperpycnal-plume deposits: Experiments, theory, and geological implications. *GSA Bulletin, 122*(9–10), 1389–1400. https://doi.org/10.1130/B30125.1

Lane, E. W. (1947). Report of the subcommittee on sediment terminology. *Eos, Transactions American Geophysical Union, 28*(6), 936–938. https://doi.org/10.1029/TR028i006p00936

Latimer, R. A., & Schweizer, C. W. (1951). *The Atchafalaya River Study: A report based upon engineering and geological studies of the enlargement of Old and Atchafalaya Rivers*. United States Army Corps of Engineers. http://hdl.handle.net/11681/30764

Lupker, M., France-Lanord, C., Lavé, J., Bouchez, J., Galy, V., Métivier, F., Gaillardet, J., Lartiges, B., & Mugnier, J.-L. (2011). A Rouse-based method to integrate the chemical

composition of river sediments: Application to the Ganga basin. *Journal of Geophysical Research: Earth Surface*, *116*(F4). https://doi.org/10.1029/2010JF001947

Mehta, A. J. (1993). *Nearshore and Estuarine Cohesive Sediment Transport* (Vol. 42). American Geophysical Union.

Mehta, A. J., & McAnally, W. H. (2008). Fine grained sediment transport. *Sedimentation Engineering: Processes, Measurements, Modeling, and Practice*, 253–306. https://doi.org/10.1061/9780784408148

Mooneyham, C., & Strom, K. (2018). Deposition of suspended clay to open and sand-filled framework gravel beds in a laboratory flume. *Water Resources Research*, *54*(1), 323–344. https://doi.org/10.1002/2017WR020748

Nezu, I., & Nakagawa, H. (1993). *Turbulence in Open-Channel Flows*. Routledge.

Nghiem, J. A., Fischer, W. W., Li, G. K., & Lamb, M. P. (2022). A Mechanistic Model for Mud Flocculation in Freshwater Rivers. *Journal of Geophysical Research: Earth Surface*, *127*(5), e2021JF006392. https://doi.org/10.1029/2021JF006392

Nghiem, J. A., Li, G. K., Harringmeyer, J. P., Salter, G., Fichot, C. G., Cortese, L., & Lamb, M. P. (2024). Testing floc settling velocity models in rivers and freshwater wetlands. *Earth Surface Dynamics*, *12*(6), 1267–1294. https://doi.org/10.5194/esurf-12-1267-2024

Nghiem, J. A., Li, G. K., Salter, G., & Lamb, M. P. (2025). *Floc cutoff diameter data for rivers and the Wax Lake Delta* [Dataset]. CaltechDATA. https://doi.org/10.22002/45yvp-xv214

Nghiem, J., Salter, G., & Lamb, M. P. (2024). Delta-X: Bed and Suspended Sediment Grain Size, MRD, LA, USA, 2019-2021, V3. *ORNL DAAC*. https://doi.org/10.3334/ORNLDAAC/2379

Nghiem, J., Salter, G., & Lamb, M. P. (2025). Delta-X: Sediment Core Grain Size Distribution, Wax Lake Delta, MRD, LA. *ORNL DAAC*. https://doi.org/10.3334/ORNLDAAC/2382

Nghiem, J., Salter, G., Wright, K. A., Passalacqua, P., & Lamb, M. P. (2022). Delta-X: Turbidity, Water and Air Pressure, Temperature, MRD, Louisiana, 2021, V4. *ORNL DAAC*. https://doi.org/10.3334/ORNLDAAC/2241

Packman, A. I., & Brooks, N. H. (2001). Hyporheic exchange of solutes and colloids with moving bed forms. *Water Resources Research*, *37*(10), 2591–2605. https://doi.org/10.1029/2001WR000477

Parker, G. (1978). Self-formed straight rivers with equilibrium banks and mobile bed. Part 1. The sand-silt river. *Journal of Fluid Mechanics*, *89*(1), 109–125. https://doi.org/10.1017/S0022112078002499

Partheniades, E. (1965). Erosion and deposition of cohesive soils. *Journal of the Hydraulics Division*, *91*(1), 105–139. https://doi.org/10.1061/JYCEAJ.0001165

Roberts, H. H., Adams, R. D., & Cunningham, R. H. W. (1980). Evolution of sand-dominant subaerial phase, Atchafalaya Delta, Louisiana. *AAPG Bulletin*, *64*(2), 264–279. https://doi.org/10.1306/2F918964-16CE-11D7-8645000102C1865D

Rouse, H. (1937). Modern conceptions of the mechanics of fluid turbulence. *Transactions of the American Society of Civil Engineers*, *102*(1), 463–505. https://doi.org/10.1061/TACEAT.0004872

Salter, G., & Lamb, M. P. (2022). Autocyclic secondary channels stabilize deltaic islands undergoing relative sea level rise. *Geophysical Research Letters*, e2022GL098885. https://doi.org/10.1029/2022GL098885

Sendrowski, A., Castañeda-Moya, E., Twilley, R., & Passalacqua, P. (2021). Biogeochemical and hydrological variables synergistically influence nitrate variability in coastal deltaic wetlands. *Journal of Geophysical Research: Biogeosciences*, *126*(9), e2020JG005737. https://doi.org/10.1029/2020JG005737

Shrivastava, S., Stewardson, M. J., & Arora, M. (2020). Distribution of clay-sized sediments in streambeds and influence of fine sediment clogging on hyporheic exchange. *Hydrological Processes*, *34*(26), 5674–5685. https://doi.org/10.1002/hyp.13988

Soulsby, R. L., & Dyer, K. R. (1981). The form of the near-bed velocity profile in a tidally accelerating flow. *Journal of Geophysical Research: Oceans*, *86*(C9), 8067–8074. https://doi.org/10.1029/JC086iC09p08067

Spasojevic, M., & Holly, F. M. (1990). 2-D bed evolution in natural watercourses—New simulation approach. *Journal of Waterway, Port, Coastal, and Ocean Engineering*, *116*(4), 425–443. https://doi.org/10.1061/(ASCE)0733-950X(1990)116:4(425)

Strom, K., & Keyvani, A. (2011). An explicit full-range settling velocity equation for mud flocs. *Journal of Sedimentary Research*, *81*(12), 921–934. https://doi.org/10.2110/jsr.2011.62

Tran, D., & Strom, K. (2019). Floc sizes and resuspension rates from fresh deposits: Influences of suspended sediment concentration, turbulence, and deposition time. *Estuarine, Coastal and Shelf Science*, *229*, 106397. https://doi.org/10.1016/j.ecss.2019.106397

Van Ledden, M., Van Kesteren, W. G. M., & Winterwerp, J. C. (2004). A conceptual framework for the erosion behaviour of sand–mud mixtures. *Continental Shelf Research*, *24*(1), 1–11. https://doi.org/10.1016/j.csr.2003.09.002

Van Leussen, W. (1988). Aggregation of Particles, Settling Velocity of Mud Flocs A Review. In J. Dronkers & W. van Leussen (Eds.), *Physical Processes in Estuaries* (pp. 347–403). Springer. https://doi.org/10.1007/978-3-642-73691-9_19

Van Rijn, L. C. (2020). Erodibility of mud–sand bed mixtures. *Journal of Hydraulic Engineering*, *146*(1), 04019050. https://doi.org/10.1061/(ASCE)HY.1943-7900.0001677

Venditti, J. G., Domarad, N., Church, M., & Rennie, C. D. (2015). The gravel-sand transition: Sediment dynamics in a diffuse extension. *Journal of Geophysical Research: Earth Surface*, *120*(6), 943–963. https://doi.org/10.1002/2014JF003328

Winterwerp, J. C. (1998). A simple model for turbulence induced flocculation of cohesive sediment. *Journal of Hydraulic Research*, *36*(3), 309–326. https://doi.org/10.1080/00221689809498621

Winterwerp, J. C. (2002). On the flocculation and settling velocity of estuarine mud. *Continental Shelf Research*, *22*(9), 1339–1360. https://doi.org/10.1016/S0278-4343(02)00010-9

Winterwerp, J. C., Van Kesteren, W. G. M., Van Prooijen, B., & Jacobs, W. (2012). A conceptual framework for shear flow–induced erosion of soft cohesive sediment beds. *Journal of Geophysical Research: Oceans*, *117*(C10). https://doi.org/10.1029/2012JC008072

Zeichner, S. S., Nghiem, J., Lamb, M. P., Takashima, N., De Leeuw, J., Ganti, V., & Fischer, W. W. (2021). Early plant organics increased global terrestrial mud deposition through enhanced flocculation. *Science*, *371*(6528), 526–529. https://doi.org/10.1126/science.abd0379

Chapter 5

SEDIMENT TRANSPORT BETWEEN CHANNELS AND ISLANDS IN A RIVER-DOMINATED DELTA

Abstract

River deltas are important landforms because they build coastal land, but they are at risk of drowning due to sea level rise. Primary channels divide deltas into islands, which must accrete with sediment fast enough for deltas to keep pace with sea level rise. However, field observations of sediment transport between primary channels and islands are lacking. We conducted a field study in the Wax Lake Delta, Louisiana, part of the Mississippi River Delta complex, to investigate island sediment transport mechanisms in a river-dominated delta. Hydraulic roughness measurements in a vegetated island wetland constrain the hitherto wide variability in roughness treatments used in past hydrodynamic models. In situ water surface elevation and sediment concentration time series reveal that tall island levees can block water and sediment. Falling tide increases bed shear stress, entrainment, and hence sediment concentration in primary channels. A simple backwater model indicates that a dynamic interplay of flow depth, velocity, and lateral water surface slope into the island determines the discharge into the island wetland, which is diminished at very high depths when the hydraulic gradient becomes too shallow. Overall, sediment flux into the island scales most importantly with discharge into the island because the variation in discharge exceeds the tidal modulation of primary channel sediment concentration. Island flows are sufficiently slow and shallow to facilitate the settling of mud in the island, including abundant mud in recent island deposits that drives recent delta growth.

5.1 Introduction

River deltas are increasingly under threat of drowning because relative sea level rate exceeds aggradation rate in many deltas (Blum and Roberts, 2009; Paola et al., 2011; Giosan et al., 2014). In deltas, channels successively bifurcate downstream (e.g., Edmonds and Slingerland, 2008) and form islands in between. Islands are the dynamic building blocks of deltas because they are the shallow hotspots of sedimentation and must keep pace with sea level rise for the delta to survive (Nardin et al., 2016; Salter and Lamb, 2022). Island sedimentation might also be an important organic carbon sink (Galy et al., 2007; Shields et al., 2017).

Understanding sediment transport between delta channels and islands is critical because it controls sediment supply to and retention in islands. The pathway of sediment into delta islands can be conceptualized into (1) sediment source from island-bounding primary

channels, (2) sediment influx into islands, and (3) sediment fluxes within islands. Primary channels (i.e., distributaries) separate individual islands and are the immediate source of water and sediment for islands (Fig. 1a). Sediment can enter the island via diffuse flooding into the shallow island wetland (Fig. 1b) and/or flow through secondary channels cutting across islands (Fig. 1a). Sediment transport within the island determines whether sediment is retained in the island.

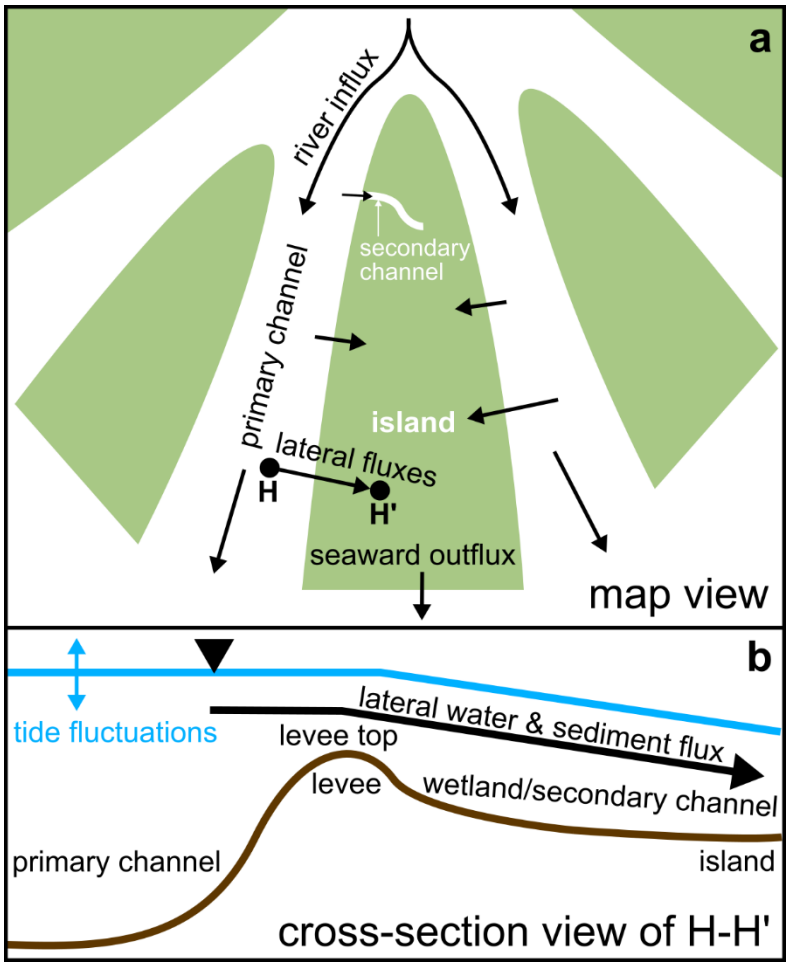

Figure 1. River delta diagram. (a) Diagram of a river delta in map view. (b) Diagram of a cross-section through a primary channel and island at the edge of an island.

Prior studies have shed light on these delta island sediment processes. Olliver et al. (2020) simulated hydrodynamics and sediment transport using a numerical model of the Wax Lake Delta (WLD), Louisiana, USA, a river-dominated delta in the Mississippi River Delta complex, and found that greater river discharge increases the net river sediment export into WLD. They also found that tides, although less important than river discharge, can enhance island inundation and sediment flux entering islands. Hiatt and Passalacqua (2015) conducted fieldwork in WLD and showed that islands diverted significant volumes of water from primary channels according to hydrological connectivity. They argued that lateral flow accesses more landward, higher elevation (i.e., proximal) parts of islands

typically through secondary channels, which bypass the taller levees that would otherwise block flow (Fig. 1b). Hydrological connectivity is greater in more seaward, lower elevation (i.e., distal) parts of islands where laterally extensive floods can frequently overtop levees. This idea is consistent with Wagner et al. (2017), who differenced two lidar surveys of WLD and showed that distal elevation parts of islands aggraded more than proximal parts because they were more often flooded. Overall, Olliver and Edmonds (2021) demonstrated in a follow up modeling study that faster island sedimentation rates are linked to greater hydrological connectivity to primary channels. In particular, river discharge not only enhances island sedimentation rate by supplying more sediment and increasing hydrological connectivity, but also decreases sediment retention efficiency because more sediment bypasses the delta (Olliver et al., 2020).

Aside from river and tides, vegetation has also been highlighted as a key factor affecting flow and sedimentation in deltas. Vegetation can not only increase sedimentation by slowing flow and inducing settling (Stumpf, 1983; Styles et al., 2021), but also prevent sedimentation by blocking flow from entering islands (Nardin et al., 2016; Olliver et al., 2020). As such, intermediate vegetation density has been suggested to optimize island sedimentation (Nardin and Edmonds, 2014). Quantitatively, the presence of vegetation modifies hydraulic roughness (Baptist et al., 2007). Past studies of river delta hydrodynamic models used enhanced roughness in vegetated islands to account for vegetation effects on the flow (e.g., Olliver et al., 2020; Wright et al., 2022; Cortese et al., 2024; Feizabadi et al., 2024). However, they used roughness as a tuning parameter because they lacked hydraulic roughness measurements in islands.

Although prior studies inform sediment transport expectations in deltas, they are limited because many of these studies rely on numerical models with simplified sediment transport physics and lack hydraulic and sediment field measurements for validation. For example, numerical models are restricted to few grain sizes (Nardin and Edmonds, 2014; Olliver et al., 2020; Cortese et al., 2024). Moreover, mud (grains < 62.5 μm) comprises much of the sediment load in river deltas (Giosan et al., 2014; Esposito et al., 2017; Nghiem et al., 2024), but predicting mud transport in models is difficult because mud cohesion is highly heterogeneous and strongly controls mud entrainment and deposition fluxes (e.g., Mehta and McAnally, 2008). Sediment transport field studies in river deltas are required to establish baseline understanding of sediment flux and accretion in islands.

We conducted fieldwork at the Wax Lake Delta to identify the mechanisms that (1) set the sediment source in primary channels, (2) drive water and sediment flux into islands, and (3) and control sediment transport and accretion within islands of a river-dominated delta. We introduce the study site and field approach in Section 2 and methods in Section 3. Although storms and waves can periodically contribute to island sedimentation and erosion in WLD (Walker and Hammack, 2000; Bevington et al., 2017; Styles et al., 2021; Cortese et al., 2024), we focused on studying river discharge and tides because they operate continuously. Our fieldwork strategy was to measure detailed local data on hydraulics (depth, flow velocity, discharge, roughness, and shear stress), suspended sediment (grain size, concentration, and flux), and bed sediment (grain size) in channels and a delta island to

compare patterns across space (Section 4). In particular, our measurements provide key observations of hydraulic roughness in a vegetated delta island that can inform river delta hydrodynamic models. Next, to interpolate our results across time, we used in situ sensors to measure water surface elevation and sediment concentration time series, from which we modeled the time series of discharge and sediment flux between primary channels and a wetland and secondary channel (Section 5). In Section 6, we summarize delta island sediment transport mechanisms and discuss their implications for delta sedimentation and resilience.

5.2 Study Site and Approach Overview

We conducted fieldwork in the Wax Lake Delta as part of the NASA Delta-X project. WLD is located along the coast of Louisiana and is fed water and sediment by the lower Mississippi River via the Atchafalaya River and the Wax Lake Outlet, which was dredged in 1942 (Fig. 2a; Latimer and Schweizer, 1951). Significant areas of delta islands became subaerial following the 1973 Mississippi River flood and have continued to aggrade and prograde seaward without major human influence (Roberts et al., 1980; Jensen et al., 2022). The exposure and inundation of islands in WLD depend on the interactions between river discharge, tides, wind, and vegetation (Geleynse et al., 2015).

We completed fieldwork in March-April 2021 (spring campaign) and August 2021 (summer campaign). The spring campaign represents a high river discharge scenario because the discharge entering WLD was ~5500 $m^3 s^{-1}$, close to the 2021 peak (Fig. 2b). The summer campaign represents a low river discharge scenario with a discharge of ~1800 $m^3 s^{-1}$, close to the 2021 minimum. We collected field data in Mike Island and its two bounding primary channels, Main and Greg Passes (Fig. 2cde). We sampled suspended sediment concentration-depth profiles by collecting suspended sediment samples at different heights above the bed. We concurrently measured flow depths, directions, and velocity profiles using an acoustic Doppler current profiler (ADCP). We also measured discharge using ADCP transects across channels, including an intensive longitudinal discharge survey of Greg Pass in the summer. We analyzed sediment core grain size and surveyed the thickness and grain size of near-surface sediment deposits capping the island (i.e., cap transect; Fig. 2d) to characterize island deposits. To obtain coverage across time, we installed in situ sensors at four sites to measure the time series of water surface elevation (WSE) and sediment concentration. We grouped the sites into two pairs, each delineating a transect spanning a primary channel and Mike Island. The Greg Pass-wetland (GP-W) transect spans the Greg Pass and wetland sites (Fig. 2e; Fig. 3ac). The Main Pass-secondary channel (MP-SC) transect spans a secondary channel connecting the Main Pass and secondary channel sites (Fig. 2d; Fig. 3bd). We selected the Main Pass and Greg Pass sites to be near the edge of the primary channel and Mike Island. We used the time series data as inputs in a backwater model to estimate the time series of discharge and sediment flux into Mike Island through each transect.

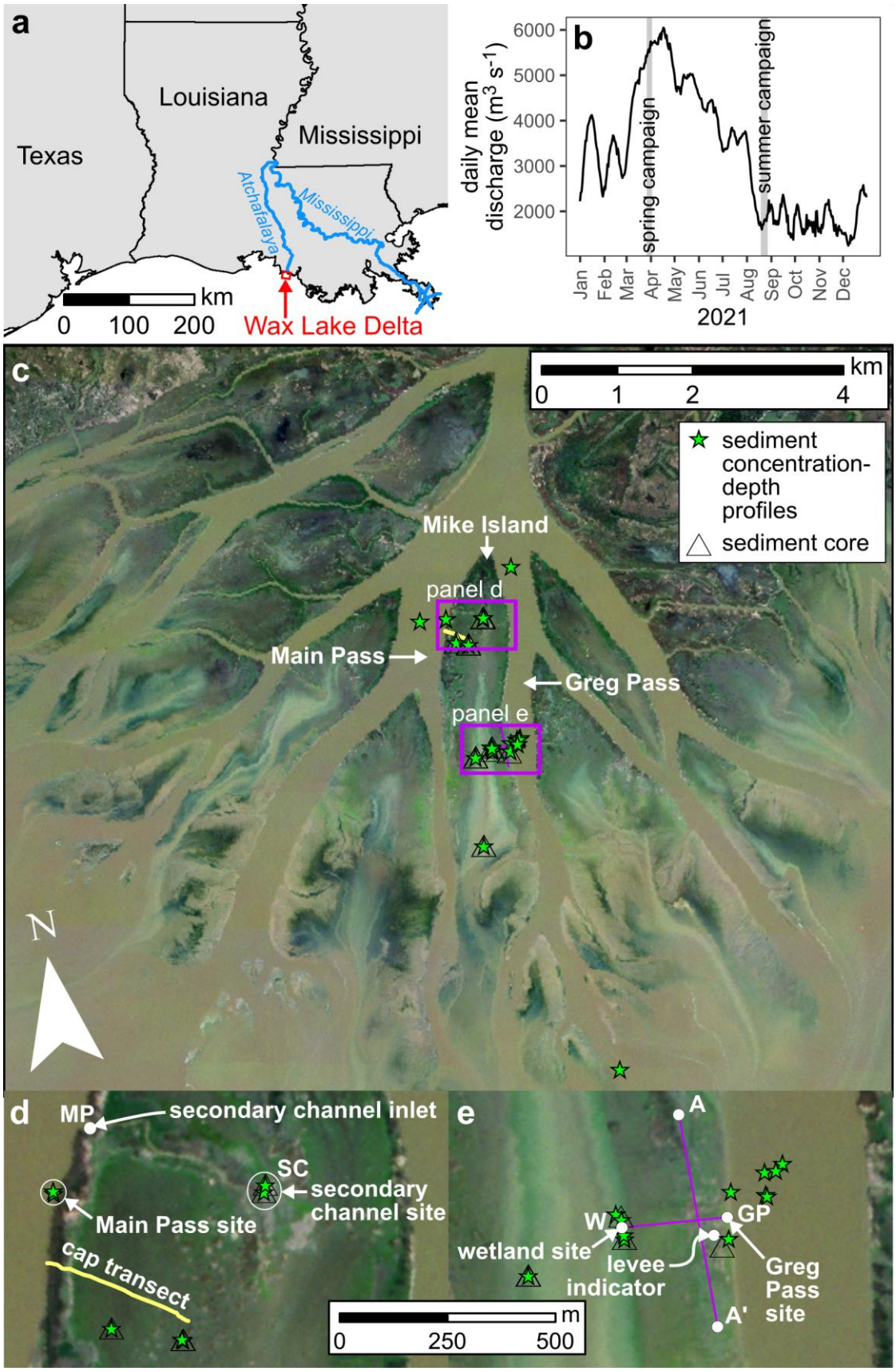
a
Louisiana
Texas
Mississippi
Atchafalaya
Mississippi
km
0 100 200
Wax Lake Delta
b
daily mean discharge (m^3 s^{-1})
6000
5000
4000
3000
2000
spring campaign
summer campaign
Jan Feb Mar Apr May Jun Jul Aug Sep Oct Nov Dec
2021
c
km
0 1 2 4
sediment concentration-depth profiles
sediment core
Mike Island
panel d
Main Pass
Greg Pass
panel e
N
d
MP
secondary channel inlet
SC
secondary channel site
Main Pass site
cap transect
m
0 250 500
e
A
W
GP
wetland site
levee indicator
Greg Pass site
A'

Figure 2. Wax Lake Delta map. (a) Map of the Louisiana coast. (b) 2021 hydrograph at Calumet, LA from USGS stream gauge 07381590 approximately 18 km upstream of the delta apex. (c) Map of the Wax Lake Delta. Satellite image is from January 2021, Image © 2021 Planet Labs PBC, at relatively low discharge and tide to highlight the full island extents. (d) Inset map of northern Mike Island. The Mike Pass-secondary channel (MP-SC) transect runs along the secondary channel between the Main Pass and secondary channel sites. (e) Inset map of southeastern Mike Island. Transect A-A' runs along the levee. The Greg Pass-wetland (GP-W) transect runs between the Greg Pass and wetland sites.

In WLD, vegetation phenology caused low vegetation density in the spring and high density in the summer (Jensen et al., 2024). In the spring, distal levees were sparsely vegetated, but vegetation density increased toward the higher elevation proximal levees (Fig. 3a). Within the island, secondary channels also build and host vegetation on levees (Fig. 3b). In the summer, the levees were relatively dense in vegetation because of the seasonal growth in the spring and summer, including some areas that were unvegetated in the spring (Fig. 3cd).

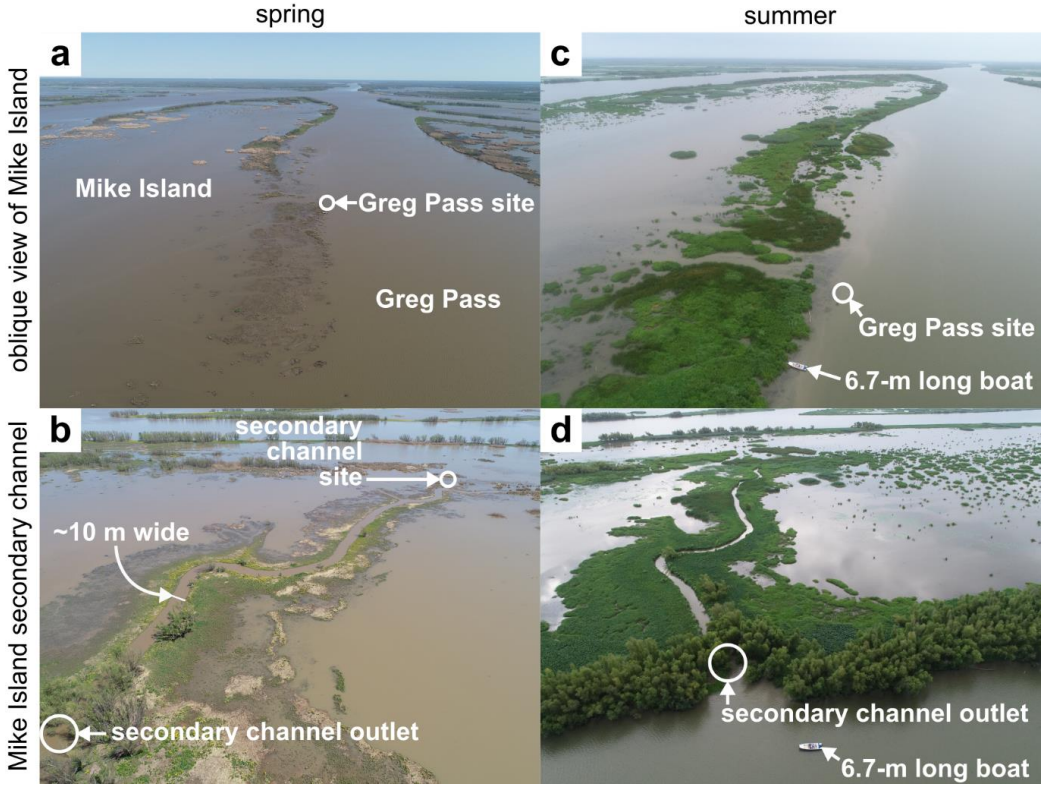

Figure 3. Drone photos of the Wax Lake Delta in the (a, b) spring and (c, d) summer. The circled locations are indicated in map view in Fig. 2de. We captured drone photos using a DJI Phantom 4 quadcopter drone.

5.3 Methods

This section documents the field methods to quantify hydraulics (Section 3.1), suspended sediment (Section 3.2), and sediment deposits (Section 3.3) in the channels and islands of WLD. We then used a simple backwater model to interpolate time series of discharge and sediment flux into an island wetland and secondary channel based on in situ WSE and sediment concentration time series (Section 3.4). We supplemented our data using a time series of river discharge entering WLD at the USGS Calumet stream gauge (ID 07381590) on the Wax Lake Outlet and a tidal time series of WSE from the offshore NOAA Eugene Island station (ID 8764314) located ~17 km southeast of the northern tip of Mike Island (Fig. 2c).

5.3.1 Hydraulics

Our hydraulics data methods are documented in Christensen et al. (2022) and Nghiem et al. (2024) and summarized here. We measured flow velocity profiles using a down-looking Teledyne RiverPro ADCP together with the concentration-depth profiles (Fig. 2c). We mounted the ADCP near the water surface on a boat (in the deeper channels) or stationary float (in the shallower islands). We measured 14 velocity profiles in the spring and 9 in the summer (Fig. 2). We combined instantaneous flow velocity profiles to average out high frequency turbulence and produce time-averaged flow directions and velocity profiles. We averaged instantaneous profiles that were close in space and time to the sediment samples in the concentration-depth profiles (Section 3.2; Nghiem et al., 2024). For each time-averaged velocity profile, we computed the 1D velocity profile by projecting the velocities in the direction of the greatest depth-averaged flow and fitted it to the law of the wall to estimate the local shear velocity, u_* (m s^{-1}), and roughness height, z_0 (m). The law of the wall states:

$$u = \frac{u_*}{\kappa} \ln \frac{z}{z_0} \quad (1)$$

and predicts the flow velocity, u (m s^{-1}), as a function of height above the bed, z (m), the dimensionless von Kármán constant, $\kappa = 0.41$, u_*, and z_0. We also calculated the flow depth, h (m) and depth-averaged flow velocity, $\bar{u}$ (m s^{-1}), from the time-averaged velocity profiles. We computed the unit discharge, q (m^2 s^{-1}), by integrating the velocity profiles over the flow depth. In association with 8 velocity profiles (4 in each season), we measured ADCP transects across the primary channel to calculate the volume discharge of water passing through. For each discharge measurement, we traversed the channel twice and averaged the two discharges to obtain the representative discharge (Christensen et al., 2022). We multiplied this discharge and the depth-averaged sediment concentration from the concentration-depth profile (Section 3.2) to obtain the sediment discharge (m^3 s^{-1}).

5.3.1.1 Greg Pass Survey

We conducted a discharge survey of Greg Pass on August 22, 2021 with discharge transects measured at ~1-km intervals from the north to the south and then back from the south to the north. For each transect in the Greg Pass survey, we collected a representative

suspended sediment sample near the water surface at the center of the channel, analyzed it for concentration (Section 3.2), and multiplied it with the discharge to estimate sediment discharge ($m^3\ s^{-1}$). We calculated the along-channel discharge differences to estimate the lateral unit discharges and multiplied them by sediment concentration to estimate sediment fluxes into the island.

Island sediment retention depends on many factors like vegetation, sedimentation rate, resuspension, and time scale. But as a proxy for island sediment retention, we used the sediment advection length, the typical horizontal distance sediment travels before reaching the bed (Ganti et al., 2014), to evaluate whether sediment supplied to the island can settle in or bypass the island. The sediment advection length, $l_a = q/w_s$ (m), depends on q and the sediment settling velocity, w_s ($m\ s^{-1}$). We used a representative settling velocity of 0.3 mm s^{-1}, a typical value for mud in WLD, because most of the suspended sediment in WLD is mud (Nghiem et al., 2024).

5.3.2 Suspended sediment

As reported in Nghiem et al. (2024), we sampled suspended sediment at multiple heights above the bed (i.e., sediment concentration-depth profiles) using a Van Dorn sampler. For each suspended sediment sample, we measured sediment concentration and the fully dispersed grain size distribution using a Malvern Mastersizer 3000E laser diffraction particle size analyzer. We partitioned the sediment concentrations by grain size class to obtain grain size-specific sediment concentration-depth profiles, from which we calculated depth-averaged sediment concentration and grain size distribution. We integrated each sediment concentration-depth profile with the corresponding time-averaged velocity profile (Section 3.1) to compute the sediment flux, q_s ($m^2\ s^{-1}$), and the portion of the sediment flux that is mud (grains < 62.5 μm) and sand (grains between 62.5 and 2000 μm).

5.3.3 Sediment deposits

We sampled the bed sediment at the concentration-depth profile locations using a Ponar grab sampler or piston core (Nghiem, Salter, and Lamb, 2024; Nghiem et al., 2025). We used the piston core in the island where the depth was shallow and sampled not only the surface bed sediment, but also sediment at shallow depth. We used a piston core to extract ~10-to-50 cm long sediment cores and sectioned them at discrete intervals (Nghiem, Salter, and Lamb, 2024; Nghiem et al., 2025). We measured the fully dispersed grain size distributions of bed sediment samples using a laser diffraction particle size analyzer.

We surveyed the thickness of the uppermost sediment (i.e., the cap) along a ~350-m transect from the western edge of Mike Island toward the island center during a separate field campaign in October 2019 (Fig. 2d). At each measurement point along the cap transect, we measured the ground elevation and probed the ground using a rod until we struck a distinct contact between the overlying muddy cap and an underlying sandy base. We measured the depth of the contact and water depth.

5.3.4 Time series data

5.3.4.1 Water surface elevation and sediment concentration time series

To better understand temporal trends, we measured the WSE and sediment concentration time series at the Greg Pass and wetland sites (transect GP-W; Fig. 2e) and the Main Pass and secondary channel sites (transect MP-SC; Fig. 2d). We used in situ water pressure sensors, documented in Nghiem, Salter, et al. (2022), to derive WSE time series (Fig. 4a). Sensors continuously measured water pressure, which we converted into local water depth assuming hydrostatic pressure and correcting for atmospheric pressure using an air pressure sensor. In the summer, we measured the ground elevation using a Trimble R12 GPS unit at each water pressure sensor, which we added to the water depth to obtain the WSE time series.

Figure 4. Example photos of in situ sensors. (a) Water pressure and turbidity sensors at the Greg Pass site (Fig. 2e). (b) Levee indicator at the Mike Island levee near the Greg Pass site (Fig. 2e).

We calibrated the spring WSE time series at the Greg Pass and wetland sites using lidar and game camera data because we did not measure the ground elevation. We used a time series of game camera photos of a levee indicator (Fig. 4b), a PVC pipe with 10-cm markings installed on the levee (Fig. 2e), from which we manually digitized the water depth time series. We extracted the ground elevation at the levee indicator using a 2020 lidar survey (Nghiem, 2022) and added it to the water depth to obtain the WSE time series at the levee indicator. We assumed that the WSE was identical between the levee indicator and the Greg Pass site and found the vertical offset to convert the Greg Pass water depth time series to WSE. To calibrate the spring WSE time series at the wetland site, we assumed the WSE was identical between Greg Pass and Mike Island at the time of the

highest WSE in Greg Pass. We could not calculate WSE in the spring for the Main Pass and secondary channel sites, so we did not report any spring time series for those sites.

We installed in situ turbidity sensors at the time series sites to measure the sediment concentration time series (Fig. 4a). Full turbidity sensor details are in Nghiem, Salter, et al. (2022). We converted the turbidity time series into sediment concentration using a turbidity-concentration relationship based on sediment concentration measured near the turbidity sensors. We used a smoothing spline to reduce noise in the concentration time series. Although the turbidity sensors can only sense sediment in a limited volume, we assumed that the concentration was representative of the whole water column because measured sediment concentration-depth profiles reveal relatively minor vertical variations in concentration (Nghiem et al., 2024).

5.3.4.2 Modeling island discharge and sediment flux

To extend our local hydraulics and sediment measurements over time, we used time series data to drive the 1D backwater equation for gradually varied flow (Chow, 1959) and model discharge and sediment flux into the island through a wetland (transect GP-W; Fig. 2e) and secondary channel (transect MP-SC; Fig. 2d). Following Salter and Lamb (2022), we computed the unit discharge into the island, q (m^2 s^{-1}), across the two transects spanning a primary channel and Mike Island (Fig. 2de) with the backwater equation:

$$\frac{\partial h}{\partial x} = \frac{S_b - \left(C_f - \frac{h}{w}\frac{\partial w}{\partial x}\right)\mathrm{Fr}^2}{1 - \mathrm{Fr}^2} \quad (2)$$

The flow depth, h (m), varies with distance into the island, x (m). The local bed slope, S_b, flow width, w (m), can also vary spatially depending on hydraulic geometry. The solution of Equation (2) also depends on Froude number, $Fr = \bar{u}/\sqrt{gh}$, and friction coefficient, $C_f = (u_*/\bar{u})^2$, where g is gravitational acceleration (9.81 m s^{-2}). $q = \bar{u}h$ is conserved along the transect. We depth-averaged the law of the wall (Eq. 2) to parametrize C_f:

$$C_f = \left(\frac{\kappa}{\frac{z_0}{h} - \ln\frac{z_0}{h} - 1}\right)^2 \quad (3)$$

For the backwater inputs, we set z_0 and used topography data to determine S_b, $\partial w/\partial x$, and width-depth ratio, w/h. We selected z_0 from values estimated at the wetland and secondary channel sites (Section 3.1). For transect GP-W (Fig. 2e), we extracted the elevation profile from a 10-m resolution digital elevation model of WLD (Christensen et al., 2023). We smoothed the extracted profile using a smoothing spline, which we differentiated to obtain S_b along the transect. We tested three different levee top elevations based on an along-levee transect (transect A-A' in Fig. 2e) to account for levee variability between the primary channel and wetland. We simply shifted the transect GP-W elevation profile vertically to

match the desired levee top elevation of each levee case. We assumed that $\partial w/\partial x = 0$ because the flow is broadly unchannelized between the primary channel and wetland.

For transect MP-SC (Fig. 2d), we used topography from a 1-m resolution 2020 lidar survey (Nghiem, 2022) because the 10-m digital elevation model cannot adequately resolve the secondary channel, which has a width of ~10 m (Fig. 3bd). However, the lidar elevations within the secondary channel are too high because water in the secondary channel attenuated the laser before it could reach the bed. To estimate the transect MP-SC elevation profile, we instead extracted and smoothed the bankfull WSE and bankfull width along the secondary channel. These measurements are reliable because the secondary channel levees were subaerial during the lidar survey. We assumed that the secondary channel had a rectangular cross-section and a constant width-depth ratio. We then inferred the elevation profile as bankfull WSE minus bankfull depth, which we calculated as bankfull width divided by width-depth ratio. We tested different width-depth ratios to find the value that yields an elevation profile matching a GPS measurement of bed elevation at the secondary channel site (Fig. 2d). We differentiated the smoothed elevation and bankfull width profiles to calculate S_b and $\partial w/\partial x$, respectively. For both transects GP-W and MP-SC, we subtracted the ground elevation of the elevation profile from the WSE time series to calculate the h time series at the transect endpoints for the backwater boundary conditions.

For transect MP-SC and the three levee cases of transect GP-W, we solved the backwater equation at 15-minute intervals for the q that satisfies the h boundary conditions. We used a predictor-corrector method and iterated over different values of q using the secant method. For each iteration, we integrated for h in the upstream direction because the flow is subcritical ($\mathrm{Fr} < 1$). We imposed the condition that the flow goes in the direction of the lower WSE between channel and island. We validated the resulting q time series using q measured from ADCP data at transect endpoints (Section 3.1). For transect GP-W only, we further validated the q time series using q from the Greg Pass Survey (Section 3.1.1) and in situ orange peel measurements at the levee indicator near the Greg Pass site in the spring (Fig. 2e). For the orange peel measurement, we recorded the time taken for a floating orange peel to travel a marked distance of 10 m and measured the corresponding flow depth. We calculated the flow velocity as 10 m divided by travel time and assumed it was representative of the depth-averaged flow velocity. Multiplying by the measured depth yields q. We only measured q once with orange peels, albeit with 6 replicates. We calculated sediment flux into the island by multiplying the backwater q time series and the sediment concentration time series in the primary channels. To analyze sediment retention, we divided the q time series by settling velocity to obtain the advection length time series (Section 3.1.1).

5.4 Point Measurement Results

We first present results from point measurements starting from flow hydraulics (Section 4.1), then the suspended sediment transported by the flow (Section 4.2), and finally island deposits built by sediment accretion (Section 4.3).

5.4.1 Hydraulics

ADCP measurements of unit discharge at the concentration-depth profiles (Section 3.1) indicate that the greatest discharges (~1 $m^2 s^{-1}$) in each season were in the primary and secondary channels. In these locations, the flow direction typically followed the channel (Fig. 5ab). For example, the northeast orientation of the secondary channel explains the northeast flow direction in the secondary channel (profile 2 in the spring and profile 8 in the summer). On the other hand, unit discharge measurements at the western edge of Mike Island (profile 11 in the spring and profile 6 in the summer) reveal a moderate component of flow directed away from the island despite differences in river discharge and ebb/flood tide between the measurements (Fig. 5cd). In contrast, unit discharge had a component into the island at the eastern edge of Mike Island further down the island (profile 5 in the spring and profile 4 in the summer) where levees were more submerged (Fig. 3a) and allowed greater hydrological connectivity between the primary channel and island. In the summer, this flow component into the island was much weaker because of the lower river discharge relative to the spring (Fig. 5cd).

Discharges were relatively smaller in the island wetland (order 0.01 to 0.1 $m^2 s^{-1}$), reflecting the loss of channelization and lateral flow spreading onto the wetland. Flow directions in the island were also mixed. In the spring, flow directions in the northern part of Mike Island (profiles 8, 9, and 13) were measured during flood tide and oriented up the island (Fig. 5a). Conversely, flow directions were oriented down the island in the southern part (profiles 6, 7, 10, and 12; Fig. 5a). Repeat measurements at the wetland site in Mike Island for both seasons (profiles 6 and 12 in the spring and profiles 2 and 9 in the summer) indicate that flow was oriented more down the island at ebb tide compared to flood tide as falling tides drew down water out of WLD (Fig. 5ab).

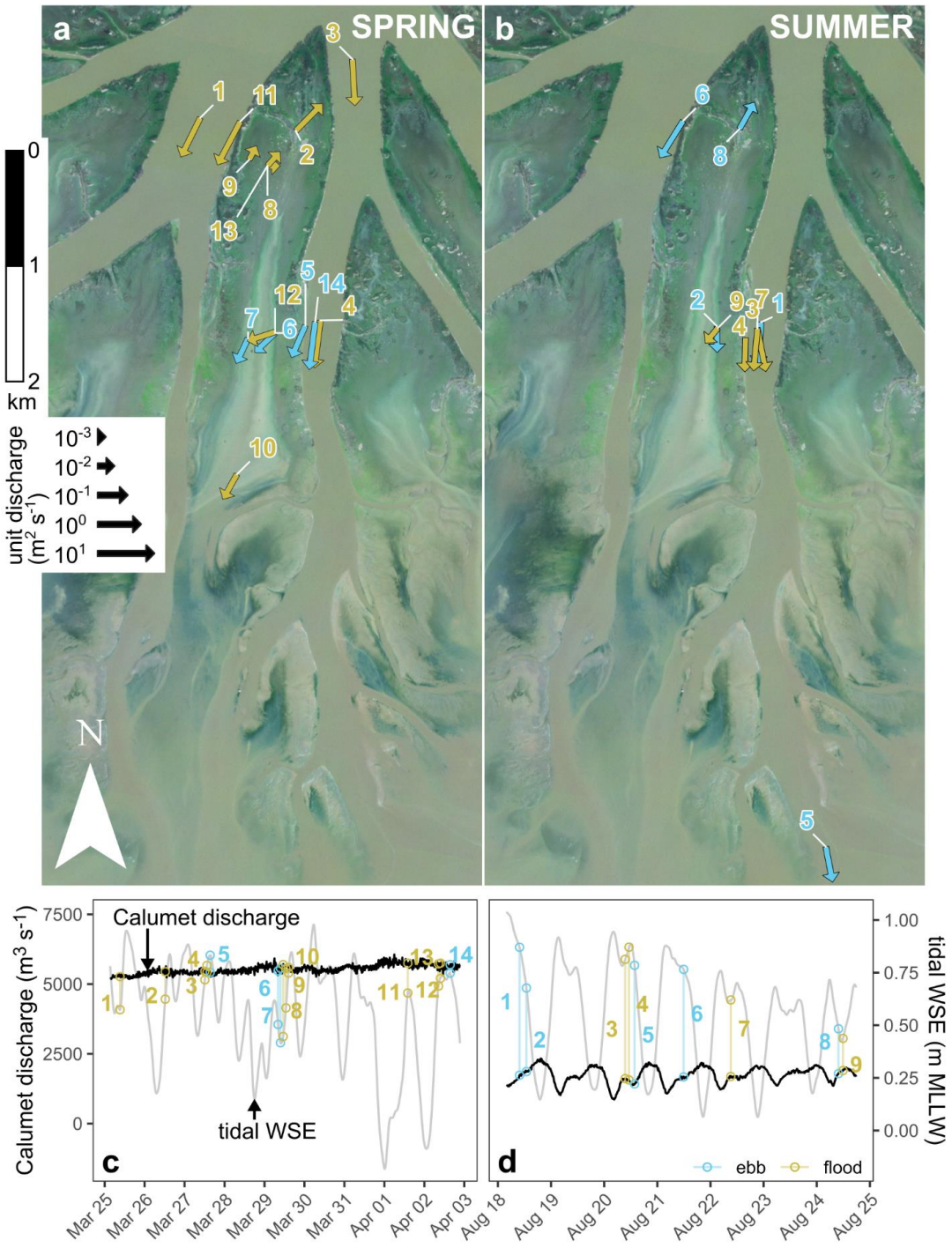

Figure 5. Unit discharge measured by ADCP in the (a) spring and (b) summer. Calumet discharge and tidal WSE time series in the (c) spring and (d) summer. We indexed sites chronologically by season.

The time-averaged flow velocity profile reveals the vertical flow velocity structure at each concentration-depth profile (Fig. 6). In general, flow velocities were slower near the bed

and faster near the water surface in accord with expectation from the law of the wall (Eq. 1). The fastest measured flow velocities occurred in the spring in the channels (i.e., primary and secondary channels) with speeds of ~0.5 to 0.75 m s^{-1} (Fig. 6a). In contrast, channel flow velocities in the summer were slower at ~0.25 m s^{-1} because of the lower river discharge delivered to the delta (Fig. 5cd). Flow velocities were much slower in the island wetland (~0.01 to 0.1 m s^{-1}) because flow was unchannelized, but still typically increased closer to the water surface.

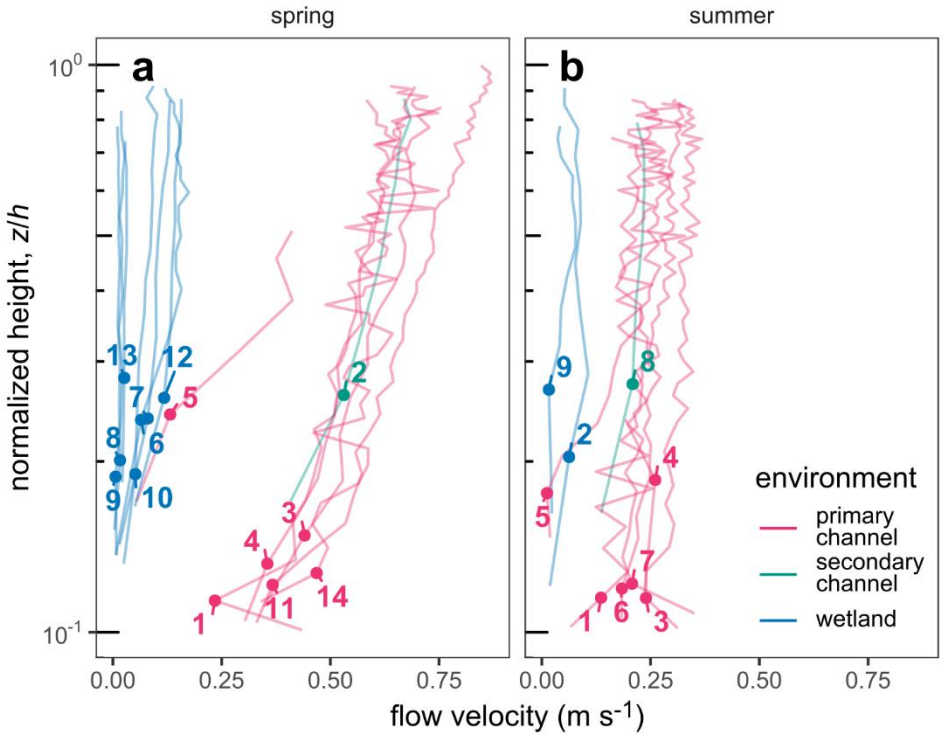

Figure 6. 1D time-averaged flow velocity profiles in the (a) spring and (b) summer. Numbers correspond to measurement sites (Fig. 5ab).

The depth-averaged flow velocity generally correlates with the flow depth (Fig. 7ab), yielding a range of q from ~0.01 to 2 m^2 s^{-1}. The flow depth in the primary channels was ~3 to 4 m in spring and summer with some shallower areas over bars and near the channel edges. The flow depth in the island (wetland and secondary channel) was shallower than ~1 m. We fitted the law of the wall (Eq. 1) to the flow velocity profiles and estimated hydraulic parameters. Roughness heights ranged from ~10^{-3} to 10^{-1} m with a typical value of 0.05 m and lack clear trends with flow depth, season, or delta environment (Fig. 7cd). Combined, the flow depth and roughness height resulted in friction coefficients of 0.005 to 0.1 (Eq. 3). The island tended to have higher friction coefficients than primary channels because the depth was shallower, leading to greater friction coefficient when the roughness height is constant. In turn, these friction coefficients produced a strong correlation between depth-averaged flow velocity and shear velocity in the spring (Fig. 7e) and an apparently weaker correlation in the summer (Fig. 7f), which might be explained by the narrower

range of measured flow velocities. In the spring, shear velocities were typically greater in channels (~0.05 m s^{-1}) than in the wetland because the faster flow velocity in the channels outweighed the greater friction coefficients in the wetland (Fig. 7e). In the summer, channel shear velocities were typically smaller than those in the spring (~0.01 to 0.05 m s^{-1}) and similar to wetland shear velocities because higher friction coefficient in wetlands largely compensated for faster flow velocity in channels in terms of shear velocity (Fig. 7f).

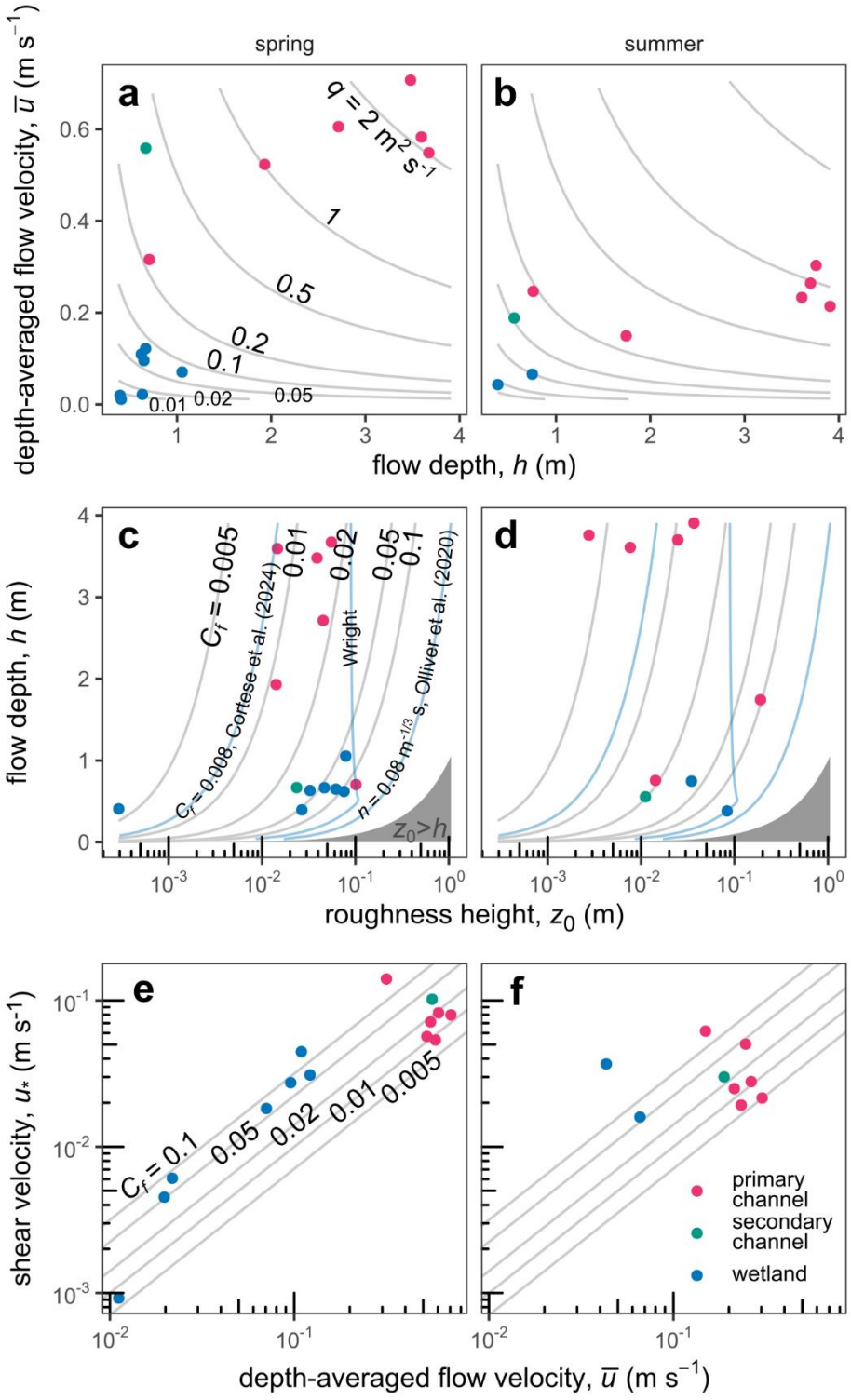

Figure 7. Hydraulic parameters. Flow depth versus depth-averaged flow velocity in the (a) spring and (b) summer. Roughness height versus flow depth in the (c) spring and (d) summer. Depth-averaged flow and shear velocities in the (e) spring and (f) summer. The

blue curves in panels c and d represent roughness relations for vegetated island wetlands used in prior WLD hydrodynamic models: Olliver et al. (2020), "subtidal marsh" in Wright et al. (2022), and "marsh" in Cortese et al. (2024).

We tested the consistency of roughness relations used to characterize vegetated wetlands in prior WLD hydrodynamic models against our wetland roughness measurements. We chose three examples that each used a different common method to prescribe the roughness of vegetated wetlands. Olliver et al. (2020) used a Manning's n of 0.08 $m^{-1/3}$ s. Wright et al. (2022) used the Baptist et al. (2007) formulation that predicts roughness based on vegetation properties and calibrated the vegetation parameters. Cortese et al. (2024) chose a Chézy coefficient of 35 $m^{1/2}$ s^{-1}, which is equivalent to $C_f = 0.008$. We converted these examples into the same space of roughness height, z_0, versus flow depth, h (Fig. 7cd). On one extreme, the Cortese treatment ($C_f = 0.008$) far underestimates the measured wetland C_f, which has a typical range of 0.05 to 0.1 across spring and summer. On the other extreme, the Olliver method overestimates C_f compared to the data. Using $h = 0.6$ m as a typical wetland flow depth, the Olliver method yields $C_f = 0.93$. The Wright method produces the best comparison with our wetland C_f data as evidenced by the fact that, at h = 0.6 m, it predicts $C_f = 0.20$, which is the closest to our data out of the three treatments. The Wright prediction is still biased slightly high compared to our wetland C_f range of 0.05 to 0.1, but at least compares well to our highest measured wetland C_f (Fig. 7d).

5.4.2 Suspended sediment

Sediment concentration-depth profiles reveal limited variation in sediment concentration with height above the bed in spring and summer (Fig. 8ab). Depth-averaged data show that, in the spring, higher sediment concentration was typically associated with lower mud fraction (i.e., higher sand fraction; Fig. 8c). This trend occurs because greater shear velocity locally suspended more sediment (Fig. 8e) and mobilized coarser sand grains in the spring, causing mud fraction to drop from ~1 to ~0.6. As such, the island wetland (lower shear velocity) tended to have lower sediment concentration (~4×10^{-5}) and higher mud fraction (~1) compared to channelized measurement sites (concentration ~ 7×10^{-5}; mud fraction ~0.86). On the other hand, measured mud fraction was relatively uniform (~1) with respect to sediment concentration in the summer (Fig. 8d) probably because the shear velocity (Fig. 8f) was too small to entrain coarser grains. Smaller shear velocity also led to smaller sediment concentration in the summer (~10^{-5}) versus that in the spring. In the same vein, greater unit discharge supported greater sediment flux as evidenced by their strong power-law correlation with the exception of two outliers in the summer with disproportionately high sediment flux given their discharge (Fig. 8gh). In the spring, the greatest sediment fluxes occurred in the channels (~2-5$\times10^{-5}$ m^2 s^{-1}) whereas sediment fluxes in the wetland were lower (< 10^{-5} m^2 s^{-1}). Sediment fluxes were lower in the summer (~10^{-6} m^2 s^{-1}) relative to those in the spring.

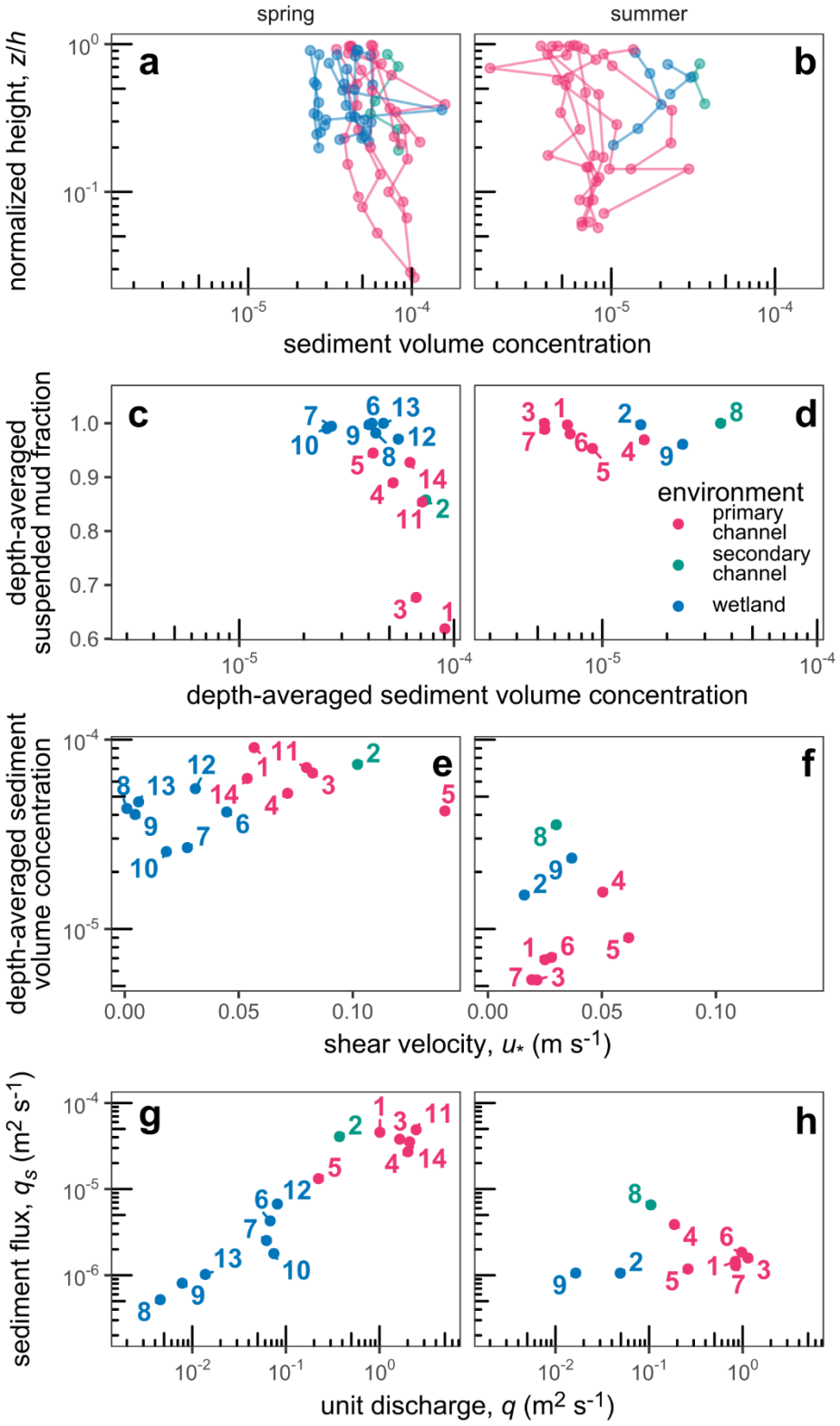
spring
summer
a
b
normalized height, z/h
sediment volume concentration
c
d
depth-averaged suspended mud fraction
depth-averaged sediment volume concentration
environment
primary channel
secondary channel
wetland
e
f
depth-averaged sediment volume concentration
shear velocity, u* (m s-1)
g
h
sediment flux, qs (m2 s-1)
unit discharge, q (m2 s-1)

Figure 8. Sediment concentration and flux results. Sediment concentration-depth profiles in the (a) spring and (b) summer. Depth-averaged sediment concentration and suspended mud fraction in the (c) spring and (d) summer. Shear velocity and sediment concentration in the (e) spring and (f) summer. Unit discharge and sediment flux in the (g) spring and (h) summer.

In map view, the spatial pattern of sediment flux (Fig. 9ab) closely follows the spatial pattern of unit discharge (Fig. 5ab; Section 4.1). Flow direction is identical between q and q_s, but the power-law scaling between discharge and sediment flux (Fig. 8gh) enhanced the sediment flux magnitude in the spring compared to that in the summer because of the higher spring discharges. Mud fluxes far exceeded sand fluxes (Fig. 9cd), highlighting the prevalence of mud in the suspended sediment (Fig. 8cd).

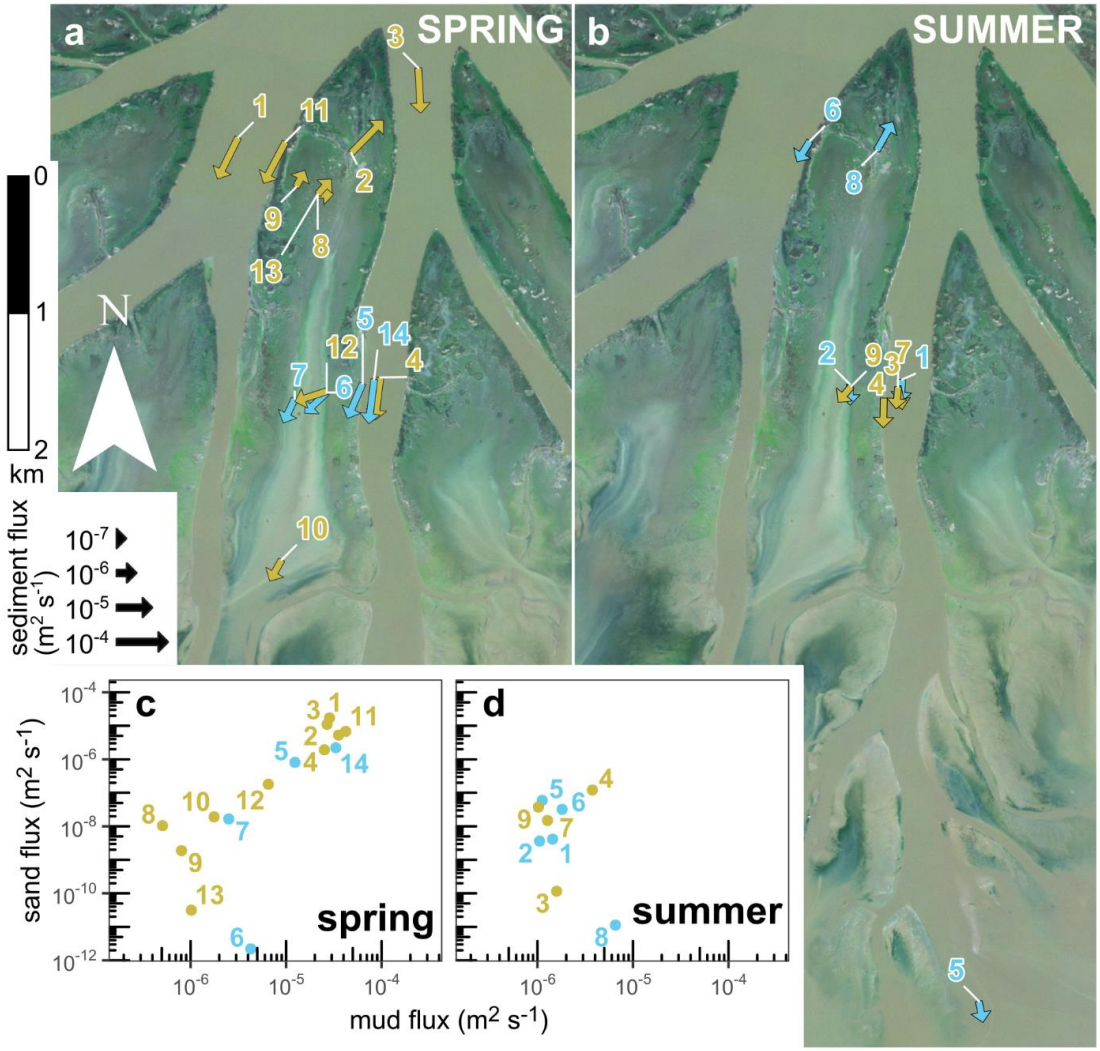

Figure 9. Sediment flux measured by ADCP and sediment-concentration depth profiles in the (a) spring and (b) summer. Mud and sand fluxes in the (c) spring and (d) summer. See Fig. 5cd for the Calumet discharge and tidal WSE time series with the measurement times indicated.

To better integrate flow at the primary channel scale, we combined ADCP transects and depth-averaged sediment concentrations (Section 3.2) to quantify total water and sediment discharge passing through primary channel cross-sections. Our measurements reveal that, in the spring, Main Pass conveyed roughly double the discharge as Greg Pass (~1700 $m^3 s^{-1}$ at profile 1 versus ~870 $m^3 s^{-1}$ at profile 3) because the greater width of Main Pass captures more of the incoming river discharge (Fig. 10ag). Greg Pass bifurcates seaward, diverting part of the discharge and leading to an even lower discharge of ~590 $m^3 s^{-1}$ (profiles 4 and 14; Fig. 10g), which is about 10% of the total discharge entering at Calumet in the spring (Fig. 10a). This discharge below the Greg Pass bifurcation is well-reproduced at profiles 4 and 14 measured at different times, but similar Calumet discharge and tidal WSE (Fig. 10ae). At the same location in the summer, we measured less than half the discharge (~240 $m^3 s^{-1}$; Fig. 10bh) with little variation across three measurements at different times (profiles 1, 3, and 7) despite the fact that the Calumet discharge varied strongly with the tide in the summer (Fig. 10bf). This consistency is probably due to the fact that we measured discharges at similar tidal WSEs near local maxima (Fig. 10f). Even further down Greg Pass toward the delta front (profile 5 in the summer; Fig. 10h), we measured a very low discharge of ~36 $m^3 s^{-1}$ in the summer because flow spreads out laterally as primary channels become fully submerged. In conclusion, Greg Pass discharge measurements show that primary channel discharge correlates highly with the input river discharge, as expected, and tended to decrease with distance seaward as a result of bifurcations and likely lateral flows into islands (Hiatt and Passalacqua, 2015).

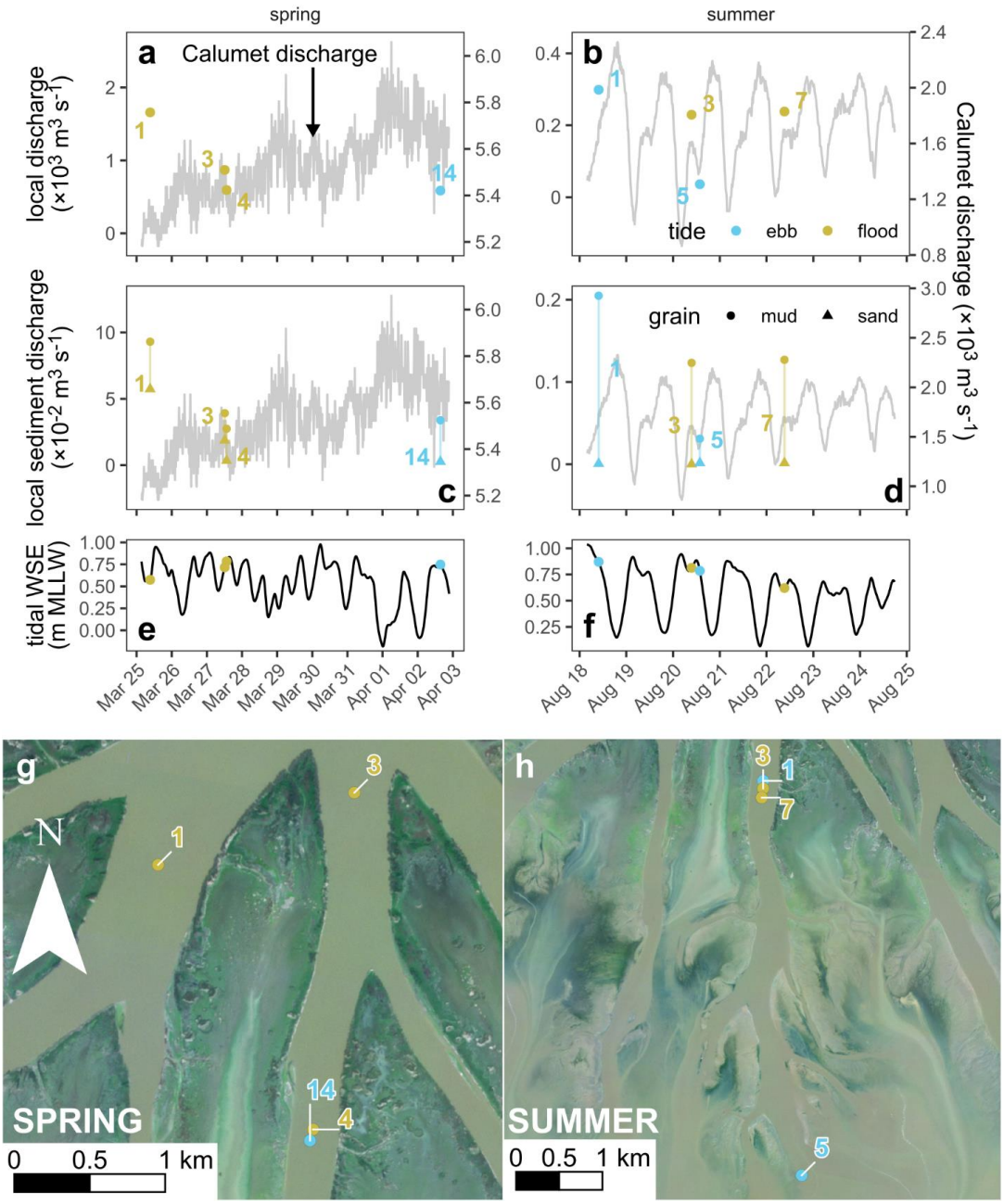

Figure 10. Primary channel discharges measured by ADCP transects. Local ADCP discharge in the (a) spring and (b) summer. Discharges are plotted together with the incoming river discharge at Calumet (gray). Local sediment discharge in the (c) spring and (d) summer. Tidal WSE time series with discharge measurements marked in the (e) spring and (f) summer. Map of channel discharge measurements in the (g) spring and (h) summer. Each point corresponds to the center of the transect.

Turning to sediment, sediment discharges measured in primary channels in the spring were much greater than those in the summer (Fig. 10cd) because of the greater discharge (Fig.

10ab) and sediment concentration (Fig. 8ef). In all cases, mud discharge exceeded sand discharge. Mud and sand discharges were the greatest at profile 1 in the spring (~0.05 and 0.1 $m^3 s^{-1}$, respectively) because of its relatively high discharge (Fig. 10a). In the spring, we measured a mud discharge entering Greg Pass of ~0.04 $m^3 s^{-1}$, which was about twice the sand discharge (profile 3; Fig. 10c). Below the bifurcation, the mud discharge dropped slightly to ~0.03 $m^3 s^{-1}$, but the sand discharge was about an order of magnitude smaller than the mud discharge (profiles 4 and 14; Fig. 10c). In the summer at the same location, we measured mud discharges that were about an order of magnitude smaller at ~2×10^{-3} $m^3 s^{-1}$ (profiles 1, 3, and 7; Fig. 10d). Near the delta front in the summer, we measured a Greg Pass mud discharge of ~3×10^{-4} $m^3 s^{-1}$, another order of magnitude smaller. Sand discharge was negligible for all sediment discharge measurements in the summer. Overall, like water discharge, mud discharge in Greg Pass tended to decline seaward.

The ADCP data in Fig. 10 are limited because they are point measurements from disparate times and locations. To better control for time and space, we conducted a focused ADCP survey of Greg Pass in the summer. We collected ADCP transects and suspended sediment samples at stations along Greg Pass (Fig. 11a) to obtain water and sediment discharges. We first collected data in Greg Pass from north to south and then did replicate measurements on our return from south to north. In general, discharge decreased down Greg Pass (Fig. 11b) from ~300 to 400 $m^3 s^{-1}$ at the most landward (station 1) to ~30 $m^3 s^{-1}$ at the most seaward (station 8). Discharges from the south-to-north survey are biased high compared to those from the north-to-south survey because the incoming river discharge at Calumet was higher during the south-to-north survey (Fig. 11f).

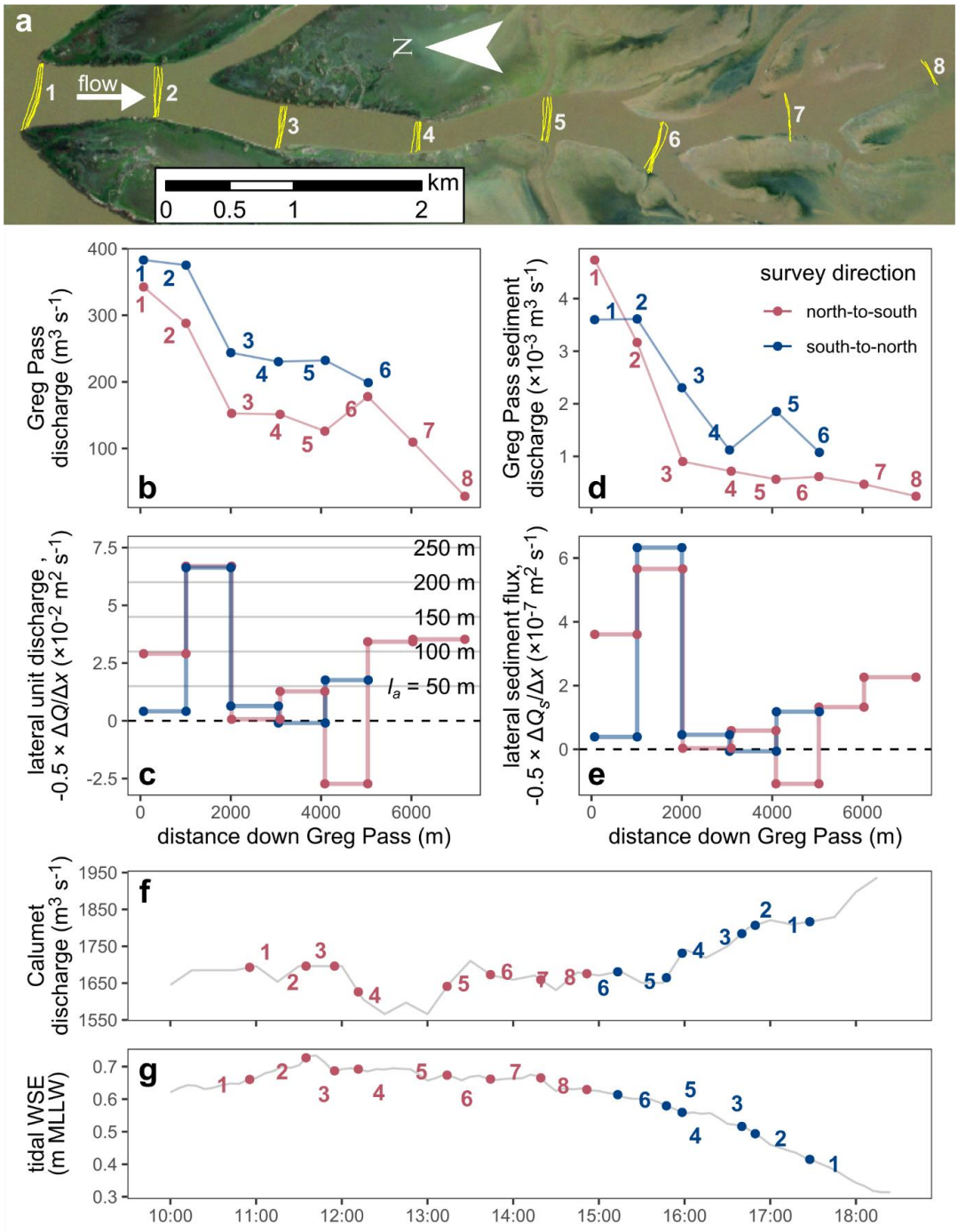

Figure 11. Greg Pass survey of ADCP discharge and sediment concentration in the summer. (a) Map of measurement stations along Greg Pass. Longitudinal profile of (b) channel discharge, (c) lateral unit discharge computed by differencing the discharges in space (positive indicates flow into island), (d) sediment discharge, and (e) lateral sediment flux computed by differencing the sediment discharges in space (positive indicates flow into island). Time series of (f) Calumet discharge and (g) tidal WSE with

measurement times marked. Point numbers in panels b-g correspond to the station numbers in panel a.

We differenced the Greg Pass discharge in space to estimate lateral unit discharge within the segments between stations, which we divided in half to represent the average lateral flow into Mike Island on one side of Greg Pass. The lateral unit discharge is mixed, but indicates that water typically flowed out of Greg Pass into islands and/or bifurcation channels (Fig. 11c). The bifurcation between stations 2 and 3 (Fig. 11a) diverted substantial flow out of Greg Pass and is highlighted by a peak in lateral unit discharge of ~0.07 $m^2 s^{-1}$, which is hence an overestimate of the lateral unit discharge into Mike Island. Discounting this bifurcation-affected segment, the highest lateral unit discharges into the island occurred between the most seaward stations (~0.03 $m^2 s^{-1}$ between stations 6 and 8) because of flow spreading as channels become more subaqueous. In terms of sediment advection length (Section 3.1.1), we calculated that this lateral unit discharge could carry sediment an average of ~100 m into Mike Island (Fig. 11c). The lateral unit discharge was typically smaller between the more landward stations (< 0.02 $m^2 s^{-1}$), leading to advection lengths shorter than ~50 m. These advection lengths are much shorter than the typical width of Mike Island (900 m), indicating that sediment can readily settle in the island. We calculated a negative lateral unit discharge (i.e., flow into Greg Pass) between stations 5 and 6 in the north-to-south survey (Fig. 11c) for unknown reasons, especially because the replicate in the south-to-north survey is positive. The river discharge at Calumet and tidal WSE did not change drastically over time as we conducted the Greg Pass survey (Fig. 11fg). However, Calumet discharge and tidal WSE were increasing and decreasing, respectively, to a greater degree during the north-to-south survey, potentially affecting the inferred lateral unit discharges and sediment fluxes (Fig. 11ce) more than in the south-to-north survey.

Like the water discharge, sediment discharge typically decreased over distance down Greg Pass from ~4×10^{-3} $m^3 s^{-1}$ landward to ~2×10^{-4} $m^3 s^{-1}$ (Fig. 11d). Sediment discharge experienced a steep decline in the first 3 km of Greg Pass (between stations 1 and 4) probably because of the nonlinear sensitivity between the decreasing discharge and sediment flux (Fig. 8gh). The bifurcation between stations 2 and 3 caused a spike in sediment flux at ~6×10^{-7} $m^2 s^{-1}$ (Fig. 11e). Otherwise, lateral sediment flux into the island approached ~2×10^{-7} $m^2 s^{-1}$ toward the most seaward stations.

5.4.3 Sediment deposits

For all concentration-depth profiles, the median grain diameter, D_{50} (μm), of the bed sediment was coarser than that of the suspended sediment in the overlying water column (Fig. 12a). Bed sediment in the island, including the secondary channel, was muddy (D_{50} of ~20 to 30 μm), but still coarser than the suspended grains. In contrast, bed sediment in primary channels was sandy with D_{50} exceeding 100 μm (Fig. 12ab). But not all primary channel beds were sandy. We measured a muddy bed in the center of Main Pass for profile 1 in the spring (Fig. 5a) because of the presence of a submerged muddy mid-channel bar (Fig. 12a). The bed at the edge of Greg Pass near the margin of Mike Island (profile 5 in the spring and profile 4 in the summer) was muddy probably because of the weaker shear

velocities at the shallow channel edge compared to the channel center (Fig. 12ab). Far down Greg Pass (profile 5 in the summer), the bed was also muddy because hydraulic sorting causes mud to be preferentially transported and deposited further offshore (Fig. 12b).

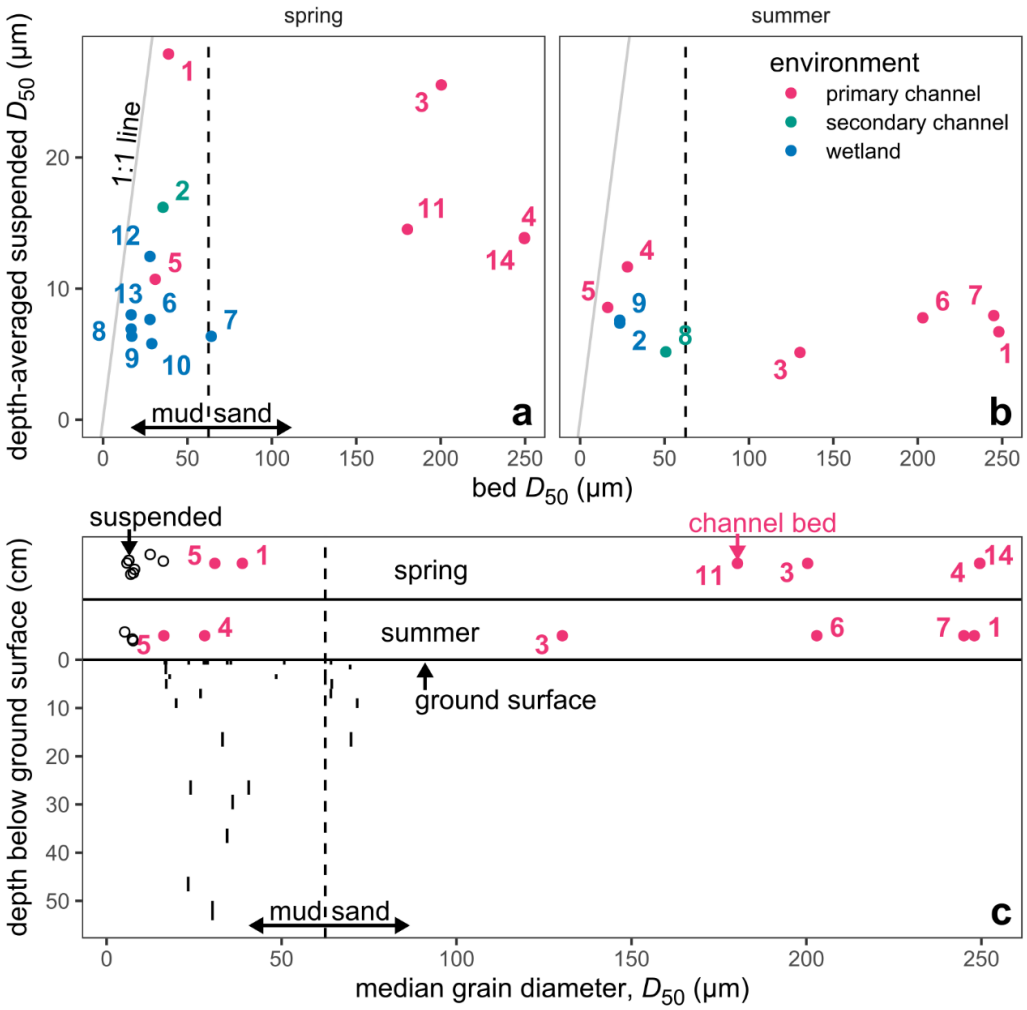

Figure 12. Sediment deposit grain size. Median grain diameter, D_{50}, of bed and suspended sediment in the (a) spring and (b) summer. (c) Median grain diameter versus depth of sediment core samples in Mike Island. Data from multiple cores (Fig. 2cde) are presented together. D_{50} of depth-averaged suspended sediment in Mike Island (black circles) is plotted above the ground surface. D_{50} of bed sediment in the channels (magenta points) is also plotted for comparison. See Fig. 5ab for the locations of the concentration-depth profiles by number.

Shallow sediment cores in Mike Island reveal muddy island deposits (D_{50} of ~20 to 70 μm) within the top ~50 cm of the ground surface (Fig. 12c), corroborating the efficient mud capture implied by short advection lengths relative to Mike Island width from the Greg

Pass survey (Fig. 11c). Clear grain size trends with depth are not evident. Island suspended sediment was finer (D_{50} of ~20 μm) than the core sediment. These island deposits were coarser probably because coarser grains preferentially settle and build deposits, but finer grains have longer advection lengths and are more likely to advect out to sea with minimal island storage. Primary channel beds were typically much coarser than any of the shallow island deposits (Fig. 12c), suggesting distinctly different sediment erosion and deposition processes between primary channel and island.

The sediment cap transect across northeast Mike Island (Fig. 2d) shows a laterally extensive ~40-cm thick muddy cap of sediment that overlies a sandy base (Fig. 13). The presence of this muddy cap is consistent with the advection length (Fig. 11c) and sediment core data (Fig. 12c) showing the ability of mud to settle in the island and build deposits. The stratigraphy of a muddy cap over a sandy base suggests that sand was formerly the main material building up WLD, but mud now dominates recent island accretion.

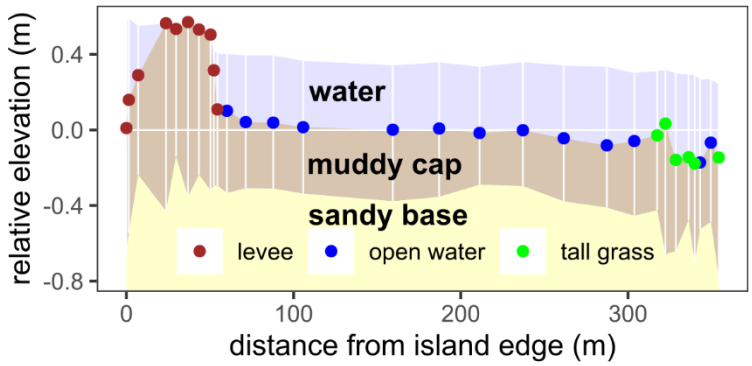

Figure 13. Mike Island cap transect. See Fig. 2d for transect location. The point classification is the field description of the local environment.

5.5 Time Series Results

Here we present time series data to better contextualize our findings in time compared to point measurements (Section 4). We structure this section to evaluate the stages of sediment transfer into the island: (1) sediment source in primary channels, (2) sediment flux entering the island, and (3) sediment transport within the island.

5.5.1 Sediment sources from primary channels

In situ WSE and sediment concentration time series in Greg and Main Passes (i.e., primary channels) reveal that WSE and sediment concentration are generally inversely correlated (Fig. 14). The water surface in the primary channels fluctuated according to the tides in both spring and summer. Higher sediment concentration was correlated with lower WSE and, equivalently, shallower channel depths and vice versa, suggesting a tidal control on the local sediment concentration in primary channels.

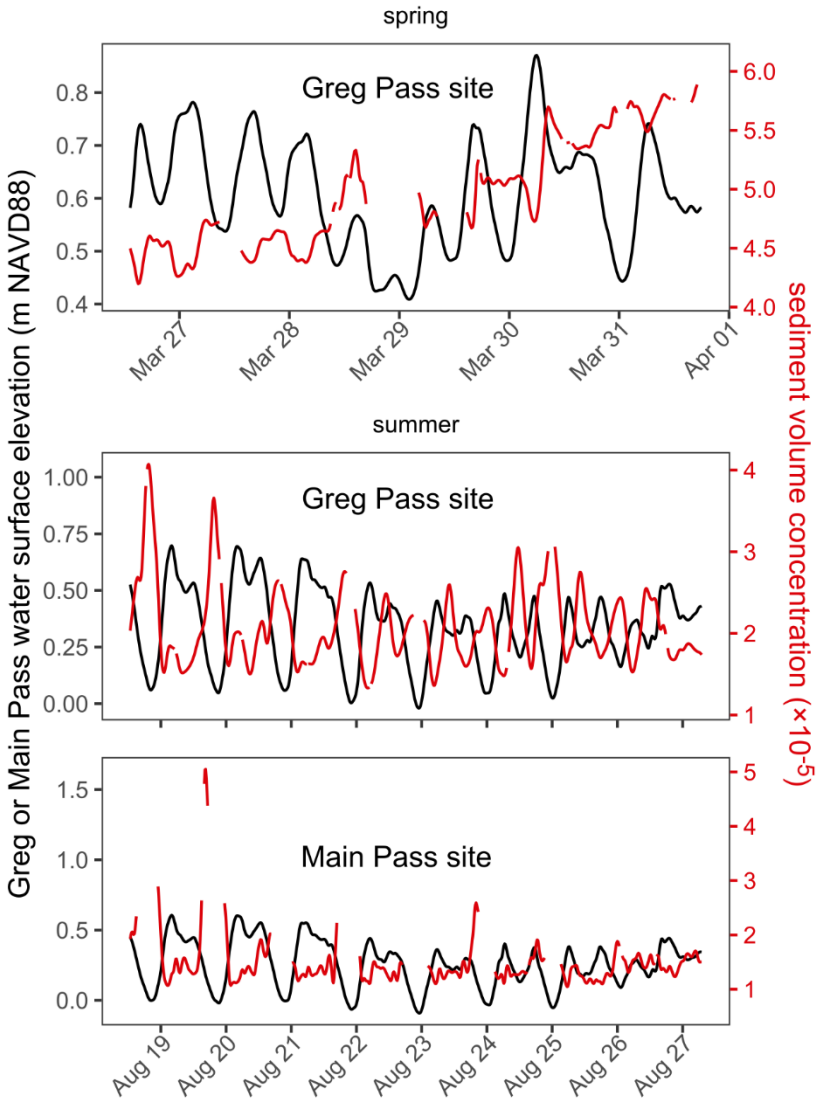

Figure 14. Time series of water surface elevation and sediment concentration in the primary channels at the measurements sites in Greg and Main Passes (Fig. 2de).

To further investigate the controls on primary channel sediment concentration, we calculated longitudinal water surface slopes down the delta to the primary channels (Greg and Main Passes). We differenced the Calumet and primary channel WSE at each time step and divided by the horizontal distance (~23.7 km) to obtain the average linear slope. Negative water surface slopes in the summer (Fig. 15ab) suggest that there were periods of time in which longitudinal water surface slope reversed orientation tilted landward, but in situ flow direction measurements do not show any landward flow in the primary channels (Fig. 5ab). We expect that the negative water surface slopes are erroneous and caused by a vertical datum mismatch between the USGS Calumet data and our primary channel data. That said, shallower flow depth into Mike Island (i.e., lower primary channel WSE)

typically correlated with steeper longitudinal water surface slope with a stronger trend in spring than in summer (Fig. 15ab). Combined with the correlation between WSE and sediment concentration (Fig. 14), our interpretation is that falling tides drop WSE first in seaward parts of WLD and draw the water surface slope steeper because the distal base level change takes time to propagate landward and vice versa. In turn, steeper water surface slope increases the shear stress on the bed and enhances local sediment entrainment from the bed, leading to greater sediment concentration (Partheniades, 1965; De Leeuw et al., 2020). Thus, this tidal regulation of water surface slope, shear stress, and sediment concentration sets the sediment concentration in primary channels that can be transported into the island.

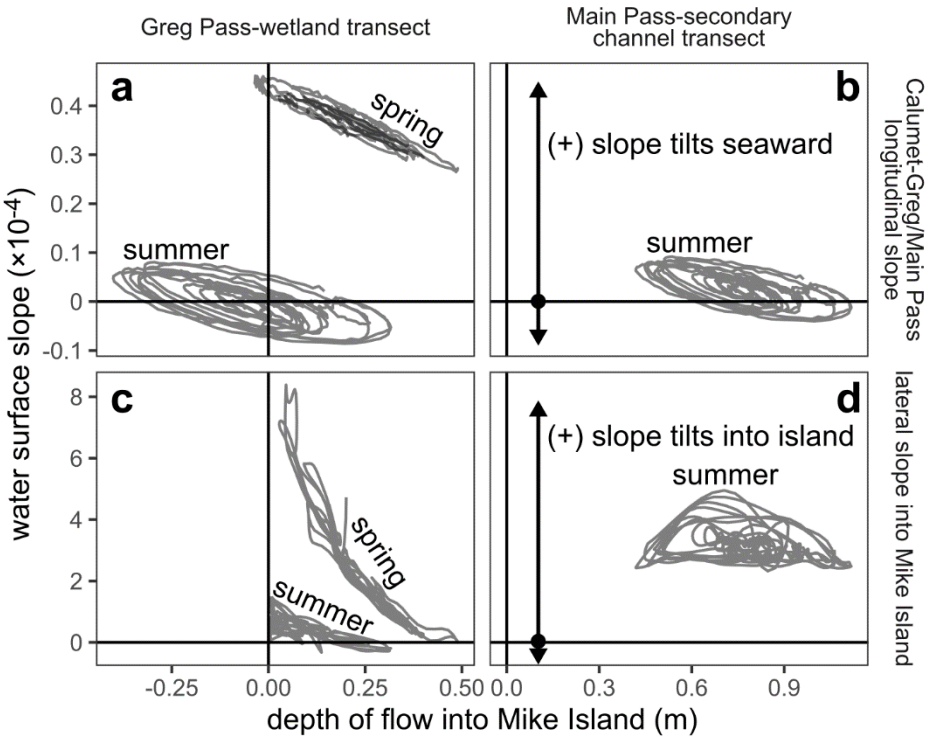

Figure 15. Longitudinal and lateral water surface slopes versus depth of flow into Mike Island for the Greg Pass-wetland and Main Pass-secondary channel transects. Negative flow depth means that the water surface elevation is below the levee top elevation. The median levee case is used for the Greg Pass-wetland transect (panels a and c).

5.5.2 Sediment flux entering the island

The next step is to understand the conditions under which water and suspended sediment in primary channels can enter the island. Hiatt and Passalacqua (2015) emphasized the importance of hydrological connectivity between primary channels and islands for facilitating sediment flux into the island. Hydrological connectivity implies, at the bare minimum, that the primary channel water surface has overtopped island levees. Beyond this condition, lateral water surface slope and depth of flow into island set the magnitude of

flow entering the island because the hydraulic gradient must be directed into the island to drive flow.

To evaluate these variables, we calculated lateral water surface slopes between the primary channel and island across the Greg Pass-wetland (GP-W) and Main Pass-secondary channel (MP-SC) transects (Fig. 2de). We differenced the primary channel and island WSE at each time step and divided by the horizontal distance (200 m for transect GP-W and 540 m for transect MP-SC). Considering only times in which the primary channel and island were hydrologically connected, shallower depth of flow from Greg Pass into the island wetland correlates with steeper lateral water surface slope into the island with a stronger trend in spring than in summer (Fig. 15c). Our interpretation is that increasing inundation fills the island and raises the island WSE to approach the primary channel WSE, thereby causing the lateral water surface slope to shallow out. In contrast, the flow depth from Main Pass into the secondary channel in the summer does not display a clear trend with the lateral water surface slope through the secondary channel (Fig. 15d). Our interpretation here is that the relationship between flow depth and lateral water surface slope is controlled by channelized flow hydraulics rather than broad filling of the wetland. But overall, the lateral water surface slope data show that the hydraulic gradient typically drives flow into the island except for a few periods in the summer between Greg Pass and the wetland (Fig. 15c).

The flow depth and lateral water surface slope data demonstrate persistent flow from primary channels into Mike Island, but do not indicate flow magnitude. To quantify flow magnitude into the island, we calculated the unit discharge, q, into the island using the backwater equation (Section 3.4.2) for the Greg Pass-wetland (Fig. 2e) and Main Pass-secondary channel transects (Fig. 2d). We chose roughness heights of 0.05 m for the Greg Pass-wetland transect and 0.01 m for the Main Pass-secondary channel transect following our hydraulics data (Fig. 7cd). At each time step, we solved the backwater equation to find the q that satisfies the observed water surface elevations at the endpoints in the primary channel and island (Fig. 16abe).

Water surface elevations extracted from the levee indicator correspond well to the WSE time series in the spring at the Greg Pass site, supporting the validity of the levee indicator for calibrating WSE (Section 3.4.1). Flow also depends on the island elevation relative to the WSE. For the Greg Pass-wetland transect, we extracted elevations along the island levee from a lidar survey (Fig. 17a) to quantify variability (transect A-A'; Fig. 2e). The levee elevation profile reveals a wide elevation range spanning ~0.5 m from the lowest to highest elevations (Fig. 16c). The lowest elevations are in small secondary channels, which have depths of ~0.3 to 0.4 m. To account for the range of levee elevation in the Greg Pass-wetland transect, we chose three representative levee top elevations, low (levee top elevation = 0.08 m NAVD88), median (0.38 m), and high (0.53 m), based on the median and 95th percentile range of the levee hypsometric curve (Fig. 16d).

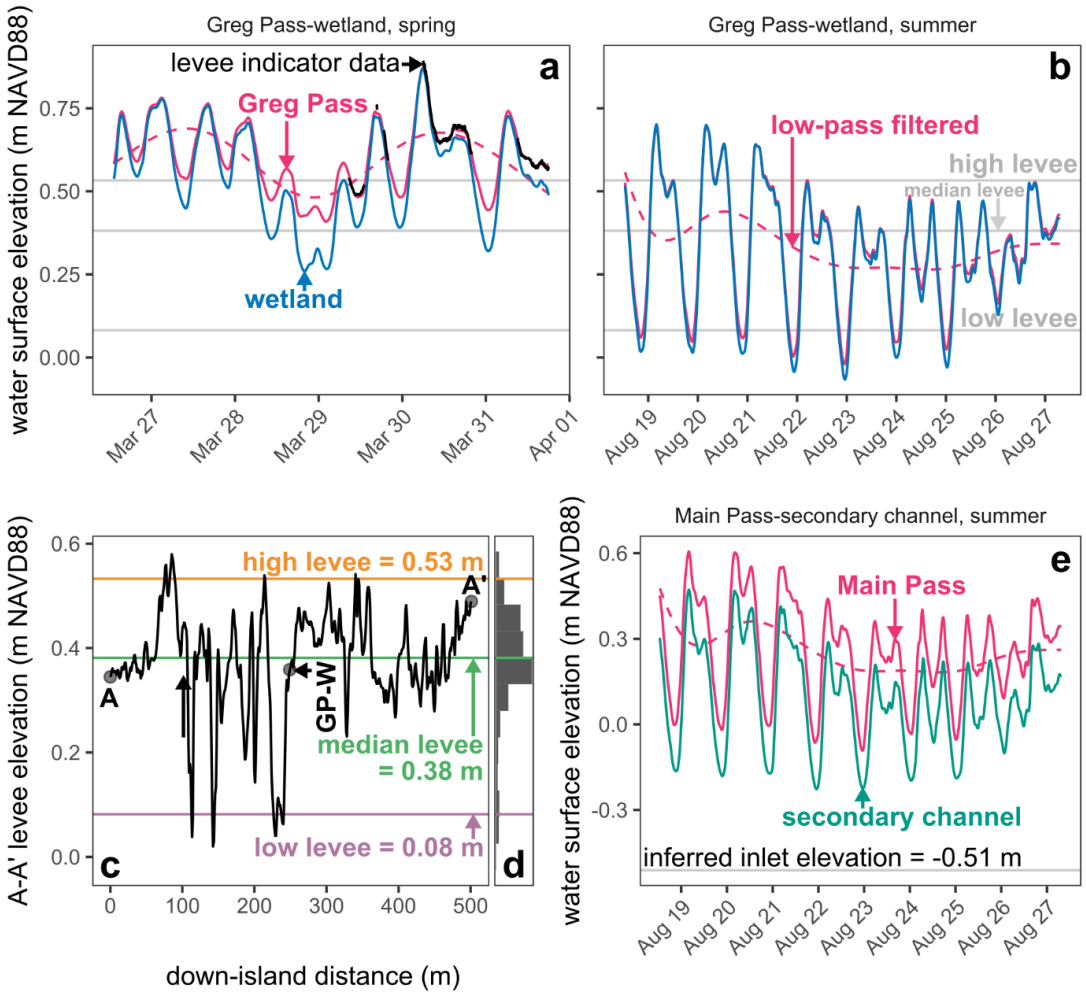

Figure 16. Primary channel and island water surface elevations for backwater modeling. Water surface elevation time series for the Greg Pass-wetland transect in the (a) spring and (b) summer. (c) Levee elevation profile along transect A-A' on the Mike Island levee (Fig. 2e) extracted from a 2020 lidar elevation map (Nghiem, 2022). (d) Hypsometric curve from the elevations in panel c. (e) Water surface elevation time series for the Main Pass-secondary channel transect in the summer.

The backwater model also relies on the elevation profile along the transect into the island. For the Greg Pass-wetland transect, the elevation profile slopes downward from the levee top into the island wetland (Fig. 17b). We discarded the portion of the elevation profile between the levee top and the Greg Pass site (i.e., point GP) and smoothed the rest for the backwater model input. We assumed that the WSE time series at the Greg Pass site and the levee top was identical. For the Main Pass-secondary channel transect, we had to infer the elevation profile because the lidar survey could not measure through the water in the secondary channel (Section 3.4.2; Fig. 17c). We determined a width-depth ratio of 12 for the smoothed elevation profile to match the measured secondary channel bed elevation.

This value of width-depth ratio is consistent with the typical range of 8 to 50 for tidal flat channels (Marani et al., 2002). The inferred elevation profile has an adverse slope from the edge of the island until ~400 m into the secondary channel, where the elevation peaks and then slopes downward further along the channel (Fig. 17d). Although the bankfull water surface elevation decreases with distance into the secondary channel (Fig. S1a), the adverse slope section occurs because the bankfull width also narrows with distance (Fig. S1b) and causes the bankfull depth to shallow faster than the bankfull water surface elevation decreases. The elevation profiles show that the inlet of the secondary channel sits at a much lower elevation (-0.51 m NAVD88) compared to the low levee case (0.08 m), allowing continuous hydrological connectivity between the primary channel and island even in a more landward, higher elevation region of Mike Island during the summer low flow (Fig. 16e). In contrast, the Greg Pass WSE often fell below the levee top elevation especially in the median and high levee cases (Fig. 16ab).

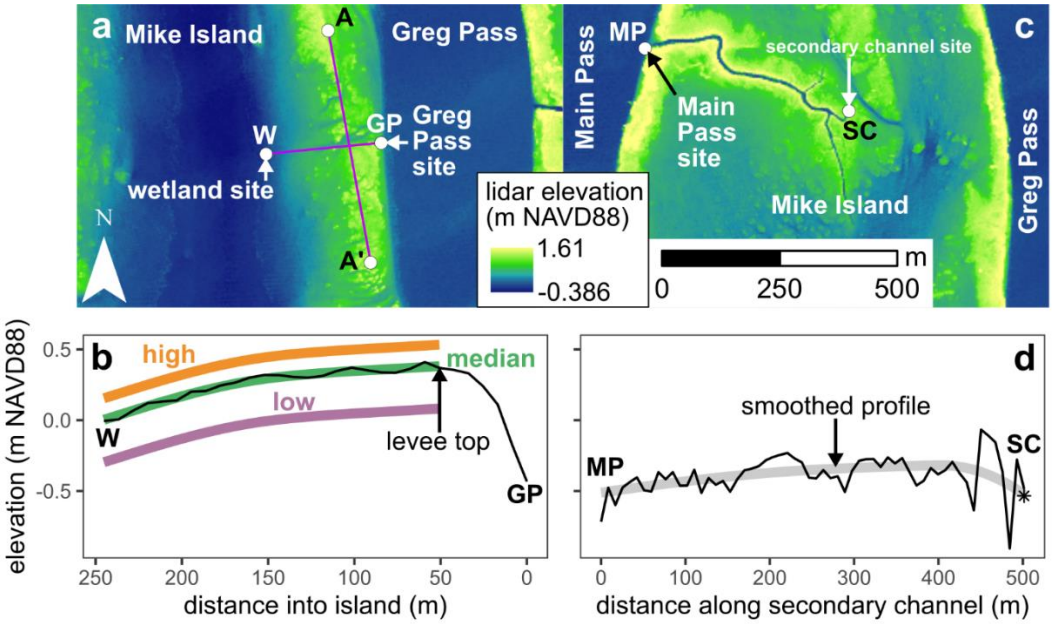

Figure 17. Backwater transect elevation data. Lidar elevation maps of the areas surrounding the (a) Greg Pass-wetland (same extent as Fig. 2e) and (b) Main Pass-secondary channel transects (same extent as Fig. 2d). Elevations in the primary channels and island center are overestimated because of water cover during the lidar survey. Extracted and smoothed elevation profiles for the (c) Greg Pass-wetland and (d) Main Pass-secondary channel transects. The star indicates the measured bed elevation in the secondary channel.

We validated the backwater-calculated *q* time series using concentration-depth profile (Fig. 8), Greg Pass survey (Fig. 11ce), and orange peel data (Section 3.4.2). Measured flow depths correspond well to the backwater model, especially considering the range of values between the low and high levee cases for the Greg Pass-wetland transect (Fig. 18, row 1). Backwater-estimated flow velocities are low compared to the orange peel-measured flow

velocities (Fig. 18, row 2), potentially due to local topographic effects at the orange peel measurement location. Unit discharge measurements agree well with backwater results (Fig. 18, row 3) because relatively shallower depths offset the relatively faster orange peel flow velocities. Measured suspended sediment concentrations were used to calibrate sediment concentration time series and hence compare well to the time series (Nghiem, Salter, et al., 2022; Fig. 18, row 4). Finally, sediment flux measurements are reasonably close to the backwater-modeled sediment flux time series (Fig. 18, row 5).

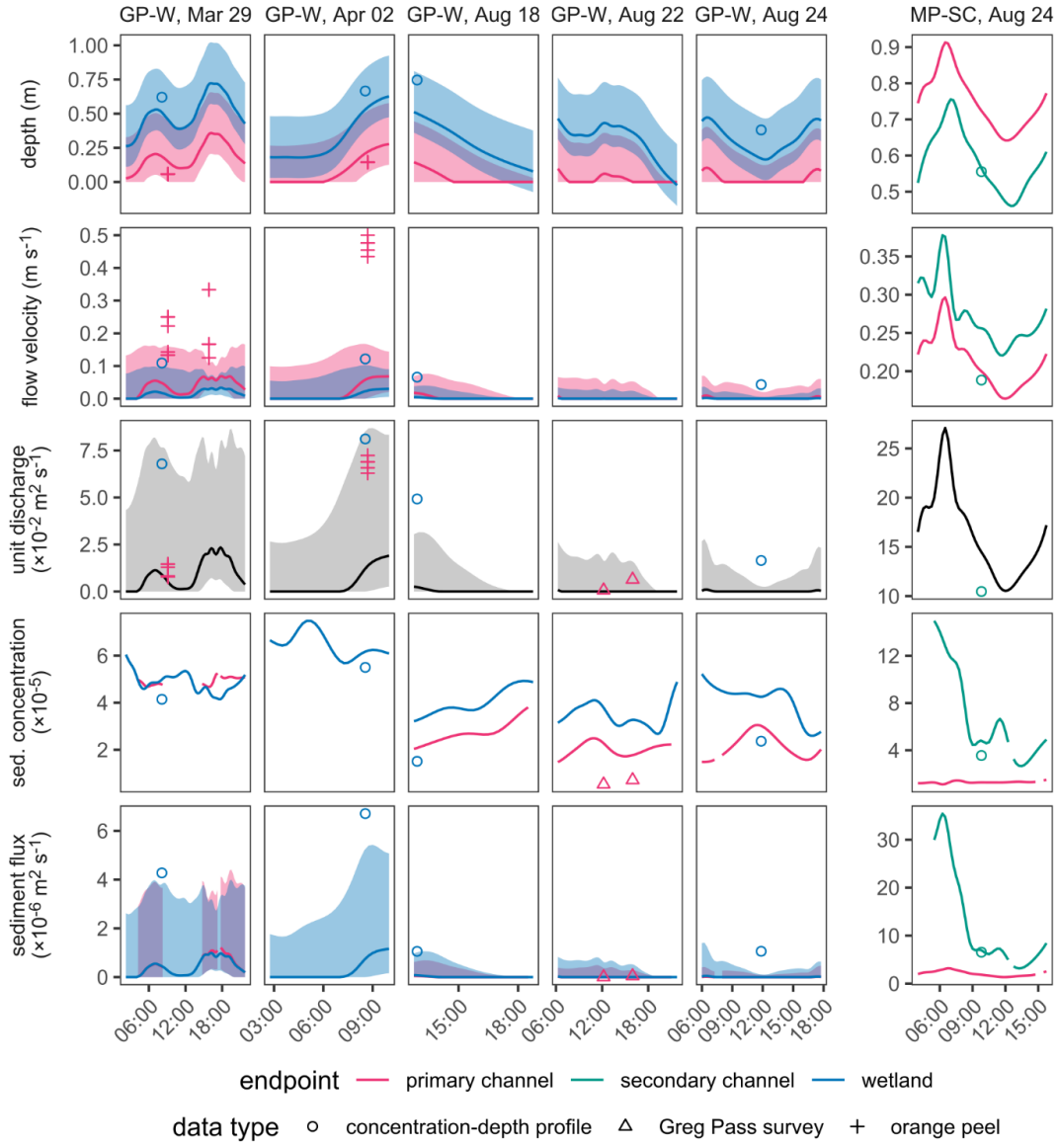

Figure 18. Backwater model results at transect endpoints clipped to times with validation data. Data for the median levee case are displayed as the solid curves in the Greg Pass-wetland (GP-W) transect panels. Shaded areas represent the range between the low and high levee cases. For all panels except the unit discharge panels (row 3), the

two colors indicate values at the transect endpoints. The unit discharge panels have only a single color because unit discharge is assumed to be conserved.

In the wetland, the backwater-modeled unit discharge time series demonstrate the importance of levee elevation for setting hydrological connectivity with the primary channel because taller levees block flow. For the Greg Pass-wetland transect, we estimated no discharge into the island when the primary channel WSE fell below the levee top elevation. Levee top elevations for the three levee cases reveal drastically different levels of hydrological connectivity between Greg Pass and the Mike Island wetland. In the spring, the Greg Pass WSE fully overtopped the low and median levees and mostly overtopped the high levee (Fig. 19abc), indicating leading to unit discharges that scaled inversely with levee top elevation. Like the unit discharge, sediment flux was the greatest for the low levee case and decreased with levee top elevation (Fig. 19d). Conversely, in the summer, the Greg Pass WSE regularly fluctuated above and below the median levee and only rarely overtopped the high levee (Fig. 19fg), indicating much weaker hydrological connectivity and, as a result, much lesser discharge and sediment flux compared to spring. The Greg Pass WSE still mostly overtopped the low levee (Fig. 19e). The low levee top elevation effectively represents small secondary channels that have dissected the levee (Fig. 16c), indicating that secondary channels are required to maintain connection between Greg Pass and the wetland. To evaluate the effect of tides, we ran a low-pass fifth-order Butterworth filter (Sendrowski and Passalacqua, 2017) on the WSE time series to remove high frequency tide fluctuations (period < 24.84 hr based on significant tidal period reported by USGS at the Calumet stream gauge). In the spring, tides did not significantly affect whether flow in Greg Pass could overtop in the three levee cases (Fig. 16a). However, in the summer, tides allowed flow in Greg Pass to overtop the median levee during times when the tide-removed WSE was consistently below the median levee top elevation (Fig. 16b).

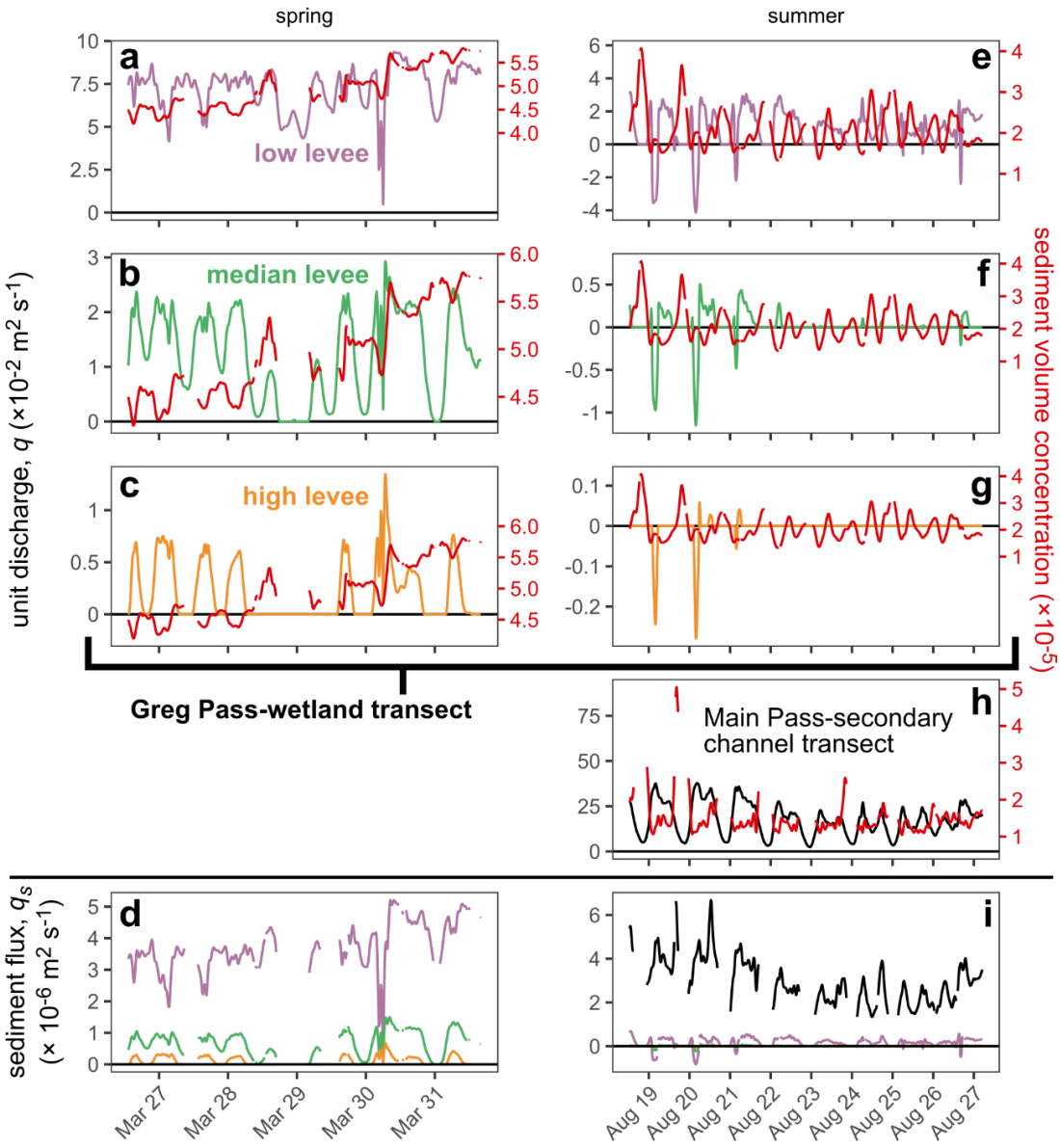

Figure 19. Backwater-modeled unit discharge and sediment flux time series in the (a-d) spring and (e-i) summer. The levee cases correspond to the Greg Pass-wetland transect. In panel i, the median and high levee curves are close to a sediment flux of 0. Missing data in the sediment concentration and sediment flux time series indicate periods in which the turbidity sensor was exposed to air.

In contrast to the levee-mediated hydrological connectivity in the wetland, the secondary channel of the Main Pass-secondary channel transect maintained flow in the summer (Fig. 19h) because the secondary channel sits at low enough elevation to tap into the flow from Main Pass (Fig. 17d). Sediment flux into the secondary channel far exceeded the sediment flux into the wetland (Fig. 19i) and is similar to the sediment flux achieved in the low levee

case of the wetland in spring (~2×10^{-6} to 4×10^{-6} m^2 s^{-1}; Fig. 19d). Tides had no effect on whether flow from Main Pass could enter the secondary channel because the Main Pass WSE was always high enough to flow into the secondary channel (Fig. 16e). Thus, the Main Pass-secondary channel transect highlights that secondary channels are important for connecting the primary channel and island especially during low flow in the summer.

We compared flow variables to better understand the relationships between overbank flow depth, velocity, and discharge into the island. In the spring for the Greg Pass-wetland transect (Fig. 20a), the flow velocity into the island wetland (i.e., q divided by flow depth) increases with depth at low depths because the lateral water surface slope into the channel is steeper (Fig. 15c) and increasing depth drives flow down the hydraulic gradient. But beyond a certain depth, velocity decreases because the driving hydraulic gradient becomes increasingly shallow and outweighs the effect of increasing depth (Fig. 15c). This tradeoff causes a peak q (e.g., q = 0.08 m^2 s^{-1} for the high levee case), which is sustained as depth increases because velocity decreases at roughly the same linear rate. However, q finally decreases at even higher depths because water surface slope becomes even shallower and causes velocity to decreases at a rate faster than linear that outpaces the increasing depth. This final stage of decreasing q with greater depth is less apparent in the median and high levee cases probably because the Greg Pass WSE did not achieve high enough depths. In the summer (Fig. 20b), this relationship between flow velocity, depth, and unit discharge for flow between Greg Pass and the wetland is similar, but more scattered probably because the lower Greg Pass WSE often disconnected flow into the island and the greater tidal versus river influence could not sustain as steep lateral water surface slopes (Fig. 15c). The peak q varies for each combination of season and levee case (Fig. 20ab) and implies that the precise feedback of depth, velocity, and discharge into the island depends on the precise inverse relationship between lateral water surface slope and depth.

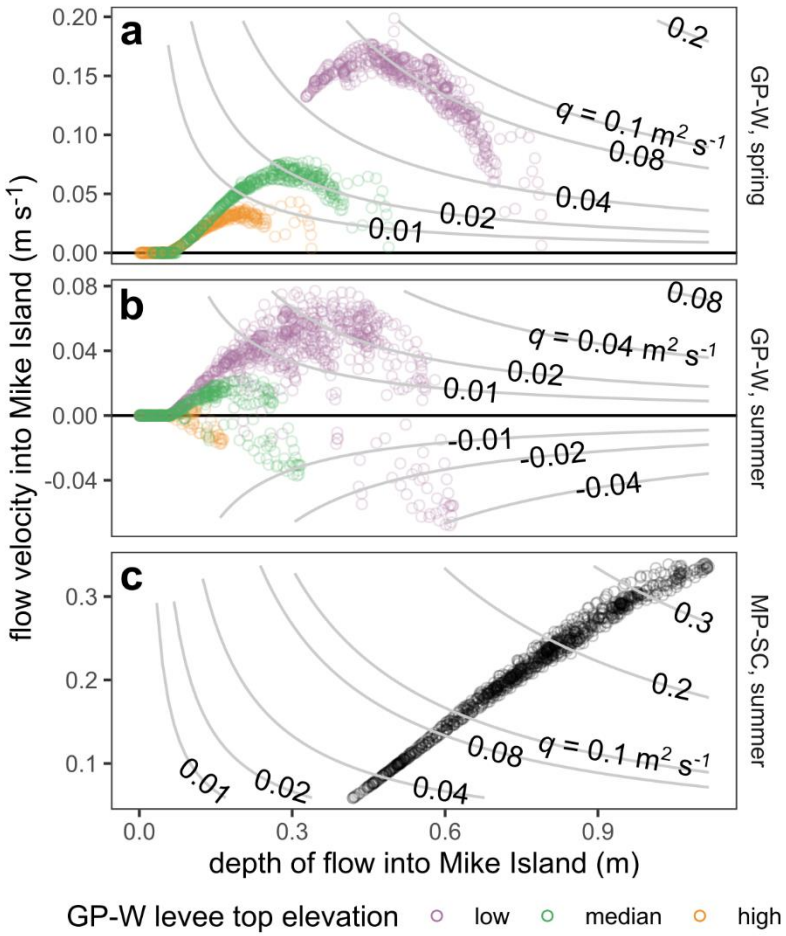

Figure 20. Backwater-modeled flow depth versus flow velocity entering Mike Island for the Greg Pass-wetland transect in the (a) spring and (b) summer and for (c) the Main Pass-secondary channel transect in the summer. Gray lines indicate contours of *q*.

In contrast to the intricate hydraulic feedback that sets flow into the wetland, the depth of flow entering the secondary channel in the summer has a strong monotonically increasing trend with flow velocity (Fig. 20c). This pattern occurs because the inverse relationship between depth and lateral water surface slope into the island (i.e., along the secondary channel) is absent in the secondary channel. Rather, the lateral water surface slope is relatively insensitive to flow depth in the secondary channel (Fig. 15d). The physical interpretation is that the WSE in the secondary channel approximately rises and falls together with the Main Pass WSE, but water is not retained and accumulated in the island interior where the secondary channel debouches. Instead, water is efficiently drawn away down the island at the roughly the same pace as it is supplied, preventing this part of the island from filling and reducing the lateral water surface slope. This hydraulic response probably occurs because the secondary channel is located in a more proximal part of Mike Island, which sits at higher elevation and is less flooded. As a result, water can be more easily drained down the island.

Discharge into the island carries suspended sediment, which we investigated using the primary channel sediment concentration time series and the backwater-calculated *q* time series to calculate the sediment flux into the island. Sediment fluxes from Greg Pass into the wetland in the spring were greater than those in the summer (Fig. 19di) because of higher *q* and sediment concentration, which was driven by higher river discharge (Fig. 2b). Levee top elevation is a critical filter on water and sediment flux into the island because the primary channel water surface must overtop the levee to have any flow into the island. This consideration is apparent in the Greg Pass-wetland transect in the summer, when the levees often blocked the flow from entering the island (Fig. 19efg). Conversely, the secondary channel was incised deep enough to bypass the levee and maintain flow from Main Pass in the summer (Fig. 19i). Beyond a simple presence or absence of flow based on levee elevation, our findings allow us to present a conceptual understanding of the dynamics of water and sediment flux into the island. In general, unit discharge and primary channel sediment concentration are inversely correlated (Fig. 19), but the variability in sediment concentration is small compared to that of unit discharge leading to a tight correlation between unit discharge and sediment flux (Fig. 19di). The inverse correlation occurs because falling tide increases the delta longitudinal slope and local sediment entrainment and concentration in the primary channel (Fig. 14; Fig. 15ab), but also lowers the primary channel WSE and hence reduces the depth of flow entering the island. In most cases, shallower flow leads to lower discharge because they are positively correlated (Fig. 20). However, an exception occurs in the wetland scenario when the flow is too deep because the island begins to fill, reducing the lateral water surface slope, flow velocity, and ultimately the unit discharge (Fig. 20ab). This inverse relationship between depth and discharge is responsible for the occasional periods of positive correlation between sediment concentration and discharge in the wetland data (Fig. 19ab).

5.5.3 Sediment transport in the island

Once sediment enters the island, sediment transport processes within the island determine whether sediment can actually settle and build land in the island. Here we explore island sediment transport mechanisms and the degree to which islands can capture sediment.

Vegetation is thought to be a key factor for facilitating sediment deposition in islands because it slows the flow in islands compared to in primary channels (Stumpf, 1983; Styles et al., 2021). Tides adjust the WSE base level over time and propagate these base level changes landward through both the primary channel and island. If vegetation slows flow in the island, then we expect tidal fluctuations to lag in the island compared to in the primary channel. We tested this idea by calculating the time lag between the primary channel and island WSE time series using peaks and troughs in WSE as points of comparison. We isolated the tidal component of the WSE time series using the high-pass version of the filter in Sect. 5.2 and Fig. 16abe and standardized the high-passed time series. We matched peaks and troughs between paired primary channel and island WSE time series according to the closest matching value and second time derivative within one hour of time lag. Results show no clear difference between peaks and troughs in terms of in time difference between the primary channel and island responses to tidal WSE changes (Fig. 21). We

found a short mean time difference between Greg Pass and the wetland in the spring that is statistically indistinguishable from zero (one-sample *t*-test $p = 0.61$; Fig. 21a). In the summer, WSE responded to tidal changes earlier in Greg Pass compared to the wetland by a statistically significant mean of 3.6 min ($p = 7.3\times10^{-3}$; Fig. 21b). Denser island vegetation in the summer (Fig. 3cd) might have slowed flow in the island and delayed the island WSE response. Although island vegetation was present in the spring (Fig. 3ab), it might not have been dense enough to significantly slow the flow. Flow depths in the island were also greater in the spring than in the summer (Fig. 15), causing smaller friction coefficient for the same roughness height (Eq. 3).

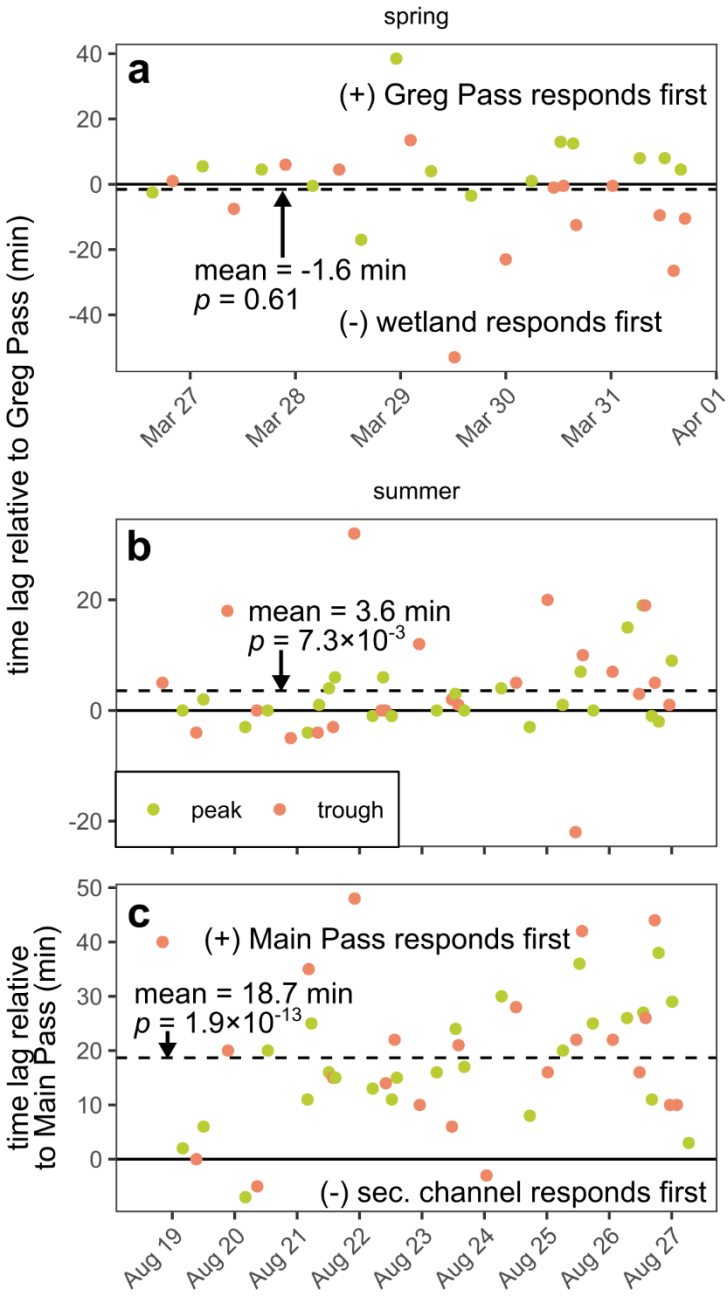

Figure 21. Time lag of peaks and troughs in the water surface elevation time series between primary channel and island for the Greg Pass-wetland transect in the (a) spring and (b) summer and for (c) the Main Pass-secondary channel transect in the summer.

In contrast to the relatively short time lags in the wetland, the secondary channel had a mean time lag of 18.7 min with Main Pass leading the secondary channel ($p = 1.9\times10^{-13}$; Fig. 21c). This time lag likely represents the time required for the Main Pass flow input to travel through the secondary channel to the measurement site (Fig. 17c), rather than

enhanced friction in the island, because the flow was confined to the secondary channel and hence relatively insensitive to landward tide propagation through the island wetland. This interpretation is consistent with our results indicating the minimal influence of island interior filling on secondary channel water surface slope (Fig. 15d; Fig. 20c). The ratio of the horizontal distance (540 m) and time lag in the secondary channel yields a velocity of 0.48 m s^{-1}, which is faster than measured and modeled flow velocities (~0.1 to 0.3 m s^{-1}; Fig. 7b; Fig. 20c) but still reasonably close.

Even if vegetation can induce slower flow in the island, sediment still must settle fast enough to deposit in the island and build land. To evaluate this question, we computed the time series of lateral sediment advection length, l_a, into the island based on the backwater-derived q time series and a representative mud settling velocity (Section 3.1.1). For the Greg Pass-wetland transect, maximal advection lengths were ~400 m and occurred in the low levee case in the spring (Fig. 22a). However, advection lengths were typically up to ~100 m and lower for all other Greg Pass-wetland cases (Fig. 22ab). In contrast, the advection length in the secondary channel in the summer was much longer (range of ~80 to 1200 m) because the unit discharge was greater (Fig. 22b). The typical width of Mike Island is 900 m, implying that much of the island sediment input, which is mostly mud (Fig. 8cd), can settle and be retained, at least temporarily, in the island because the advection length is usually much shorter than the island width. However, advection length in the secondary channel exceeded Mike Island width at times (Fig. 22b), indicating that this sediment might bypass the island altogether. But we expect this bypass to be minimal because advection length exceeded Mike Island width for only brief periods of time (Fig. 22b) and the secondary channel flow spreads out laterally once it drains into the island interior and likely induces deposition. But ultimately, short advection length does not guarantee longer term storage and burial in the island because sediment might be dynamically settling and entrained in the island.

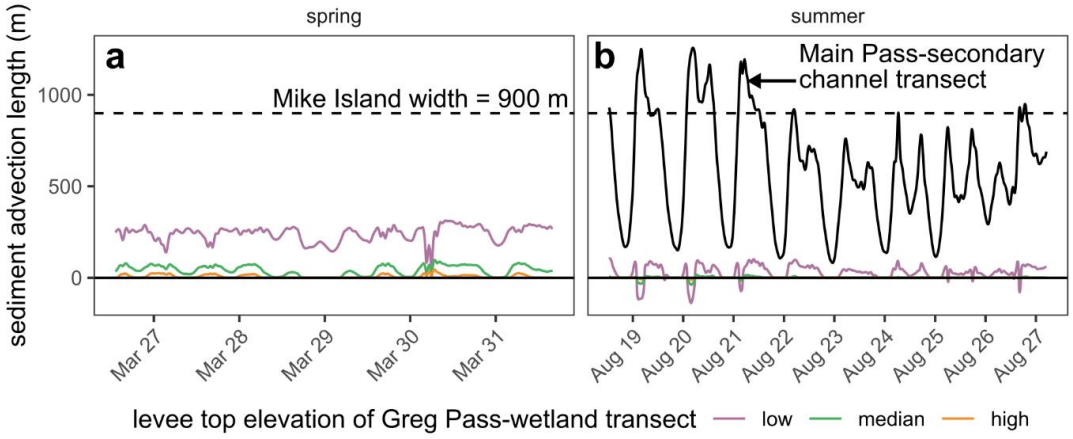

Figure 22. Sediment advection length in the (a) spring and (b) summer using the backwater-derived q time series (Fig. 19) and a representative mud settling velocity of 0.3 mm s^{-1}.

To assess the degree to which entrainment affects island sediment concentration, we computed the ratio of island and primary channel sediment concentrations, $\tilde{C}$, at each time step of the sediment concentration time series for the two transects (i.e., at the transect endpoints). If no entrainment occurred in the island, then we expect sediment concentration to decay exponentially with distance from the primary channel into the island under steady flow due to sediment advection and settling (e.g., Zeichner et al., 2021): $\tilde{C} = \exp(-l_a \Delta x)$ where l_a comes from Fig. 22 and Δx (m) is the distance transported into the island. In the spring, Greg Pass and wetland sediment concentrations were roughly equal over time (Fig. 23a). In contrast, sediment concentration in the island (i.e., wetland and secondary channel sites) was systematically higher than the concentration in the corresponding primary channel by a factor of ~1.5 for Greg Pass-wetland and ~3 for Main Pass-secondary channel. All of these observations are inconsistent with sediment transport by advection and settling in the absence of entrainment, which predicts smaller island sediment concentration compared to the primary channel (Fig. 23). So although sediment entering the island still advected and settled with distance, island sediment entrainment probably counterbalanced the vertical sediment settling flux and prevented a decrease of sediment concentration into the island.

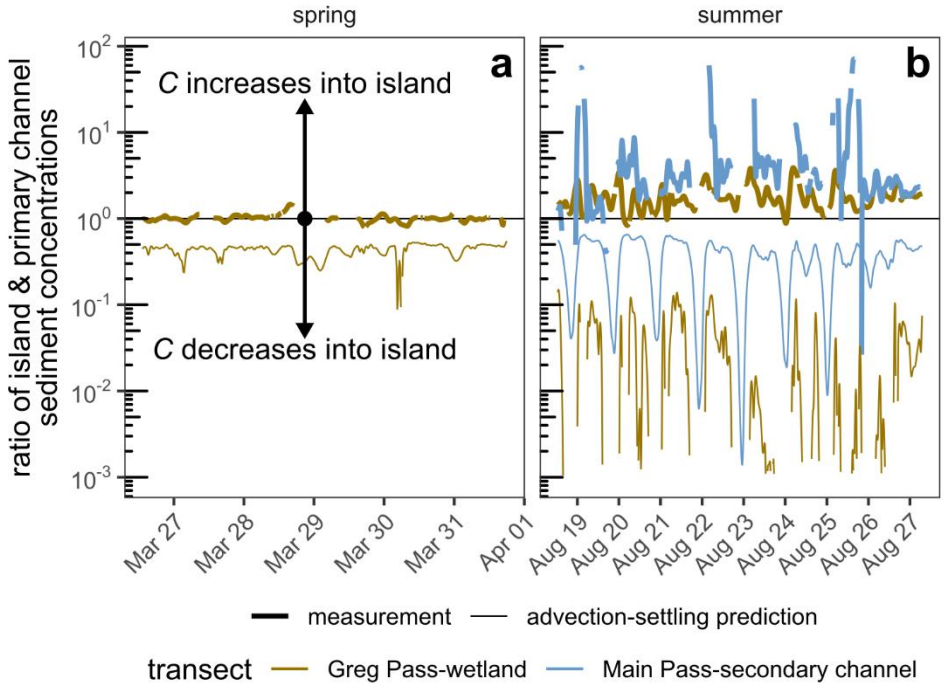

Figure 23. Ratio of primary channel and island sediment concentration time series in the (a) spring and (b) summer.

5.6 Discussion

5.6.1 Sediment transport mechanisms between delta channels and islands

5.6.1.1 Field Data Conclusions

Although our point measurements of hydraulics and sediment at WLD are discontinuous in time and space, they provide conceptual insight into the fluvial and tidal processes that deliver sediment from channels to islands in a river-dominated delta. First, we highlight the importance of island levee elevation relative to the water surface elevation (Fig. 1) for controlling spatial patterns of water and sediment flow in the island. We showed that the unit discharge, measured by ADCP during flood tide, and sediment flux flowed in the landward direction in northern proximal parts of Mike Island, but flowed in the seaward direction in more southern distal parts of the island (Fig. 5a; Fig. 9a). One possible explanation is that the higher elevation island levees in the northern part of the island reduced the hydrological connectivity between the island and the adjacent channel, as evidenced by the subaerial levees in the drone photos (Fig. 3ac). During flood tide, water and sediment could be funneled up the island from the lower elevation distal areas that were better connected to adjacent channels and the offshore tidal boundary. We also measured unit discharge and sediment flux directed into the island in the more distal location, but away from the island in the more proximal location (Fig. 5ab; Fig. 9ab). This pattern suggests that taller levees can block flow from entering the island, but shorter levees can facilitate flow into the island.

Flow in the channels tended to be deeper, faster (Fig. 7ab), and have greater shear velocity (Fig. 7ef) than that in the island, implying that loss of channelization and lateral spreading when water and sediment flow into the island aids deposition of the supplied sediment. Roughness heights from the law of the wall (Eq. 1) were similar between channel and island (Fig. 7cd), but the island had greater friction coefficients because of the shallower depth relative to roughness height. Similar roughness heights between the channel and island appear counterintuitive because the bed in the channel was much sandier than that in the island (Fig. 12ab), but submerged vegetation might have contributed to increasing roughness in the island (e.g., Baptist et al., 2007).

The suspended sediment in WLD was mostly mud (Fig. 8cd; Fig. 9cd), which can settle fast enough relative to the flow to be readily captured in the island (Fig. 10ce). Individual grains of mud have slow settling velocity because of their small size, suggesting that mud might settle too slowly to build any appreciable island deposits and simply be advected out to sea. However, Nghiem et al. (2024) found that mud in WLD tended to flocculate into aggregates (i.e., flocs) that settle faster than individual grains. Using their typical floc settling velocity of 0.3 mm s^{-1} and estimates of unit discharge into the island from a longitudinal survey of Greg Pass discharge, we found horizontal sediment advection lengths of 100 m and shorter (Fig. 10c), which are much shorter than the width of Mike Island and imply that suspended mud can readily settle in the island. This tradeoff should vary between deltas depending on the sediment settling velocity (set by grain size and flocculation) and island size. In line with the advection length results, recent island deposits, sampled using shallow sediment cores (Fig. 12c) and a sediment cap transect (Fig. 13), were muddy.

5.6.1.2 Time Series Data Conclusions

Water surface elevation time series reveal the frequency of primary channel overflow into the island. Overtopping was typical in the spring between the Greg Pass and wetland sites (Fig. 16a) because the river discharge entering WLD was high (Fig. 2b). However, the Greg Pass and wetland sites were often disconnected, depending on the levee top elevation (Fig. 16b), during low river discharge conditions in the summer (Fig. 2b). High tides can temporarily reestablish connection when the primary channel water surface elevation is, on average, lower than the levee top elevation (Fig. 16b). In contrast to the wetland, the secondary channel (Fig. 2d) maintained flow in the summer because it has incised through the levee at low enough elevation (Fig. 17d), consistent with the idea that secondary channels nourish island centers with sediment for them to keep pace with sea level rise (Salter and Lamb, 2022).

Once the water level in the primary channel overtops the edge of the island, the primary channel supplies the island with water and sediment. We used time series data to understand mechanisms of sediment transfer into the island via (1) sediment source in primary channels, (2) sediment flux entering the island, and (3) sediment transport within the island. Our main findings are demonstrated in Fig. 24.

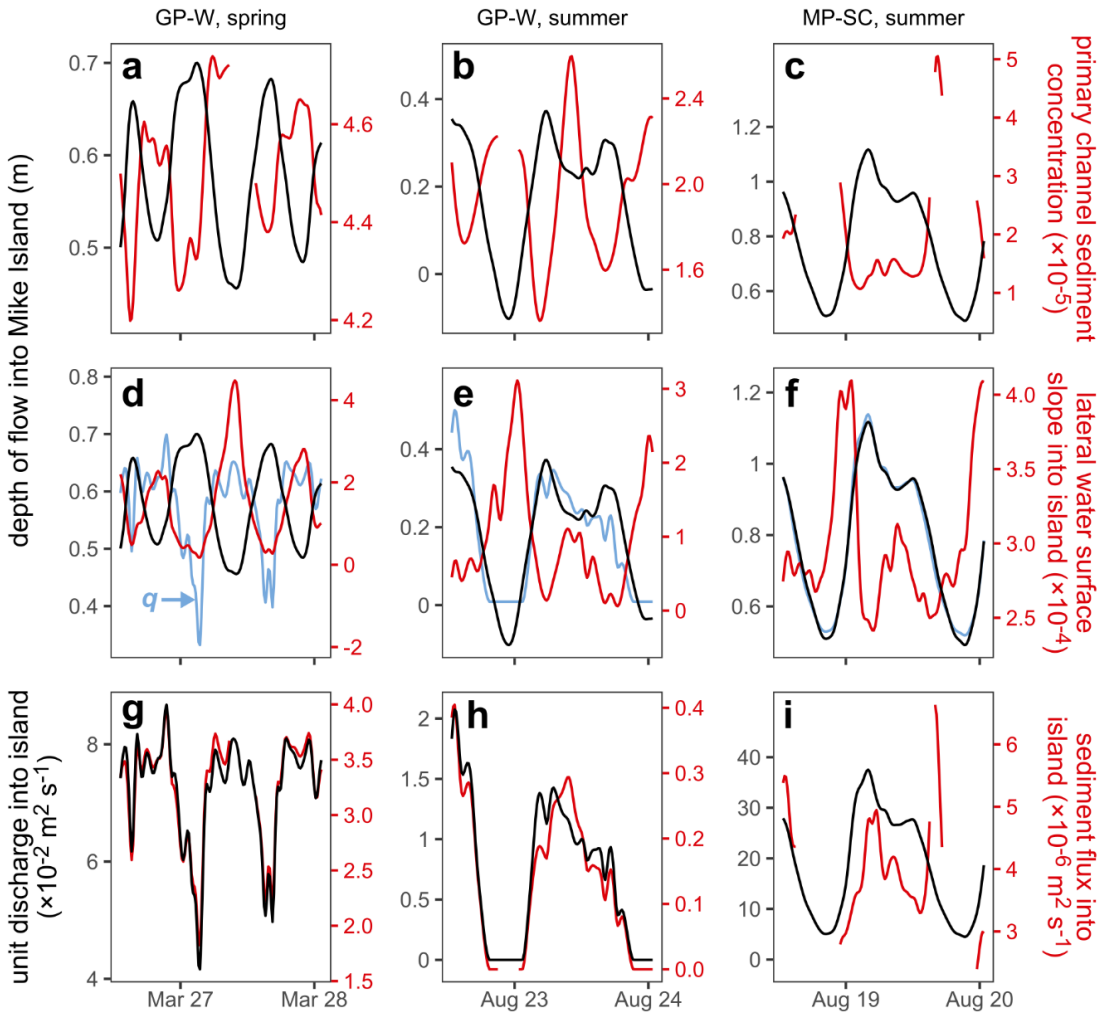

Figure 24. Summary time series of primary channel and island sediment transport for the Greg Pass-wetland and Main Pass-secondary channel transects at representative times. The blue time series in panels d, e, and f represent the unit discharge, *q*. We used low levee case for the Greg Pass-wetland panels.

First, the primary channel sediment concentration inversely correlates with the primary channel water surface elevation and depth of flow into the island (Fig. 24abc) because falling tide draws down the water surface and enhances the longitudinal water surface slope along the delta as the tide signal takes time to propagate landward and vice versa (Fig. 15ab). Greater longitudinal water surface slope causes greater shear stress in primary channels, thereby locally entraining more sediment and increasing sediment concentration (Partheniades, 1965; De Leeuw et al., 2020).

Next, the sediment flux into the island is the product of an intricate hydrodynamic feedback between the primary channel and island. The inverse feedback between primary channel entrainment and water surface elevation causes lower sediment concentration to be linked

to greater depth of flow into the island. For the wetland, greater flow depth into the island causes faster flow velocity and, hence, unit discharge into the island despite a concurrent reduction in lateral water surface slope into the island as the island fills with water (Fig. 24de). But beyond a certain flow depth, increasing depth causes the lateral water surface slope to shallow to such an extent that the flow velocity begins to decrease and the unit discharge achieves the maximum. The peak unit discharge is maintained momentarily as the depth further increases because greater depth balances out slower flow velocity (Fig. 20ab). But even greater depths eventually cause flow velocity to decrease faster than depth increases, producing a net decrease in unit discharge that can be observed at the greatest depths in Fig. 24de. On the other hand, flow depth and velocity increase together at all observed flow depths for the secondary channel (Fig. 20c) because water does not substantially accumulate and raise the water surface elevation (i.e., decrease lateral water surface slope) in the vicinity of the secondary channel in the island. Overall, sediment flux into the island is tightly correlated with unit discharge into the island (Fig. 24ghi), despite the fact that primary channel sediment concentration is often inversely related to discharge via flow depth (Fig. 19), because the variability of discharge outstrips the variability of sediment concentration. These facts imply that, although tides drive dynamic fluctuations in unit discharge and sediment flux entering the island, river discharge is more important for maximizing discharge and sediment flux because it increases island inundation and primary channel sediment concentration through local sediment entrainment and sediment supply from upstream. Tides are also more likely to rework existing delta deposits.

Finally, island hydrodynamics control the distribution and potential longer term accretion of sediment in the island. Mud can readily settle in Mike Island because the advection length is typically shorter than island width (Fig. 22). Furthermore, near-surface deposits of Mike Island (Fig. 12c; Fig. 13) were muddy, proving the ability of the island to build land out of mud. Despite the capacity of the island to accrete mud, sediment does not simply fall out of suspension quiescently and deposit on the island. Bed sediment entrainment in the island occurs simultaneously and leads to the absence of sediment concentration decay with distance into the island (Fig. 23). The net difference between sediment deposition and entrainment fluxes in the island over sufficiently long timescales ultimately sets island accretion rate.

5.6.2 The effect of vegetation on flow through islands

Past hydrodynamic modeling studies have often selected roughness relations for vegetated island wetlands without field data constraints. Three different treatments of vegetated wetland roughness in WLD produced a wide range of friction coefficients (Fig. 7cd), indicating that the treatment of vegetated wetland roughness has been highly variable and somewhat arbitrary to date because roughness is typically treated as a tuning parameter. Our in situ wetland roughness measurements provide new data to better characterize vegetated wetland roughness for future studies.

Vegetation has been often cited as a mechanism to baffle and slow flow in wetlands (Stumpf, 1983; Styles et al., 2021). Our time lag analysis supports this behavior because tidal changes in the wetland lagged behind those in a primary channel during the summer when vegetation was dense (Fig. 21b). In contrast, we did not detect a statistically significant time lag in the spring, likely because of the sparser vegetation and greater flow depths in the wetland.

5.6.3 Stratigraphy of the Wax Lake Delta

The near-surface stratigraphy of the WLD islands has been classically described as sand-rich (Roberts et al., 1980; Roberts et al., 1997), an observation that is paradoxical to our muddy shallow sediment core samples (Fig. 11) and the muddy cap on Mike Island (Fig. 12). We suggest that the evolution of sediment supply and island accretion in WLD can explain the paradox. Prior to 1973, large volumes of sand had accumulated in Grand Lake, just upstream of the Wax Lake Outlet (Roberts et al., 1980). At this time, sediment supply to WLD was mud-rich, building up the muddy bay bottom. The 1973 Mississippi River flood flushed large amounts of sand from Grand Lake into WLD, building up the subaerial sand-rich islands (Roberts et al., 1980; Roberts et al., 1997). Recent sediment transport in WLD is mud-dominated (Nghiem et al., 2024), which has probably since deposited the muddy cap on top of the island sand bodies. This scenario is consistent with efficient mud retention implied by the short sediment advection lengths relative to island size (Fig. 10). Mud will likely continue to be the main driver of sediment accretion in WLD because of the muddy suspended sediment supply and the observed erosion of distributary channels (Shaw et al., 2013), which makes it more difficult for coarser sand grains traveling closer to the bed to reach the upper water column and be transported into islands.

5.6.4 Implications for delta island resilience

Delta islands must aggrade through sedimentation to keep pace with relative sea level rise in order for a river delta to be sustainable. It is well known that increased flooding of deltas encourages sedimentation via increased sediment supply, providing a negative feedback to help maintain the delta elevation in the face of flooding caused by sea level rise (Paola et al., 2011). In line with prior work (e.g., Olliver et al., 2020), we found greater sediment fluxes into the island at higher river discharge because of the higher sediment concentration and degree of hydrological connectivity between primary channel and island. But at the same river discharge, the island discharge and sediment flux increase with lower levee elevation and secondary channels. Secondary channels deliver sediment directly into the island interior at greater sediment fluxes than those at taller levees. Thus, sediment flux via secondary channels supplies island interiors with sediment and stabilizes them against sea level rise, especially when flow cannot overtop levees (Salter and Lamb, 2022).

Although some flooding via sea level rise aids sediment supply and sedimentation in delta islands, too much sea level rise will simply drown islands with insufficient sediment input to compensate. We observed this drowning effect at high tides. High depths of flow into the island cause the discharge to decline with increasing overbank depth (Fig. 20a). Island

discharge falls at these high depths because the lateral water surface slope into the channel becomes too shallow, which slows the flow velocity to the extent that it outweighs the effect of higher depth on island discharge. In the extreme case, complete drowning eliminates discharge and sediment flux into the island altogether by total flattening of the lateral water surface slope. At this point, delta islands are in danger of being irreversibly lost to sea level rise. On the other hand, flooding via river discharge can counteract drowning because it can carry greater sediment concentration from upstream and deposit this sediment to aggrade the island, such as in WLD during the 1973 Mississippi River flood (Roberts et al., 1980).

Finally, sufficient amounts of sediment must be captured and retained in deltas for sedimentation to be effective at offsetting sea level rise (Kolker et al., 2012; Esposito et al., 2017). Much attention has been focused on the trapping and retention of sand to improve coastal land resilience (Nittrouer et al., 2012; Nittrouer and Viparelli, 2014; Meselhe et al., 2016). However, our observations of muddy surface deposits in Mike Island support the idea that mud retention might also be important for maintaining coastal land (Esposito et al., 2017).

5.7 Conclusion

We conducted fieldwork in the Wax Lake Delta, a river-dominated delta in the Mississippi River Delta complex, to evaluate how sediment is supplied to delta islands. We first measured detailed local data on hydraulics, suspended sediment, and sediment deposits in primary channels, an island wetland, and a secondary channel in the spring and summer. In particular, we measured flow velocity profiles in the Mike Island wetland, providing key constraints on hydraulic roughness in vegetated island wetlands compared to the wide variability from past modeling studies that empirically tuned roughness. Consecutive discharge measurements in Greg Pass, one of the primary channels bounding Mike Island, show that flow depths and speeds entering the island were small enough for mud, which formed the bulk of the suspended sediment, to gravitationally settle in the island. This high potential mud retention is reflected in recent muddy deposits on the bed and at shallow depth in Mike Island. The abundance of mud in Mike Island highlights the importance of mud, not only sand, for accreting coastal land.

We next used time series data to explore the mechanisms that set sediment concentration in primary channels, bring water and sediment into the island, and transport sediment within the island. We used in situ water surface elevation and sediment concentration time series at two transects, one between Greg Pass and a wetland and one between Main Pass (another primary channel of Mike Island) and a secondary channel. Water surface elevation time series reveal that tall levees block flow from entering the island, but the secondary channel bypass this barrier because it has incised deeper and maintains connection with the primary channel.

But once the primary channel floods into the island, sediment and hydraulic feedbacks cascade together to determine sediment transport between primary channels and islands.

Primary channels are the source of sediment for islands. Water surface elevation and sediment concentration data show that primary channel sediment concentration increases as the tide falls because the longitudinal water surface slope becomes steeper and increases bed stress and local sediment entrainment, and vice versa. However, in terms of sediment flux into the island, backwater modeling results reveal that tidal variation in unit discharge into the island dwarfs the tidal variation in primary sediment concentration. In the wetland, flow depth, velocity, and discharge into the island initially increase with depth at low depths because of greater depth and steeper lateral water surface slope set by tides. Water surface slope shallows as the tide and depth rises and the island fills with water, eventually reducing the flow velocity and discharge into the island akin to island drowning by sea level rise. These dynamics are absent in the secondary channel because its water and sediment flux directly reflect supply from the primary channel. Thus, discharge and sediment flux into the island scale strongly together except for brief periods of high inundation in the wetland when increasing depth causes decreasing island discharge. Within Mike Island, a time lag of tidal water surface elevation changes suggests that dense summer vegetation likely slowed flow in the island wetland relative to the primary channel, in line with conventional ideas of flow baffling by vegetation. Typical horizontal advection lengths for mud were typically shorter than the width of Mike Island and indicate efficient sediment capture in the island, which is consistent the abundance of mud deposits in Mike Island. However, comparison of sediment concentration between the primary channel and island shows that sediment concentration did not decrease into the island probably because bed sediment entrainment in the island counteracted the deposition flux in the island. Thus, the difference between sediment deposition and entrainment fluxes in the island determines the long-term aggradation and survival of delta islands.

5.8 References

Baptist, M. J., Babovic, V., Rodríguez Uthurburu, J., Keijzer, M., Uittenbogaard, R. E., Mynett, A., & Verwey, A. (2007). On inducing equations for vegetation resistance. *Journal of Hydraulic Research*, *45*(4), 435–450. https://doi.org/10.1080/00221686.2007.9521778

Bevington, A. E., Twilley, R. R., Sasser, C. E., & Holm Jr, G. O. (2017). Contribution of river floods, hurricanes, and cold fronts to elevation change in a deltaic floodplain, northern Gulf of Mexico, USA. *Estuarine, Coastal and Shelf Science*, *191*, 188–200. https://doi.org/10.1016/j.ecss.2017.04.010

Blum, M. D., & Roberts, H. H. (2009). Drowning of the Mississippi Delta due to insufficient sediment supply and global sea-level rise. *Nature Geoscience*, *2*(7), 488–491. https://doi.org/10.1038/ngeo553

Chow, V. T. (1959). *Open-Channel Hydraulics*. McGraw-Hill.

Christensen, A. L., Denbina, M. W., & Simard, M. (2023). Delta-X: Digital Elevation Model, MRD, LA, USA, 2021. *ORNL DAAC*. https://doi.org/10.3334/ORNLDAAC/2181

Christensen, A. L., Mallard, J. M., Nghiem, J., Simard, M., Pavelsky, T. M., & Lamb, M. P. (2022). Delta-X: Acoustic Doppler Current Profiler Channel Surveys, MRD, Louisiana, 2021, V2. *ORNL DAAC*. https://doi.org/10.3334/ORNLDAAC/2081

Cortese, L., Donatelli, C., Zhang, X., Nghiem, J. A., Simard, M., Jones, C. E., Denbina, M., Fichot, C. G., Harringmeyer, J. P., & Fagherazzi, S. (2024). Coupling numerical models of deltaic wetlands with AirSWOT, UAVSAR, and AVIRIS-NG remote sensing data. *Biogeosciences*, *21*(1), 241–260. https://doi.org/10.5194/bg-21-241-2024

De Leeuw, J., Lamb, M. P., Parker, G., Moodie, A. J., Haught, D., Venditti, J. G., & Nittrouer, J. A. (2020). Entrainment and suspension of sand and gravel. *Earth Surface Dynamics*, *8*(2), 485–504. https://doi.org/10.5194/esurf-8-485-2020

Edmonds, D. A., & Slingerland, R. L. (2008). Stability of delta distributary networks and their bifurcations. *Water Resources Research*, *44*(9). https://doi.org/10.1029/2008WR006992

Esposito, C. R., Shen, Z., Törnqvist, T. E., Marshak, J., & White, C. (2017). Efficient retention of mud drives land building on the Mississippi Delta plain. *Earth Surface Dynamics*, *5*(3), 387–397. https://doi.org/10.5194/esurf-5-387-2017

Feizabadi, S., Li, C., & Hiatt, M. (2024). Response of river delta hydrological connectivity to changes in river discharge and atmospheric frontal passage. *Frontiers in Marine Science*, *11*, 1387180. https://doi.org/10.3389/fmars.2024.1387180

Galy, V., France-Lanord, C., Beyssac, O., Faure, P., Kudrass, H., & Palhol, F. (2007). Efficient organic carbon burial in the Bengal fan sustained by the Himalayan erosional system. *Nature*, *450*(7168), 407–410. https://doi.org/10.1038/nature06273

Ganti, V., Lamb, M. P., & McElroy, B. (2014). Quantitative bounds on morphodynamics and implications for reading the sedimentary record. *Nature Communications*, *5*(1), 3298. https://doi.org/10.1038/ncomms4298

Geleynse, N., Hiatt, M., Sangireddy, H., & Passalacqua, P. (2015). Identifying environmental controls on the shoreline of a natural river delta. *Journal of Geophysical Research: Earth Surface*, *120*(5), 877–893. https://doi.org/10.1002/2014JF003408

Giosan, L., Syvitski, J., Constantinescu, S., & Day, J. (2014). Climate change: Protect the world's deltas. *Nature News*, *516*(7529), 31. https://doi.org/10.1038/516031a

Hiatt, M., & Passalacqua, P. (2015). Hydrological connectivity in river deltas: The first-order importance of channel-island exchange. *Water Resources Research*, *51*(4), 2264–2282. https://doi.org/10.1002/2014WR016149

Jensen, D. J., Cavanaugh, K. C., Thompson, D. R., Fagherazzi, S., Cortese, L., & Simard, M. (2022). Leveraging the historical Landsat catalog for a remote sensing model of wetland

accretion in coastal Louisiana. *Journal of Geophysical Research: Biogeosciences, 127*(6), e2022JG006794. https://doi.org/10.1029/2022JG006794

Jensen, D., Thompson, D. R., Simard, M., Solohin, E., & Castañeda-Moya, E. (2024). Imaging spectroscopy-based estimation of aboveground biomass in Louisiana's coastal wetlands: Toward consistent spectroscopic retrievals across atmospheric states. *Journal of Geophysical Research: Biogeosciences*, *129*(9), e2024JG008112. https://doi.org/10.1029/2024JG008112

Kolker, A. S., Miner, M. D., & Weathers, H. D. (2012). Depositional dynamics in a river diversion receiving basin: The case of the West Bay Mississippi River Diversion. *Estuarine, Coastal and Shelf Science, 106*, 1–12. https://doi.org/10.1016/j.ecss.2012.04.005

Latimer, R. A., & Schweizer, C. W. (1951). *The Atchafalaya River Study: A report based upon engineering and geological studies of the enlargement of Old and Atchafalaya Rivers*. United States Army Corps of Engineers. http://hdl.handle.net/11681/30764

Marani, M., Lanzoni, S., Zandolin, D., Seminara, G., & Rinaldo, A. (2002). Tidal meanders. *Water Resources Research, 38*(11), 7-1-7–14. https://doi.org/10.1029/2001WR000404

Mehta, A. J., & McAnally, W. H. (2008). Fine grained sediment transport. *Sedimentation Engineering: Processes, Measurements, Modeling, and Practice*, 253–306. https://doi.org/10.1061/9780784408148

Meselhe, E. A., Sadid, K. M., & Allison, M. A. (2016). Riverside morphological response to pulsed sediment diversions. *Geomorphology*, *270*, 184–202. https://doi.org/10.1016/j.geomorph.2016.07.023

Nardin, W., & Edmonds, D. A. (2014). Optimum vegetation height and density for inorganic sedimentation in deltaic marshes. *Nature Geoscience*, *7*(10), 722–726. https://doi.org/10.1038/ngeo2233

Nardin, W., Edmonds, D. A., & Fagherazzi, S. (2016). Influence of vegetation on spatial patterns of sediment deposition in deltaic islands during flood. *Advances in Water Resources*, *93*, 236–248. https://doi.org/10.1016/j.advwatres.2016.01.001

Nghiem, J. (2022). *Sediment Accretion Rates and Spatial Patterns in the Wax Lake Delta, LA 2020* [Dataset]. OpenTopography. https://doi.org/10.5069/G99W0CP6

Nghiem, J. A., Li, G. K., Harringmeyer, J. P., Salter, G., Fichot, C. G., Cortese, L., & Lamb, M. P. (2024). Testing floc settling velocity models in rivers and freshwater wetlands. *Earth Surface Dynamics*, *12*(6), 1267–1294. https://doi.org/10.5194/esurf-12-1267-2024

Nghiem, J., Salter, G., & Lamb, M. P. (2024). Delta-X: Bed and Suspended Sediment Grain Size, MRD, LA, USA, 2019-2021, V3. *ORNL DAAC*. https://doi.org/10.3334/ORNLDAAC/2379

Nghiem, J., Salter, G., & Lamb, M. P. (2025). Delta-X: Sediment Core Grain Size Distribution, Wax Lake Delta, MRD, LA. *ORNL DAAC*. https://doi.org/10.3334/ORNLDAAC/2382

Nghiem, J., Salter, G., Wright, K. A., Passalacqua, P., & Lamb, M. P. (2022). Delta-X: Turbidity, Water and Air Pressure, Temperature, MRD, Louisiana, 2021, V4. *ORNL DAAC*. https://doi.org/10.3334/ORNLDAAC/2241

Nittrouer, J. A., Best, J. L., Brantley, C., Cash, R. W., Czapiga, M., Kumar, P., & Parker, G. (2012). Mitigating land loss in coastal Louisiana by controlled diversion of Mississippi River sand. *Nature Geoscience, 5*(8), 534–537. https://doi.org/10.1038/ngeo1525

Nittrouer, J. A., & Viparelli, E. (2014). Sand as a stable and sustainable resource for nourishing the Mississippi River delta. *Nature Geoscience*, *7*(5), 350–354. https://doi.org/10.1038/ngeo2142

Olliver, E. A., & Edmonds, D. A. (2021). Hydrological connectivity controls magnitude and distribution of sediment deposition within the deltaic islands of Wax Lake Delta, LA, USA. *Journal of Geophysical Research: Earth Surface*, *126*(9), e2021JF006136. https://doi.org/10.1029/2021JF006136

Olliver, E. A., Edmonds, D. A., & Shaw, J. B. (2020). Influence of Floods, Tides, and Vegetation on Sediment Retention in Wax Lake Delta, Louisiana, USA. *Journal of Geophysical Research: Earth Surface, 125*(1), e2019JF005316. https://doi.org/10.1029/2019JF005316

Paola, C., Twilley, R. R., Edmonds, D. A., Kim, W., Mohrig, D., Parker, G., Viparelli, E., & Voller, V. R. (2011). Natural Processes in Delta Restoration: Application to the Mississippi Delta. *Annual Review of Marine Science, 3*(1), 67–91. https://doi.org/10.1146/annurev-marine-120709-142856

Partheniades, E. (1965). Erosion and deposition of cohesive soils. *Journal of the Hydraulics Division, 91*(1), 105–139. https://doi.org/10.1061/JYCEAJ.0001165

Roberts, H. H., Adams, R. D., & Cunningham, R. H. W. (1980). Evolution of sand-dominant subaerial phase, Atchafalaya Delta, Louisiana. *AAPG Bulletin, 64*(2), 264–279. https://doi.org/10.1306/2F918964-16CE-11D7-8645000102C1865D

Roberts, H. H., Walker, N., Cunningham, R., Kemp, G. P., & Majersky, S. (1997). *Evolution of sedimentary architecture and surface morphology: Atchafalaya and Wax Lake Deltas, Louisiana (1973-1994).* https://archives.datapages.com/data/gcags/data/047/047001/0477.htm

Salter, G., & Lamb, M. P. (2022). Autocyclic secondary channels stabilize deltaic islands undergoing relative sea level rise. *Geophysical Research Letters*, e2022GL098885. https://doi.org/10.1029/2022GL098885

Sendrowski, A., & Passalacqua, P. (2017). Process connectivity in a naturally prograding river delta. *Water Resources Research*, *53*(3), 1841–1863. https://doi.org/10.1002/2016WR019768

Shaw, J. B., Mohrig, D., & Whitman, S. K. (2013). The morphology and evolution of channels on the Wax Lake Delta, Louisiana, USA. *Journal of Geophysical Research: Earth Surface*, *118*(3), 1562–1584. https://doi.org/10.1002/jgrf.20123

Shields, M. R., Bianchi, T. S., Mohrig, D., Hutchings, J. A., Kenney, W. F., Kolker, A. S., & Curtis, J. H. (2017). Carbon storage in the Mississippi River delta enhanced by environmental engineering. *Nature Geoscience*, *10*(11), 846–851. https://doi.org/10.1038/ngeo3044

Stumpf, R. P. (1983). The process of sedimentation on the surface of a salt marsh. *Estuarine, Coastal and Shelf Science*, *17*(5), 495–508. https://doi.org/10.1016/0272-7714(83)90002-1

Styles, R., Snedden, G. A., Smith, S. J., Bryant, D. B., Boyd, B. M., Gailani, J. Z., Couvillion, B., & Race, E. (2021). Seasonal controls on sediment delivery and hydrodynamics in a vegetated tidally influenced interdistributary island. *Journal of Geophysical Research: Oceans*, *126*(7), e2020JC016146. https://doi.org/10.1029/2020JC016146

Wagner, W., Lague, D., Mohrig, D., Passalacqua, P., Shaw, J., & Moffett, K. (2017). Elevation change and stability on a prograding delta. *Geophysical Research Letters*, *44*(4), 1786–1794. https://doi.org/10.1002/2016GL072070

Walker, N. D., & Hammack, A. B. (2000). Impacts of winter storms on circulation and sediment transport: Atchafalaya-Vermilion Bay region, Louisiana, USA. *Journal of Coastal Research*, 996–1010.

Wright, K., Passalacqua, P., Simard, M., & Jones, C. E. (2022). Integrating connectivity into hydrodynamic models: An automated open-source method to refine an unstructured mesh using remote sensing. *Journal of Advances in Modeling Earth Systems*, *14*(8), e2022MS003025. https://doi.org/10.1029/2022MS003025

Zeichner, S. S., Nghiem, J., Lamb, M. P., Takashima, N., De Leeuw, J., Ganti, V., & Fischer, W. W. (2021). Early plant organics increased global terrestrial mud deposition through enhanced flocculation. *Science*, *371*(6528), 526–529. https://doi.org/10.1126/science.abd0379

5.9 Supporting Information

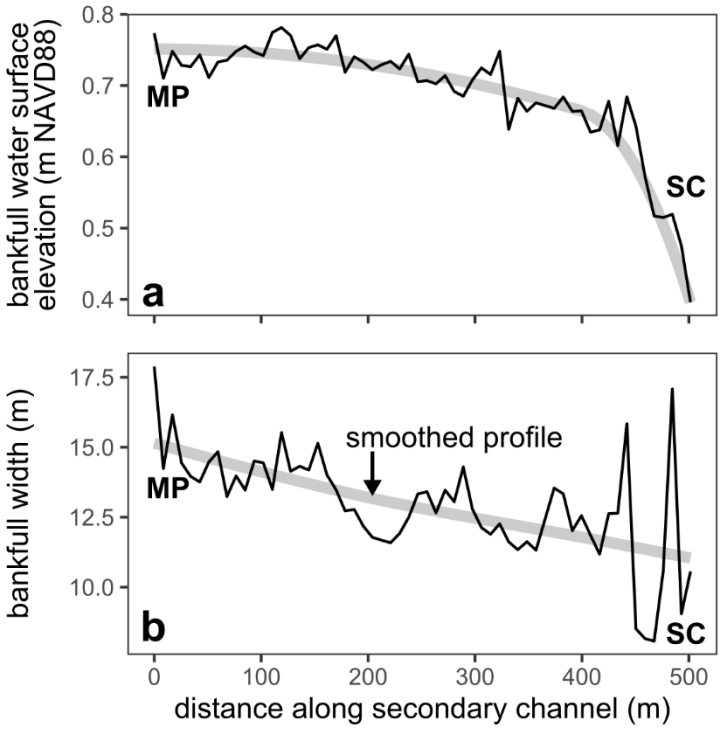

Figure S1. Longitudinal profiles of (a) bankfull water surface elevation and (b) bankfull width in the secondary channel along the Main Pass-secondary channel transect.

Chapter 6

FLOCCULATED SILT, NOT CLAY MINERALS, DOMINATES RIVER SUSPENDED SEDIMENT LOAD

Justin A. Nghiem, Gen K. Li, Miguel Zepeda-Rosales, Youli Li, and Michael P. Lamb

Abstract

Mud widely contributes to earth surface processes from land building to the carbon cycle. Riverine mud transport depends on grain size and mineralogy because they affect the degree to which mud flocculates into aggregates with faster settling velocity. However, the relationships between these factors are poorly known. Here we investigate the grain size, mineralogy, and flocculation state of mud using a suspended sediment data compilation from lowland rivers and new measurements from the Mississippi River Delta complex. Results show that most river suspended sediment is silt (~77% by mass) and most of the mud is flocculated (~88%). X-ray diffraction data reveal that clay minerals compose the majority of sediment in the clay size class (i.e., finer than 2 μm), giving clay size a quantitative mineralogical interpretation. However, the paucity of clay-sized suspended sediment indicates that clay minerals are sparse among flocculated sediment (~17%). The prevalence of silt flocculation and deficiency of clay minerals in rivers pose a paradox against the classical paradigm that clay minerals and salinity drive flocculation and instead support organic matter binding and physical trapping as the causes of silt flocculation. Lowland rivers primarily transport flocculated silt (~62%), highlighting its importance in the global sediment cycle.

6.1 Main Text

Mud (grains < 62.5 μm) dominates sediment transported from the continents to the oceans (Lane and Kalinske, 1941; Johnson, 1943; Jordan, 1965). Mud is a critical resource because it builds land (Asselman and Middelkoop, 1995; Esposito et al., 2017) and transports pollutants (Nelson and Lamothe, 1993) and organic carbon (Bouchez et al., 2014; Bianchi et al., 2024). However, mud transport in rivers has conventionally been difficult to predict because river mud is thought to behave as washload. The washload hypothesis predicts that mud grains are so small and settle so slowly that they act as passive tracers supplied by external sources, like soil erosion and landslides, and hence cannot be predicted with local river variables (Einstein et al., 1940; Einstein and Chien, 1953). But recent work has challenged this view. In many rivers, mud is flocculated into aggregates called flocs that have substantially faster settling velocities akin to those of coarse silt and fine sand (Lamb et al., 2020; Nghiem et al., 2022). Enhanced floc settling velocity promotes dynamic local exchange of mud between the bed and the flow and facilitates mud concentration predictions based on local sediment and hydraulic conditions (Lamb et al., 2020).

The transport behavior of river mud relies on flocculation. Mud is conventionally thought to flocculate due to the cohesive interaction of surface charges on clay minerals (i.e., phyllosilicates) and salinity in saltwater (Van Leussen, 1988; Manning and Dyer, 2007; Verney et al., 2009) and freshwater environments (Gibbs, 1983; Gibbs and Konwar, 1986; Goldberg and Forster, 1990). Theory describing the salt-driven flocculation of clay minerals is well-developed (Derjaguin and Landau, 1941; Verwey, 1947). In contrast, the precise cause of mud flocculation in rivers is unclear because river mud is a heterogeneous mixture of grain sizes and minerals (Partheniades, 1977; Krishnappan, 2000; Droppo, 2001). A simplifying assumption is that clay minerals correspond to the finest sediment because crystal defects limit their size to the sub-μm to μm scale (Velde, 1995; Meunier, 2006). This fact was recognized even in the 1920s when Wentworth (1922) surveyed leading geologists to devise the now-standard grain size classification of clastic sediment in which mud represents the finest grains and is composed of clay- and silt-sized grains. The silt size class represents the sediment coarser than clay size but finer than sand and is thought to be rich in feldspar and quartz and devoid of clay minerals (Russell, 1937). Wentworth assumed that the clay size class is composed exclusively of clay minerals. Although Wentworth originally proposed 4 μm as the boundary between clay and silt sizes, here we use 2 μm (e.g., Velde, 1995; Assallay et al., 1998; García, 2008) because it better separates clay and non-clay minerals (Jackson et al., 1948; Milliken and Hayman, 2019).

Field measurements show that silt composes much of the suspended sediment in many rivers (Bouchez et al., 2011; Lupker et al., 2011; Baronas et al., 2020; Moodie et al., 2020), suggesting that clay minerals might compose a small fraction of suspended sediment. If so, a paradox emerges: How does river mud flocculate with sparse clay minerals? Contrary to well-established flocculation theory (Derjaguin and Landau, 1941), can silt flocculate in the absence of clay minerals? Or are silt grains in rivers actually silt-sized clay minerals, counter to Wentworth's assumption that clay minerals are clay-sized? For example, Dunne et al. (2024) proposed that flocculated silt grains are hyper-stable aggregates of smaller clay minerals that withstand mechanical and chemical dispersion in grain size analysis protocols. Ultimately, these questions stand because of a lack of mechanistic understanding of the interplay between mud grain size, mineralogy, and flocculation state in lowland rivers.

To address these questions, we compiled a global dataset of suspended sediment concentration-depth profiles and grain size distributions from 12 lowland rivers and new measurements from the Wax Lake Delta, Louisiana, USA, part of the Mississippi River Delta complex. We determined which grain sizes were flocculated using in situ settling velocities inferred from grain size-specific concentration-depth profiles (Lamb et al., 2020; Nghiem et al., 2022). In addition, we analyzed the mineral composition of our Wax Lake Delta sediment samples with X-ray diffraction (XRD) and compiled separate river suspended sediment XRD datasets to quantify the relationship between grain size and mineralogy of river suspended sediment. Our analysis reveals that lowland rivers primarily transport mud as flocculated silt dominated by non-clay minerals. These findings demonstrate that river mud can flocculate under low clay abundances, suggesting that alternative flocculation mechanisms like organic matter binding and physical trapping of silt, rather than salt-driven processes, occur in lowland rivers.

Silt dominates river suspended sediment

First, to quantify the grain size of river suspended sediment, we computed depth-averaged silt and mud fractions using a data compilation of suspended sediment concentration-depth profiles and grain size distributions from rivers and the Wax Lake Delta (Methods). We used 117 profiles from 12 rivers that span diverse environmental conditions globally from the Nghiem et al. (2022) data compilation and 27 profiles from the Wax Lake Delta.

In most rivers, silt dominates depth-averaged suspended sediment (median of 77% and IQR/2 = 10% by mass hereon) (Fig. 1). Mud is similarly prevalent in river suspended sediment (median of 79% and IQR/2 = 11%), reflecting the fact that most of the mud is silt (median of 97% silt within mud). Accordingly, the median of the suspended D_{50} is 23 μm in the silt range. In contrast, clay-sized sediment is a very small proportion of river suspended sediment (median of 2.4% and IQR/2 = 1.7%). Although individual mud grains settle very slowly, we show in the next section that the in situ settling velocity of mud in rivers ultimately depends on flocculation.

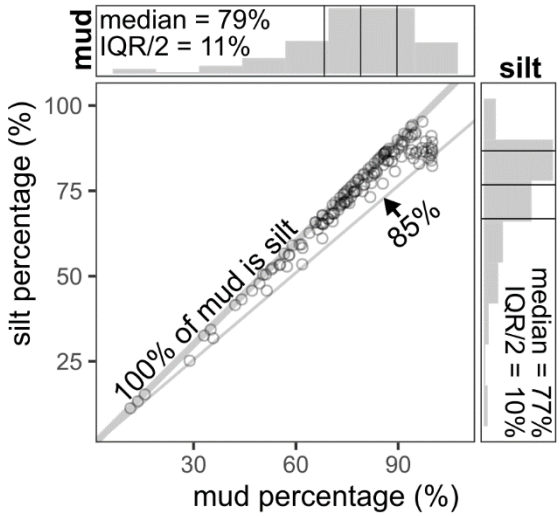

Figure 1. Mud and silt percentages (by mass) of depth-averaged river suspended sediment. Each point represents a sediment concentration-depth profile. In each marginal histogram, the central line indicates the median. The lines on each side of the central line indicate the median plus and minus IQR/2.

Mud in rivers is flocculated

To test the degree to which mud flocculates in rivers, we followed Lamb et al. (2020) and inferred in situ settling velocity as a function of grain size by fitting the Rouse-Vanoni equation (Rouse, 1937) to grain size-specific sediment concentration-depth profiles (Methods). The Rouse-Vanoni equation predicts sediment concentration as a function of height above the bed and the in situ settling velocity. We partitioned concentration-depth profiles from the same data compilation used in Fig. 1 into profiles for individual grain size

classes and calculated in situ settling velocities that best fit the observed concentrations according to the Rouse-Vanoni equation.

We found that suspended mud in global rivers and the Wax Lake Delta has enhanced in situ settling velocity relative to the expected settling velocity of individual grains (Fig. 2a). We attribute this pattern to in situ flocculation that aggregates these grain sizes into faster settling flocs (Lamb et al., 2020). Direct evidence of flocculation from in situ particle size and settling velocity measurements corroborate this interpretation for the Wax Lake Delta data (Nghiem et al., 2024). For each concentration-depth profile, the floc cutoff diameter indicates the grain size threshold below which grains are flocculated and above which grains are unflocculated (Nghiem et al., 2022). We calculated the flocculated sediment percentage—the mass percentage of depth-averaged suspended sediment finer than the floc cutoff diameter and hence flocculated.

We found that a majority of the depth-averaged suspended sediment is flocculated sediment (median of 68% and IQR/2 = 20%) (Fig. 2b). In particular, most of the mud is flocculated (median of 88% and IQR/2 = 17%) (Fig. 2c). This fact, combined with the fact that most of the mud is silt (Fig. 1), implies that most of the silt is flocculated. Given that flocculation is typically associated with clay minerals (Van Leussen, 1988; Manning and Dyer, 2007) and river flocs are dominated by silt, how is it then that flocs form in rivers? One possibility is that clay mineral grains are larger than expected and extend into silt sizes. We explore this idea next using XRD to measure suspended sediment mineralogy.

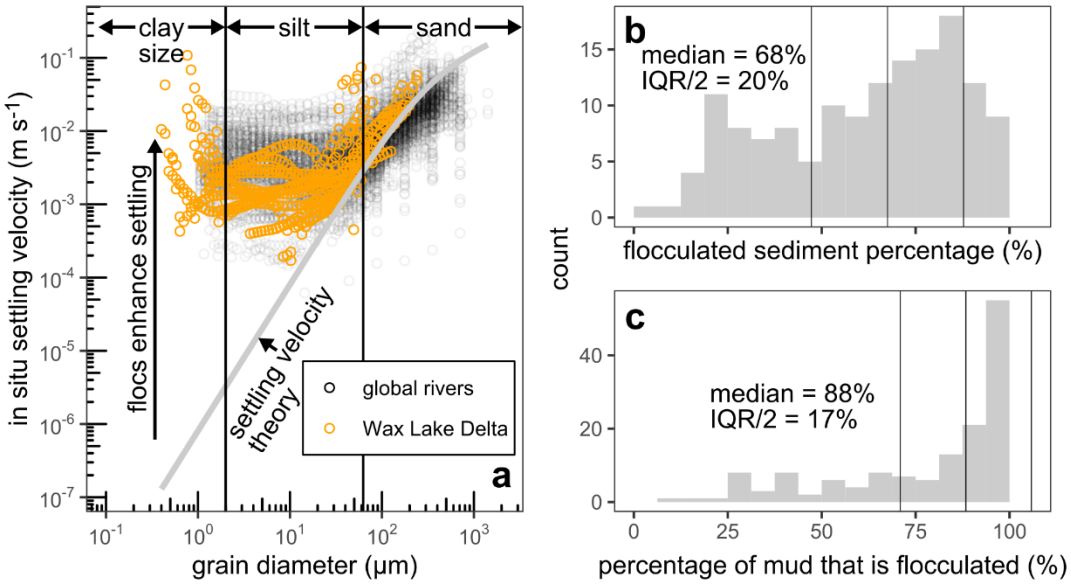

Figure 2. River suspended sediment flocculation. (a) Grain diameter and in situ settling velocity inferred from grain size-specific concentration-depth profiles (Lamb et al., 2020). Settling velocity theory is the predicted settling velocity for individual sediment grains using the Ferguson and Church (2004) model. Histograms of (b) flocculated sediment percentage and (c) percentage of mud that is flocculated (by mass) for depth-

averaged river suspended sediment. Each count represents a sediment concentration-depth profile. In each histogram, the central line indicates the median. The lines on each side of the central line indicate the median plus and minus IQR/2.

Clay-sized sediment is mostly clay minerals

We tested whether clay sizes correspond to clay minerals in river suspended sediment using measurements of grain size distribution and mineral compositions for our Wax Lake Delta samples. We measured bulk (i.e., whole sample) mineral percentages with quantitative XRD analysis (Methods) for 28 suspended samples as well as 2 bed and 8 shallow core sediment samples as constraints on the coarse-grained end member.

For the Wax Lake Delta samples, bulk quartz and clay mineral percentages correlate positively and negatively, respectively, with median grain diameter, D_{50} (μm), in a nearly symmetrical pattern (Fig. 3a). These trends are consistent with the classical idea that clay minerals tend to be finer than quartz (Wentworth, 1922; Russell, 1937). We tested many grain size thresholds to find the optimal grain size, 3.3 μm (R^2 = 0.70), where the percentage finer achieves the highest linear correlation with bulk clay mineral percentage (Fig. 3b). This optimal threshold is close to the typical clay-silt size boundaries of 2 and 4 μm, but the precise interpretation is unclear because these bulk clay mineral percentages average over many grain sizes.

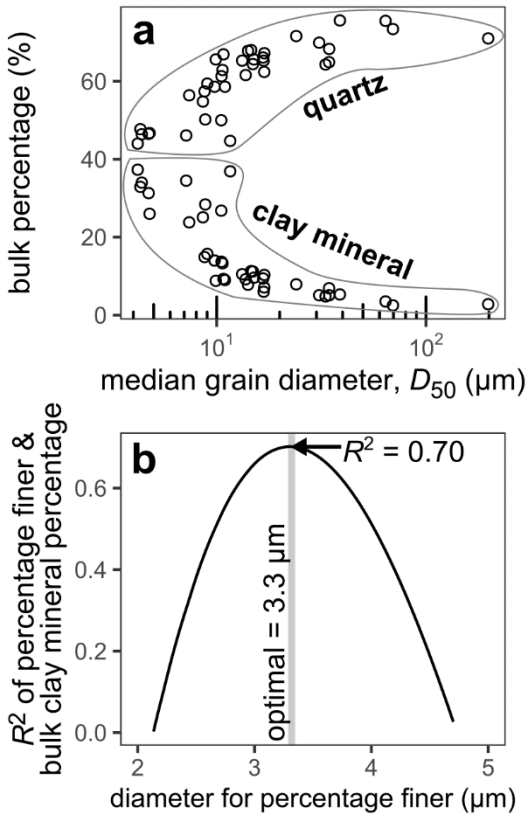

Figure 3. Bulk grain size and mineralogy of Wax Lake Delta sediment samples. (a) Median grain diameter, D_{50}, versus bulk quartz and clay mineral percentages. (b) Diameter for fraction finer versus R^2 of the linear correlation with bulk clay mineral percentage.

To more precisely connect grain size and clay mineral percentage, we compiled a dataset of XRD clay mineral percentages measured in known grain size classes of suspended sediment in many lowland rivers (Methods). The data show a clear decrease of clay mineral percentage with grain diameter (Fig. 4a). The clay size class has high clay mineral percentages (~75 to 100%), while the silt size class has moderate clay mineral percentages (~25 to 50%). This pattern adheres to the expectation that clay minerals tend to be finer, but the lack of a sharp grain size threshold between the total absence and presence of clay minerals indicates that clay and non-clay minerals each have a broad spectrum of grain sizes spanning clay and silt sizes.

To identify the full grain size distributions of clay and non-clay minerals, we developed a grain size-clay mineral model that mixes clay and non-clay mineral grain size distributions weighted by the bulk relative abundance of clay and non-clay minerals (Methods). We assumed that the grain size distributions are log-normal, which is a well-tested approximation for sediment (Harris, 1958; Spencer, 1963; Folk, 1966). We fitted the model to the data compilation to invert for the relative clay mineral abundance and the log-normal mean and standard deviation of each grain size distribution. The fit matches the data well (R^2 = 0.86; Fig. 4a). The inverted log-normal distributions reveal that non-clay minerals tend to be coarser (mode = 17.7 μm) than clay minerals (mode = 10.1 μm), but they have similar geometric standard deviations of ~2 μm (Fig. 4b). Put another way, non-clay minerals are almost totally coarser than clay sizes (~99.9% of non-clay minerals coarser than 2 μm) because they are likely dominated by feldspar and quartz (Russell, 1937). But similarly, nearly all (~99%) clay minerals are coarser than clay sizes (2 μm), a result that conflicts with the idea that the clay minerals are clay-sized. However, clay minerals might still comprise the majority of sediment in the clay size class, a possibility that we evaluate next.

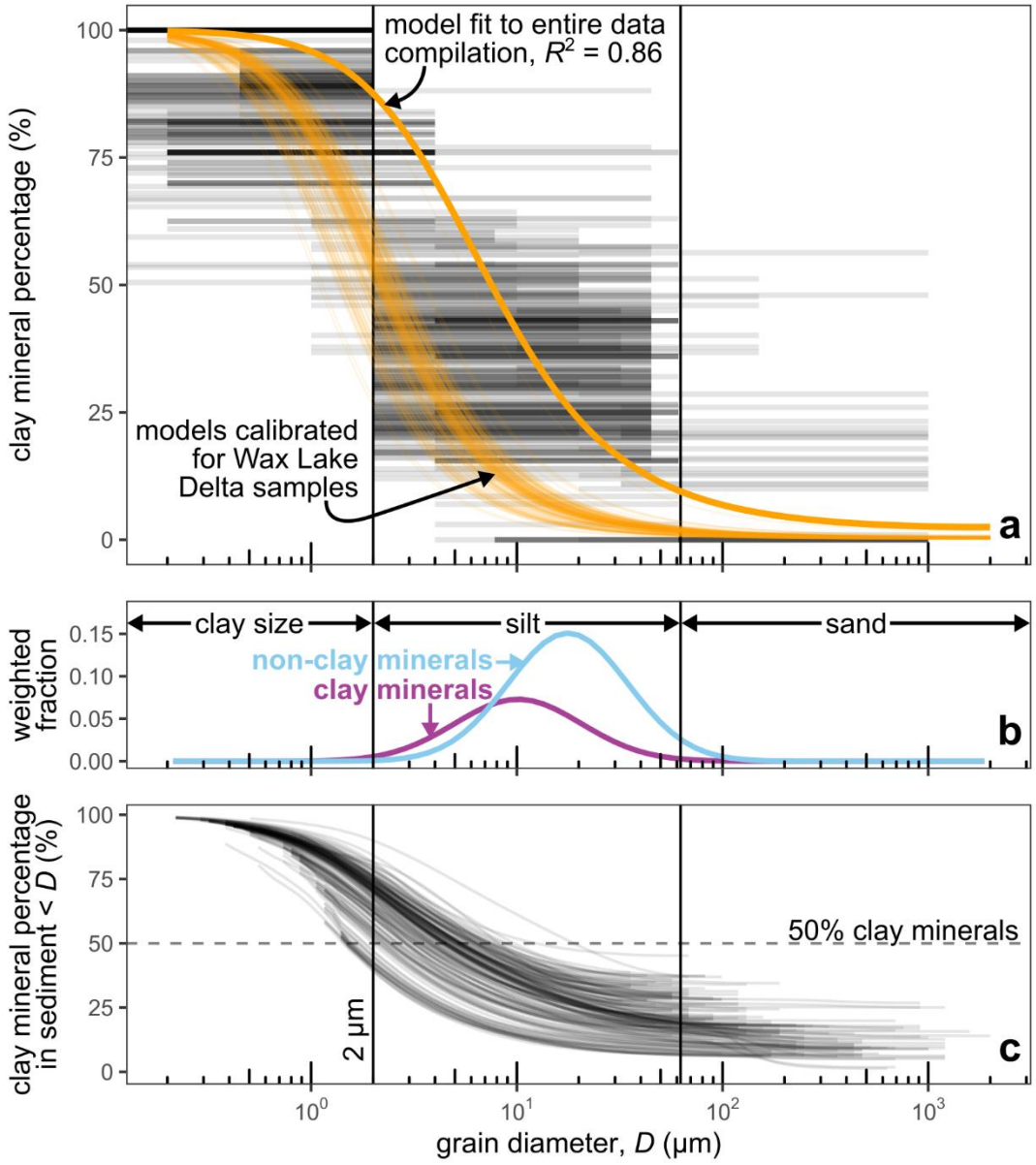

Figure 4. Clay minerals by grain size in river suspended sediment. (a) Grain size versus clay mineral percentage in river suspended sediment. Line segments represent XRD clay mineral percentages in known grain size classes from the clay mineral data compilation. The parameters for the total fit are K = 1.96, (μ_c = 2.32, σ_c = 0.71) for clay minerals, and (μ_n = 2.87, σ_n = 0.67) for non-clay minerals, in which grain diameters, D_1 and D_2, have units of µm. See Methods for explanations of model parameters. The thin curves represent models calibrated for Wax Lake Delta suspended sediment samples (Methods). (b) Grain size distributions of clay and non-clay minerals in river suspended sediment inferred from the fitted grain size-clay mineral model. Distributions are weighted

according to *K*. (c) Grain size versus clay mineral percentage in sediment finer than that grain size for Wax Lake Delta suspended sediment samples.

To test the extent to which clay sizes are clay minerals, we calculated the clay mineral percentage in sediment finer than a series of grain size thresholds by integrating the grain size distribution and modeled clay mineral percentages (Methods). Here we focused on the Wax Lake Delta suspended sediment samples because the other XRD clay mineral data lack grain size measurements. For each sample, we calibrated the grain size-clay mineral model by tuning the relative clay mineral abundance so that the modeled bulk clay mineral percentage matches the measured value (Fig. 4a). We also added data for 153 Wax Lake Delta suspended sediment samples that have grain size distribution measurements but lack XRD data by predicting the bulk clay mineral percentage with the percentage finer than 3.3 μm (Fig. 3b). Results reveal that the grain size at which clay minerals compose half of the finer sediment ranges from 1.4 to 18.9 μm (Fig. 4c). The minimum is close to the common clay-silt size boundary of 2 μm, at which clay minerals dominate the sediment finer (median of 70%, IQR/2 = 6.7%, and range of 39 to 90%). In fact, the clay mineral percentage exceeds 50% for sediment finer than 2 μm in almost all samples (~87%). We expect this fact to be robust in rivers beyond the Wax Lake Delta because the clay mineral percentage for Wax Lake Delta samples for each grain size is near the lower bound of the river clay mineral data (Fig. 4a), implying that clay minerals would typically be the majority of sediment finer than 2 μm in river suspended sediment. These facts suggest a quantitative interpretation of the clay size class: Suspended sediment finer than 2 μm is at least half clay minerals by mass.

This new interpretation of the clay size class implies that silt contains only a minor amount of clay minerals. Depth-averaged clay mineral percentages within silt for the Wax Lake Delta concentration-depth profiles confirm that clay minerals constitute a minor part of the silt (median of 17% and IQR/2 = 4.4%). To evaluate flocculated silt specifically for the Wax Lake Delta concentration-depth profiles, we calculated the depth-averaged flocculated silt percentage using the floc cutoff diameter to delineate flocculated grain sizes (Nghiem et al., 2024; Methods). We further determined the clay mineral portion of the flocculated silt using the modeled clay mineral percentages (Methods). For the Wax Lake Delta, flocculated silt-sized clay minerals compose a minor part of the total suspended sediment (median of 15% and IQR/2 = 4.8%; Fig. 5a). Similarly, clay minerals are only a modest part of the flocculated silt (median of 17% and IQR/2 = 4.0%). The Wax Lake Delta data indicate that flocculated silt composes a major part of the total suspended sediment (median of 67% and IQR/2 = 12%). To more broadly evaluate the flocculated silt percentage, we extended the data to the global river data compilation (Nghiem et al., 2022) using the same approach. Across the combined river and Wax Lake Delta data, flocculated silt is a major portion of river suspended sediment (median 62% and IQR/2 = 18%; Fig. 5b).

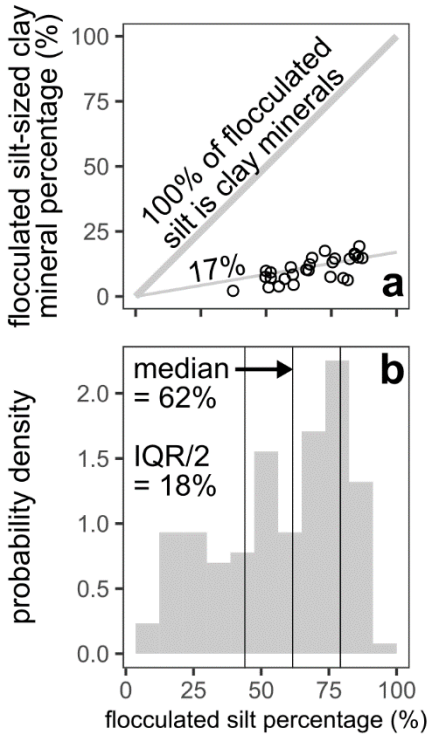

Figure 5. Silt flocculation in river suspended sediment. (a) Depth-averaged flocculated silt and silt-sized clay mineral percentages (by mass) in the Wax Lake Delta. Each point represents a sediment concentration-depth profile. (b) Histogram of flocculated silt fraction for the combined Wax Lake Delta and global river data compilation (Nghiem et al., 2022). The central line indicates the median. The lines on each side of the central line indicate the median plus and minus IQR/2. All percentages are out of the total depth-averaged suspended sediment concentration.

Resolving the paradox of silt flocculation

Our results support three facts about suspended silt in rivers: (1) most river suspended sediment is silt (Fig. 1), (2) most suspended silt is flocculated (Fig. 2bc), and (3) most suspended silt, total and flocculated, is composed of non-clay minerals (Fig. 5a). Combined, we conclude that flocculated silt, poor in clay minerals, forms the majority of river suspended sediment (Fig. 5b). This finding is consistent with the fact that soil (e.g., Allen and Hajek, 1989; Lynn et al., 2002; Journet et al., 2014) and marine mudrock (e.g., Milliken and Hayman, 2019), which represent the input and output sediment of rivers respectively, are commonly composed of silt dominated by non-clay minerals. Crucially, the preponderance of flocculated silt in rivers reaffirms the paradox of silt flocculation: If the interaction between clay minerals and salinity causes flocculation, why does river silt, deficient in clay minerals, flocculate? We suggest the answer is that alternative flocculation mechanisms are in play in rivers. Studies have suggested that silt flocculates because of physical trapping in initially clay mineral-rich flocs (Te Slaa et al., 2013; Shchepetkina et al., 2017; Tran and Strom, 2017; Xu et al., 2022) and binding by sticky organic matter (Chase, 1979; Furukawa

et al., 2014; Lee et al., 2019). In fact, Zeichner et al. (2021) hypothesized that the introduction of large amounts of organic matter by early land plants caused widespread mud flocculation in rivers and, ultimately, the dramatic increase of alluvial mudrock beginning in the Silurian.

Although we found that silt is depleted in clay minerals overall, we also found evidence that clay minerals are predominately silt-sized in river suspended sediment (Fig. 4b). This idea appears to conflict with the fact that crystal growth constraints inherently limit the grain size of clay minerals to a few μm and finer (i.e., clay to fine silt size) (Velde, 1995; Meunier, 2006). We reconcile these facts by interpreting silt-sized clay minerals as being contained in stable silt-sized aggregates (Virto et al., 2008; Tan et al., 2017; Dunne et al., 2024). These aggregates host individual sub-μm to μm sized clay mineral crystals and possibly silt grains too, but effectively behave in situ in rivers as primary grains, rather than fragile flocs, because they withstand dispersion associated with sampling and lab treatment. Past work showing scanning electron microscope images of clay minerals associated with silt-sized aggregates supports this explanation (Bohor and Hughes, 1971; Woodward and Walling, 2007). Aggregates can develop in hillslope soil and erode into the river (Slattery and Burt, 1997; Cantón et al., 2009) where hydrodynamic forces break up aggregates and leave only the most stable aggregates intact (Grangeon et al., 2014). In addition, the experiments of Tan et al. (2017) showed that, even in the absence of organic matter, clay minerals can naturally form 10 to 20 μm sized aggregates resistant to breakage in water, which is consistent with the 10.1 μm mode of our inverted clay mineral grain size distribution (Fig. 4b).

Our study applies very broadly to suspended sediment in lowland alluvial rivers because we relied on large data compilations. As such, the precise conditions in specific rivers can differ from our conclusions. However, we expect some consistency between rivers. Rivers drain continents composed of largely felsic crust, which supplies rivers with sediment rich in quartz and feldspar that eventually weathers into clay minerals. Rivers sort sediment downstream by particle abrasion and selective deposition (e.g., Paola et al., 1992), which are mediated not only by sediment properties and hydraulics (Joseph et al., 2001; Frings, 2008; Trower et al., 2017) but also the formation of flocs and stable aggregates (Tan et al., 2017). The universality of these processes in rivers might thus support the validity of our results for lowland alluvial river in general. Finally, the culmination of river and sediment processes might lead to the emergence of a consistent clay-silt size boundary in which 2 μm is the grain size at which at least half of the sediment finer is clay minerals (Fig. 4c). This definition contrasts with the classic clay-silt size boundary, motivated by clay mineral crystal properties, because natural river sediment processes blur clay minerals across clay and silt sizes and necessitate a more nuanced interpretation as proposed here.

6.2 Methods

6.2.1 Wax Lake Delta sediment sampling

We sampled suspended, bed, and core sediment in the Wax Lake Delta as part of the NASA Delta-X project in two field campaigns in spring and summer 2021. The sampling protocols

and data are fully documented in Nghiem et al. (2024), Nghiem, Salter, and Lamb (2024), and Nghiem et al. (2025) and summarized here. We sampled suspended sediment from a boat using a Van Dorn sampler at multiple heights above the bed to obtain suspended sediment concentration-depth profiles in channels and a flooded delta island. We sampled bed sediment using a Ponar grab sampler. We sampled sediment cores in shallow water areas using a custom piston core. We filtered suspended and bed samples through 0.2-μm pore size filter paper and measured the sediment concentration of the suspended samples in the lab by weighing the dry sediment. We measured the dispersed grain size distribution of all samples using a Malvern Mastersizer 3000E laser diffraction particle size analyzer. We computed depth-averaged grain size distributions using the trapezoidal rule between suspended sediment samples in the vertical (Nghiem et al., 2024). For each concentration-depth profile, we measured the flow velocity profile using an acoustic Doppler current profiler mounted to the boat. We fitted the flow velocity profile using the law of the wall (García, 2008) to estimate shear velocity, u_* (m s^{-1}).

6.2.2 Inferring in situ settling velocity from concentration-depth profiles

We used inferred in situ settling velocities as a function of grain size reported in Nghiem et al. (2022) and Nghiem et al. (2024), and summarize their method here. Following the Lamb et al. (2020) method, they calculated in situ settling velocity by fitting the concentration-depth profiles to the Rouse-Vanoni equation (Rouse, 1937). The Rouse-Vanoni equation assumes a vertical sediment flux balance between turbulence and gravitational settling and models sediment concentration, *C*, as a function of height above the bed, *z* (m), in a flow of depth *h* (m):

$$C = C_b \left(\frac{\frac{h - z}{z}}{\frac{h - h_b}{h_b}} \right)^p \quad (1)$$

The near-bed concentration, C_b, is the reference concentration at the near-bed height, h_b (m), which is the bottom boundary of the concentration-depth profile. We assumed $\frac{h_b}{h} = 0.1$ (De Leeuw et al., 2020). The Rouse number, $p = \frac{w_s}{(\kappa \beta u_*)}$, controls the shape of the concentration-depth profile and depends on the von Kármán constant, κ = 0.41, the ratio of the in situ sediment setting velocity, w_s (m s^{-1}), and shear velocity, u_*, and the ratio of sediment and turbulent momentum diffusivities, β. Higher *p* causes greater concentration closer to the bed compared to that near the water surface and vice versa.

We divided each concentration-depth profile in the data compilation into individual profiles for each grain size class using the grain size distribution measurements. We fitted the Rouse-Vanoni equation (equation (1)) to each grain size-specific concentration-depth profile and estimated the grain size-specific Rouse number, which we combined with shear velocity measurements to calculate settling velocity. Although β is difficult to predict (De Leeuw et

al., 2020), we assumed $\beta = 1$ because the choice of different β treatments has limited effect on the enhanced settling velocity pattern in Fig. 2a.

6.2.3 X-ray diffraction mineralogy analysis of Wax Lake Delta sediment

We used ~100-mg splits of 38 sediment samples (2 bed, 8 core, and 28 suspended sediment samples) from the Wax Lake Delta (Nghiem et al., 2024) to measure the bulk mass percentages of minerals using XRD analysis. We analyzed each sample in a Malvern Panalytical Empyrean powder diffractometer (45 kV, 40 mA Cu source with a Bragg-Brentano mirror and 1D solid-state detector) in the Materials Research Laboratory at the University of California, Santa Barbara. For each sample, we scanned continuously from 5 to 40°2θ for ~15 minutes at a step size of 0.013°2θ. We performed XRD phase quantification using background fitting, peak identification, and Rietveld refinement in the HighScore Plus software. We used crystal structure data from the Inorganic Crystal Structure Database (Zagorac et al., 2019) and American Mineralogist Crystal Structure Database (Downs and Hall-Wallace, 2003). We refined the March-Dollase factor to correct for preferred orientation of clay minerals (Dollase, 1986). The Rietveld-refined XRD patterns capture the key features of the measured XRD patterns despite goodness-of-fit values greater than 1 (Fig. 6). Goodness-of-fit values closer to 1 typically, but not always, indicate a better Rietveld fit (McCusker et al., 1999; Toby, 2006). We quantified the mineral mass percentages of each sample in bulk (i.e., not size fractionated) for quartz and a suite of clay, feldspar, and carbonate minerals included to best match the measured and Rietveld-refined XRD spectra. We summed the percentages of the different clay minerals (chlorite, illite, kaolinite, mica, montmorillonite, and vermiculite) into a single clay mineral percentage for each sample.

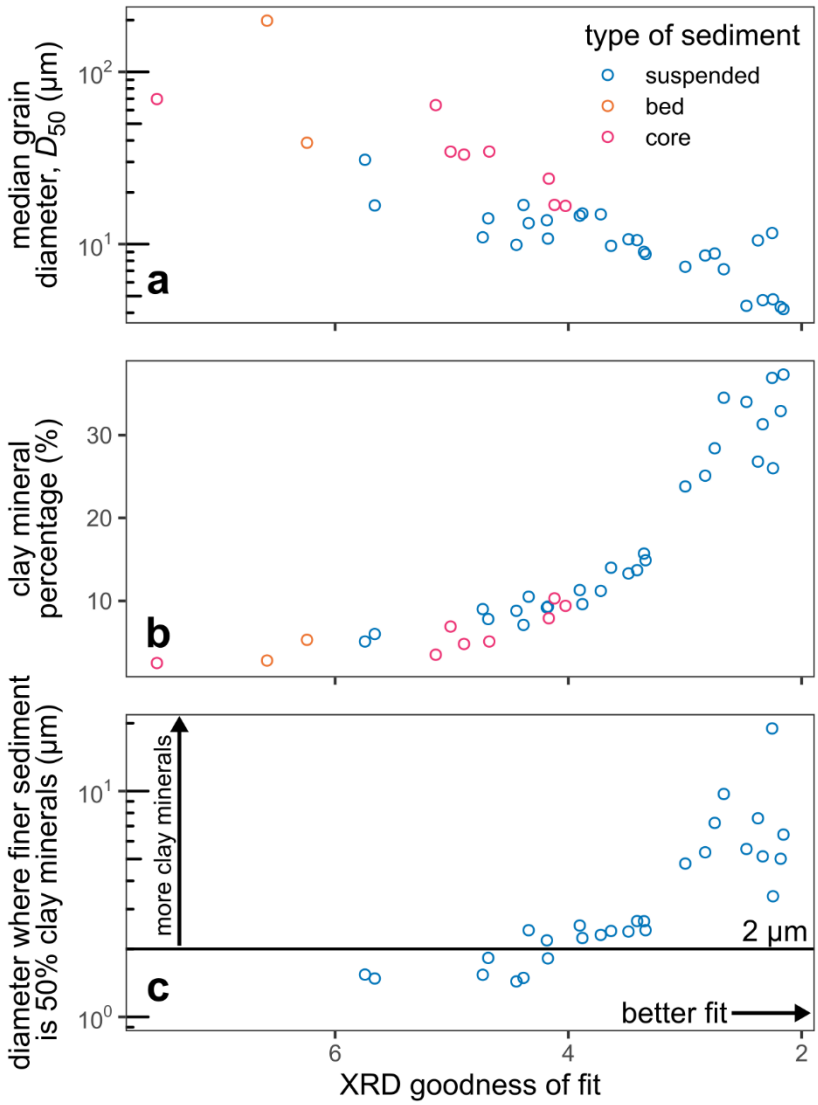

Figure 6. XRD goodness of fit of Wax Lake Delta sediment samples versus (a) median grain diameter, (b) clay mineral percentage, and (c) diameter where finer sediment is 50% clay minerals calculated from grain size-clay mineral model (Fig. 4c). The legend in panel a applies to all panels.

Goodness of fit values range from about 2 to 6, indicating imperfect Rietveld fits to measured XRD patterns (Fig. 6). Rietveld fits better match measured XRD patterns for sediment samples that are finer (Fig. 6a) and more rich in clay minerals (Fig. 6b). Lower quality Rietveld fits occur for coarser samples because Rietveld refinement struggles to reproduce feldspar peaks (Fig. 7a). On the other hand, the feldspar peaks are smaller and well-captured for finer, more clay mineral-rich samples (Fig. 7b). Overall, we expect our XRD phase quantifications to be reliable despite the relatively high goodness of fit values because Rietveld refinement captures the dominant peaks in the XRD patterns well for our

heterogeneous natural samples (Fig. 7). Diffuse scattering from amorphous material, which is not modeled by the Rietveld method, and orientation effects might be sources of mismatch between fitted and measured XRD patterns. These sources might have larger effects in coarser samples, leading to relatively poorer fits (Fig. 6a).

The feldspar percentage is likely underestimated for coarser samples because two key feldspar peaks are not well fitted (Fig. 7a), leading to overestimation of the clay mineral percentage. In this case, the true sediment would be even more depleted in clay minerals and provide further support for our finding of sparse clay minerals in flocculated sediment (Fig. 5a). At the same time, overestimated clay mineral percentage would mean that the diameter where finer sediment is 50% clay minerals should be smaller than reported (Fig. 6c). Thus, the conclusion that suspended sediment finer than 2 μm is at least half clay minerals might need to be shifted down to a finer grain size threshold (Fig. 4c). However, this scenario would still favor 2 μm rather than 4 μm for the clay-silt size boundary because a finer grain size threshold would always be closer to 2 μm.

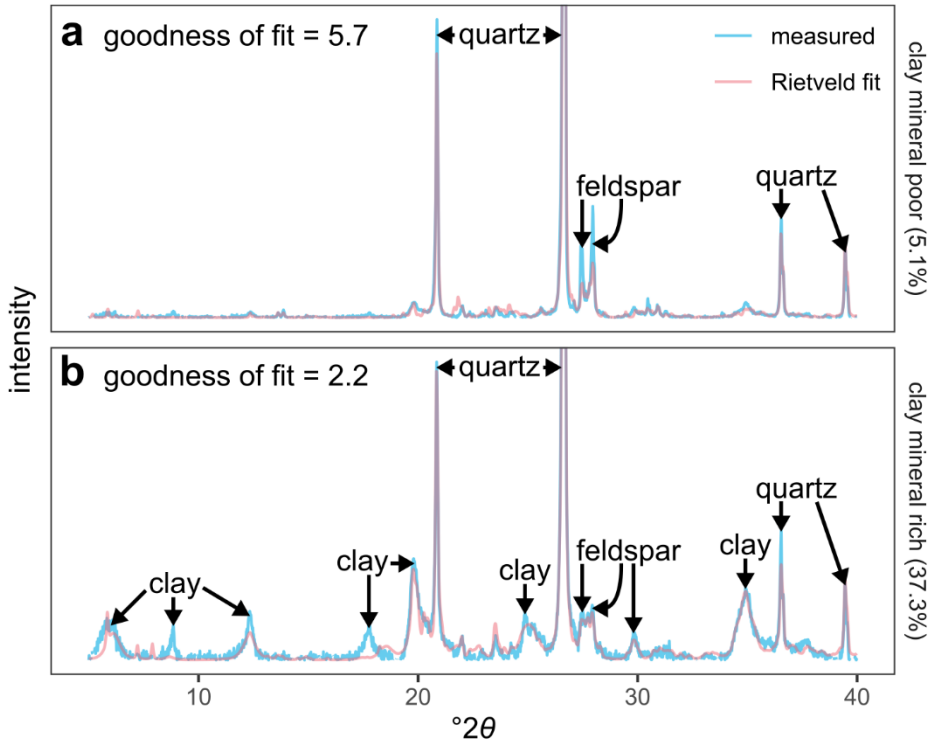

Figure 7. Example measured and Rietveld fitted XRD patterns for a (a) clay mineral-rich and (b) clay mineral-poor suspended sediment sample from the Wax Lake Delta. Clay minerals include chlorite, illite, kaolinite, mica, montmorillonite, and vermiculite. Feldspars include andesine, anorthite, anorthoclase, bytownite, labradorite, microcline, oligoclase, orthoclase, plagioclase, and sanidine. Background has been subtracted from the patterns for display purposes.

6.2.4 Clay mineral fraction data compilation and model

The XRD clay mineral data compilation contains XRD clay mineral percentage measured within known grain size classes from physically separated river suspended sediment fractions. The data compilation covers 54 rivers, 314 unique suspended sediment samples, and 643 total grain size splits of those samples across the Amazon basin (Gibbs, 1965), United States (Kennedy, 1965; Hsieh, 1972; Johnson and Kelley, 1984; Piper et al., 2006), and the Ganges and Brahmaputra Rivers (Garzanti et al., 2011). The data show strong decreasing trend between clay mineral percentage and grain size (Fig. 4a) despite scatter probably caused by differences in the precise mineralogy between samples and source lithology between rivers. The large size of the data compilation also mitigates the fact that the precise grain size and XRD methods varied between data sources.

The grain size-clay mineral model predicts the clay mineral percentage, f_c (%), of sediment between grain sizes D_1 and D_2 (μm) assuming a mixture of log-normal clay and non-clay mineral mass-based grain size distributions:

$$f_c = 100 \times \left[1 + K \frac{\Phi\left(\frac{\ln D_2 - \mu_n}{\sigma_n}\right) - \Phi\left(\frac{\ln D_1 - \mu_n}{\sigma_n}\right)}{\Phi\left(\frac{\ln D_2 - \mu_c}{\sigma_c}\right) - \Phi\left(\frac{\ln D_1 - \mu_c}{\sigma_c}\right)} \right]^{-1} \quad (2)$$

where μ_c and σ_c are the log-normal mean and standard deviation for clay minerals and μ_n and σ_n for non-clay minerals. The relative mineral abundance, K, is the bulk mass ratio of the non-clay and clay minerals. For the total fit, we fitted the model parameters (μ_c, σ_c, μ_n, σ_n, and K) against measured grain size-specific clay mineral percentages from the entire XRD clay mineral data compilation (Fig. 4a). In the data compilation, we counted all phyllosilicates as clay minerals and summed their fractions into a single clay mineral percentage. We used a nonlinear optimization algorithm (Kraft, 1994; Johnson, 2007) to find the parameter values that minimize the residual sum of squares between the data and predictions from equation (2). We used a constraint in the optimization to force a monotonic decrease of clay mineral fraction with grain size up to the coarsest sand size of 2000 μm (Fig. 4a). We interpret the negligible sand fractions of the inverted grain size distributions (Fig. 4b) not as a lack of suspended sand, but as showing that the sand part of the distributions is not necessary to fit the data (Fig. 4a). As a result, K = 1.96 for the total fit indicates that non-clay minerals are about twice as abundant as clay minerals in suspended sediment within the grain size limits required for model fitting.

For showing grain size versus clay mineral fraction (Fig. 4a), we derived a version of the clay mineral fraction model (equation (2)) that predicts the clay mineral fraction given a precise grain diameter, D (μm), using l'Hôpital's rule:

$$f_c = 100 \times \left[1 + K \frac{\sigma_c}{\sigma_n} \exp\left(\frac{(\ln D - \mu_c)^2}{2\sigma_c^2} - \frac{(\ln D - \mu_n)^2}{2\sigma_n^2} \right) \right]^{-1} \quad (3)$$

6.2.5 Calculating clay mineral fractions for Wax Lake Delta suspended sediment

We calibrated the grain size-clay mineral model for each Wax Lake Delta suspended sediment sample by tuning the relative mineral abundance, *K* (equation (2)). We kept the log-normal parameters from the total fit (Fig. 4a) and found the *K* value that, given the grain size distribution, perfectly reproduces the bulk clay mineral percentage, $\bar{f_c}$ (%), according to

$$\bar{f_c} = \sum_{i=1}^{n} f_i \, f_{ci} \quad (4)$$

where f_i (dimensionless) is the mass fraction in the *i*th grain size class and f_{ci} is the clay mineral percentage in the *i*th size class calculated using equation (2). Although the Mastersizer measures grain size distribution in terms of volume fractions for f_i, we assumed that the volume and mass fractions are equivalent because we expect sediment density to vary little across grain size and common minerals (i.e., quartz, feldspar, and clays). We used Newton's method on equation (4) with the measured $\bar{f_c}$ to solve for *K*. Similarly, we calculated the fraction of clay minerals in *i*th size class versus the total suspended sediment as $f_i f_{ci}$ and summed across classes to compute total clay mineral contributions from clay, silt, and mud size classes (Fig. 4c; Fig. 5a). We calculated depth-averaged fractions by weighting by concentration and integrating using the trapezoidal rule (Nghiem et al., 2024).

6.3 Acknowledgements

The NASA Delta-X project is funded by the Science Mission Directorate's Earth Science Division through the Earth Venture Suborbital-3 Program NNH17ZDA001N-EVS3. We thank Mark Simard, Cathleen Jones, and staff at NASA/Caltech Jet Propulsion Lab for leading and administering the Delta-X project. We acknowledge funding from NASA FINESST Grant 80NSSC20K1645 to JAN. The research reported here made use of shared facilities in the Materials Research Science and Engineering Center (MRSEC) at UC Santa Barbara supported by NSF DMR award number 2308708. The UC Santa Barbara MRSEC is a member of the Materials Research Facilities Network.

6.4 References

Allen, B. L., & Hajek, B. F. (1989). Mineral occurrence in soil environments. *Minerals in Soil Environments*, *1*, 199–278. https://doi.org/10.2136/sssabookser1.2ed.c5

Assallay, A. M., Rogers, C. D. F., Smalley, I. J., & Jefferson, I. F. (1998). Silt: 2–62 μm, 9–4φ. *Earth-Science Reviews*, *45*(1–2), 61–88. https://doi.org/10.1016/S0012-8252(98)00035-X

Asselman, N. E., & Middelkoop, H. (1995). Floodplain sedimentation: Quantities, patterns and processes. *Earth Surface Processes and Landforms*, *20*(6), 481–499. https://doi.org/10.1002/esp.3290200602

Baronas, J. J., Stevenson, E. I., Hackney, C. R., Darby, S. E., Bickle, M. J., Hilton, R. G., Larkin, C. S., Parsons, D. R., Myo Khaing, A., & Tipper, E. T. (2020). Integrating suspended

sediment flux in large alluvial river channels: Application of a synoptic Rouse-based model to the Irrawaddy and Salween rivers. *Journal of Geophysical Research: Earth Surface*, *125*(9), e2020JF005554. https://doi.org/10.1029/2020JF005554

Bianchi, T. S., Mayer, L. M., Amaral, J. H., Arndt, S., Galy, V., Kemp, D. B., Kuehl, S. A., Murray, N. J., & Regnier, P. (2024). Anthropogenic impacts on mud and organic carbon cycling. *Nature Geoscience*, 1–11. https://doi.org/10.1038/s41561-024-01405-5

Bohor, B. F., & Hughes, R. E. (1971). Scanning electron microscopy of clays and clay minerals. *Clays and Clay Minerals*, *19*(1), 49–54. https://doi.org/10.1346/CCMN.1971.0190105

Bouchez, J., Gaillardet, J., France-Lanord, C., Maurice, L., & Dutra-Maia, P. (2011). Grain size control of river suspended sediment geochemistry: Clues from Amazon River depth profiles. *Geochemistry, Geophysics, Geosystems*, *12*(3). https://doi.org/10.1029/2010GC003380

Bouchez, J., Galy, V., Hilton, R. G., Gaillardet, J., Moreira-Turcq, P., Pérez, M. A., France-Lanord, C., & Maurice, L. (2014). Source, transport and fluxes of Amazon River particulate organic carbon: Insights from river sediment depth-profiles. *Geochimica et Cosmochimica Acta*, *133*, 280–298. https://doi.org/10.1016/j.gca.2014.02.032

Cantón, Y., Solé-Benet, A., Asensio, C., Chamizo, S., & Puigdefábregas, J. (2009). Aggregate stability in range sandy loam soils relationships with runoff and erosion. *Catena*, *77*(3), 192–199. https://doi.org/10.1016/j.catena.2008.12.011

Chase, R. R. (1979). Settling behavior of natural aquatic particulates. *Limnology and Oceanography*, *24*(3), 417–426. https://doi.org/10.4319/lo.1979.24.3.0417

De Leeuw, J., Lamb, M. P., Parker, G., Moodie, A. J., Haught, D., Venditti, J. G., & Nittrouer, J. A. (2020). Entrainment and suspension of sand and gravel. *Earth Surface Dynamics*, *8*(2), 485–504. https://doi.org/10.5194/esurf-8-485-2020

Derjaguin, B. V., & Landau, L. (1941). Theory of the stability of strongly charged lyophobic sol and of the adhesion of strongly charged particles in solutions of electrolytes. *Acta Physico Chimica URSS*, *14*, 633–662.

Dollase, W. A. (1986). Correction of intensities for preferred orientation in powder diffractometry: Application of the March model. *Journal of Applied Crystallography*, *19*(4), 267–272. https://doi.org/10.1107/S0021889886089458

Downs, R. T., & Hall-Wallace, M. (2003). The American Mineralogist crystal structure database. *American Mineralogist*, *88*(1), 247–250.

Droppo, I. G. (2001). Rethinking what constitutes suspended sediment. *Hydrological Processes*, *15*(9), 1551–1564. https://doi.org/10.1002/hyp.228

Dunne, K. B. J., Nittrouer, J. A., Abolfazli, E., Osborn, R., & Strom, K. B. (2024). Hydrodynamically-driven deposition of mud in river systems. *Geophysical Research Letters*, *51*(4), e2023GL107174. https://doi.org/10.1029/2023GL107174

Einstein, H. A., Anderson, A. G., & Johnson, J. W. (1940). A distinction between bed-load and suspended load in natural streams. *Eos, Transactions American Geophysical Union*, *21*(2), 628–633. https://doi.org/10.1029/TR021i002p00628

Einstein, H. A., & Chien, N. (1953). Can the rate of wash load be predicted from the bed-load function? *Eos, Transactions American Geophysical Union*, *34*(6), 876–882. https://doi.org/10.1029/TR034i006p00876

Esposito, C. R., Shen, Z., Törnqvist, T. E., Marshak, J., & White, C. (2017). Efficient retention of mud drives land building on the Mississippi Delta plain. *Earth Surface Dynamics*, *5*(3), 387–397. https://doi.org/10.5194/esurf-5-387-2017

Ferguson, R. I., & Church, M. (2004). A Simple Universal Equation for Grain Settling Velocity. *Journal of Sedimentary Research*, *74*(6), 933–937. https://doi.org/10.1306/051204740933

Folk, R. L. (1966). A review of grain-size parameters. *Sedimentology*, *6*(2), 73–93. https://doi.org/10.1111/j.1365-3091.1966.tb01572.x

Frings, R. M. (2008). Downstream fining in large sand-bed rivers. *Earth-Science Reviews*, *87*(1–2), 39–60. https://doi.org/10.1016/j.earscirev.2007.10.001

Furukawa, Y., Reed, A. H., & Zhang, G. (2014). Effect of organic matter on estuarine flocculation: A laboratory study using montmorillonite, humic acid, xanthan gum, guar gum and natural estuarine flocs. *Geochemical Transactions*, *15*(1), 1. https://doi.org/10.1186/1467-4866-15-1

García, M. H. (2008). Sediment Transport and Morphodynamics. *Sedimentation Engineering: Processes, Measurements, Modeling, and Practice*, 21–163. https://doi.org/10.1061/9780784408148.ch02

Garzanti, E., Andó, S., France-Lanord, C., Censi, P., Vignola, P., Galy, V., & Lupker, M. (2011). Mineralogical and chemical variability of fluvial sediments 2. Suspended-load silt (Ganga–Brahmaputra, Bangladesh). *Earth and Planetary Science Letters*, *302*(1–2), 107–120. https://doi.org/10.1016/j.epsl.2010.11.043

Gibbs, R. J. (1965). *The geochemistry of the Amazon river basin*. University of California, San Diego.

Gibbs, R. J. (1983). Coagulation rates of clay minerals and natural sediments. *Journal of Sedimentary Research*, *53*(4), 1193–1203. https://doi.org/10.1306/212F8341-2B24-11D7-8648000102C1865D

Gibbs, R. J., & Konwar, L. (1986). Coagulation and settling of Amazon River suspended sediment. *Continental Shelf Research*, *6*(1–2), 127–149. https://doi.org/10.1016/0278-4343(86)90057-9

Goldberg, S., & Forster, H. S. (1990). Flocculation of reference clays and arid-zone soil clays. *Soil Science Society of America Journal*, *54*(3), 714–718. https://doi.org/10.2136/sssaj1990.03615995005400030014x

Grangeon, T., Droppo, I. G., Legout, C., & Esteves, M. (2014). From soil aggregates to riverine flocs: A laboratory experiment assessing the respective effects of soil type and flow shear stress on particles characteristics. *Hydrological Processes*, *28*(13), 4141–4155. https://doi.org/10.1002/hyp.9929

Harris, S. A. (1958). Probability curves and the recognition of adjustment to depositional environment. *Journal of Sedimentary Research*, *28*(2), 151–163. https://doi.org/10.1306/74D7078B-2B21-11D7-8648000102C1865D

Hsieh, Y.-P. (1972). *A source study of the suspended solids in the Gallatin River*. Montana State University-Bozeman, College of Agriculture.

Jackson, M. L., Tyler, S. A., Willis, A. L., Bourbeau, G. A., & Pennington, R. P. (1948). Weathering sequence of clay-size minerals in soils and sediments. I. Fundamental generalizations. *The Journal of Physical Chemistry*, *52*(7), 1237–1260. https://doi.org/10.1021/j150463a015

Johnson, A. G., & Kelley, J. T. (1984). Temporal, spatial, and textural variation in the mineralogy of Mississippi River suspended sediment. *Journal of Sedimentary Research*, *54*(1), 67–72. https://doi.org/10.1306/212F83A5-2B24-11D7-8648000102C1865D

Johnson, J. W. (1943). Distribution graphs of suspended-matter concentration. *Transactions of the American Society of Civil Engineers*, *108*(1), 941–956. https://doi.org/10.1061/TACEAT.0005615

Johnson, S. G. (2007). *The NLopt nonlinear-optimization package* [Computer software]. https://github.com/stevengj/nlopt

Jordan, P. R. (1965). Fluvial sediment of the Mississippi River at St. Louis, Missouri. *USGS Numbered Series*. https://doi.org/10.3133/wsp1802

Joseph, G. G., Zenit, R., Hunt, M. L., & Rosenwinkel, A. M. (2001). Particle–wall collisions in a viscous fluid. *Journal of Fluid Mechanics*, *433*, 329–346. https://doi.org/10.1017/S0022112001003470

Journet, E., Balkanski, Y., & Harrison, S. P. (2014). A new data set of soil mineralogy for dust-cycle modeling. *Atmospheric Chemistry and Physics*, *14*(8), 3801–3816. https://doi.org/10.5194/acp-14-3801-2014

Kraft, D. (1994). Algorithm 733: TOMP–Fortran modules for optimal control calculations. *ACM Transactions on Mathematical Software (TOMS)*, *20*(3), 262–281. https://doi.org/10.1145/192115.192124

Krishnappan, B. G. (2000). In situ size distribution of suspended particles in the Fraser River. *Journal of Hydraulic Engineering*, *126*(8), 561–569. https://doi.org/10.1061/(ASCE)0733-9429(2000)126:8(561)

Lamb, M. P., De Leeuw, J., Fischer, W. W., Moodie, A. J., Venditti, J. G., Nittrouer, J. A., Haught, D., & Parker, G. (2020). Mud in rivers transported as flocculated and suspended bed material. *Nature Geoscience*, *13*(8), 566–570. https://doi.org/10.1038/s41561-020-0602-5

Lane, E. W., & Kalinske, A. A. (1941). Engineering calculations of suspended sediment. *Eos, Transactions American Geophysical Union*, *22*(3), 603–607. https://doi.org/10.1029/TR022i003p00603

Lee, B. J., Kim, J., Hur, J., Choi, I. H., Toorman, E. A., Fettweis, M., & Choi, J. W. (2019). Seasonal Dynamics of Organic Matter Composition and Its Effects on Suspended Sediment Flocculation in River Water. *Water Resources Research*, *55*(8), 6968–6985. https://doi.org/10.1029/2018WR024486

Lupker, M., France-Lanord, C., Lavé, J., Bouchez, J., Galy, V., Métivier, F., Gaillardet, J., Lartiges, B., & Mugnier, J.-L. (2011). A Rouse-based method to integrate the chemical composition of river sediments: Application to the Ganga basin. *Journal of Geophysical Research: Earth Surface*, *116*(F4). https://doi.org/10.1029/2010JF001947

Lynn, W. C., Ahrens, R. J., & Smith, A. L. (2002). Soil minerals, their geographic distribution, and soil taxonomy. *Soil Mineralogy with Environmental Applications*, *7*, 691–709. https://doi.org/10.2136/sssabookser7.c23

Manning, A. J., & Dyer, K. R. (2007). Mass settling flux of fine sediments in Northern European estuaries: Measurements and predictions. *Marine Geology*, *245*(1–4), 107–122. https://doi.org/10.1016/j.margeo.2007.07.005

McCusker, L. B., Von Dreele, R. B., Cox, D. E., Louër, D., & Scardi, P. (1999). Rietveld refinement guidelines. *Applied Crystallography*, *32*(1), 36–50. https://doi.org/10.1107/S0021889898009856

Meunier, A. (2006). Why are clay minerals small? *Clay Minerals*, *41*(2), 551–566. https://doi.org/10.1180/0009855064120205

Milliken, K. L., & Hayman, N. W. (2019). Mudrock components and the genesis of bulk rock properties: Review of current advances and challenges. *Shale: Subsurface Science and Engineering*, 1–25. https://doi.org/10.1002/9781119066699.ch1

Moodie, A. J., Nittrouer, J. A., Ma, H., Carlson, B. N., Wang, Y., Lamb, M. P., & Parker, G. (2020). Suspended-sediment induced stratification inferred from concentration and velocity profile measurements in the lower Yellow River, China. *Water Resources Research*, *58*(5), e2020WR027192. https://doi.org/10.1029/2020WR027192

Nelson, C. H., & Lamothe, P. J. (1993). Heavy metal anomalies in the Tinto and Odiel river and estuary system, Spain. *Estuaries*, *16*(3), 496–511. https://doi.org/10.2307/1352597

Nghiem, J. A., Fischer, W. W., Li, G. K., & Lamb, M. P. (2022). A Mechanistic Model for Mud Flocculation in Freshwater Rivers. *Journal of Geophysical Research: Earth Surface*, *127*(5), e2021JF006392. https://doi.org/10.1029/2021JF006392

Nghiem, J. A., Li, G. K., Harringmeyer, J. P., Salter, G., Fichot, C. G., Cortese, L., & Lamb, M. P. (2024). Testing floc settling velocity models in rivers and freshwater wetlands. *Earth Surface Dynamics*, *12*(6), 1267–1294. https://doi.org/10.5194/esurf-12-1267-2024

Nghiem, J., Salter, G., & Lamb, M. P. (2024). Delta-X: Bed and Suspended Sediment Grain Size, MRD, LA, USA, 2019-2021, V3. *ORNL DAAC*. https://doi.org/10.3334/ORNLDAAC/2379

Nghiem, J., Salter, G., & Lamb, M. P. (2025). Delta-X: Sediment Core Grain Size Distribution, Wax Lake Delta, MRD, LA. *ORNL DAAC*. https://doi.org/10.3334/ORNLDAAC/2382

Paola, C., Parker, G., Seal, R., Sinha, S. K., Southard, J. B., & Wilcock, P. R. (1992). Downstream fining by selective deposition in a laboratory flume. *Science*, *258*(5089), 1757–1760. https://doi.org/10.1126/science.258.5089.1757

Partheniades, E. (1977). Unified view of wash load and bed material load. *Journal of the Hydraulics Division*, *103*(9), 1037–1057. https://doi.org/10.1061/JYCEAJ.0004825

Piper, D. Z., Ludington, S., Duval, J. S., & Taylor, H. E. (2006). Geochemistry of bed and suspended sediment in the Mississippi river system: Provenance versus weathering and winnowing. *Science of the Total Environment*, *362*(1–3), 179–204. https://doi.org/10.1016/j.scitotenv.2005.05.041

Rouse, H. (1937). Modern conceptions of the mechanics of fluid turbulence. *Transactions of the American Society of Civil Engineers*, *102*(1), 463–505. https://doi.org/10.1061/TACEAT.0004872

Russell, R. D. (1937). Mineral composition of Mississippi River sands. *Bulletin of the Geological Society of America*, *48*(9), 1307–1348. https://doi.org/10.1130/GSAB-48-1307

Shchepetkina, A., Gingras, M. K., Zonneveld, J.-P., & Pemberton, S. G. (2017). Silt-and bioclastic-rich flocs and their relationship to sedimentary structures: Modern observations

from the Petitcodiac River Estuary. *Estuaries and Coasts*, *40*, 947–966. https://doi.org/10.1007/s12237-016-0186-x

Slattery, M. C., & Burt, T. P. (1997). Particle size characteristics of suspended sediment in hillslope runoff and stream flow. *Earth Surface Processes and Landforms: The Journal of the British Geomorphological Group*, *22*(8), 705–719. https://doi.org/10.1002/(SICI)1096-9837(199708)22:8%3C705::AID-ESP739%3E3.0.CO;2-6

Spencer, D. W. (1963). The interpretation of grain size distribution curves of clastic sediments. *Journal of Sedimentary Research*, *33*(1), 180–190. https://doi.org/10.1306/74D70DF8-2B21-11D7-8648000102C1865D

Tan, X., Liu, F., Hu, L., Reed, A. H., Furukawa, Y., & Zhang, G. (2017). Evaluation of the particle sizes of four clay minerals. *Applied Clay Science*, *135*, 313–324. https://doi.org/10.1016/j.clay.2016.10.012

Te Slaa, S., He, Q., van Maren, D. S., & Winterwerp, J. C. (2013). Sedimentation processes in silt-rich sediment systems. *Ocean Dynamics*, *63*, 399–421. https://doi.org/10.1007/s10236-013-0600-x

Toby, B. H. (2006). R factors in Rietveld analysis: How good is good enough? *Powder Diffraction*, *21*(1), 67–70. https://doi.org/10.1154/1.2179804

Tran, D., & Strom, K. (2017). Suspended clays and silts: Are they independent or dependent fractions when it comes to settling in a turbulent suspension? *Continental Shelf Research*, *138*, 81–94. https://doi.org/10.1016/j.csr.2017.02.011

Trower, E. J., Lamb, M. P., & Fischer, W. W. (2017). Experimental evidence that ooid size reflects a dynamic equilibrium between rapid precipitation and abrasion rates. *Earth and Planetary Science Letters*, *468*, 112–118. https://doi.org/10.1016/j.epsl.2017.04.004

Van Leussen, W. (1988). Aggregation of Particles, Settling Velocity of Mud Flocs A Review. In J. Dronkers & W. van Leussen (Eds.), *Physical Processes in Estuaries* (pp. 347–403). Springer. https://doi.org/10.1007/978-3-642-73691-9_19

Velde, B. (1995). Composition and Mineralogy of Clay Minerals. *Origin and Mineralogy of Clays*, 8–42. https://doi.org/10.1007/978-3-662-12648-6_2

Verney, R., Lafite, R., & Brun-Cottan, J.-C. (2009). Flocculation potential of estuarine particles: The importance of environmental factors and of the spatial and seasonal variability of suspended particulate matter. *Estuaries and Coasts*, *32*(4), 678–693. https://doi.org/10.1007/s12237-009-9160-1

Verwey, E. J. W. (1947). Theory of the stability of lyophobic colloids. *The Journal of Physical Chemistry*, *51*(3), 631–636. https://doi.org/10.1021/j150453a001

Virto, I., Barré, P., & Chenu, C. (2008). Microaggregation and organic matter storage at the silt-size scale. *Geoderma*, *146*(1–2), 326–335. https://doi.org/10.1016/j.geoderma.2008.05.021

Woodward, J. C., & Walling, D. E. (2007). Composite suspended sediment particles in river systems: Their incidence, dynamics and physical characteristics. *Hydrological Processes: An International Journal*, *21*(26), 3601–3614. https://doi.org/10.1002/hyp.6586

Xu, C., Odum, B., Chen, Y., & Yao, P. (2022). Evaluation of the role of silt content on the flocculation behavior of clay-silt mixtures. *Water Resources Research*, *58*(11), e2021WR030964. https://doi.org/10.1029/2021WR030964

Zagorac, D., Müller, H., Ruehl, S., Zagorac, J., & Rehme, S. (2019). Recent developments in the Inorganic Crystal Structure Database: Theoretical crystal structure data and related features. *Journal of Applied Crystallography*, *52*(5), 918–925. https://doi.org/10.1107/S160057671900997X

Zeichner, S. S., Nghiem, J., Lamb, M. P., Takashima, N., De Leeuw, J., Ganti, V., & Fischer, W. W. (2021). Early plant organics increased global terrestrial mud deposition through enhanced flocculation. *Science*, *371*(6528), 526–529. https://doi.org/10.1126/science.abd0379

Chapter 7

CONCLUSION

In Chapter 1, I introduced the three topics of my thesis in order of increasing spatial scale of flocculation: predicting river floc settling velocity (Chapters 2 and 3), linking floc settling velocity to mud transport theory and delta land building (Chapters 4 and 5), and characterizing the grain size, mineralogy, and flocculation state of suspended sediment across alluvial rivers globally (Chapter 6).

In Chapter 2, I developed a semi-empirical model to predict floc diameter and settling velocity in rivers as a function of turbulence, sediment concentration and mineralogy, organic matter concentration, and water chemistry. I calibrated the model using a data compilation of inferred river floc settling velocity. Importantly, the model incorporates explicitly the effects of sediment mineralogy, organic matter concentration, and water chemistry on flocs, which had been missing from the original floc model. The model was somewhat limited because the floc settling velocity data were indirect. Thus, in Chapter 3, I verified the model using direct field data of flocs from the Wax Lake Delta, including floc photos, sediment samples, and in situ particle size and concentration data. I also tested a physics-based floc settling velocity and identified two overlooked factors. First, mixed grain sizes and the approximate fractal structure of flocs lead to an effectively smaller primary particle diameter than would be expected from primary particle size distribution. Second, flow through the floc can enhance floc settling velocity, but this effect remains difficult to predict because permeability models often do not consider a distribution of particle sizes.

Chapters 4 and 5 are dedicated to investigating mud transport. In contrast to conventional washload theory for rivers, I showed that mud is more consistent with bed-material load due to flocculation in the Wax Lake Delta using suspended and bed sediment data, in situ water depth and sediment concentration time series, and remotely sensed sediment concentration maps (Chapter 4). The bed-material load treatment for flocculated mud paves the way to improve predictions of mud concentration using local flow and bed measurements in the bed-material entrainment theory, even for muddy cohesive beds found in river deltas. Chapter 5 focuses on the sediment transport from primary channels into islands at the Wax Lake Delta. Point measurements and time series data of hydraulics and sediment flux across the Wax Lake Delta show that island levee elevation relative to primary channel water surface elevation is a key control because flow from the channel must overtop the levee to carry water and sediment into the island. I interpreted the field data as telling an intricate feedback between tides, river discharge, and sediment entrainment. Increasing inundation of island wetlands promotes discharge and sediment flux into the island, but only up to a certain point beyond which the hydraulic gradient between primary channel and island wetland shallows out and reduces the flow. Conversely, secondary channels are incised deep enough to bypass the barrier of levee top elevation and can consistently route water and sediment into the island

with little tidal modulation. Mud can be readily captured in the island because the settling velocity, enhanced by flocculation, is fast compared to the flow for mud to settle in the island rather than bypassing it.

Chapter 6 probes fundamental questions about the characteristics and transport state of mud in rivers. Using suspended sediment grain size and mineralogy data from the Wax Lake Delta and a river data compilation, I showed that most river suspended sediment is flocculated silt. This silt contains only a minor proportion of clay minerals, indicating that the flocculation of clay minerals is probably not responsible for much of the mud flocculation in rivers. Instead, organic matter binding and physical trapping of silt in flocs are likely the main flocculation mechanisms in rivers.

This thesis provides a starting point to predict the transport and fate of mud in rivers and deltas. Despite the advances demonstrated here, much is still unknown about mud flocculation and transport. For example, the river floc model in Chapter 2 still relies on empirical factors, highlighting the lack of fundamental understanding of flocculation mechanisms. The physics-based floc settling velocity model in Chapter 3 is also uncertain because floc permeability is difficult to predict. These shortcomings exist because flocculation is an inherently complicated interaction between heterogeneous flow and sediment factors. The novel combination of floc data measured in Chapter 3 will likely continue to yield useful insights into floc settling velocity, especially permeability, but in the end will be limited by the inability to investigate at the micro-scale. Instead, observations at the individual floc scale will be key to pushing first-principles knowledge of the detailed interactions between floc factors. These advances will then be valuable for even further improving predictions of mud concentration and flux in rivers and deltas like those presented in Chapters 4 and 5.